

Universität Stuttgart

Fakultät 3

On the Minimization of Contact Resistance in Organic Thin-Film Transistors

Von der Fakultät Chemie der Universität Stuttgart zur Erlangung der Würde eines

Doktors der Naturwissenschaften (Dr. rer. nat.) genehmigte Abhandlung

vorgelegt von

James William Borchert

aus Franklinville, New Jersey, USA

Hauptberichterin: Prof. Dr. Sabine Ludwigs

Mitberichter: Prof. Dr. Joachim Maier

Prüfungsvorsitzender: Prof. Dr. Guido Schmitz

Tag der mündlichen Prüfung: 31.08.2020

Institut für Polymerchemie

2020

Eidesstattliche Erklärung

Hiermit versichere ich, dass ich die vorliegende Arbeit mit dem Titel

On the Minimization of Contact Resistance in Organic Thin-Film Transistors

selbstständig verfasst habe und keine anderen als die angegebenen Quellen verwendet habe.

Aus fremden Quellen entnommene Passagen und Zitate sind als solche kenntlich gemacht.

Declaration

I hereby certify that the dissertation with the title

On the Minimization of Contact Resistance in Organic Thin-Film Transistors

is entirely my own work except where otherwise indicated. Passages and quotes from other sources have been clearly indicated.

James W. Borchert

2020

Summary

Semiconductor devices are perhaps the most transformative technological development in human history. Virtually every aspect of modern society, from communication to transportation, depends in some way on a computer system dependent on (mostly) silicon-based semiconductor devices. In particular, the metal-oxide-semiconductor field-effect transistor (MOSFET) and variations of this technology have enabled ever-greater computing power through miniaturization using ever-more advanced processes, in practice following the famous Moore's Law of transistor scaling. While there are indications that this scaling trend in transistor technology is coming to its end, new developments in materials science and processing look to charge forward into the 'More than Moore' era [1], [2]. This steady progress would not have been possible without the parallel advancements in fundamental knowledge about the solid-state physics and physical chemistry that govern the charge transport in these devices. Likely, this will continue to lead to further advancements in individual computing capabilities and power efficiency for processors into the technological future of the 2020's and beyond. However, as the world around us becomes more interconnected, demand for novel applications and cost efficiency, compounded with a growing desire for more environmentally friendly solutions to our technological challenges, has led to alternative materials systems being explored and developed to replace silicon in some applications where raw computing power is no longer of paramount importance. This includes large-area electronics applications, such as information displays, solar cells and sensors, ideally fabricated on flexible or conformable substrates like plastic foil, textiles, and paper.

The challenge for the realization of these new applications is that the incumbent semiconductor materials for the thin-film transistors (TFTs) implemented in these applications, hydrogenated amorphous silicon (a-Si:H) and low-temperature polysilicon (LTPS), typically require processing temperatures well above 100 °C, limiting their implementation to only very specialized substrates with high thermal stability, such as polyimide (PI) and glass. This has led to a boom in research into various alternative semiconductors for large-area applications, especially with respect to displays. In this area, semiconducting metal oxides such as indium gallium zinc oxide (IGZO) [3] have made perhaps the most significant progress in the development of TFT backplanes for active-matrix liquid crystal displays (AMLCDs), with projected 23% of the tablet and 21% of the laptop display market shares through 2024 [4]. However, in commercial IGZO TFT fabrication, relatively high processing temperatures are

still prevalent which largely prevents their application on flexible substrates, and other issues such as bias-stress instability and a lack of suitable hole-transport (p-channel) semiconductors to enable complementary circuit design have so far prevented implementation of metal-oxide TFTs in the generally more-demanding active-matrix organic light-emitting diode (AMOLED) displays [5].

Conjugated small-molecule and polymer-organic semiconductors present another important alternative semiconductor technology, both for the active-matrix displays as well as for other potential applications in Internet of Things and biomedical applications [6]. The main advantage that organic semiconductors have over inorganic semiconductors is that they can be utilized on virtually any substrate including unconventional flexible substrates, such as plastics with low glass-transition temperatures and paper [7]. This is due to the generally much-lower processing temperatures (typically <100 °C) required for the fabrication of functional organic-semiconductor devices. Another advantage is that many organic semiconductors can be fabricated using solution-processing approaches, which may help to drive down the costs of fabrication of large-area electronic circuits [8]. These application-driven motivations aside, organic semiconductor research has proven to be a staggeringly complex and rich field for physicists, chemists, and material scientists alike to explore the fundamental processes in these materials. These two motivating factors have often intertwined, where the discovery or examination of a fundamental process has at times directly led to an application. The most notable example is that of the organic light-emitting diode (OLED), invented by researchers at the Eastman Kodak company in 1987 during their studies on the charge-recombination and light-emission phenomena in organic semiconductors [9].

The successful commercialization of OLEDs may be followed in the near future by organic photodetectors and organic solar cells, owing to recent breakthroughs in energy conversion efficiency [10]. Unfortunately, the development of organic TFTs has lagged behind compared to OLEDs and organic solar cells in many performance metrics important for circuit applications, most notably the maximum frequency of operation [11]. The reasons for this are both practical and fundamental. From a materials-engineering perspective, small-form-factor requirements for high-frequency organic TFTs place demands on the patterning approaches that are implemented for the different layers of the TFTs (source and drain contacts, gate, gate dielectric) that have so far been challenging to address completely.

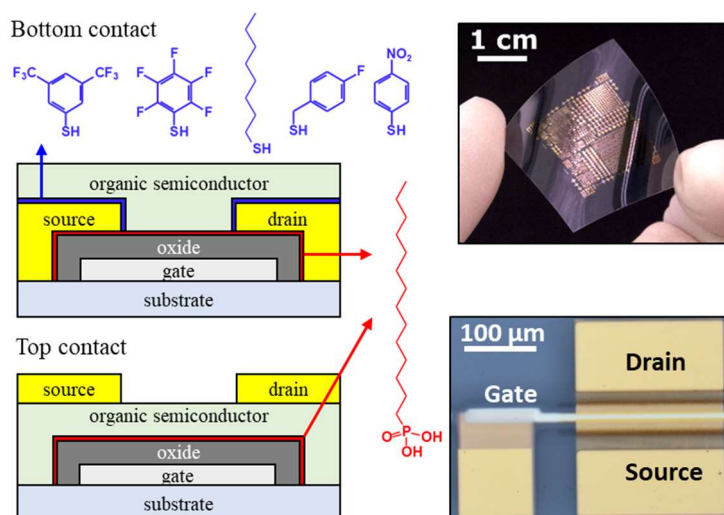
Concomitantly, the functional interfaces of organic TFTs intended for high-frequency applications have in some ways proven to be much more demanding and abstruse than in either

OLEDs or organic solar cells. This is especially true of the interface between the (typically metal) source and drain contacts and the organic-semiconductor layer of a TFT. The complex physicochemical characteristics of this interface govern the charge injection (extraction) into (out of) organic semiconductors, which for organic TFTs is typically quantified by an often very large, non-Ohmic contact resistance (typically much greater than $100 \text{ } \Omega\text{cm}$)¹ [12]. The most crucial practical consequence is that the effective charge-carrier mobility is often drastically suppressed in scaled-down organic TFTs, regardless of the intrinsic charge-carrier mobility, making it inherently difficult to achieve substantial improvements in the maximum operating frequency [13]. It is perhaps this characteristic, more than any other, that has had the effect that, while e.g. AMOLED displays show clear performance advantages over the incumbent AMLCD technology, such as better image contrast and faster response times [14], no such raw performance advantages have been realized thus far for organic TFTs compared to inorganic TFTs. The industry-standard LTPS and IGZO TFTs, or TFTs based on certain two-dimensional semiconductors like transition-metal dichalcogenides (TMD), all show typically much lower contact resistances and higher maximum operating frequencies than organic TFTs [5]. This pinpoints the reduction of the contact resistance, concurrent to the reduction of the lateral transistor dimensions, as the most crucial parameter in developing organic TFTs for high-frequency applications [15]. As a point of reference, for TFTs with lateral dimensions of approximately $1 \text{ } \mu\text{m}$, the contact resistance must be no greater than about $10 \text{ } \Omega\text{cm}$ to obtain a unity current-gain (transit) frequency of 1 GHz at supply voltages of about 3 V , i.e., sufficiently low to allow the devices to be powered by small batteries, solar cells or other energy-harvesting devices.

Therefore, the primary focus of the research work presented in this thesis is placed on studying the physicochemical characteristics of the contact-to-organic semiconductor interface and exploring possible avenues for reducing the contact resistance in organic TFTs. Achieving a contact resistance of even $100 \text{ } \Omega\text{cm}$ in organic TFTs has already proven immensely challenging compared to other semiconductors (for comparison, TMDs can already achieve contact resistances on the order of $0.01 \text{ } \Omega\text{cm}$ [16]). This generally depends on many different factors including the organic-semiconductor thin-film morphology in the vicinity of the contact interface, the contact work function, and the energetic landscape of the organic semiconductor.

¹ Note about units: Contact resistance is typically normalized by the width of the channel region in a set of TFTs.

For the first part of this thesis, especial focus is given to the influence of the device architecture, which has received comparatively less study than the other factors that can influence charge injection in organic TFTs, namely the Schottky barrier height and the work function of the contacts. The most influential



aspect in this regard is the position of the (typically metal) source and drain contacts with respect to the channel region formed at the organic semiconductor-dielectric interface upon application of a gate-source voltage (see figure). The interest in this aspect was precipitated by theoretical simulation studies of organic TFTs by Karin Zojer et al. [17], [18], wherein a previously unobserved relationship between the device architecture, contact resistance and gate-dielectric thickness was reported. Contrary to much of the conventional wisdom in the community, it was found that due to geometrical attributes of the electric field imposed by the gate-source voltage, the contact resistance could be made to be lower in a coplanar (bottom-contact) TFT architecture than in a staggered (top-contact) TFT architecture, provided the gate-dielectric layer is sufficiently thin and the Schottky-barrier height is sufficiently low (0.5 eV). The predictions from these theoretical works were tested experimentally for the first time, leading to both verification and to new record metrics for the contact resistance (as small as 10 Ωcm) as well as records for other figures of merit for organic TFTs. These include subthreshold swings at ambient temperature as low as 59 mV/decade, on/off current ratio as high as 10^{10} , signal delays below 80 ns in inverters and ring oscillators, and unity-current-gain (transit) frequencies as high as 21 MHz, all at operating voltages of around 3 V.

Motivated by the results of this first part, the second part of the thesis focuses on further investigations of the physicochemical properties of the contact interface in bottom-contact organic TFTs. In particular, the influence of the contact work function on charge injection was investigated through functionalization of the surface of the gold source and drain contacts in bottom-contact TFTs with thiol-based chemisorbed molecular monolayers (CMLs) and alkyl thiol self-assembled monolayers (SAMs). The contact-resistance results from the TFTs were complemented with various materials characterizations of the CMLs and SAMs including

ultraviolet photoemission spectroscopy (UPS), x-ray photoelectron spectroscopy (XPS), contact-angle goniometry, and polarization-modulation infrared reflection-absorption spectroscopy (PM-IRRAS). The preliminary results of these experiments suggest that, analogous to transistor technologies based on other semiconductors, the charge-injection efficiency in organic TFTs is severely limited by Fermi-level pinning. These findings are possibly of crucial importance for the further development of organic TFTs for novel electronics applications.

Zusammenfassung in deutscher Sprache

Halbleiterbauelemente sind vielleicht die transformativste technologische Entwicklung in der Geschichte der Menschheit. Praktisch jeder Aspekt der modernen Gesellschaft, von der Kommunikation bis zum Transport, wird in irgendeiner Weise von Computersystemen gesteuert, die auf Silizium-Halbleiterbauelementen basieren. Insbesondere der Metalloxid-Halbleiter-Feldeffekttransistor (MOSFET) und Variationen dieser Technologie haben eine immer größere Rechenleistung durch Miniaturisierung unter Verwendung immer fortschrittlicherer Verfahren ermöglicht, die in der Praxis dem berühmten Mooresches Gesetz der Transistorskalierung folgen. Dieser stetige Fortschritt wäre ohne die parallelen Fortschritte im Grundwissen über die Festkörperphysik und die physikalische Chemie, die den Ladungstransport in diesen Geräten steuern, nicht möglich gewesen. Zwar gibt es Hinweise darauf, dass dieser Skalierungstrend in der Transistortechnologie zu Ende geht, doch scheinen neue Entwicklungen in der Materialwissenschaft in die Ära „More than Moore“ vorzudringen [1], [2]. Dies wird aller Wahrscheinlichkeit nach weiterhin zu Fortschritten bei den individuellen Rechenkapazitäten und der Energieeffizienz für Prozessoren in der technologischen Zukunft der 2020er Jahre und darüber hinaus führen. Mit zunehmender Vernetzung der Welt um uns herum hat die Nachfrage nach neuartigen Anwendungen und Kosteneffizienz, verbunden mit einer wachsenden Bedeutung für umweltfreundlichere Lösungen für unsere technologischen Herausforderungen, dazu geführt, dass alternative Materialsysteme erforscht und entwickelt wurden, um Silizium in einigen Anwendungen zu ersetzen, wo rohe Rechenleistung nicht mehr von größter Bedeutung ist. Dies umfasst großflächige elektronische Anwendungen wie Bildschirme, Solarzellen und Sensoren, die idealerweise auf mechanisch flexiblen Substraten wie Kunststofffolien, Textilien und Papier hergestellt werden können.

Die Herausforderung für die Realisierung dieser neuen Anwendungen besteht darin, dass etablierte Halbleitermaterialien wie einkristallines Silizium, amorphes Silizium (a-Si:H) und polykristallines Silizium (LTPS) typischerweise Verarbeitungstemperaturen von weit über 100 °C erfordern, was den Einsatz dieser Halbleitermaterialien auf Substrate mit hoher thermischer Stabilität wie Quarz, Glas oder Polyimid (PI) beschränkt. Dies hat zu einem Boom bei der Erforschung alternativer Halbleiter, insbesondere für die Realisierung der Dünnschicht-Transistoren (TFTs) in Aktiv-Matrix-Bildschirmen. In diesem Bereich haben halbleitende Metalloxide wie Indium-Gallium-Zinkoxid (IGZO) [3] möglicherweise die bedeutendsten

Fortschritte erzielt. Es wird erwartet, dass im Jahr 2024 bereits mehr als 20% aller Tablet- und Laptop-Computer über Flüssigkristall-Bildschirme (AMLCDs) basierend auf IGZO-TFTs verfügen werden [4]. Bei der kommerziellen IGZO-TFT-Herstellung sind jedoch immer noch relativ hohe Verarbeitungstemperaturen notwendig, was deren Verwendung auf flexiblen Polymersubstraten stark einschränkt. Ein weiterer Nachteil halbleitender Metalloxide ist das Fehlen geeigneter p-Kanal-Halbleiter, was die Realisierung energiesparender komplementärer integrierter Schaltungen verhindert. In den im Vergleich zu AMLCDs allgemein anspruchsvolleren Bildschirmen auf der Basis organischer Leuchtdioden (AMOLED) werden die Metalloxid-TFTs voraussichtlich auch in Zukunft die LTPS-TFTs nicht ersetzen [5].

Konjugierte organische Halbleiter sind eine weitere wichtige alternative Halbleitertechnologie, sowohl für die Bildschirmtechnologie als auch für andere potenzielle Anwendungen im Internet der Dinge (IoT) und für biomedizinische Anwendungen [6]. Der wichtigste Vorteil organischer gegenüber anorganischen Halbleitern besteht darin, dass sie auf praktisch jedem Substrat verwendet werden können, einschließlich unkonventioneller flexibler Substrate wie Kunststoffen mit niedrigen Glasübergangstemperaturen und Papier [7]. Dies ist auf die im Allgemeinen viel niedrigeren Verarbeitungstemperaturen (typischerweise $<100\text{ }^{\circ}\text{C}$) zurückzuführen, die für die Herstellung organischer Halbleiterbauelemente erforderlich sind. Ein weiterer Vorteil besteht darin, dass viele organische Halbleiter aus Lösung verarbeitet werden können, was dazu beitragen kann, die Kosten für die Herstellung großflächiger elektronischer Schaltungen zu senken [8]. Abgesehen von diesen anwendungsbedingten Motivationen hat sich die Forschung an organischen Halbleitern für Physiker, Chemiker und Materialwissenschaftler als erstaunlich komplexes und reichhaltiges Feld erwiesen, um die grundlegenden Prozesse in diesen Materialien zu untersuchen. Diese beiden motivierenden Faktoren haben sich oft miteinander verflochten, wo die Entdeckung oder Untersuchung eines grundlegenden Prozesses zuweilen direkt zu einer Anwendung geführt hat. Das bemerkenswerteste Beispiel ist die organische Leuchtdiode (OLED), die 1987 von Forschern der Firma Eastman Kodak während ihrer Untersuchungen zu Ladungsrekombinations- und Lichtemissionsphänomenen in organischen Halbleitern erfunden wurde [9].

Nach der erfolgreichen Vermarktung von OLEDs könnten in naher Zukunft organische Solarzellen (OPV) und organische Fotodetektoren folgen [10]. Im Vergleich dazu verlief die Entwicklung organischer TFTs in Hinblick auf wichtige Leistungskriterien bisher deutlich weniger dynamisch, insbesondere in Bezug auf die Grenzfrequenz organischer TFTs [11]. Die Gründe dafür sind sowohl grundlegend als auch praktisch. Aus materialtechnischer Sicht stellt

die für Hochfrequenzanwendungen notwendige Miniaturisierung der Transistoren enorme Anforderungen an die Strukturierung der Materialien, die für die verschiedenen Schichten der TFTs (Source- und Drain-Kontakte, Gate, Gate-Dielektrikum) zum Einsatz kommen.

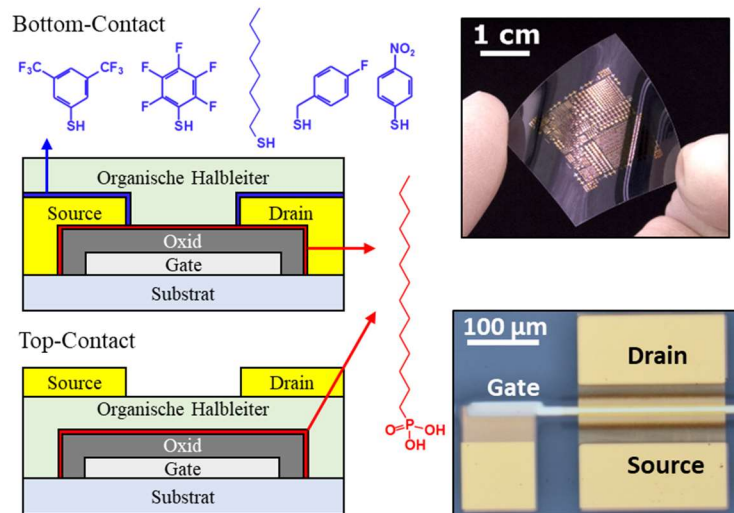
Gleichzeitig haben sich die Grenzflächen zwischen den verschiedenen Materialien in organischen TFTs in gewisser Weise als viel anspruchsvoller erwiesen als in OLEDs oder organischen Solarzellen. Dies gilt insbesondere für die Grenzflächen zwischen den (typischerweise metallischen) Source- und Drain-Kontakten einerseits und der organischen Halbleiterschicht andererseits. Die komplexen physikalischen und chemischen Eigenschaften dieser Grenzflächen haben einen großen Einfluss auf die Effizienz des Ladungsaustauschs zwischen den Metallkontakten und der organischen Halbleiterschicht. Typischerweise ist der Kontaktwiderstand organischer TFTs nichtlinear und auch deutlich größer als in Transistoren auf der Basis anorganischer Halbleiter (typischerweise größer als $100 \Omega\text{cm}^2$) [12]. Der hohe Kontaktwiderstand hat zur Folge, dass die für die Erhöhung der Grenzfrequenz organischer TFTs unbedingt notwendige Reduzierung der Kanallänge zu einer oft dramatischen Erhöhung der effektiven Ladungsträgerbeweglichkeit (unabhängig von der intrinsischen Ladungsträgerbeweglichkeit) führt [13]. Um die Grenzfrequenz organischer TFTs signifikant zu erhöhen ist es daher zwingend notwendig, sowohl den Kontaktwiderstand als auch die lateralen Abmessungen der TFTs deutlich zu verringern [15]. Eine Grenzfrequenz von 1 GHz bei einer Versorgungsspannung von 3 V erfordert z.B. laterale Abmessungen deutlich unterhalb von $1 \mu\text{m}$ und einen Kontaktwiderstand unterhalb von $10 \Omega\text{cm}$.

Daher liegt der Schwerpunkt der hier zusammen gefassten Forschungsarbeiten auf der Untersuchung der physikalischen und chemischen Eigenschaften der Grenzflächen zwischen den Source- und Drain-Kontakten und der organischen Halbleiterschicht und der Entwicklung von Ansätzen zur deutlichen Verringerung des Kontaktwiderstands organischer TFTs.

Im ersten Teil der Arbeit liegt der Schwerpunkt auf der Abhängigkeit des Kontaktwiderstands vom Aufbau des Transistors (siehe Abbildung). Dieser Zusammenhang wurde schon häufig untersucht, meist mit dem Ergebnis, dass der „Top-Contact“-Aufbau zu kleineren Kontaktwiderständen führt als der „Bottom-Contact“-Aufbau. Allerdings wurde dabei nie der Einfluss der Schichtdicke des Gate-Dielektrikums auf den Kontaktwiderstand berücksichtigt, sondern es wurde stets davon ausgegangen, dieser sei unabhängig von der Schichtdicke des Gate-Dielektrikums. Kürzlich von Karin Zojer et al. durchgeführte Simulationen [17], [18] haben allerdings gezeigt, dass der Kontaktwiderstand organischer

² Hinweis zu Einheiten: Der Kontaktwiderstand wird in der Regel auf die Kanalbreite des TFTs normalisiert.

TFTs im „Bottom-Contact“-Aufbau stark von der Schichtdicke des Gate-Dielektrikums abhängt, vorausgesetzt, die Schottky-Barriere an der Grenzfläche zwischen Kontakt und Halbleiterschicht ist ausreichend niedrig ($\leq 0,5$ eV). In der vorliegenden Arbeit wurden diese Vorhersagen erstmals



experimentell getestet und bestätigt, mit dem Ergebnis einer deutlichen Verringerung des Kontaktwiderstands im Vergleich zu den besten zuvor publizierten Ergebnissen ($10 \Omega\text{cm}$). Zudem wurden so auch neue Bestwerte für den Unterschwellenanstieg (59 mV/Dekade), das Modulationsverhältnis (10^{10}), die Signalverzögerung in Ringoszillatoren (79 ns) und die Grenzfrequenz (21 MHz) organischer Transistoren erzielt, alle bei vergleichsweise niedrigen versorgungsspannungen von ca. 3 V.

Motiviert durch die Ergebnisse dieses ersten Teils konzentriert sich der zweite Teil der Arbeit auf weitere Untersuchungen der physikalischen und chemischen Eigenschaften der Grenzflächen organischer TFTs im „Bottom-Contact“-Aufbau. Insbesondere wurde untersucht, inwieweit die Austrittsarbeit der Source- und Drain-Kontakte durch die gezielte Funktionalisierung mit Thiol-basierten Monolagen an die Orbitalenergien des organischen Halbleiters angepasst werden kann und welchen Einfluss dies auf den Kontaktwiderstand der TFTs hat. Diese Untersuchungen erfolgten u. a. mittels Ultraviolet-Photoemissionsspektroskopie (UPS), Röntgen-Photoelektronenspektroskopie (XPS), Kontaktwinkelgoniometrie und Polarisations-Modulations-Infrarot-Reflexions-Absorptionsspektroskopie (PM-IRRAS). Die vorläufigen Ergebnisse dieser Experimente legen nahe, dass die untere Grenze des Kontaktwiderstands in organischen TFTs (wie auch in Transistoren basierend auf anorganischen Halbleitern) durch das Fermi-Level-Pinning definiert wird. Diese Erkenntnisse sind möglicherweise von entscheidender Bedeutung für die Weiterentwicklung organischer TFTs.

Acknowledgements

First and foremost, the work presented in this thesis would not have been possible without the opportunity given by Dr. Hagen Klauk at the Max Planck Institute and Professor Dr. Sabine Ludwigs at the University of Stuttgart. I would also like to give my sincerest gratitude to the members of my committee, Professor Dr. Joachim Maier and Professor Dr. Guido Schmitz, for taking the time out of their busy schedules to review and evaluate my work.

Various other individuals deserve my gratitude for their advice, collaboration, intellectually stimulating discussions, and/or help with experiments over the course of my studies. The help and support of my group mates, past and present, was essential to my success: Dr. Ute Zschieschang, Michael Geiger, Rachana Acharya, Tobias Wollandt, Sabrina Steffens, Mélanie Brouillard, Dr. Mahdiah Schmidt, Dr. Sibani Bisoyi, Dr. Klaus Dirnberger, Sherri Liu, Dr. Daniel Trefz, and Zheyu Wu.

Acknowledgement must also go to Professor Dr. Jürgen Weiss and the entire Nanostructuring team for maintaining the outstanding facilities at the MPI. In particular, I want to thank Marion Hagel for her contribution to essential parts of the sample fabrication for the gate-dielectric thickness study presented in Chapter 5.

Thank you to Dr. Rotraut Merkle for her excellent guidance as my external advisor at the MPI and to Dr. Hans Boschker for reviewing both of my now-published articles and for his generally helpful advice on all matters scientific and otherwise.

I have also had the pleasure to work closely with various individuals at other institutions: Professor Dr. Karin Zojer, Dr. Boyu Peng, Professor Dr. Paddy K. L. Chan, Dr. Michele Giorgio, Professor Dr. Mario Caironi, Professor Dr. Joachim Burghartz, Professor Dr. R. Thomas Weitz, Dr. Florian von Wrochem, and the group of Professor Dr. Alexander Kloes.

Special regards go also to my fellow 2017 PhD representatives for a fun year working together to make PhD life at the MPI as rewarding as possible: Dr. Jan-Philipp Günther, Dr. Katrin Fürsich, Dr. Alessio Scavuzzo, Dr. Maryam Nojabae, and Dr. Elham Sharifikolouei.

Finally, I wish to acknowledge the steadfast support from my family, friends, and most especially my wife, Laura. This would not have been possible without you by my side.

Contents

Eidesstattliche Erklärung	iii
Summary	v
Zusammenfassung in deutscher Sprache	xi
Acknowledgements	xv
Contents	xvii
List of figures	xxi
List of tables	xxv
1 Introduction to organic electronics	1
1.1 Organic semiconductor materials	2
1.1.1 Polymers	2
1.1.2 Small molecules	4
1.1.3 N-type organic semiconductors	6
1.2 Organic semiconductor thin-film morphology	9
1.2.1 Polymers	10
1.2.2 Small molecules	11
1.3 Charge transport physics in organic semiconductors	17
1.3.1 Modeling charge transport in organic semiconductors	20
1.3.2 Generalized Einstein relation with attenuated delocalization	21
1.3.3 Transient localization and the path towards higher carrier mobility in organic semiconductors	24
1.3.4 Doping of organic semiconductors	25
1.4 Dinaphtho[2,3-b:2',3'-f]thieno[3,2-b]thiophene (DNFTT) and its functional derivatives	29
2 Organic thin-film transistors	31

2.1	Static operation of organic thin-film transistors.....	33
2.1.1	Subthreshold regime	35
2.1.2	On-state: linear regime.....	36
2.1.3	On-state: saturation regime	36
2.1.4	Field-effect mobility	37
2.1.5	Off-state regime	38
2.2	Dynamic operation of organic thin-film transistors	39
2.2.1	Measurement of the transit frequency.....	41
2.2.2	Inverters and ring oscillators.....	43
2.3	Contact resistance in organic thin-film transistors.....	45
2.4	Measuring the contact resistance in TFTs.....	52
2.4.1	The gated transmission line method	52
2.4.2	Small-signal measurements	54
2.4.3	Extraction from measurements of the transit frequency	56
2.4.4	Other single-device extraction methods.....	57
3	The functional interfaces in organic thin-film transistors.....	59
3.1	The organic semiconductor-contact interface	60
3.1.1	Energy-level alignment at interfaces between organic semiconductors and metals	60
3.1.2	Fermi-level pinning.....	64
3.1.3	Charge injection physics	67
3.2	The organic semiconductor-gate dielectric interface	71
3.3	Interface-modification approaches.....	73
3.3.1	Interlayers and contact doping to improve charge injection.....	73
3.3.2	Chemisorbed molecular monolayers and self-assembled monolayers	74
4	Experimental.....	79
4.1	Fabrication of TFTs and circuits	79

4.1.1	TFTs with different gate-oxide thicknesses and contact treatments on silicon substrates.....	80
4.1.2	TFTs and circuits on flexible PEN substrates.....	83
4.2	Semiconductor thin-film morphology characterization	85
4.3	Characterization of chemisorbed molecular monolayers on Au substrates	86
4.4	DC and AC electrical measurements of organic thin-film transistors and circuits...	88
4.5	Two-port network analysis.....	88
5	Analysis of the effects of device architecture on organic thin-film transistors	89
5.1	Gate-dielectric thickness and the contact resistance	92
5.1.1	Semiconductor thin-film morphology characterization.....	94
5.1.2	Evaluation of the contact resistance.....	97
5.2	Low-voltage transistors on flexible substrates	103
5.2.1	Static electrical performance and contact resistance	104
5.2.2	Temperature dependence of the electrical characteristics of bottom-contact thin-film transistors based on DPh-DNTT	109
5.2.3	Extension to transistors with small channel lengths	116
5.2.4	Low-voltage circuit performance characteristics.....	118
5.2.5	Two-port network analysis	121
5.2.6	Influence of the channel length on dynamic performance.....	124
5.2.7	Influence of the gate-to-contact overlaps.....	128
5.3	Additional points of consideration and ongoing research.....	134
5.3.1	Bias-stress stability	134
5.3.2	Reproducibility of the bottom-contact transistors.....	135
5.3.3	Bottom-contact TFTs based on C ₁₀ -DNTT.....	137
5.3.4	N-channel organic TFTs based on N1100	139
5.4	Conclusions	141

6	Charge injection in bottom-contact organic thin-film transistors using contacts functionalized with thiol-based chemisorbed molecular monolayers.....	143
6.1	Chemisorbed monolayer characterization.....	146
6.1.1	Contact angle, XPS and UPS measurements	146
6.1.2	Infrared spectroscopy of thiols used to form chemisorbed monolayers on gold	149
6.2	Dependence of the contact resistance on the thickness (chain length) of an alkyl-thiol monolayer	163
6.3	Dependence of the contact resistance on work-function tuning using thiols with large dipoles	170
6.3.1	DNTT morphology characterization.....	170
6.3.2	UPS measurements of DNTT on substrates with different work functions.....	174
6.3.3	Static electrical performance of the DNTT TFTs	175
6.3.4	Contact resistance analysis	177
6.4	Conclusions	180
7	Final conclusions and remarks.....	181
	Symbols and Abbreviations	186
	Appendix.....	193
A.1	SEM micrographs of bottom-contact organic TFTs presented in Chapter 5	193
A.2	Additional measurements of organic TFTs.....	196
A.3	Literature overview of contact resistance in organic thin-film transistors.....	197
	Bibliography	202
	Publications.....	224

List of figures

Figure 1.1 Conjugation	1
Figure 1.2 Conjugated polymers.....	2
Figure 1.3 Conjugated small molecules.....	4
Figure 1.4 BTBT and DNNT	5
Figure 1.5 N-type organic semiconductors.....	7
Figure 1.6 Length scales of organic semiconductor structure-property relationships.	9
Figure 1.7 Polymer morphology.	10
Figure 1.8 Crystal packing of small molecules.....	11
Figure 1.9 Pentacene thin-film morphology.	13
Figure 1.10 Liquid crystalline organic semiconductors.....	16
Figure 1.11 Semiconductor energy band diagrams.....	18
Figure 1.12 Charge transport in organic semiconductors	20
Figure 1.13 Application of the generalized Einstein-relation approach for the description of charge transport in organic semiconductors.	23
Figure 1.14 Doping organic semiconductors with small molecules.....	25
Figure 1.15 Trap-state filling in organic semiconductors with dopants	27
Figure 1.16 DNNT synthesis and device performance properties	29
Figure 2.1 Device architectures of organic thin-film transistors.	31
Figure 2.2 Static operation regimes of organic thin-film transistors.	33
Figure 2.3 Energetics of channel formation in an organic thin-film transistor.....	34
Figure 2.4 Dynamic small-signal operation of an organic thin-film transistor.....	39
Figure 2.5 Two-port network analysis of a thin-film transistor.....	42
Figure 2.6 Biased-load inverter and ring-oscillator circuits.	43
Figure 2.7 Literature summary of the width-normalized contact resistance ($R_C W$) reported in organic thin-film transistors (TFTs).....	46
Figure 2.8 Charge carrier injection and transport in organic thin-film transistors.	47
Figure 2.9 Electric field in organic thin-film transistors.....	49
Figure 2.10 Transmission line method analysis of organic-thin film transistors.....	54

Figure 2.11 Lumped circuit-element model of organic thin-film transistors.....	55
Figure 2.12 Dependence of transit frequency on channel length and contact resistance.	57
Figure 3.1 Metal-organic semiconductor contact.	60
Figure 3.2 Origins of the interface dipole.....	62
Figure 3.3 Organic semiconductor-metal interfaces.....	63
Figure 3.4 Fermi-level pinning at organic semiconductor-metal interfaces.	65
Figure 3.5 Charge-carrier injection from a metal contact into an organic semiconductor.	67
Figure 3.6 Chemisorbed molecular monolayers for interface modification.	75
Figure 3.7 Contact modification with pentafluorobenzenethiol.	77
Figure 4.1 Schematic diagram of the apparatus for sample fabrication	79
Figure 4.2 Fabrication of flexible organic thin-film transistors.....	83
Figure 5.1 Organic thin-film transistors with a global-back-gate electrode in the top -contact and bottom-contact architecture.	93
Figure 5.2 AFM and SEM morphological characterization of vacuum-deposited DPh-DNTT films on rigid substrates.....	95
Figure 5.3 Grazing incidence x-ray diffraction characterization of vacuum-deposited DPh-DNTT films on rigid substrates.....	96
Figure 5.4 Transfer characteristics of organic thin-film transistors with different gate-dielectric thicknesses.	97
Figure 5.5 Application of the transmission line method (TLM) to organic thin-film transistors with different gate-dielectric thicknesses.....	98
Figure 5.6 Width-normalized contact resistance as a function of the gate overdrive voltage.	99
Figure 5.7 Estimation of the interface resistance.....	101
Figure 5.8 Inverted organic thin-film transistors on flexible substrates.....	103
Figure 5.9 Thin-film morphology of DPh-DNTT deposited on flexible substrates.	104
Figure 5.10 Organic thin-film transistors fabricated on flexible PEN substrates employed for the TLM analysis.	105
Figure 5.11 Static electrical characteristics of top-contact and bottom-contact organic thin-film transistors on flexible PEN substrates.....	107

Figure 5.12 Flexible bottom-contact organic thin-film transistor showing record on/off ratio and subthreshold swing.....	108
Figure 5.13 Static TFT characteristics at different temperatures.....	109
Figure 5.14 Temperature-dependent TLM: Intrinsic-channel mobility.....	111
Figure 5.15 Temperature dependent TLM: Contact-resistance modelling.....	113
Figure 5.16 TLM analysis of organic thin-film transistors on a flexible PEN substrate with small channel lengths.....	116
Figure 5.17 Estimation of the interface resistance for TFTs with small channel lengths.....	117
Figure 5.18 Dynamic performance of unipolar ring oscillators on flexible substrates.....	119
Figure 5.19 Static and dynamic inverter characteristics.....	120
Figure 5.20 Two-port network analysis of flexible organic transistors.....	123
Figure 5.21 Static characteristics of transistors for two-port network analysis with different channel lengths.....	124
Figure 5.22 Gain and capacitance of organic thin-film transistors with different channel lengths.	126
Figure 5.23 Contact-resistance extraction from the channel-length dependence of the transit frequency.....	127
Figure 5.24 Static characteristics of transistors for two-port network analysis with asymmetric gate-to-contact overlaps.....	128
Figure 5.25 Au-nanocluster channel penetration due to shadowing effects in top-contact TFTs.	129
Figure 5.26 Gain, transit frequency and capacitance of organic thin-film transistors with asymmetric overlaps.....	131
Figure 5.27 Capacitance contributions in organic thin-film transistors with asymmetric gate-to-contact overlaps.....	132
Figure 5.28 Bias-stress stability of bottom-contact and top-contact TFTs.....	134
Figure 5.29 Reproducibility of small-channel bottom-contact DPh-DNTT TFTs.....	136
Figure 5.30 Flexible bottom-contact C ₁₀ -DNTT TFTs and circuits.....	137
Figure 5.31 Delamination of C ₁₀ -DNTT over time.....	138
Figure 5.32 Flexible bottom-contact TFTs using the n-channel semiconductor N1100.....	140

Figure 6.1 Surface energy and work function of various CML/SAM-functionalized Au contacts.	147
Figure 6.2 X-ray photoemission spectroscopy (XPS) of chemisorbed monolayers on Au.	149
Figure 6.3 Infrared spectroscopy of alkyl thiol SAMs on Au.....	151
Figure 6.4 Infrared spectroscopy of pentafluorobenzenethiol (PFBT).....	153
Figure 6.5 Infrared spectroscopy of 4-nitrothiophenol (NOTP).....	155
Figure 6.6 Infrared spectroscopy of 4-fluorobenzylmercaptan (FBM)	157
Figure 6.7 Infrared spectroscopy of 3,5-bis-trifluoromethylbenzenethiol (BTFMBT).	159
Figure 6.8 Infrared spectroscopy of 1H,1H,2H,2H-perfluoro-1-decanethiol (PFDT).....	161
Figure 6.9 Surface morphology of nominally 40-nm-thick DNTT layers deposited by sublimation in vacuum onto gold contacts with and without functionalization with 1-decanethiol.	164
Figure 6.10 Static TFT characteristics: influence of contact functionalization with alkyl-thiols with various chain lengths.	165
Figure 6.11 TLM analysis: influence of contact modification with alkyl thiols.	167
Figure 6.12 Electron microscopy and grazing-incidence x-ray diffraction analyses of DNTT films on Au contacts functionalized with various thiols.....	171
Figure 6.13 Flexible DNTT thin-film transistors with various contacts.....	173
Figure 6.14 Evidence of Fermi-level pinning in DNTT.	174
Figure 6.15 Static TFT characteristics: tuning the contact work function with different thiols.	176
Figure 6.16 TLM analysis results for TFTs with various contact work functions.	178
Figure A1.1 Small-channel length TFTs used for TLM analysis shown in Figure 5.16.	193
Figure A1.2 Small-channel length bottom-contact TFTs used for two-port network analysis shown in Figure 5.21.....	194
Figure A1.3 Small-channel length top-contact TFTs used for two-port network analysis shown in Figure 5.21.	195
Figure A1.4 Bottom-contact DNTT transistors fabricated with electron-beam lithography.....	196

List of tables

Table 2.1: Methods for extracting the contact resistance using single devices.	58
Table 4.1: Thiols used for the formation of chemisorbed molecular monolayers (CML) and self-assembled monolayers (SAM) on gold contacts in this work.....	82
Table 5.1: Width-normalized transconductance and transit frequency of DPh-DNTT TFTs as a function of device geometry and channel length.	125
Table 5.2: Summary of TFT and circuit performance parameters reported in this chapter.....	142
Table 6.1: Infrared vibrational assignments for <i>n</i> -alkyl-thiol self-assembled monolayers (SAMs) on Au.....	151
Table 6.2: Infrared vibrational assignments for pentafluorobenzenethiol (PFBT).....	153
Table 6.3: Infrared vibrational assignments for 4-nitrothiophenol (NOTP).....	155
Table 6.4: Infrared vibrational assignments for 4-fluorobenzylmercaptan (FBM)	157
Table 6.5: Infrared vibrational assignments for 3,5-bis-trifluoromethylbenzenethiol (BTFMBT)	159
Table 6.6: Infrared vibrational assignments for 1H,1H,2H,2H-perfluoro-1-decanethiol (PFDT)	161
Table A.1: Channel-width-normalized contact resistance (R_{cW}) reported for the maximum reported gate overdrive voltage or gate voltage.....	197

1 Introduction to organic electronics

The idea of using conjugated organic molecules to conduct electronic charge in electronic devices dates back to the 1940s [19]. Exceptional interest for real applications, however, did not fully manifest itself until the discovery and development of conductive polyacetylene by Heeger, MacDiarmid, and Shirakawa in the 1970s; work for which they were awarded the 2000 Nobel Prize in Chemistry. Since then, tremendous research efforts in both academia and industry have led to the development of organic-semiconductor devices for the marketplace.

The physical origin of electronic conductivity in some classes of organic molecules stems from the ability of carbon to form molecules with molecular conjugation through hybridized sp^2 orbitals. This results from a resonance in the ordering of the alternating single and double bonds between each of the atoms either in a conjugated chain (e.g. polyacetylene) or in an aromatic ring (e.g. benzene, see Figure 1.1). Delocalization of the electrons in the π -molecular orbitals of the molecule then provides a charge-conduction pathway and improves the overall stability of the molecule. In thin films, neighboring molecules interact via weak van der Waals interactions such that interorbital overlap (often referred to as ‘ π -stacking’) enables intermolecular transport of charge carriers in crystals and polycrystals. The π -electron density of the interacting molecules in the film can greatly affect both the optical and transport properties of the material, determining properties such as the optical band gap, the electrical band gap and the charge-carrier mobility [20].

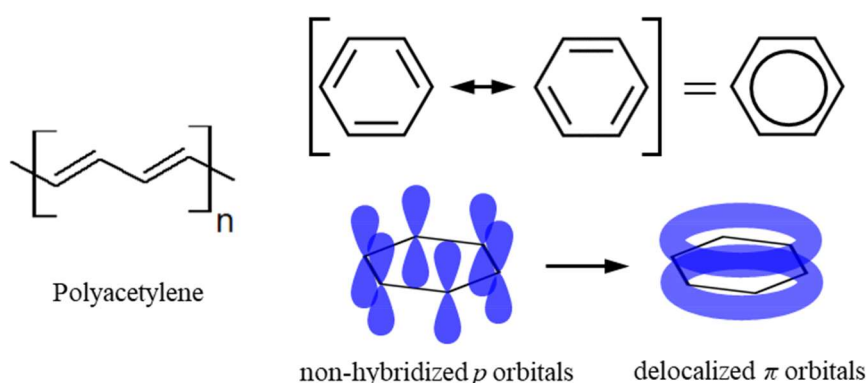


Figure 1.1 Conjugation

Conjugation in polyacetylene and benzene. Resonance of the single and double bonds results in delocalized π orbitals, providing an intermolecular conduction pathway.

1.1 Organic semiconductor materials

1.1.1 Polymers

Generally, organic semiconductors can be grouped into two classes: small molecules (oligomers) and polymers. The chemical structures of some of the most notable of these are shown in Figure 1.2. Polyaniline is one of the most well-known and widely-studied conjugated polymers, though prior to the discovery of its electrical conductivity in the 1960s, it was mainly used as a dye material [21]. The conductivity of thin films composed of conjugated polymers depends primarily on the oxidation state of the molecules and the structural properties of the molecule, which in turn can determine the morphology of the thin films. In a prototypical example, the addition of alkyl side groups to a polythiophene backbone as in the case of poly(3-hexylthiophene) (P3HT) enhances the electrical and optical properties of the polymer via side-chain-induced ordering of the thin films, such that a lamellar structure with a small π -stacking separation distance of about 3.8 Å and an interlayer spacing of about 16.0 Å were determined from x-ray diffraction measurements [22]. This development enabled the use of P3HT in organic thin-film transistors (TFTs) [23] and serves as an initial highlight of the structure-property relations that are often key to the development of materials for organic

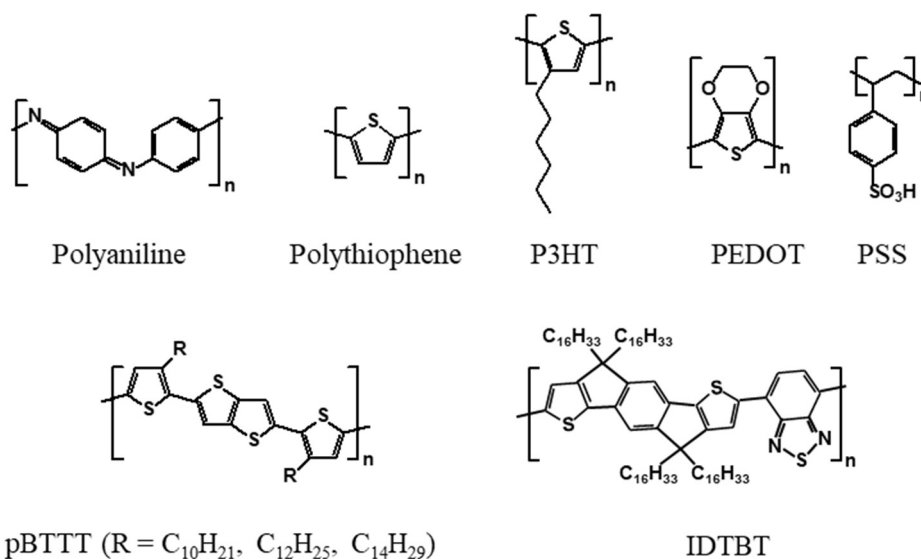


Figure 1.2 Conjugated polymers

Exemplary polymers investigated in organic-electronics applications. P3HT: poly(3-hexylthiophene), PEDOT: poly(3,4-ethylenedioxythiophene), PSS: polystyrene sulfonate, pBTTT: poly(2,5-bis(3-alkylthiophen-2-yl)thieno[3,2-*b*]thiophene), IDTBT: poly(indacenodithiophene-benzothiadiazole).

electronics. In the extreme case of polymer conductors (also termed ‘synthetic metals’), high conductivity can be induced by, e.g., halogenation of polyacetylene as was done by Heeger, MacDiarmid, and Shirakawa in their ground-breaking work [24]. However, this method is rather unstable in practice due to the rapid evaporation of the halogen from the polymer in ambient conditions, a fact which led to fervent research to improve the stability of conducting polymers by adopting other means to render them highly conductive. An important result was the development of poly(3,4-ethylenedioxythiophene) (PEDOT) which, owing to a lower redox potential and more moderate band gap, shows high stability in ambient conditions in addition to being transparent and highly conductive [25]. The only drawback to PEDOT is that it is largely insoluble in most industrial solvents. This issue can mostly be circumvented by synthesizing PEDOT in poly(styrenesulfonic acid) to produce a water-emulsion solution of PEDOT mixed with polystyrene sulfonate (PSS) (the mixed material is commonly denoted as PEDOT:PSS) [26]. Crispin et al. showed that with the addition of a secondary dopant such as diethylene glycol to induce phase separation of the conducting PEDOT from the insulating PSS component, PEDOT:PSS thin films could show conductivity on the order of 10 S/cm [27]. Since then, further developments in post-processing approaches of PEDOT:PSS thin films has led to conductivities in excess of 1400 S/cm, making them useful for contacts in flexible electronics applications [28].

For the further development of high-mobility polymer semiconductors, the recent trend has been focused on donor–acceptor (D–A) copolymers with alternating electron-rich and electron-deficient units along the backbone of the polymer chains [29], [30]. Two such notable materials are the family of poly(2,5-bis(3-alkylthiophen-2-yl) thieno[3,2-*b*]thiophene) (pBTTT) polymers and poly(indacenodithiophene-benzothiadiazole) (IDTBT) originally reported by Iain McCulloch et al. [31]–[33]. It is now common for such polymer semiconductors to exceed charge carrier mobilities above $1 \text{ cm}^2 \text{ V}^{-1} \text{ s}^{-1}$, making them useful for applications in bulk-heterojunction solar cells with excellent efficiency and organic thin-film transistors (TFTs).

1.1.2 Small molecules

Along with polymers, organic semiconductor small molecules (Figure 1.3) have also seen fervent research and development over the past decades, both in terms of chemical and device engineering and investigations into their underlying physics and chemistry. The most ubiquitous of the small-molecule variety of organic semiconductors is undoubtedly pentacene, with some of the first pentacene TFTs reported in 1996-97 by the group of Thomas N. Jackson at the Pennsylvania State University [34]–[36]. Small molecules like pentacene can in principle be either deposited in vacuum or from solution, though the addition of alkyl or other side groups is usually needed to increase the solubility. For instance, the solubility of pure pentacene and other linear acenes is generally very poor in standard organic solvents, and so fabrication methods were relegated to vacuum processing until the advent of 6,13-bis(triisopropylsilyl)ethynyl)pentacene (TIPS pentacene) which solubilizes the pentacene core molecule by the attachment of triisopropyl groups to the 6 and 13 positions, enabling solution-cast films that proved especially interesting for use in organic TFTs [37]. Further,

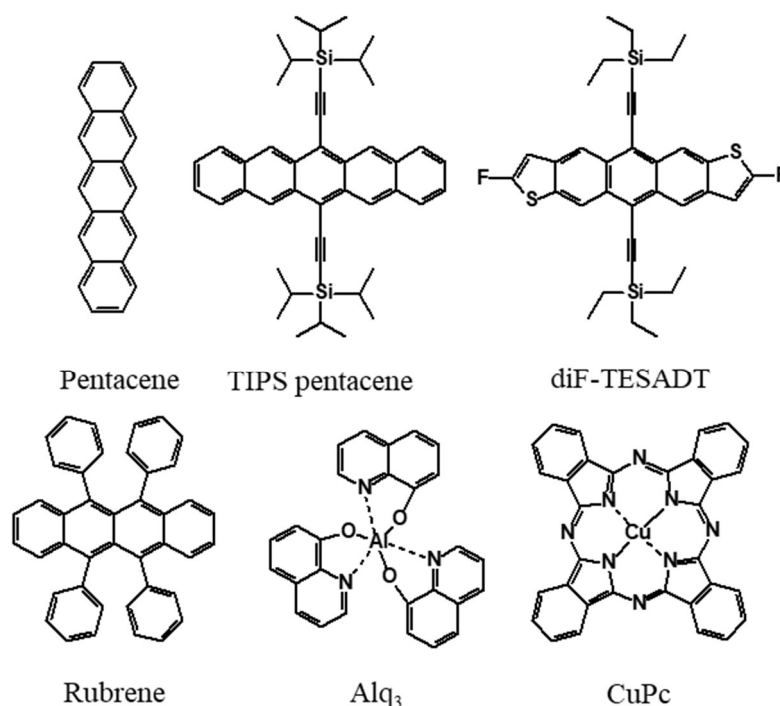


Figure 1.3 Conjugated small molecules

Exemplary small molecules investigated in organic-electronics applications. TIPS pentacene: 6,13-bis(triisopropylsilyl)ethynyl)pentacene, diF-TESADT: 2,8-difluoro-5,11-bis(triethylsilyl)ethynyl)anthradithiophene, rubrene: 5,6,11,12-tetraphenyltetracene, Alq₃: tris(8-hydroxyquinolinato)aluminum, CuPc: copper phthalocyanine.

improvements of the crystal packing of acenes and heteroacenes can be achieved by functionalization with other side groups and/or by careful processing (see the following section on morphology) [38]. A notable example is a tetracene-core molecule functionalized with phenyl side groups (5,6,11,12-tetraphenyltetracene, more commonly known as rubrene). Podzorov et al. showed that the intrinsic band-like transport of charge carriers in rubrene single crystals can be observed when it is used as the active layer in transistors [39], [40]. Later, highly ordered single crystals of rubrene with the highest room-temperature mobility yet reported³ for organic transistors were demonstrated by Takeya et al. [41]. In organic light-emitting diodes (OLEDs) and organic photovoltaic (OPV) devices, metal-coordination complexes such as tris(8-hydroxyquinolino)aluminum (Alq₃) play important roles as electron transporters with high electroluminescence efficiency [42]. Metal phthalocyanines such as copper phthalocyanine (CuPc) have been used as dyes and also as the active materials in organic transistors, in some cases showing carrier mobilities up to 10 cm²/Vs [43]. In more recent developments, increased attention has been given to heteroacenes containing fused chalcogenophene compounds such as benzothieno[3,2-b]benzothiophene (BTBT) and dinaphtho[2,3-b:2',3'-f]thieno[3,2-b]thiophene (DNNT) and their functionalized derivatives which have been implemented in high-performance organic TFTs which show increased

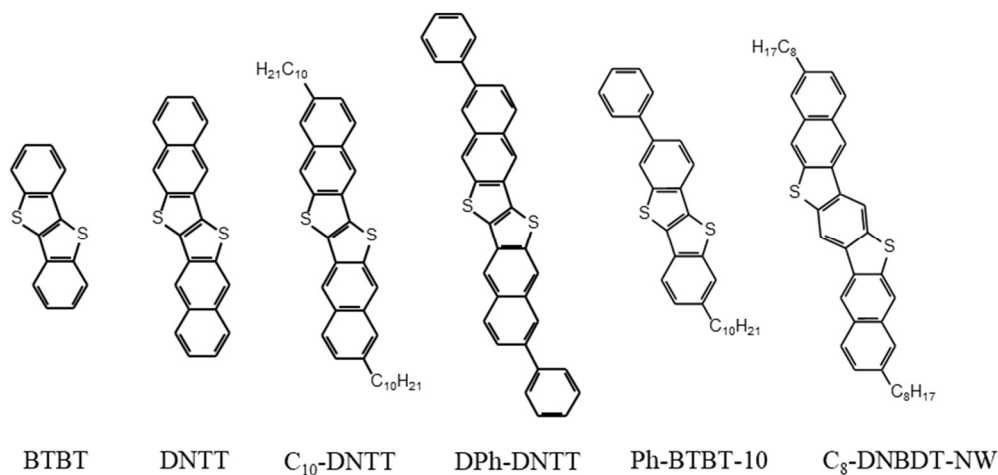


Figure 1.4 BTBT and DNNT

Benzothienobenzothiophene (BTBT) and dinaphtho[2,3-b:2',3'-f]thieno[3,2-b]thiophene (DNNT) and functionalized derivatives C₁₀-DNNT, DPh-DNNT, and Ph-BTBT-C₁₀. Also shown is 3,11-dioctyldinaphtho[2,3-d:2',3'-d']benzo[1,2-b:4,5-b']dithiophene (C₈-DNBDT-NW).

³ It should be noted that the mobility in [41] and in other reports of high mobility in organic transistors were likely overestimated due to non-ideal transport characteristics primarily attributed to contact resistance effects and was recently addressed by various groups [51][323].

stability and a higher carrier mobility than pentacene (Figure 1.4). The enhanced environmental stability over pentacene is achieved by substitution of the central ring, which is prone to oxidation when exposed to ambient UV light [44]. The additional thiophene units largely prevent this degradation route by lowering the HOMO level and increasing the band gap [45]. In addition to the increased stability, the charge carrier mobility is also increased, in part since DNNT and BTBT derivatives show a higher packing density (see following section) which leads to a greater degree of π -orbital overlap and larger charge transfer integrals [29]. More details about the various aspects that determine the charge carrier transport in organic semiconductors in general, with a particular focus on small-molecule morphology, are discussed in the following sections of this chapter.

1.1.3 N-type organic semiconductors

In general, stable materials for hole transport in organic TFTs have been easier to develop than materials for electron transport. This is primarily due to the fact that in order for charges to be injected into the organic semiconductor, the work function of the source drain contacts should be close to the transport level of the organic semiconductor. The above-mentioned organic semiconductors tend to have highest occupied molecular orbitals (HOMO) close to 5 eV, meaning that efficient hole injection can be achieved through the use of a high-work-function noble metal such as Au, Ag, or Pd [46]. However, the lowest unoccupied molecular orbital (LUMO) tends to be around 3 eV or less in these molecules. Therefore, to achieve efficient electron injection a very low-work-function contact material must be used such as Ca, which can lead high device instability since these materials will readily oxidize in air, leading additionally to large injection barriers due to the insulating interface layer that will prevent efficient electron injection from the contact to the semiconductor. In OLEDs, this is commonly addressed by adopting a ‘bottom-emission’ configuration in which the transparent anode is fabricated first and is typically composed of a stable transparent conducting oxide such as indium-doped tin oxide (ITO). After subsequent hole-injection/transport layers, light-emission layer, and electron-transport/hole-blocking layer, the Ca cathode is then encapsulated with a metal such as Al or Ag. The OLED array is then completely encapsulated with a cover glass to prevent oxygen and moisture ingress [47]. While such a stacked-contact approach is effective for preventing degradation of the electronic injection in OLEDs, it is difficult to implement this

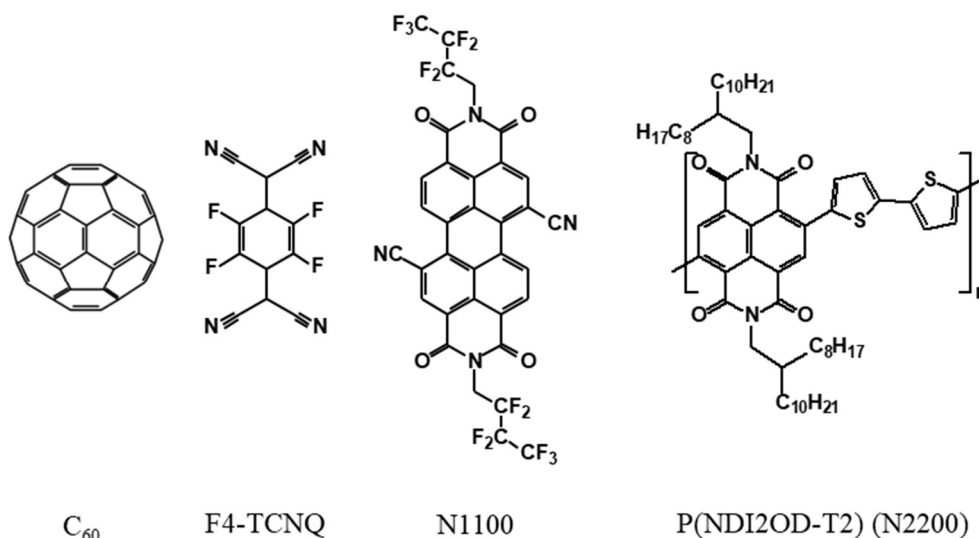


Figure 1.5 N-type organic semiconductors

Buckminster fullerene (C_{60}), tetrafluoro-tetracyanoquinodimethane (F_4 -TCNQ), N,N' -bis(2,2,3,3,4,4,4) heptafluorobutyl-1,7-dicyano-perylene-(3,4:9,10)-tetracarboxylic diimide (Polyera ActivInk™ N1100), and poly {[N,N' -bis(2-octyldodecyl)-naphthalene-1,4,5,8-bis(dicarboximide)-2,6-diyl]-alt-5,5'-(2,2'-bithiophene)} (P(NDI2OD-T2), Polyera ActivInk™ N2200).

approach in organic TFTs in a robust manner. The primary reason is that the required lateral patterning dimension of the source and drain contacts imposes significant practical difficulties for the precise alignment of a multi-layered contact, especially if the channel length of the TFT is small (around a few microns or less required for high-frequency circuits [13]) and a top-contact (TC) TFT architecture is implemented (see Chapter 2). The most straight-forward alternative to low-work function contacts for n-type organic TFTs has therefore been to use known or develop new ‘n-type’ organic semiconductors with deep LUMO levels.

Examples of prominent n-type organic semiconductors are shown in Figure 1.5. The first example of note is Buckminster fullerene (C_{60}) which has a LUMO level of 4 eV thus allowing for injection of electrons from relatively high-work function contacts [48]. In a highlight result by Masatoshi Kitamura et al. [49], n-channel organic TFTs using C_{60} and thiol-functionalized-Au contacts were demonstrated that had high effective electron mobilities up to $2.2 \text{ cm}^2 \text{ V}^{-1} \text{ s}^{-1}$ in addition to (at the time) record-high unity-current-gain (transit) frequencies of 27 MHz. Another prominent example of a small molecule that shows pronounced electron mobility is tetrafluoro-tetracyanoquinodimethane (F_4 -TCNQ). F_4 -TCNQ is an electron acceptor that has a very deep LUMO level (5.2 eV) but also a very large bandgap of about 3 eV, making it mostly of interest as an electron transporting layer in OLEDs or as a dopant for p-type organic

semiconductors (see Section 1.3.4 for more information on doping) [48]. Stability is again a big issue in n-type materials like C_{60} as well as other organic semiconductors with low LUMO levels, due primarily to oxidation of the molecules in ambient conditions if they are not sufficiently electron deficient (i.e. with reduction potentials that are lower than about half that of oxygen or water) [50]. Therefore, another significant area of research for organic chemists has been to develop electron-deficient, environmentally-stable organic semiconductors which can also show high electron mobilities [51]. The general approach for both polymers and small molecules has been to adopt a central building block such as naphthalene diimide (NDI) and tune both the morphological properties and electron deficiencies through the addition of functional side groups [50]. Another trend has been to extend the conjugated core in order to enhance the degree of π -orbital overlap and to influence the hydrogen-bonding interactions of some of the molecular constituents [52] to promote a planar conformation with small intermolecular separation in thin films, thereby enhancing electron transport in organic n-type TFTs. Notable examples of a combination of these approaches are the small molecule N,N'-bis(2,2,3,3,4,4,4) heptafluorobutyl-1,7-dicyano-perylene-(3,4:9,10)-tetracarboxylic diimide (Polyera ActivInkTM N1100) [53] and the closely-related polymer-NDI variant, poly {[N,N'-bis(2-octyldodecyl)-naphthalene-1,4,5,8-bis(dicarboximide)-2,6-diyl]-alt-5,5'-(2,2'-bithiophene)} (P(NDI2OD-T2)), Polyera ActivInkTM N2200) [54]. N1100 is briefly investigated in flexible bottom-contact organic TFTs in this thesis in Chapter 5. It has a deep LUMO level of 4.5 eV [55] allowing for electron injection from Au contacts in organic TFTs and has been demonstrated to produce air stable organic TFTs with electron mobility up to $0.8 \text{ cm}^2 \text{ V}^{-1} \text{ s}^{-1}$, enabling the development of complementary organic circuits [56], [57]. The increased environmental stability of N1100 over other electron transport materials as well as the good electron conductivity are owed to the addition of cyano (-CN) substituents at the bay positions and fluoroalkyl (-CH₂(CF₂)₂CF₃) substituents at the imide positions [52], [53], [57].

1.2 Organic semiconductor thin-film morphology

The governing thermodynamics of thin-film formation in organic semiconductors leads to morphologies that vary from completely amorphous to well-ordered single crystals [40]. The precise ordering of the molecules in a condensed state depends on the molecular structure and electrostatic properties of the molecules which influence the intermolecular van der Waals and at times hydrogen bonding forces. In practice, this is compounded by additional extrinsic factors, such as the reactivity of the surface of the substrate, the presence of impurities such as water, the environment during thin-film formation, and the method by which the thin film is deposited. Of most crucial importance for organic electronics applications is to enable efficient charge transport in the organic semiconductor thin-film(s) in a device, which usually goes hand in hand with maximizing the degree of π -orbital overlap between adjacent molecules. In general the ultimate structure-property relationships of organic semiconductor thin films are often exceedingly complex, with the various important properties of the thin film morphology extending over a large length scale [58] (Figure 1.6). In the following, the important morphological characteristics of thin films of organic semiconductor polymers and small molecules are discussed. While the discussion of polymers is in the form of a brief overview,

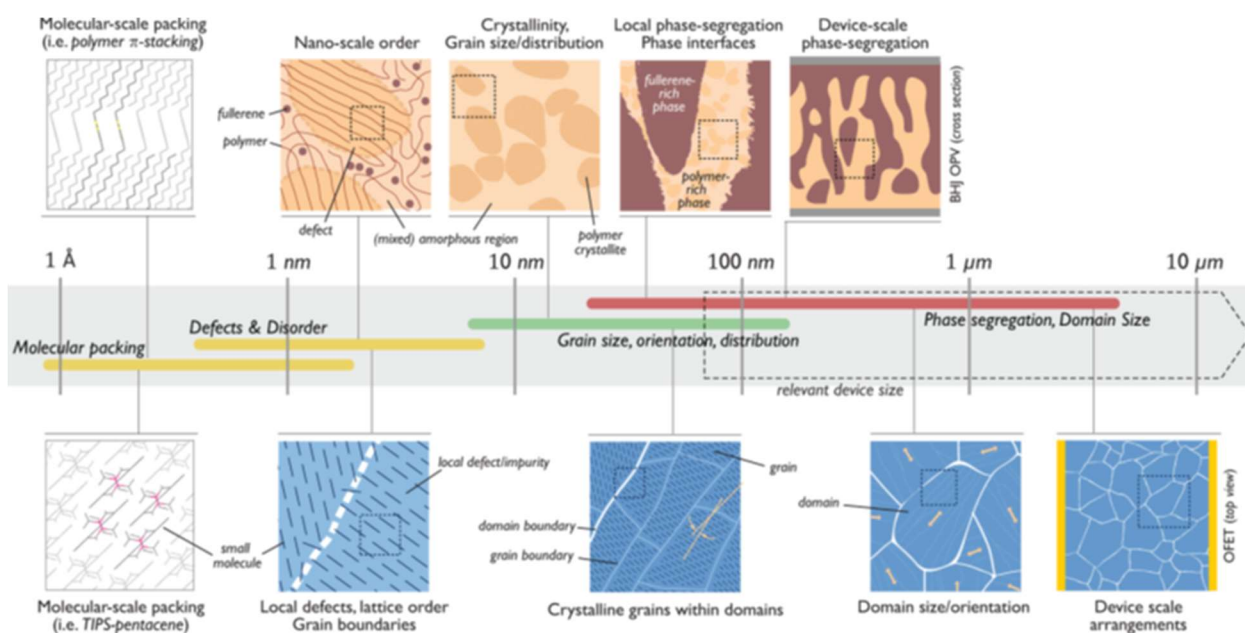


Figure 1.6 Length scales of organic semiconductor structure-property relationships.

Length scales of the various morphological features of organic semiconductor thin-films: (top) polymers, (bottom) small molecules (from Rivnay et al. [58]).

the discussion of small molecules is given in significantly more detail, since they are a focus material of this thesis.

1.2.1 Polymers

For conjugated polymers, various methods have been implemented to control the alignment of the molecular chains in a thin-film through, e.g., changes of solvent or the addition of alkyl side chains to the polymer backbone [51], in order to maximize charge transport and processability. Solution-sheering methods such as blade coating and gravure printing can motivate different levels of alignment of the polymer chains by changing the coating speed, with a higher degree of alignment realized by higher coating speeds [59], [60]. Another way to motivate different alignments of, e. g., the polymer lamellae in a block copolymer, is by applying a DC electrical bias to the film that will act to align the lamellae via grain boundary migration and grain rotation depending on the concentration of polymer in solution and the temperature [61]. More-controlled crystallization has also been demonstrated in P3HT films through solvent swelling methods that create nucleation sites for ordered crystal growth within the film that then enhances the charge-carrier mobility (Figure 1.7a) [62].

Even with these approaches, a truly single-crystalline film of a polymer semiconductor has never been demonstrated. The morphology of the highest-mobility polymers usually is characterized by a mixture of polycrystalline and amorphous regions, with the highest charge carrier mobilities in the aggregated polycrystalline regions where the π -stacking in the (010) direction is most prominent and has the highest charge-transfer integral [58], [63].

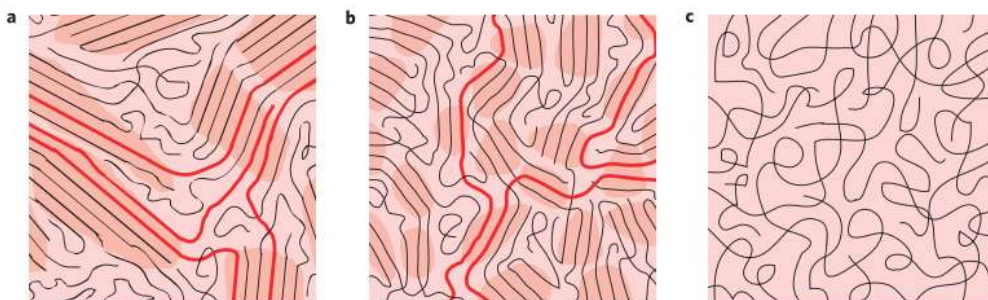


Figure 1.7 Polymer morphology.

Schematics of the molecular-scale morphology of polymer semiconductors. From left to right, the polymer layer becomes more disordered (from Noriega et al. [63]).

1.2.2 Small molecules

In some cases, clean reactive surfaces lead to chemisorption of small molecules to the surface, such as in the case of the strong electron acceptor tetrafluoro-tetracyanoquinodimethane (F₄-TCNQ) on Au (111) surfaces, wherein the surface states of Au adatoms are hybridized with the molecular orbitals of F₄-TCNQ and the molecules assemble on the surface with ‘flat’ conformation [64]. This molecular orientation can be useful for the fabrication of organic devices such as OLEDs and OPVs where the primary charge transport direction is perpendicular to the substrate. For planar devices such as organic TFTs, however, the charge transport direction is in the plane of the surface of the device, so it is preferable for the molecules to conform to an orientation such that the π -orbital overlap is in-plane. The most efficient charge transport is then taking place within the 2D-plane between π -stacked molecules of an individual layer, while interlayer (vertical) transport is typically far less efficient due to decreased orbital overlap in that direction [65].

The thin films of small organic semiconductor molecules in organic TFTs are predominantly physisorbed, with often complex chemical and physical interactions which influence the nucleation and crystal growth modes [66]. Since the intermolecular interactions between constituent molecules and the substrate are via weak van der Waals forces, the thin-film formation is determined by a delicate balance between intermolecular interactions and

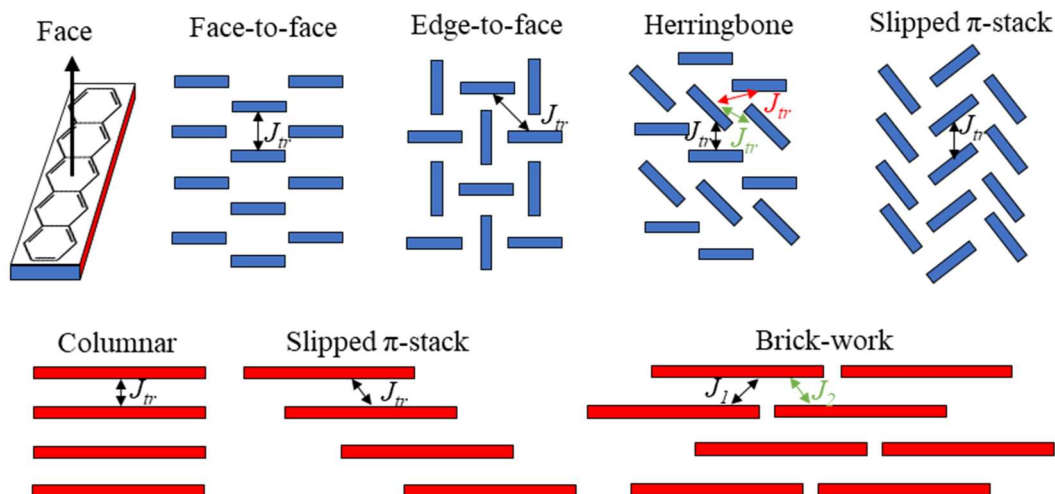


Figure 1.8 Crystal packing of small molecules.

Summary of the most common crystal-packing motifs in thin films of planar small-molecule organic semiconductors (adapted from Curtis et al. [68] and Anthony et al. [69]).

molecule-substrate interactions. These interactions and thus the resulting morphology can be controlled to an extent by the conditions under which the film is deposited (substrate temperature and deposition rate) as well as by the surface energy of the substrate, which is a reflection of the surface roughness and chemical purity and reactivity of the surface [36].

Nucleation and crystal growth of small molecules generally proceeds according to several distinct modes: layer-by-layer (Frank-van der Merwe), layer-plus-island (Stranski-Krastanov), and island (Volmer-Weber) growth [67]. In general, the more 2-dimensional van der Merwe growth mode is favored for the fabrication of organic devices in which the charge transport direction is in the plane of the substrate, such as organic TFTs, since the 3-dimensional growth modes lead to a greater density of grain boundaries and possibly voids within the thin film. Thus, much of the theoretical and experimental work on the growth of molecular crystals for organic TFTs has been focused on understanding the governing principles that lead to 2-dimensional growth. Heterogeneous nucleation and thin-film growth generally depend on balancing the energy barriers associated with diffusion, desorption, and the thermodynamic free-energy barrier required to form a stable crystal island on a surface [66]. The asymmetry of intermolecular interactions adds an additional complication, since this increases the variety of possible thin-film crystal-packing motifs (Figure 1.8) [68], [69], which must also be balanced with the the substrate-molecule interactions. The charge transport in an organic semiconductor crystal for a particular direction is typically quantified by the transfer integrals (J_{tr}) which can vary significantly depending on the packing motif (arrows in Figure 1.8).

Detailed morphological and crystallographic analyses of pentacene thin films deposited on various surfaces and under various conditions have been studied by various groups early on and were reviewed by Ricardo Ruiz et al. [67] (Figure 1.9). In general, it has been found that pentacene and other linear organic molecules can conform to a variety of morphologies depending on the nature of the substrate and the deposition conditions. In the case of pentacene deposited on chemically-inert substrates, such as Au contacts functionalized with a self-assembled monolayer (SAM) composed of an alkanethiol with various terminal groups and chain lengths [70], [71] or SiO₂ with various surface treatments [72], [73], a near-upright orientation of the pentacene molecules on the surface is adopted, increasing the in-plane transfer integrals. The molecules tend to arrange in a layered-‘herringbone’ structure (Figure 1.8 and Figure 1.9a) with large domain sizes in such cases where the small magnitude of the pentacene-pentacene interactions within a layer are well-balanced with the substrate

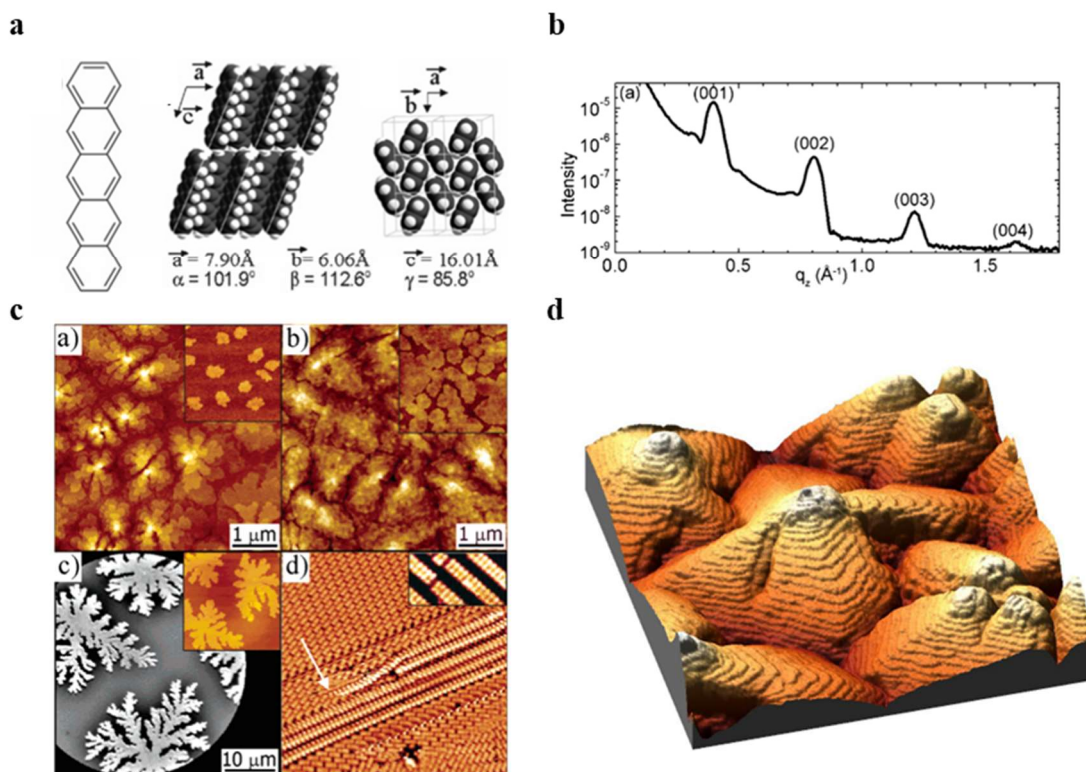


Figure 1.9 Pentacene thin-film morphology.

(a-c) Summary of key results from morphological and crystallographic investigations of pentacene thin films on various substrates reviewed by Ruiz et al. [67]. a) Crystal structure of pentacene. b) Out-of-plane x-ray diffraction of a multilayer of pentacene showing the strong Bragg peaks in the $(00l)$ direction, indicating highly-ordered, layer-by-layer growth of pentacene on H-terminated Si substrate. c) AFM, SEM, and STM analyses of pentacene thin films on (a) SiO_2 , (b) PEDOT:PSS, (c) Si with a flat-lying initial monolayer of pentacene, and (d) Ag. d) 3D AFM micrograph of a pentacene thin film on Topas® cyclo-olefin copolymer substrate reported by Schiefer et al. [73].

interactions. In the layered-herringbone structure, which is common to many other organic small molecules when deposited on inert substrates, a monoclinic unit cell is formed with the molecular long axis roughly aligned with the c -axis of the unit cell (Figure 1.9a,b). In the ab -plane, the π -stacking between adjacent molecules is then reduced by ‘rolling’ of the molecules with respect to the molecular long axis and a ‘pitch’ shift of $\frac{1}{2}$ with respect to the position of the molecules in adjacent rows in the π -stacking direction [68]. This can be compared to untreated Au surfaces where the molecules lay on their long edge and de-wet rapidly from the surface to form isolated crystallite islands due to increased interaction with the substrate [71].

Charge-transport anisotropy is often present within the plane of the layers of the molecules depending on the specific crystallographic ordering that is adopted within the layer (Figure 1.8). Accounting for and controlling the high degree of charge-transport anisotropy in organic

crystals composed of small molecules remains one of the biggest topics of research for chemists and device engineers [29]. Relatively small changes to the chemistry of an organic semiconductor can motivate drastic changes in the *ab*-symmetry of the deposited layers. For example, vacuum-deposited DNTT and functional derivatives C₁₀-DNTT and 2,9-diphenyl-dinaphtho[2,3-b:2',3'-f]thieno[3,2-b]thiophene (DPh-DNTT) show distinct differences in the thin-film morphology in the films [74]. In general, the phenyl or alkyl groups in this case result in a smaller intermolecular distance between neighboring molecules within a layer in the thin films, as well as greater in-plane symmetry of the transfer integrals compared to DNTT [75], ultimately leading to higher charge carrier mobility in organic TFTs. The highly-anisotropic brick-work conformations that are formed by TIPS pentacene and 2,8-difluoro-5,11-bis(triethylsilylethynyl)anthradithiophene (diF-TESADT) [76] show high maximum hole mobilities in the π -stacking direction (y-direction in Figure 1.8), but far lower mobilities in the direction that points along the long axis of the molecules (x-direction in Figure 1.8). Expanding upon the development of TIPS pentacene for solution-processed thin films, John Anthony and coworkers have pursued further variations on the original concept to graft various constituents to the TIPS pentacene core to motivate the formation of different morphologies in their solution-processed thin films that show a greater degree of orbital overlap and charge-carrier higher mobilities in organic TFTs [69]. Changes in the substituent chemistry or size can generally lead to controlled changes between the different packing structures shown in Figure 1.8.

A final important point of consideration is the influence that grain boundaries can have on the charge transport in an organic device [77]–[79]. For many organic semiconductors such as pentacene, the charge-carrier mobility is strongly dependent on the grain size and the density of grain boundaries, which can act as scattering centers for mobile charges and create trap states that will lower the charge-carrier mobility. Thus a recent burgeoning interest is on small-molecule organic semiconductors that show liquid-crystalline properties which allow for the growth of very large crystal domains [80]. A liquid crystal is a crystal whose component molecules may be reoriented into different mesophases by an external force, such as an applied electric field, which is in fact part of the operating principle for a liquid crystal display (LCD). Semi-permanent reorientation can also be achieved by annealing the thin films of a liquid-crystalline material above a mesophase transition temperature after deposition to promote steric

rearrangement into a preferred mesophase which is then maintained upon subsequent cooling [81]–[83].

The key advantage of organic-semiconductor molecules which can show liquid-crystalline properties is that highly-ordered films can be formed using simple solution-processing methods that, under the right circumstances, can promote single-crystal monolayer growth, leading to films with at times only one or two single-crystalline monolayers, covering large areas (several square-centimeters or more) [82]. BTBT derivatives have received especially increased interest in this regard recently, with single-crystalline TFTs using 2-decyl-7-phenyl-benzothieno[3,2-b]benzothiophene (Ph-BTBT-C₁₀) showing hole mobility in excess of 10 cm²/Vs and band-like charge transport [83], [84]. In other works using 3,11-dioctyl-dinaphtho[2,3-*d*:2',3'-*d'*]benzo[1,2-*b*:4,5-*b'*]dithiophene (C₈-DNBDT-NW), excellent transistor and circuit performances were achieved with 2-monolayer-thick single crystals deposited using meniscus-guided crystallization on a centimeter scale [81]. The TFTs fabricated in that work notably showed (at the time) record-low contact resistance of 46.9 Ωcm and a unity-current-gain (transit) frequency of 20 MHz. Other heteroacenes such as DNNT can also show liquid-crystalline properties when long alkyl-side chains are added to the ends of the long axis of the molecule [85]. The addition of alkyl-sidechains to the 2 and 9 positions on DNNT not only renders the resulting C_n-DNNT molecules soluble and therefore open to solution processing and liquid crystals, but also generally leads to enhanced in-plane intermolecular charge transport. This is due to the van der Waals interactions between the alkyl side chains, which cause the C_n-DNNT molecules to pack with a smaller separation distance between each of the molecules [85]. Boyu Peng et al. used these properties to fabricate TFTs using C₁₀-DNNT deposited through meniscus-driven coating which show charge carrier mobilities in excess of 12 cm² V⁻¹ s⁻¹ and low contact resistance of 40 Ωcm [86]. Furthermore, the monolayer films that are produced by liquid crystalline organic semiconductors have been demonstrated to be mechanically robust enough that, despite the weak van der Waals forces holding the layer together, they can be transferred from solution to the substrate [87]. This enabled, e.g., Schaffroth et al. to fabricate organic TFTs utilizing membranes of N,N'-di((S)-1-methylpentyl)-1,7(6)-dicyano-perylene-3,4:9,10-bis(dicarboximide) (PDI1MPCN2) that were freely suspended over an air gap that extended over several hundred nanometers [87]. Such films are then isolated almost entirely from their environment, which allow for more extensive

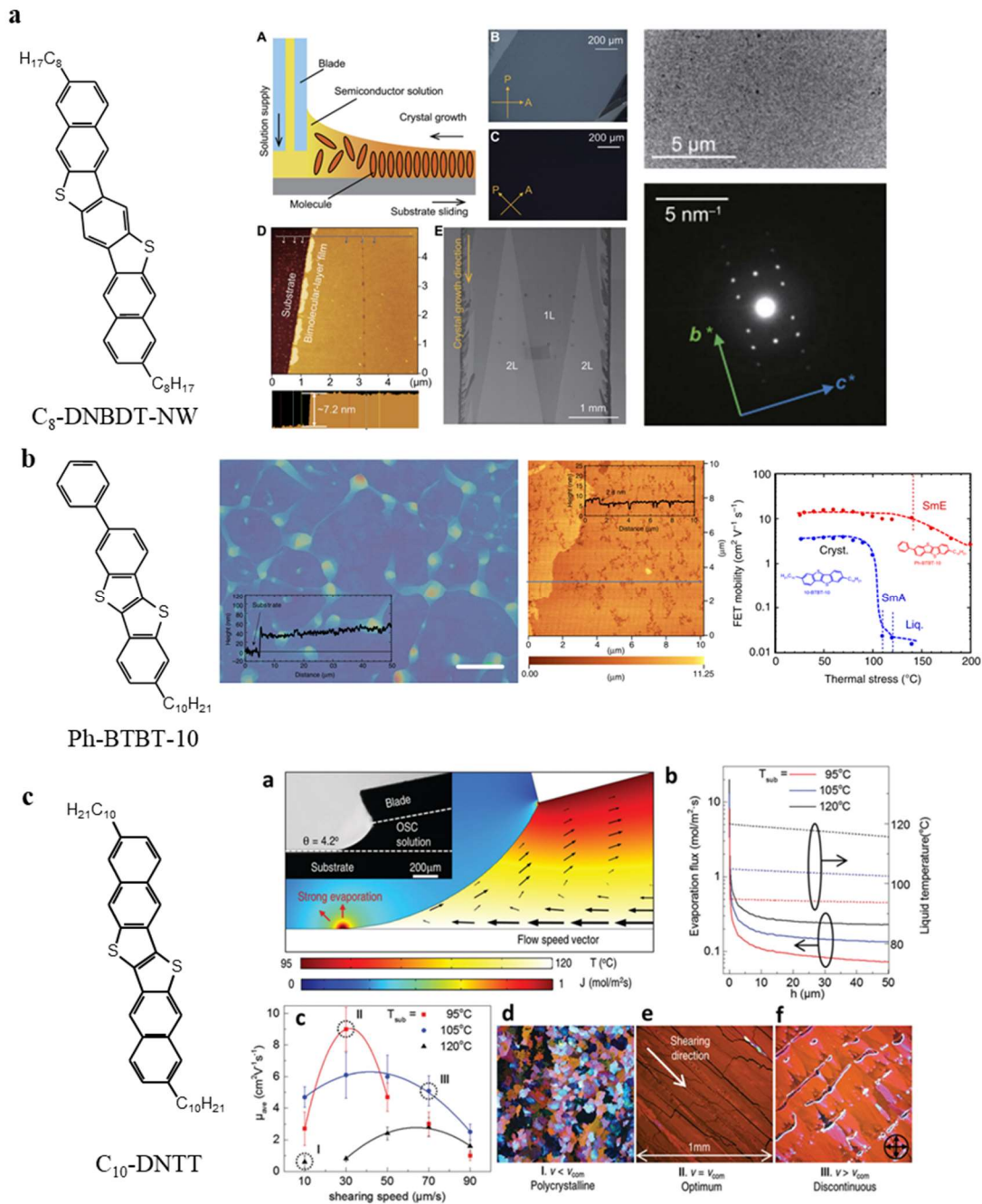


Figure 1.10 Liquid crystalline organic semiconductors.

Recent examples from literature of liquid-crystal organic semiconductors utilized in high-performance organic thin-film transistors. a) Ref [81], b) Ref [83] (scale bars correspond to 20 μm), and c) Ref [82].

fundamental studies into morphological features such as the chirality of the organic films and the electrical transport properties without the influence of, e.g., the particular gate-dielectric material in an organic TFT.

1.3 Charge transport physics in organic semiconductors

The development of models to describe the charge transport in organic semiconductors has historically been a challenging endeavor, owing to the complex structure-property relationships and the wide variety of different materials [65]. This is compounded by difficulties that often arise in obtaining consistent experimental data on charge-transport phenomena, since different organic semiconductors can show varying transport properties depending upon extrinsic factors including the method by which the data was obtained, the fabrication processes used, and the other materials involved as in the case of devices like organic TFTs or metal-insulator-semiconductor-metal (MISM) capacitors. Nevertheless, some general principles are well understood. In an organic-semiconductor crystal, the formation of narrow transport bands (conduction band: CB, valence band: VB) similar to inorganic semiconductors occurs due to interactions of the highest occupied molecular orbital (HOMO) and/or lowest unoccupied molecular orbital (LUMO) levels of the material, where the width of the bands and the subsequent carrier mobility are determined by the strength of the π - π interactions [20]. In most organic semiconductors such continuous band levels are not present due to energetic disorder which results in distributions of discrete occupied and unoccupied states. The ionization energy (IE) and electron affinity (EA) are then rather defined as the difference between the vacuum energy level (E_{vac}) and the HOMO or LUMO edge, respectively (Figure 1.11).

$$IE = E_{vac} - E_{HOMO} \quad (1)$$

$$EA = E_{vac} - E_{LUMO} \quad (2)$$

To induce charge transport, excess charge carriers must be accumulated in the conduction and/or valence band by injecting carriers from an external source such as the contacts in an OLED or organic TFT or by inducing carriers via photoexcitation in an OPV device. The resulting accumulated space charge consists of both mobile polarons and bound charges, with only the former contributing to the electric current in the material. In the absence of any external potential, charge transport in organic semiconductors can be considered entirely diffusive [65]. The mean free path of charges in the material ($\langle x^2 \rangle$) is then described by a simple diffusion equation:

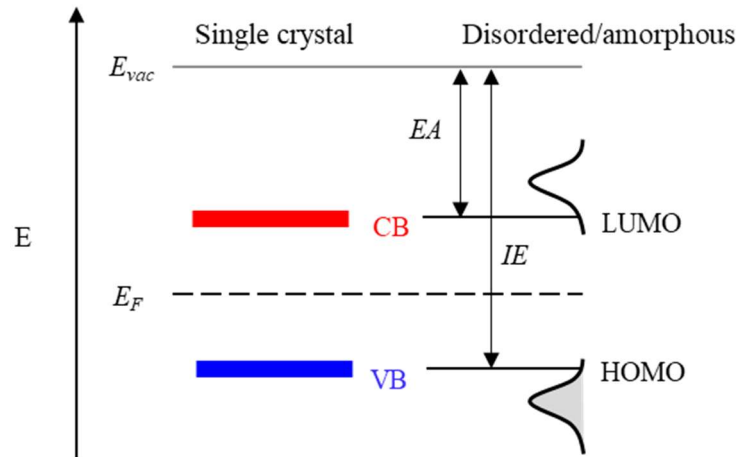


Figure 1.11 Semiconductor energy band diagrams

Schematic energy diagrams of single-crystalline and disordered/amorphous organic semiconductor. CB: conduction band, VB: valence band, E_{vac} : vacuum-level energy, E_F : Fermi level, EA: electron affinity, IP: ionization potential, LUMO: lowest unoccupied molecular orbital, HOMO: highest occupied molecular orbital.

$$\langle x^2 \rangle = nDt \quad (3)$$

Where D is the diffusion coefficient, t is time, and n is 2, 4, or 6 for one-, two-, and three-dimensional systems, respectively. The charge-carrier mobility (μ), defined as the rate of change of the drift velocity of a charge carrier (v_d) in response to an applied electric field (F) is related to D by the Einstein relation:

$$\mu = \frac{v_d}{F} = \frac{qD}{k_B T} \quad (4)$$

Where q is the elementary electric charge, k_B is the Boltzmann constant and T is the absolute temperature. Alternatively, if diffusion contributions are neglected, a specific case of Child's Law can be applied for the current density (J), provided that transport in the device is bulk-limited rather than contact-limited and the density of trap states inhibiting charge transport is negligible. Here, a so-called space-charge limited current (SCLC) is formed at low electric-field magnitudes, and the J - V characteristics can be expressed as:

$$J = \frac{9}{8} \epsilon_0 \epsilon_r \mu \frac{V^2}{d^3} \quad (5)$$

Where ϵ_0 is the permittivity in vacuum, ϵ_r is the dielectric constant of the transport material and d is the thickness of the layer between two planar electrodes. This is commonly known as the

Mott-Gurney equation [88]. Experimentally, such an idealized scenario rarely is realized, though it has been achieved in single crystals [40]. In the presence of a distribution of trap states within the semiconductor, this relationship is only recovered at much higher electric fields, i.e., when all trap states have been filled [88]. Also an important note is that μ itself is typically a function of the electric field in the semiconductor through the Poole-Frenkel effect [89], [90], inexorably linking μ to changes in the charge-carrier density.

$$\mu(F) = \mu(0) \exp\left(\frac{q}{k_B T} \sqrt{\frac{qF}{\pi \epsilon_o \epsilon_r}}\right) \quad (6)$$

$$J \propto F \exp\left(\frac{q}{k_B T} \left(\sqrt{\frac{qF}{\pi \epsilon_o \epsilon_r}} - \Phi_{PF}\right)\right) \quad (7)$$

Where Φ_{PF} is the energetic barrier for bound (trapped) charge carriers. Both trapped and mobile charges in the material contribute to the electric field. Transport of mobile charges strongly depends on the temperature and the applied voltage(s). In most practical cases, the amorphous or polycrystalline films formed by organic-semiconductor materials lead to non-ideal (i.e. non-band-like) transport behavior. This is mostly due to trap states arising from grain boundaries or other defects. Trap states can either capture mobile charge carriers or act as scattering centers if already occupied. Various models have been developed to describe charge transport from one localized state to another in systems with various degrees of disorder, including the multiple trapping and release (MTR) [89] and variable range hopping (VRH) [91] models (Figure 1.12). Shallow trap states within a few multiples of $k_B T$ of the transport level within the energetic band gap are those states in which a carrier can be thermally excited out of the trap state and contribute to the charge flow. Charges trapped in deep localized states, such as those occurring at grain boundaries can no longer escape via thermal activation but may be released via a sufficient external stimulus such as a high electrical potential. Models for electronic transport in organic semiconductors are thus strongly dependent on the energetic landscape of the active materials involved through intimate dependencies on extrinsic qualities such as the morphology of the semiconductor layer.

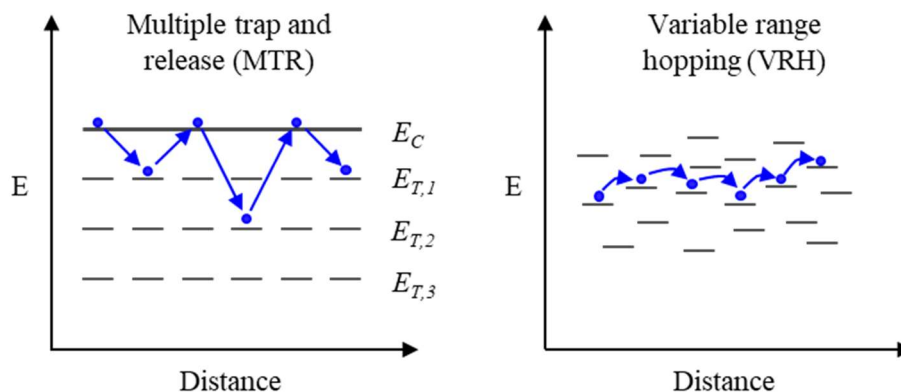


Figure 1.12 Charge transport in organic semiconductors

Schematic energy diagrams of charge transport in organic semiconductors with discrete localized energy levels for charges to be transported. In the multiple trap and release (MTR) model, charges are transported in a continuous band but intermittently fall into discrete trap state energies ($E_{T,n}$). In the variable range hopping (VRH) model charges move through the material via discrete ‘hops’ between energetic states. In both cases, the charge transport through the material is primarily thermally activated and follows the direction of the electric field.

In most organic semiconductors, it has historically been easier to achieve efficient hole transport than electron transport. This does not in principle reflect the intrinsic mobility in a material of one charge carrier over the other but is rather determined by the energetics at the injecting interface of a device. An organic semiconductor is often referred to as a hole (electron) transporter when its ionization energy (electron affinity) closely matches the Fermi level of the source and drain contact material in an organic TFT [65]. Efficient injection of electrons often requires a low-work-function metal for source and drain contacts and/or an organic semiconductor with a deep electron affinity [92]. This frequently leads to issues of materials stability for the contacts, since in both cases oxidation in ambient conditions becomes more prevalent. Hence, most of the organic semiconductor research and device development has focused on hole transporters, as is also done in this thesis.

1.3.1 Modeling charge transport in organic semiconductors

Generally speaking, different charge-transport models for organic semiconductors are distinguished by how trap states in the material are accounted for and the effect they have on the charge-carrier mobility. In lieu of a detailed description of each of the most prominent individual models that have been developed to describe charge transport in organic semiconductors, this section summarizes two important recent efforts to unify the

understanding of charge transport and to enable rational design of the next generations of high-mobility organic semiconductors [29], [93], [94].

1.3.2 Generalized Einstein relation with attenuated delocalization

In the approach by Liu et al. [93], the various transport models are unified into a framework based on the generalized Einstein relation (GER) developed for disordered semiconductors by Roichman and Tessler [95], taking into account attenuated delocalization at the electronic states near the band edge or the energy gap. This first entails a modification to equation (4) to account for the dependence of the charge-carrier mobility on the total carrier concentration (n_C).

$$\mu(n) = qD \frac{1}{n_C(E_F)} \frac{\partial n(E_F, T)}{\partial E_F} \quad (8)$$

Next, owing to the weak van der Waals interactions between neighboring molecules and assuming spatial uniformity, the overall density of states (DOS) as a function of the energy E within an organic-semiconductor layer ($N(E)$) can be considered to follow a Gaussian distribution:

$$N(E) = \frac{N_t}{\sqrt{2\pi}\Delta E} \exp\left[-\frac{(E - E_0)^2}{2\Delta E^2}\right] \quad (9)$$

Where N_t is the characteristic band DOS (typically in the range of 10^{21} cm^{-3}), ΔE is the variance of the energy levels in the distribution and E_0 is the energy around which the DOS is centered. To account for degeneration, the Fermi-Dirac distribution is used to calculate n_C and the microscopic conductivity (σ') of the electronic states is considered to be energy-dependent rather than constant. This leads to the following general expression for μ :

$$\mu = \frac{\sigma}{qn_C} = \frac{q \int N(E)D(E) \left[-\frac{\partial f(E)}{\partial E}\right] dE}{\int N(E)f(E)dE} \quad (10)$$

Where $D(E)$ is the diffusivity for each energy. Finally, the attenuation of the conductivity resulting from the formation of tail states in the DOS due to various sources of microscopic disorder such as voids in the organic layer, grain boundaries, disorder in polymeric chains, and chemical impurities is generally described by:

$$\sigma'(E) = \frac{\sigma_{0,c}}{\sqrt{2\pi}(\Delta D \cdot \Delta E)} \exp \left[\frac{(E - E_0)^2}{2(\Delta D \cdot \Delta E)^2} \right] \quad (11)$$

$$\sigma_{0,c} = \frac{1}{2} N_c q \mu_{0,c} \quad (12)$$

Where $\sigma_{0,c}$ and $\mu_{0,c}$ are the material-specific characteristic conductivity and mobility, respectively. This approach can then in principle be applied using any of the various models for charge transport in organic semiconductors (Figure 1.13) [93] by changing the variances (ΔE , ΔD).

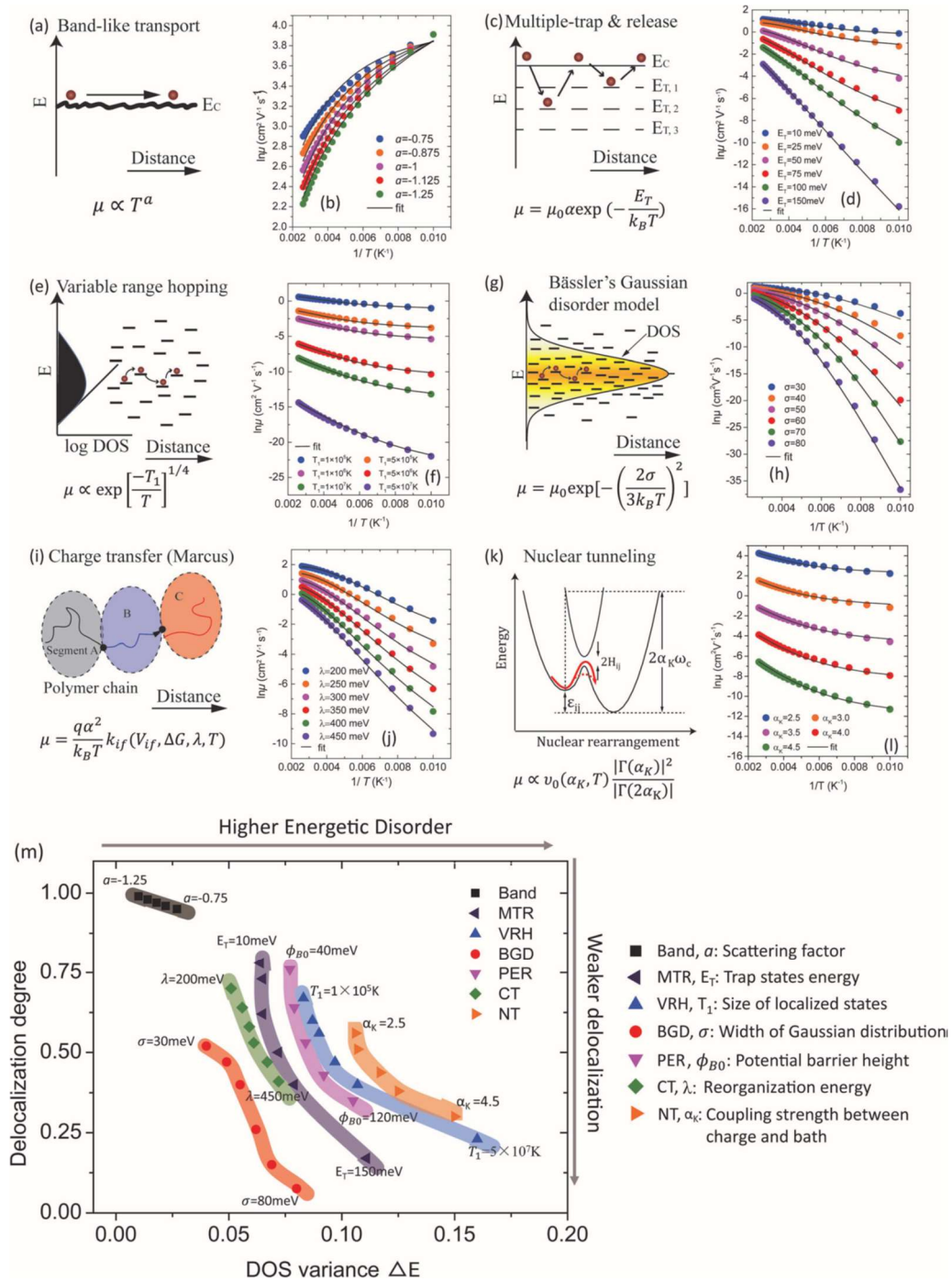


Figure 1.13 Application of the generalized Einstein-relation approach for the description of charge transport in organic semiconductors.

The different charge transport theories that can be applied for organic semiconductors are generally captured according to the charge-carrier delocalization degree and the variance in energy of the density of states (DOS). Figure is from Liu et al. [93].

1.3.3 Transient localization and the path towards higher carrier mobility in organic semiconductors

In the recent works by Fratini et al. [29], [94], [96], [97] the quantum localizations arising from the dynamic lattice disorder in high-mobility organic semiconductors and the resulting consequences for charge-carrier transport were theoretically derived and shown to agree well with experiments. The critical message from these works is that the charge-carrier mobility is limited by the large fluctuations of the intermolecular transfer integrals within an organic-semiconductor crystal. This arises primarily as a result of the weak van der Waals forces which hold a molecular crystal together, allowing for large and slowly decaying thermal fluctuations, resulting in a highly disordered energetic landscape for a charge carrier to navigate. This most importantly serves as an alternate paradigm to the conventional phonon-interaction-centered charge-transport theories which often are insufficient to explain the deviations from band transport of the experimentally measured charge-transport phenomena in many high-mobility organic semiconductors. In this so-called ‘transient localization’ paradigm, the charge-carrier mobility (μ) is elegantly put in terms of a temperature-dependent localization length within the crystal lattice (L_{tr}) and the timescale of intermolecular vibrations (τ_{vib}).

$$\mu = \frac{qL_{tr}^2}{2k_B T \tau_{vib}} \quad (13)$$

Even in pure molecular crystals, L_{tr} is relatively short (only a few lattice spacings) and τ_{vib} is large due to the typically large molecular mass, which combined lead to lower μ than might be expected from semi-classical band transport theories or a higher mobility than expected from hopping transport [98]. One of the great qualities of this latest theoretical work is its predictive capabilities loaning itself to application of direct strategies to improve the charge-carrier mobility by molecular design. This may then prove to represent an important breakthrough towards predicting the chemical structures that will yield new higher-mobility organic semiconductors.

1.3.4 Doping of organic semiconductors

An important concept in semiconductor devices is ‘doping.’ Classically, this is simply the presence of impurities (intentional or unintentional) within the host semiconductor that increase/suppress conductivity for holes (electrons) in the host semiconductor by shifting the Fermi level closer to the valence (conduction) band. Several recent excellent reviews cover the subject for organic semiconductors [99]–[102] and they, along with the references therein, will be the basis for the following discussion. To start, a distinction between the standard practice of doping in inorganic semiconductors, such as Si and Ge, and organic semiconductors should be clarified. In inorganic semiconductors, doping is implemented by either substituting a number of atoms or inserting atoms within the interstitials of the crystal lattice of the host semiconductor. The dopant atoms are chosen based on their ability to donate free electrons or acceptor states within the host. In an analogous way, dopants are typically applied in the form

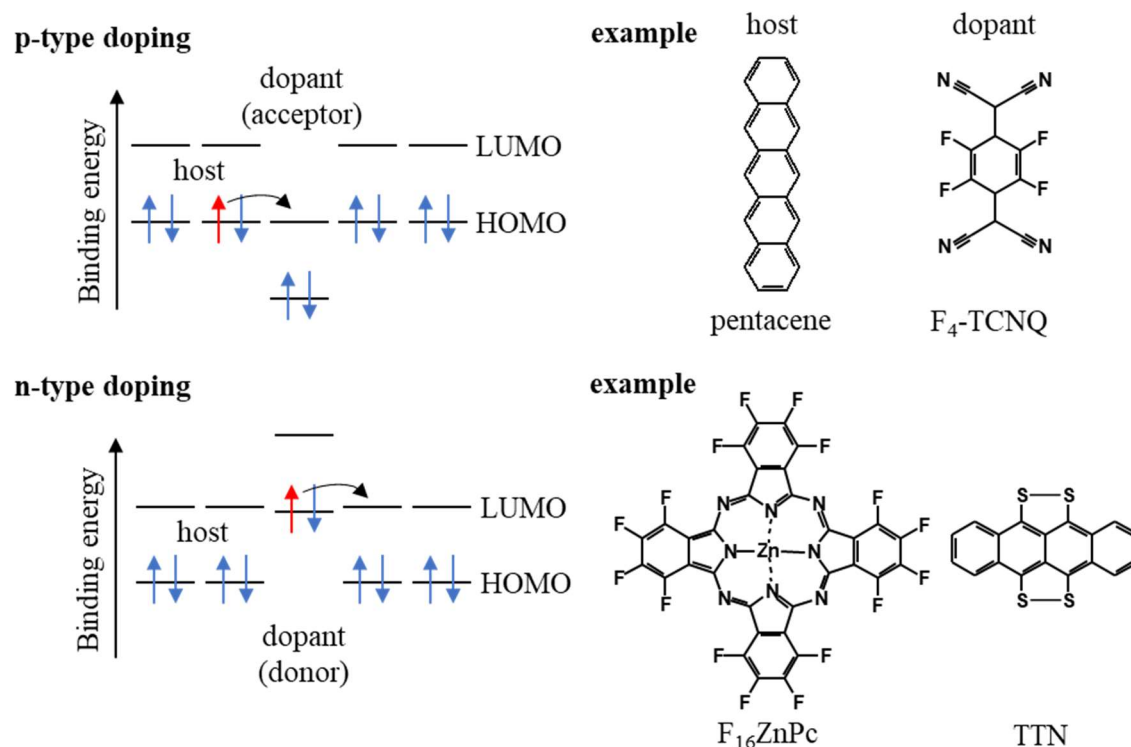


Figure 1.14 Doping organic semiconductors with small molecules

Doping mechanisms for p-type (top) and n-type (bottom) organic semiconductor hosts. At right are example host-dopant systems. Tetrafluoro-tetracyanoquinodimethane (F_4 -TCNQ) acts as an electron acceptor in a pentacene host, while tetrathianaphthacene (TTN) as an electron donor in a hexadecafluorophthalocyaninatozinc (F_{16} ZnPc) host. From ref. [99-102].

of small molecules in organic semiconductor host films (Figure 1.14). The dopants can be co-evaporated or solution-cast simultaneously with the organic semiconductor or otherwise integrated into the thin film in an additional step in the fabrication of a device. While ‘atomistic’ doping is possible in organic semiconductors (e.g. oxygen and water ingress are common sources of impurities in organic semiconductors [103]), it is typically not implemented in a purposeful manner, since the relatively weak van der Waals interactions between semiconductor molecules allow for the small atomic dopants to diffuse uncontrollably within the thin film. Indeed, more efforts are often necessary to prevent unwanted atomic dopants, which can cause instabilities in the device performance [104].

The application of molecular and ionic dopants has been especially important in improving the efficiency of charge injection/extraction in OLEDs and OPV devices as well as in improving the overall conductivity of the host organic layer in some organic TFTs. The free carrier (hole) density (p) that is present in a p-doped semiconductor generally follows [105]

$$p = N_A^- = \frac{N_A}{1 + e^{\left(\frac{E_A - E_F}{k_B T}\right)}} \quad (14)$$

Where N_A^- is the ionized dopant density, N_A is the neutral dopant density, and E_A is the acceptor energy level. The precise underlying mechanisms by which dopants increase the conductivity in organic semiconductors is still the subject of significant debate, mostly with regards to the origins of E_A , though recent efforts have been undertaken to clarify the underlying physics and chemistry that are responsible for the changes in the charge carrier density [105]. Thus, dopant molecules are often chosen empirically based on their observed propensity to increase either the electron or hole density in an organic semiconductor host. Wave-function hybridization between the dopant and host molecules and integer charge transfer (ICT) between a donor and acceptor ground state are thought to be an important step in the doping process. One phenomenological explanation for the conductivity improvement in some host-dopant systems, especially at low doping levels and in disordered semiconductor films, is through the filling of deep trap states within the semiconductor band gap, with larger densities of mobile majority carriers being present after the traps are filled [65], [106], [107]. This is demonstrated convincingly by the example shown in Figure 1.15 from Sabine Olthof et al. [106]. Here, thin films of C_{60} were doped with the air-stable n-dopant precursor ruthenium(pentamethylcyclopentadienyl)(1,3,5-trimethylbenzene) $[RuCp^*(mes)]_2$, which reacts with the C_{60} to give two $[RuCp^*(mes)]^+$ cations and two C_{60} radical anions. At low

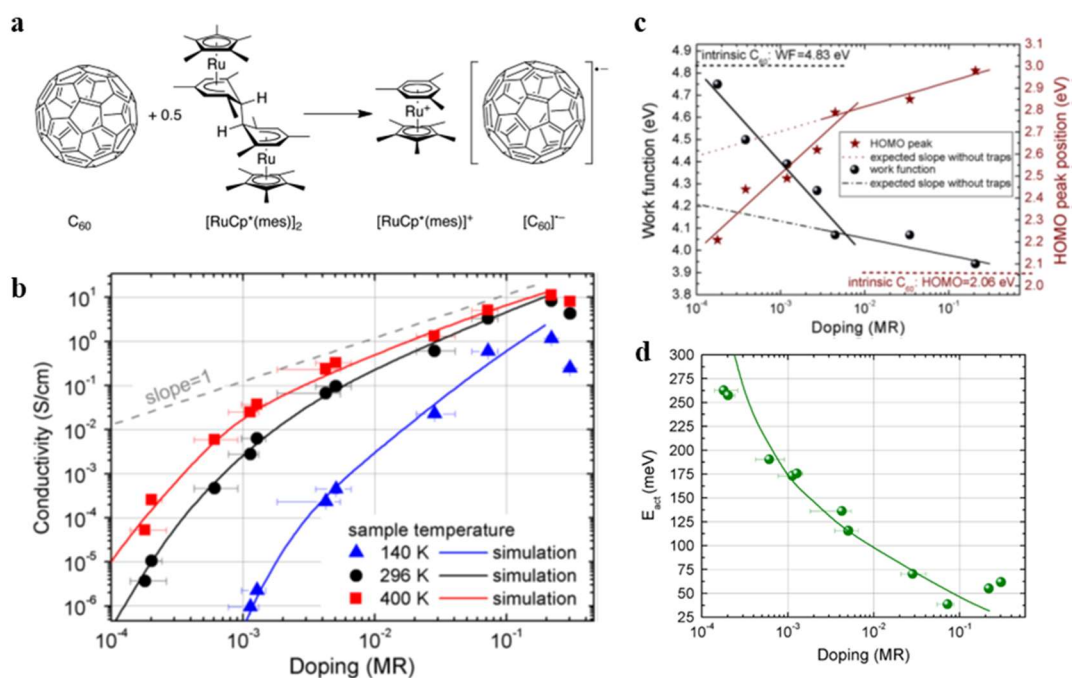


Figure 1.15 Trap-state filling in organic semiconductors with dopants

Results from Sabine Olthof et al. [106] showing how dopants can primarily increase the conductivity of organic semiconductors by filling trap states at low dopant concentrations. a) Schematic diagram of the doping mechanism for the n-type dopant precursor $[\text{RuCp}^*(\text{mes})]_2$ and C_{60} . b) Conductivity as a function of doping molar ratio (MR). c) Work function and HOMO peak position determined from UPS measurements. d) Activation energy for hopping transport.

doping concentrations (molar ratio (MR) between 10^{-4} and 10^{-2}) the conductivity of the film was increased by over four orders of magnitude at room temperature. The contribution from deep-trap-state filling was confirmed by comparing the work function and HOMO peak position changes as a function of the doping concentration to the trend expected from semiconductor theory (dotted lines in Figure 1.15c). Further, by assuming a hopping transport process which would be expected for a semiconductor film containing deep trap states, the temperature-dependent conductivity measurements were examined with an Arrhenius equation for the conductivity, yielding a significant reduction of the extracted activation energy (E_{act}) (Figure 1.15d).

While doping has been essential for improving charge transport in organic semiconductors for several applications, it has been shown to have several limitations and undesirable characteristics that are typically not observed in inorganic semiconductors. First, an upper limit in the effective increase of the charge carrier density as a function of the dopant concentration often exists. This results from several possible origins. One is that the broad distribution of

states in organic semiconductors results in Fermi level pinning above a certain dopant concentration, and thus the barrier between the Fermi level and the transport level cannot be reduced beyond a minimum value [99]. Another issue is that too many dopant molecules incorporated into the semiconductor thin film can disrupt the intermolecular order such that the conductivity will level off or can even start to decrease with high dopant concentrations [99], [106], [108]. Moreover, dopants have been shown to migrate and diffuse throughout the organic-semiconductor layer, an effect exacerbated by high applied electric fields during device operation leading to performance instabilities [109]. Finally, in organic TFTs certain device characteristics such as on/off current ratio and subthreshold swing can be adversely affected by the presence of high concentrations of dopants within the channel region [110]. By limiting the dopants to the contact regions of organic TFTs (contact doping), some improvements in the device characteristics can be realized (see Section 3.3.1 for more detailed discussion on this topic) and so far remains the only practical use for doping in the pursuit of down-scaled high-performance organic transistors.

1.4 Dinaphtho[2,3-b:2',3'-f]thieno[3,2-b]thiophene (DNNT) and its functional derivatives

The development of organic semiconductors based on fused chalcogenophene compounds represented a watershed moment in the development of air-stable organic semiconductor materials with high charge-carrier mobility [111]. For the majority of the organic TFTs that were investigated in this thesis, the diacene-fused thienothiophene dinaphtho[2,3-b:2',3'-f]thieno[3,2-b]thiophene (DNNT) and two of its functional derivatives, C₁₀-DNNT and DPh-DNNT (chemical structures in Figure 1.4) were used. DNNT was first synthesized in the group of Kazuo Takimiya [45] via a straight-forward three-step synthesis process (summarized in the scheme in Figure 1.16a), which was later improved to produce

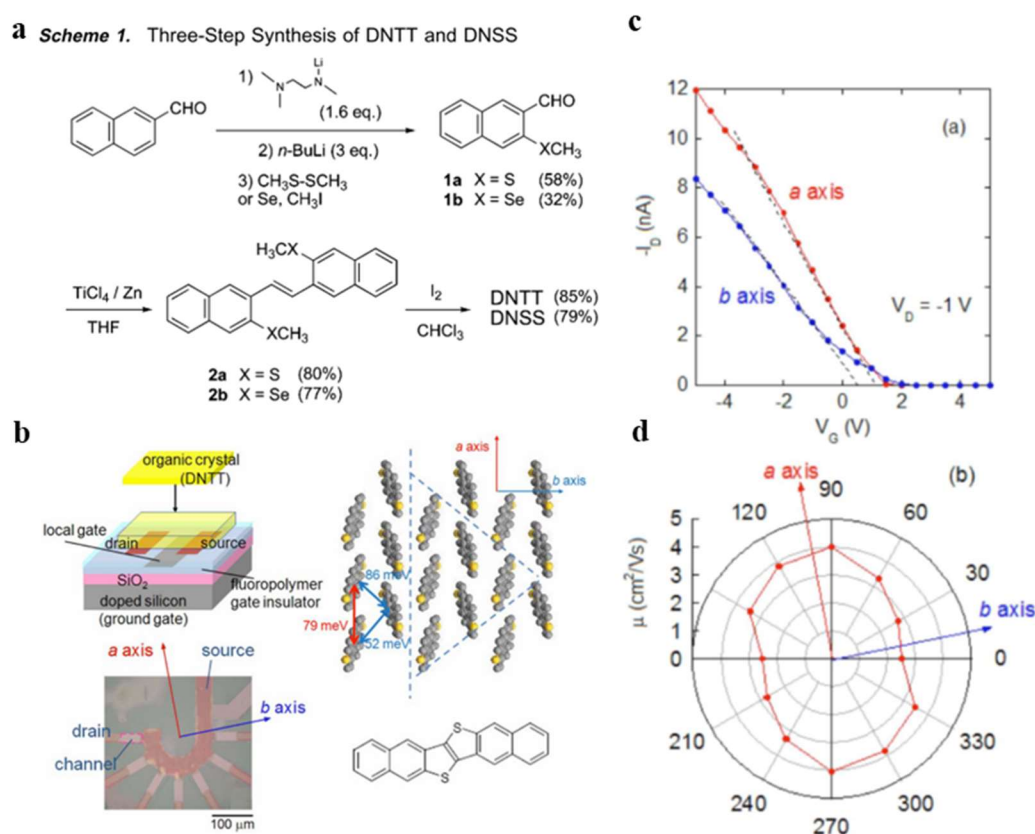


Figure 1.16 DNNT synthesis and device performance properties

a) 3-step synthesis scheme originally reported by Yamamoto et al. [45]. b) Schematic diagram and optical image of single-crystalline TFTs and view along the c-axis of the herringbone structure of the DNNT crystal. c) Transfer curves with the channel running parallel to the indicated axes of the DNNT single crystal used to determine the hole mobility (μ). d) Angular dependence of μ determined from measurements of the device shown in (b). Ref Uno et al. [114].

DNTT with higher yields via an even simpler process [112], ultimately allowing DNTT to become widely commercially available.

The good stability of DNTT against oxidation from the ambient environment compared to pentacene is owed to the low-lying HOMO (5.18 eV compared to 5.0 eV) and the high-lying LUMO (1.81 eV). The large HOMO coefficients on the sulfur atoms of DNTT and the larger atomic radius of the sulfur atoms in the centralized-thiophene groups enhances the π -orbital overlap in thin films of DNTT [111] (Figure 1.16b), resulting in high hole mobilities of up to nearly $3 \text{ cm}^2 \text{ V}^{-1} \text{ s}^{-1}$ as well as other excellent performance characteristics measured in the organic TFTs that were reported in the original publication. In thin films, the molecules tend to pack in a layered-herringbone structure in the *ab*-plane ($a = 6.187 \text{ \AA}$, $b = 7.662 \text{ \AA}$) with a layer spacing of 16.21 \AA in the *c*-direction [45] with charge transport anisotropy that has been shown to be comparatively smaller to pentacene both theoretically [113] and experimentally [114], [115]. These features have led to DNTT being one of the most widely-studied organic small molecules in high-performance organic TFTs and circuits to date. DNTT has been implemented as the channel material in a variety of organic-TFT-based applications including flexible sensors for medical applications [116]–[118], as well as high-frequency organic circuits on flexible plastic [56], [119], [120] and paper substrates [56]. Functional derivatives of DNTT [75], [85] have been demonstrated that show further-improved hole mobilities in excess of $10 \text{ cm}^2 \text{ V}^{-1} \text{ s}^{-1}$ [82] and, most crucially for the main subject of this thesis, they show among the lowest contact resistances measured in organic TFTs to date [12], [74], [86], [121].

2 Organic thin-film transistors

The organic field-effect transistor (FET) is an organic-semiconductor device which acts as the analogue to the metal-oxide-semiconductor field-effect transistor (MOSFET) in traditional semiconductor technology. The first true organic FET reported was an organic thin-film transistor (TFT) based on polythiophene demonstrated in 1987 by Koezuka, Tsumura, and Ando [122]. This early device had a hole mobility of $2 \times 10^{-5} \text{ cm}^2 \text{ V}^{-1} \text{ s}^{-1}$. Since then many improvements in device manufacturing and materials engineering have followed, with a major milestone being the first pentacene thin-film transistors with effective hole mobility above $1 \text{ cm}^2 \text{ V}^{-1} \text{ s}^{-1}$, matching the mobility of hydrogenated amorphous silicon (a-Si:H) TFTs reported by the group of Thomas N. Jackson in 1997 [123]. More recently, organic TFTs have achieved effective hole and electron mobilities in excess of $10 \text{ cm}^2 \text{ V}^{-1} \text{ s}^{-1}$ and operating frequencies in the tens of megahertz, making them possibly suitable for use in various devices such as displays and RFID tags [11]. However, the parasitic contact resistance (R_C) at the contact-organic semiconductor interface is still a major issue in organic FETs overall and is the major limiting factor in organic-TFT-application development. After a brief introduction into the general device physics and operating principles of organic TFTs in Sections 2.1 and 2.2., the physical origins and consequences of R_C as well as the most prominent approaches to eliminate it will be expounded upon in more detail.

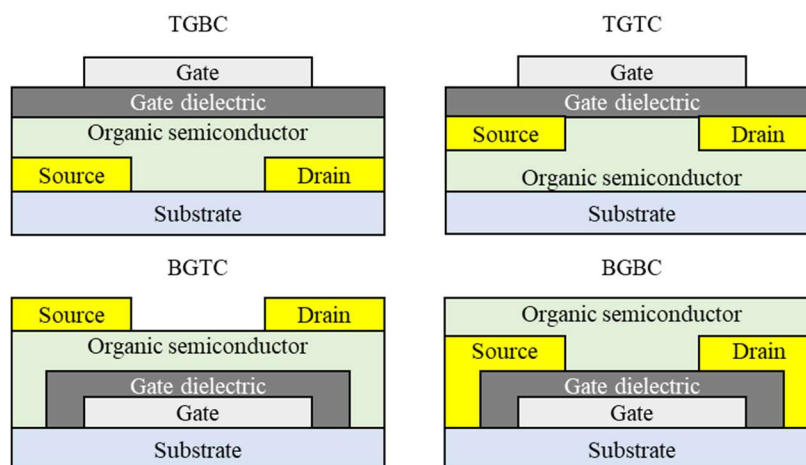


Figure 2.1 Device architectures of organic thin-film transistors.

Schematic diagrams of the four main geometries for organic thin-film transistors (TFTs): Top Gate - Bottom Contact (TGBC), Top Gate - Top Contact (TGTC), Bottom Gate - Top Contact (BGTC), and Bottom Gate - Bottom Contact (BGBC).

Organic TFTs are the most common form of organic FETs and form the backbone for circuit applications and materials development of organic semiconductors. They are generally fabricated by sequential steps in which the gate electrode, gate dielectric, source and drain contacts, and organic semiconductor are deposited as thin films on a substrate. The layers are fabricated usually by vacuum deposition or solution processing approaches, such as inkjet or meniscus-driven printing. Depending on the fabrication sequence, generally four different architectures are realized for organic TFTs (Figure 2.1). Each of these has advantages and disadvantages which will be discussed in some detail in Section 2.3 and investigated in Chapter 5 with regards to R_C , but to a first approximation they all generally follow the same operation principles adapted from the MOSFET formalism outlined below [124], [125].

2.1 Static operation of organic thin-film transistors

The static operation regimes of organic TFTs will be discussed in terms of four different regions of interest as highlighted in Figure 2.2. Note that the static operation principles will be described in terms of p-channel TFTs, since the significant majority of the organic TFTs studied in this thesis behave as such, though the same general descriptions will apply to n-channel TFTs with the appropriate changes in polarity. According to the Drude model, under thermal equilibrium conditions, the current measured at the drain contact (I_D) is determined simply by the conductivity of the channel region separating the source and drain contacts (σ_{ch}) and the drain-source voltage (V_{DS}). σ_{ch} is subsequently determined by the density of charge carriers in the semiconductor (p) and the charge-carrier mobility (μ).

$$I_D \propto \sigma_{ch} \cdot V_{DS} = p \cdot q \cdot \mu \cdot V_{DS} \quad (15)$$

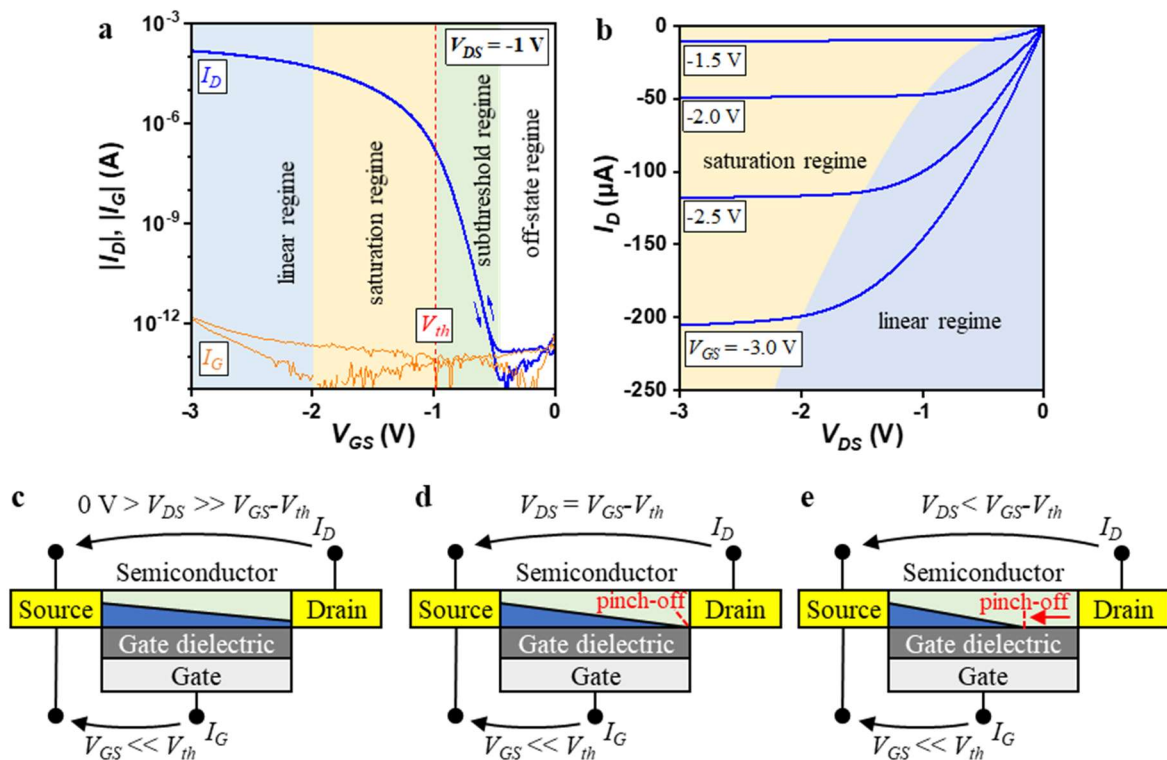


Figure 2.2 Static operation regimes of organic thin-film transistors.

Static transfer (a) and output (b) curves of a p-channel organic thin-film transistor. The different regimes of operation are highlighted. c-e) Schematic diagrams for the linear (c), onset of saturation (d) and full saturation (e) regimes highlighting the evolution of the charge carrier density in the channel region (blue area) with the applied drain-source voltage (V_{DS}).

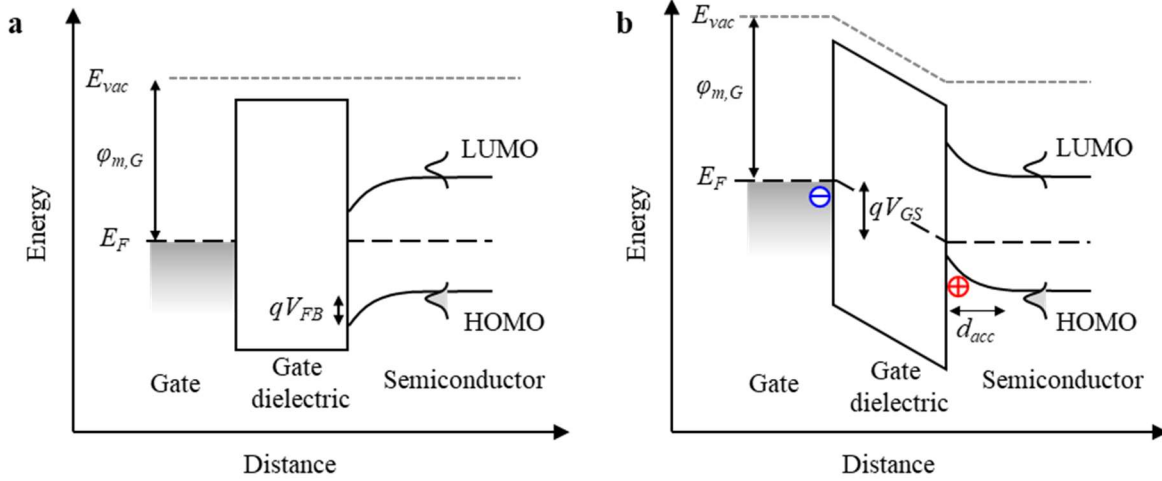


Figure 2.3 Energetics of channel formation in an organic thin-film transistor.

Schematic energy diagrams for the MIS capacitor formed by the gate, gate-dielectric layer, and organic semiconductor. a) Interface at equilibrium with no external applied potential. b) An applied potential between the gate and source (V_{GS}) above the flat-band voltage (V_{FB}) results in an accumulation of holes in the semiconductor region close to the interface with the gate-dielectric layer.

Where q is the elementary charge. Since organic semiconductors are nominally intrinsic semiconductors, organic TFTs operate almost exclusively in the accumulation mode, i.e. the TFT is operated by populating the channel with mobile carriers by applying an additional external gate-source voltage (V_{GS}) across the capacitor formed by the gate/gate-dielectric/semiconductor stack. The channel region is assumed to be confined to a very thin sheet of charges located in the semiconductor layer close to the interface with the gate dielectric and is coupled to the charges accumulated on the gate electrode. The areal density of mobile charge carriers in the channel region (Q_s) varies as a function of the distance (x) from the edge of the source contact from which the charges are injected into the semiconductor. This carrier density is modulated by the electric potential, taking into account V_{GS} and the monotonically decreasing potential contribution along the channel ($V(x)$), and is proportional to the area-normalized capacitance of the gate-dielectric layer (C_{diel}), such that

$$Q_s(x) = C_{diel}[V_{GS} - V(x)] \quad (16)$$

However, in real devices there typically exists an offset potential in the form of a threshold voltage (V_{th}) that must be surmounted for the accumulation of mobile charges to take place within the channel region. This generally arises due to imperfections in the charge coupling of the gate with the semiconductor layer [125], [126]. Within this offset term is the ‘flat-band’

voltage (V_{FB}) required to compensate for the initial band-bending of the semiconductor transport levels (Figure 2.3a) close to the interface with the gate dielectric that arises from the mismatch between the work function of the gate-electrode material ($\varphi_{m,G}$) and the work function of the organic semiconductor (φ_{osc}), as well as the possible presence of charged states within the bulk of the gate-dielectric layer ($Q_{s,die}$) and/or carriers trapped in defect sites in the organic-semiconductor layer (N_{it}).

$$V_{th} = \frac{\varphi_{m,G} - \varphi_{osc}}{q} - \frac{Q_{s,die}(x)}{C_{die} + qN_{it}} \quad (17)$$

For low power consumption, it is often preferable for V_{th} to be close to 0 V, and can often be tuned by modifying the gate-dielectric material that is used in the TFT [127], [128].

2.1.1 Subthreshold regime

As V_{GS} is decreased beyond V_{FB} and charge accumulation begins to occur, I_D increases exponentially until just below V_{th} (green portion of Figure 2.2a). The inverse slope of the logarithm of I_D as a function of V_{GS} in this region is known as the subthreshold swing (SS). The I - V response in this region is a characteristic of the efficiency of coupling between the accumulated charge in the channel region and the gate electrode at a given operating temperature (T).

$$SS = \frac{\partial V_{GS}}{\partial \log(I_D)} = \frac{k_B T}{q} \ln(10) \left(1 + \frac{qN_{it}}{C_{die}} \right) \quad (18)$$

SS is critically dependent on the density of trapped carriers N_{it} at a given measurement temperature. In practice, SS is often much larger than the trap-free ($N_{it} = 0$) theoretical minimum in TFTs, due to disorder in the semiconductor layer which may contain grain boundaries, etc. and/or form an imperfect interface with the gate dielectric leading to interface trap states. Additionally, SS may not become smaller with lower temperatures or worse still will increase in organic TFTs, since insufficient thermal energy may prevent the expulsion of charges from deeper trap states in the TFT. For low-power devices, minimization of SS is often critical and therefore various approaches have been pursued in order to eliminate sources of traps such as by modifying the gate oxide with a hydrophobic self-assembled monolayer (SAM) to promote greater order of the subsequent organic-semiconductor layer and to reduce

water adsorption onto the gate-dielectric surface [129]. See section 3.2 and 3.3.2 for more details on the organic semiconductor-gate dielectric interface and SAMs, respectively.

2.1.2 On-state: linear regime

The channel region of a p-channel TFT operating in the accumulation mode is populated with mobile carriers (holes) and is in the ‘On’ state when $V_{GS} < V_{th}$. Assuming the mobile charge carriers have an intrinsic field-independent mobility (μ_0) in the channel region, application of an additional voltage along the channel $V(x)$ will result in current flow described by

$$I_D = \frac{\mu_0 W}{L} \int_0^{V_{DS}} Q_s(x) dV(x) \quad (19)$$

with the channel width (W) and length (L) being the dimensions of the channel region perpendicular and parallel to the x -direction, respectively. According to the gradual channel approximation (GCA), ignoring possible space-charge effects [130], it is assumed that Q_s is uniform along the channel and that the voltage drop from the source to the drain contacts in the TFT is linear for the condition where V_{DS} is much smaller in magnitude than the gate overdrive voltage $V_{GS} - V_{th}$. Inserting equation (16) along with the offset V_{th} and performing the integration leads to the equation for the induced current flow

$$I_D = \frac{\mu_0 W C_{diel}}{L} \left(V_{GS} - V_{th} - \frac{V_{DS}}{2} \right) V_{DS} \quad (20)$$

For a V_{DS} that is constant and small compared to $V_{GS} - V_{th}$, the drain current will vary linearly with changes in V_{GS} . This allows us to then determine the channel transconductance (g_m) from the derivative of the transfer curve in the On-state

$$g_m = \frac{\partial I_D}{\partial V_{GS}} = \frac{\mu_0 W C_{diel}}{L} V_{DS} \quad (21)$$

2.1.3 On-state: saturation regime

If V_{DS} is increased to the extent that it approaches $V_{GS} - V_{th}$, the carrier-concentration profile along the channel of the TFT changes, such that the density of mobile carriers induced by the charge coupling with the gate electrode approaches zero in the region of the channel near the

drain contact. At $V_{DS} = V_{GS} - V_{th}$, the semiconductor is depleted directly next to the drain contact so that the channel is ‘pinched off’ at the contact edge (Figure 2.2d). Further increase of V_{DS} moves this pinch-off point closer and closer to the source contact (Figure 2.2e). The result is that I_D becomes saturated, since the potential provided by V_{GS} can no longer meet the demand set by V_{DS} . This can be accounted for in the equation for the drain current by inserting $V_{DS} = V_{GS} - V_{th}$ into equation (20) so that I_D now follows

$$I_D = \frac{\mu_0 W C_{diel}}{2L} (V_{GS} - V_{th})^2 \quad (22)$$

As such, the transconductance no longer varies linearly with V_{DS} but rather with $V_{GS} - V_{th}$

$$g_m = \frac{\partial I_D}{\partial V_{GS}} = \frac{\mu_0 W C_{diel}}{L} (V_{GS} - V_{th}) \quad (23)$$

2.1.4 Field-effect mobility

Up to now, it was assumed that a constant, field-independent mobility (μ_0) is present in the semiconductor layer. However, the mobility in organic semiconductors is often dependent on the charge-carrier density and therefore on the total electric field, so it is often more appropriate to consider the measured mobility in a TFT as an effective mobility (μ_{eff}) to account for a particular point of operation. Indeed, the mobilities reported most frequently for organic semiconductors in the literature are the effective mobilities extracted from TFTs. For the linear regime of operation, simply replace μ_0 in equation (21) and rearrange such that

$$\mu_{eff,lin} = \frac{L}{W C_{diel} V_{DS}} \frac{\partial I_D}{\partial V_{GS}} \quad (24)$$

In the saturation regime, the effective mobility is likewise determined from the change in $\sqrt{I_D}$ in response to a change in V_{GS} .

$$\mu_{eff,sat} = \frac{2L}{W C_{diel}} \left(\frac{\partial \sqrt{I_D}}{\partial V_{GS}} \right)^2 \quad (25)$$

It is important to note that the effective mobility in either operation regime should in principle never exceed the intrinsic mobility if thermal equilibrium conditions are maintained. For very small channel lengths and high electric fields, the resulting high current density can induce

‘self-heating’ that can actually increase the measured mobility, as well as possibly resulting in thermal runaway which can destroy the transistor [131]. Most relevant for the primary topics of discussion in this thesis, the contact resistance (R_C) between the source and drain contacts and the semiconductor can cause a reduction of the effective mobility if the channel length is small and can lead to errors in mobility extraction [132]. The contact resistance is treated separately in greater detail in Section 2.3 and 2.4, as it is one of the main topics of this thesis.

2.1.5 Off-state regime

In the off-state of a p-channel TFT ($V_{GS} > V_{FB}$) the only mobile carriers in the channel are those that are thermally activated or that are induced by doping of the organic-semiconductor thin film. In general, the off-state current should be minimized as much as possible to avoid excess power loss in circuits based on organic TFTs. This is especially relevant when considering mobility enhancement of organic semiconductors through doping, as excessive quantities of dopant molecules in the channel region can result in a significant increase of the off-state drain current; an effect which can be exacerbated in TFTs with shorter channel lengths [110]. Large leakage currents through the gate dielectric in the off-state can also occur, especially when a gate dielectric with a high density of defects is used and/or if the gate-to-contact overlaps (L_{ov}) of the TFT are large. In large-bandgap organic semiconductors such as the ones used in this work, the off-state currents can be exceedingly low ($<10^{-14}$ A) as the energetic mismatch between the minority-carrier transport level and the work function of the source and drain contacts is often very large.

2.2 Dynamic operation of organic thin-film transistors

The response time to a variation of an input signal of an electronic device such as an organic TFT is typically a function of the input-signal frequency and amplitude. A number of different figures of merit (FOM) are utilized to evaluate the response time of FETs. The most common FOM that is used in both organic electronics and other microelectronics technologies overall is the unity-gain, or transit, frequency (f_T). It is defined as the frequency (f) of the input signal, in this case a small oscillating gate-source voltage (v_{gs}) superimposed on the DC voltage (V_{GS}), at which the small-signal current gain is unity (Figure 2.4). Above this frequency the TFT can no longer act as a current amplifier (in fact, above this frequency it behaves like a capacitor). Therefore, f_T is determined from the small-signal drain current (i_d) and gate current (i_g) [124], [133]

$$i_d = g_m v_{gs} \quad (26)$$

$$i_g = j2\pi f v_{gs} C_G \quad (27)$$

$$f_T = f \left(\frac{|i_d|}{|i_g|} = 1 \right) = \frac{g_m}{2\pi C_G} \quad (28)$$

Where C_G is the total gate capacitance of the device. Notice that since g_m is independent of the frequency, f_T is to a first order mostly a consequence of the increasing magnitude of i_g with the operating frequency, as it is the displacement current arising from the charges moving into and

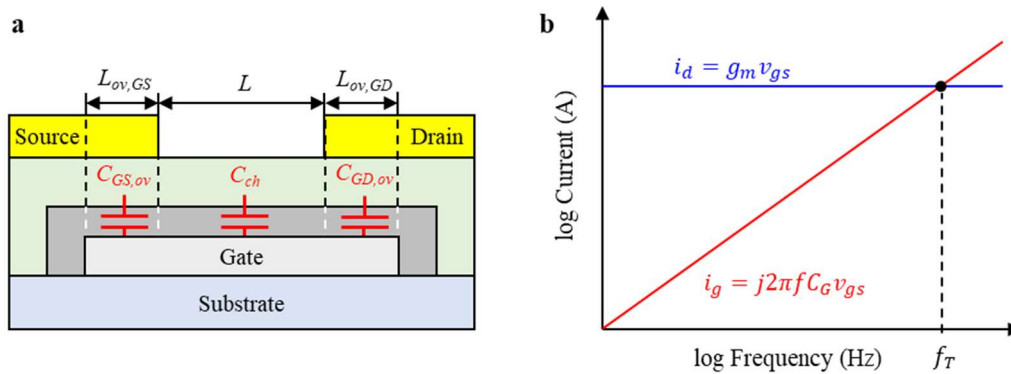


Figure 2.4 Dynamic small-signal operation of an organic thin-film transistor.

a) Schematic of an organic thin-film transistor highlighting the capacitive components attributed to the gate-to-source overlap ($C_{GS,ov}$, $L_{ov,GS}$), the gate-to-drain overlap ($C_{GD,ov}$, $L_{ov,GD}$) and the channel region (C_{ch} , L). b) Small-signal drain (i_d) and gate (i_g) currents as a function of the frequency (f). The unity-current-gain (transit) frequency (f_T) is determined by $f(i_d = i_g)$.

out of the gate electrode in response to v_{gs} [124]. C_G can generally be separated into parallel contributions from the source (C_{GS}) and drain (C_{GD}) sides of the TFT. These terms include capacitances resulting from the charges accumulated in the channel region (C_{ch}) as well as the parasitic capacitances from the gate-to-source overlap ($C_{GS,ov}$) and the gate-to-drain overlap ($C_{GD,ov}$) of the TFT. The magnitudes of the parasitic capacitances are determined by the area defined by the gate-to-contact overlaps and the channel width (W) and the area-normalized capacitance of the gate dielectric (C_{diel}). If the gate-to-contact overlaps are equivalent ($L_{ov,GS} = L_{ov,GD} = L_{ov}$) then

$$C_{GS,ov} = C_{GD,ov} = C_{diel}WL_{ov} \quad (29)$$

To determine the contribution from C_{ch} , the regime of operation of the TFT must first be considered. For both the linear and saturation regimes, Meyer's lumped capacitance model is adopted as it has been shown to correspond well with the measured electrical characteristics of organic TFTs [134]. In the linear regime, the total area of the channel of the intrinsic TFT ($W \times L$) is assumed to be populated with carriers, so that one can simply consider the channel and parasitic capacitances to be connected in parallel.

$$C_G = C_{GS,ov} + C_{GD,ov} + C_{ch} = C_{diel}W(L + 2L_{ov}) \quad (30)$$

As V_{DS} is made more negative, the distribution of charges in the channel region near the source and drain sides of the TFT becomes more uneven, due to the 'pinch off' effects described in Section 2.1.3. In the saturation regime, the depletion of charges from the drain side means that the C_{ch} is dominated entirely by the charges accumulated near the source side which are located in an area equal to 2/3 of the intrinsic channel area in an ideal TFT.

$$C_G = C_{diel}W \left(\frac{2}{3}L + 2L_{ov} \right) \quad (31)$$

Substituting equations (21) and (23) for g_m and (30) and (31) for C_G for the linear and saturation regime of operation, respectively, expressions for f_T highlighting the physical and geometrical parameters of the TFT are then obtained.

$$\text{linear} \quad f_T = \frac{\mu_{eff,lin}V_{DS}}{2\pi C_{diel}L(L + 2L_{ov})} \quad (32)$$

$$\textit{saturation} \quad f_T = \frac{\mu_{eff,sat}(V_{GS} - V_{th})}{2\pi C_{diel}L \left(\frac{2}{3}L + 2L_{ov}\right)} \quad (33)$$

2.2.1 Measurement of the transit frequency

In principle, f_T can be determined by directly measuring the apparent small-signal currents of an individual TFT, though in practice this approach is cumbersome and limited to a maximum measurement frequency of a few megahertz because of extrinsic parasitic capacitances added by standard measurement probes [133], [135]. For TFTs with higher transit frequencies, this can then require extrapolation of the i_g and i_d data over one or more orders of magnitude of the frequency, increasing the measurement uncertainty [136]. This problem can be circumvented to some extent by using special inductive probes, allowing measurement of TFTs at frequencies above 10 MHz [81], [137].

A more useful approach to determine the transit frequency of TFTs that has been used in microelectronics engineering of high-frequency semiconductor devices for decades is two-port network analysis [133], [135], [138]. In this method, the TFT is considered to be a device under test (DUT) in a two-port network (Figure 2.5). In practice, the frequency response characteristics of the DUT are obtained by measuring incident and reflected power waves (a and b , respectively) using a vector network analyzer and a specialized probe fixture which can be de-embedded from the DUT. The power waves are then related to each other by the so-called scattering (S) parameter matrix:

$$\begin{bmatrix} b_1 \\ b_2 \end{bmatrix} = \begin{bmatrix} S_{11} & S_{12} \\ S_{21} & S_{22} \end{bmatrix} \begin{bmatrix} a_1 \\ a_2 \end{bmatrix} \quad (34)$$

Well-established mathematical transformations can then be used to convert the S -parameters to other matrix characterizations of the DUT [138]. For the determination of the transit frequency of a TFT, the admittance (Y) parameters contain the desired information about the small-signal voltages and currents.

$$Y_{11} = \left. \frac{i_g}{v_{gs}} \right|_{v_{ds}=0} = j2\pi f(C_{GS} + C_{GD}) \quad (35)$$

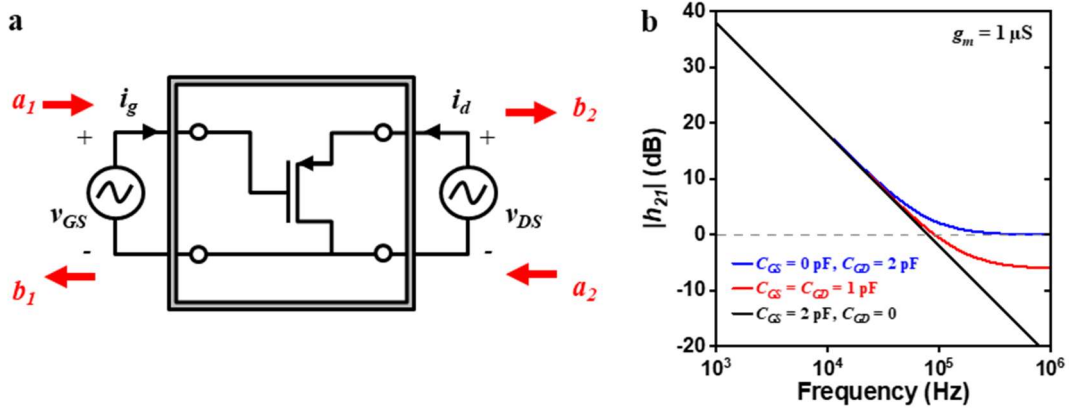


Figure 2.5 Two-port network analysis of a thin-film transistor.

a) Schematic diagram of the TFT treated as a device under test (DUT) with a matched load arrangement. Small-signal currents and voltages can be replaced by incident (a_1, a_2) and reflected (b_1, b_2) power waves which are related by a matrix of scattering (S) parameters. b) Example calculations of the gain ($|h_{21}|$) calculated using equation (40) for a transconductance (g_m) of $1 \mu\text{S}$ and total parasitic capacitance (C_G) of 2 pF . The relative contributions of the gate-to-source and gate-to-drain capacitances (C_{GS} and C_{GD} , respectively) are varied to illustrate the effect on the $|h_{21}|$.

$$Y_{12} = \left. \frac{i_g}{v_{ds}} \right|_{v_{gs}=0} = -j2\pi f C_{GD} \quad (36)$$

$$Y_{21} = \left. \frac{i_d}{v_{gs}} \right|_{v_{ds}=0} = g_m - j2\pi f C_{GD} \quad (37)$$

$$Y_{22} = \left. \frac{i_d}{v_{ds}} \right|_{v_{gs}=0} = \frac{1}{r_0} + j2\pi f C_{GD} \quad (38)$$

Where r_0 is the TFT's output resistance, g_m is the transconductance, and C_{GS} and C_{GD} are the individual components of the total gate capacitance associated with the source and drain sides of the TFT, respectively. Considering the case with $v_{ds} = 0$, the small-signal current gain in response to an alternating small-signal gate-source voltage with amplitude v_{gs} and frequency f is simply the ratio of Y_{21} and Y_{11} .

$$h_{21} = \frac{Y_{21}}{Y_{11}} = \frac{g_m - j2\pi f C_{GD}}{j2\pi f (C_{GS} + C_{GD})} \quad (39)$$

The gain is here denoted as h_{21} , since it corresponds to one of the dimensionless hybrid (h) parameters which can also be used to characterize the network [138]. The magnitude of the gain converted to units of decibel (dB) is then:

$$|h_{21}| = 20 \log \left(\frac{C_{GD}}{C_{GS} + C_{GD}} \sqrt{\left(\frac{g_m}{2\pi f C_{GD}} \right)^2 + 1} \right) \quad (40)$$

Assuming a short-circuited output, the measured S -parameters can be used to calculate any of the above parameters including $|h_{21}|$:

$$|h_{21}| = \frac{-2S_{11}}{(1 - S_{11})(1 + S_{22}) + S_{21}S_{12}} \quad (41)$$

As can be seen in the example plots of $|h_{21}|$ (dB) as a function of $\log(f)$ in Figure 2.5, for $C_G = 2$ pF and $g_m = 1$ μ S, ideally at low frequency $|h_{21}|$ decreases with a slope of -20 dB/decade and at high frequency $|h_{21}|$ saturates to approximately -6 dB for $C_{GS} = C_{GD}$. In this case, f_T can be extracted by inspection of the frequency at which $|h_{21}| = 0$ dB. When $C_{GS} = 0$, $|h_{21}|$ will approach zero asymptotically at high frequency. Note that for an ideal TFT, f_T should not vary for these different scenarios so long as g_m and C_G remain constant. This would imply that the total gate-to-contact overlap (L_{ov}) must be reduced in order to increase f_T . However, in practice f_T can be enhanced in real organic TFTs by reducing the gate-to-source overlap ($L_{ov,GS}$) only, while keeping L_{ov} constant. In Section 5.2.7, the extent of this enhancement and its dependence on the TFT architecture and is investigated in some more detail.

2.2.2 Inverters and ring oscillators

In lieu of two-port network analysis, the dynamic performance of TFTs can also be evaluated using simple circuits such as inverters and ring oscillators (RO). Inverters are circuit

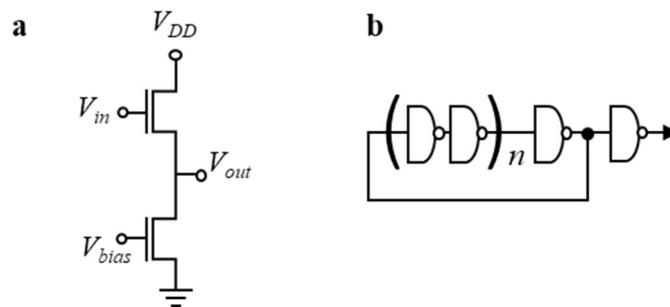


Figure 2.6 Biased-load inverter and ring-oscillator circuits.

Schematic circuit diagrams for (a) a biased-load unipolar inverter and (b) a ring oscillator with $n + 1$ stages within the ring, where $n \geq 1$. V_{DD} : supply voltage, V_{in} : input voltage, V_{out} : output voltage, V_{bias} : bias voltage.

logic elements which contain one or more transistors to invert an input signal from high to low, and vice versa. Using unipolar organic TFTs, various inverter designs can be realized with different static and dynamic characteristics [139]. For shorter switching times at the expense of lower intrinsic gain and higher static power consumption, the ‘biased load’ variant can be used (Figure 2.6a). Here, two TFTs (drive and load) are utilized, with a smaller W/L in the load TFT to reduce the output-signal loss caused by the voltage drop across the load TFT. The output voltage (V_{out}) of the inverter is determined by the gate-source voltage applied to the load TFT (V_{bias}), the supply voltage (V_{DD}) and the input voltage applied to the gate of the drive TFT (V_{in}). Higher V_{DD} generally enables shorter discharge times of the inverter and by changing V_{bias} , the trip voltage (value of V_{in} with the maximum gain, dV_{out}/dV_{in}) can be tuned, especially at lower operating voltages. The dynamic performance of the inverter can be evaluated by applying a square-wave input signal and recording the corresponding output signal (V_{out}). Delay constants in the rise (τ_{rise}) and fall (τ_{fall}) of the output signal can then be extracted with simple exponential fits and provide a metric for the dynamic performance of the inverter.

In ring oscillator (RO) circuits, an odd number of inverters are arranged in a ‘ring,’ such that the output of an individual inverter in the circuit is connected to the input of the subsequent inverter in the circuit (Figure 2.6b). Upon application of appropriate V_{bias} and V_{DD} , V_{out} is then an oscillating signal with frequency (f_{osc}) determined by the signal delay of each inverter and the number of inverters ($2n + 1$) in the ring.

$$f_{osc} = \frac{1}{2(2n + 1)\tau} \quad (42)$$

Where τ is the average signal delay time of the individual inverter stages [134]. Setting $n = 0$ then provides an average equivalent frequency (f_{eq}) for the individual TFTs in the inverters. Note that f_{eq}/f_T is typically about $\frac{1}{2}$ [15]. Of course, the signal delays in inverters and ring oscillators also depend on the parasitic capacitances of the individual organic TFTs, and therefore L and L_{ov} must be minimized for high f_{eq} . The circuits fabricated in this work have $L = 1 \mu\text{m}$ and $L_{ov} = 5 \mu\text{m}$ or $2 \mu\text{m}$, and the ring oscillators all have $n = 5$.

2.3 Contact resistance in organic thin-film transistors

The charge-carrier-injection behavior of the contacts in organic-semiconductor devices is fundamentally non-Ohmic [125]. However, for devices in which the semiconductor itself is limiting the charge flow in the device (i.e. the greatest portion of the overall resistance is determined by the sheet resistance of the semiconductor layer), such as in organic TFTs with sufficiently large channel lengths, the I - V characteristics of the TFT can show Ohmic-like behavior. In other words, the voltage drop due to the contacts must be negligible compared to the total voltage drop in the device [140] and an ‘Ohmic’ contact resistance is accomplished in organic electronic devices only when the voltage is sufficiently low that fewer charge carriers per unit volume are injected than are present in the bulk via thermal activation [88]. The derivations for the drain current and field-effect mobility outlined in Section 2.1.4 were developed assuming that the contact resistance between the source and drain contacts and the semiconductor channel during TFT operation is negligible. However, as organic TFTs are scaled to smaller dimensions, particularly in terms of the channel length, the contact resistance arising due to the reasons discussed in Section 3.1 will become the dominating source of resistance in the device. To account for the contact resistance, equation (20) is reformulated to include the contribution from the voltage drops at the source and drain contacts (V_C)

$$I_D = \frac{\mu_0 W C_{diel}}{L} \left(V_{GS} - V_{th} - \frac{V_{DS} - V_C}{2} \right) (V_{DS} - V_C) \quad (43)$$

Where $V_C = I_D R_C$ with R_C being the contact resistance. Subsequently, the effective mobility can be reformulated to include the contact resistance

$$\text{linear} \quad \mu_{eff,lin} = \frac{\mu_0}{1 + \frac{\mu_0}{L} R_C W C_{diel} \left(V_{GS} - V_{th} - \frac{V_{DS}}{2} \right)} \quad (44)$$

$$\text{saturation} \quad \mu_{eff,sat} = \frac{\mu_0}{1 + \frac{\mu_0}{2L} R_C W C_{diel} (V_{GS} - V_{th})} \quad (45)$$

Either of these two above equations can subsequently be simplified to define a channel length at which the effective mobility is equivalent to half of the intrinsic mobility ($L_{1/2}$).

$$\mu_{eff} = \frac{\mu_0}{\left(1 + \frac{L_{1/2}}{L}\right)} \quad (46)$$

It is important to note that these formulations neglect the influence of V_{GS} on the contact resistance. In reality, R_C can be profoundly dependent on V_{GS} in organic TFTs because of the dependence of the mobility in the semiconductor on the carrier density and because of the dependence of the width of the Schottky barrier at the interface between the contact and the semiconductor on the gate-source voltage (see Section 3.1.3 on charge injection physics).

In organic TFTs, the contact resistance is greatly affected not only by the choice of materials, but also by the TFT architecture. The historical record on the precise influence of device architecture on the contact resistance in organic TFTs is, however, somewhat ambiguous (Figure 2.7) [141]. The conventional wisdom is that TFTs fabricated in a staggered architecture should have smaller contact resistance than TFTs in a coplanar architecture, based on experimental data from organic TFTs comprising the same materials and layer thicknesses [142]–[145], device simulations and physical models [143], [146]–[148]. The fact that the

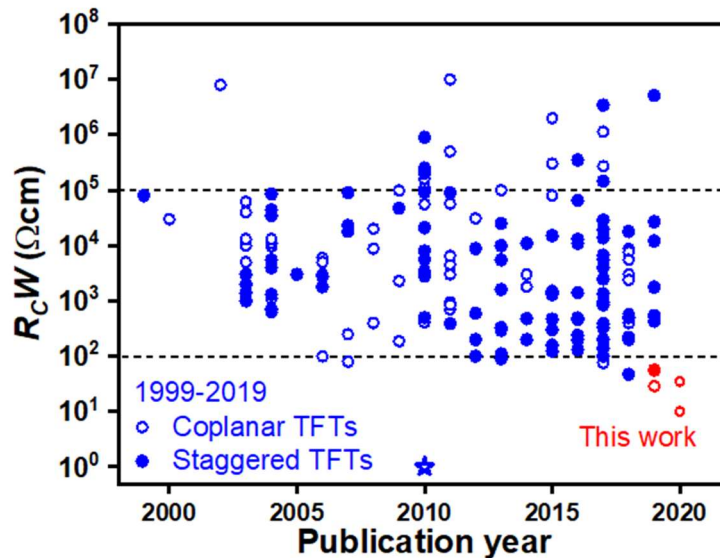


Figure 2.7 Literature summary of the width-normalized contact resistance ($R_C W$) reported in organic thin-film transistors (TFTs).

Literature summary of the width-normalized contact resistance ($R_C W$) reported in organic thin-film transistors (TFTs). The data is grouped into coplanar and staggered device architectures. The data point represented with ☆ at $R_C W = 1 \text{ } \Omega\text{cm}$ is for the electrolyte-gated TFT presented by Braga et al. [263]. See Table A.1 in the Appendix for a list of the contact resistances in the figure and the corresponding references. Adapted from Borchert et al. [141].

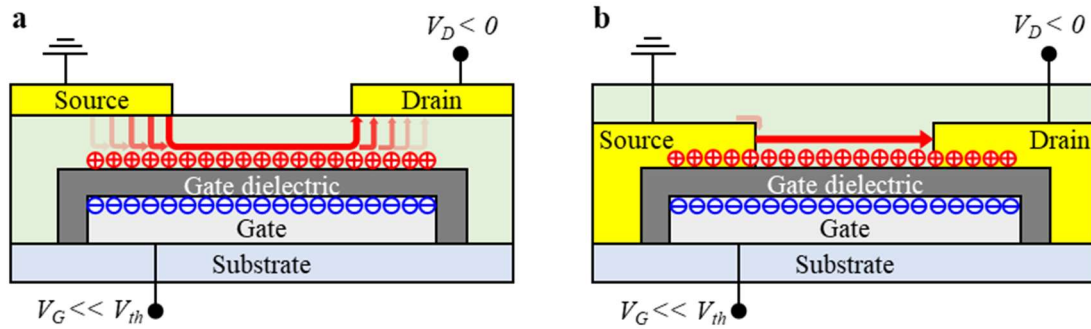


Figure 2.8 Charge carrier injection and transport in organic thin-film transistors.

Schematic diagram of the charge accumulation and transport in organic TFTs with the a) bottom-gate, top-contact (BGTC) and b) bottom-gate, bottom-contact (BGBC) geometries. In the BGTC geometry, current-crowding effects are present under the source contact. In the BGBC geometry, the charge carrier injection primarily takes place at the edge of the contact, whereas negligible injection occurs from the top of the contact due to screening of the potential between the gate and source.

contact resistance of staggered organic TFTs is often smaller than that of otherwise equivalent coplanar organic TFTs has been ascribed primarily to the overlap between the contacts and a portion of the gate-induced carrier channel positioned directly under the contacts, leading to more efficient charge injection (Figure 2.8) [17], [149], [150]. Additionally, the electrical conductivity in the contact regions may be enhanced (inadvertently) by metal clusters penetrating into the semiconductor layer upon deposition of the contact metal which can act as dopants within the semiconductor host [151], by intentional contact doping with other small molecules [152], and by the relatively large area for charge injection between the contact metal and the gate-induced carrier channel (current crowding, shown schematically in Figure 2.8a) [140], [149]. However, as can be noted from the historical record of the reported contact resistances (Figure 2.7), coplanar devices have actually shown the record for lowest contact resistance since 2004, with the lowest reported value⁴ from 2007 to 2017 being 80 Ωcm , reported by Stadlober et al. [78]. The primary reasons for this very low contact resistance were attributed to a very-thin Au-oxide interlayer that formed upon exposure to UV/Ozone treatment as well as a significant increase of large islands of pentacene which formed on the contacts. Between 2011 and 2017, a vast majority of the reported contact resistances were then for staggered devices, many of which achieved relatively low contact resistances (<1 $\text{k}\Omega\text{cm}$) with

⁴ A notable exclusion from consideration is the contact resistance of 1 Ωcm reported by Braga et al. [263] In this special case, the implemented electrolyte dielectric actively doped the contacts of the TGBC device, thereby significantly reducing the contact resistance.

the smallest value being $\sim 90 \text{ } \Omega\text{cm}$ achieved in BGTC TFTs based on DNNT reported by Matsumoto et al. [121]. In 2017, Kitamura reported a new record⁵ of $75 \text{ } \Omega\text{cm}$ for the contact resistance using the BGBC geometry with C₁₀-DNNT as the semiconductor, wherein gold source and drain contacts were functionalized with a chemisorbed molecular monolayer (CML) of pentafluorobenzenethiol (PFBT) and the crystal morphology of the liquid-crystalline C₁₀-DNNT layer was optimized by post-deposition annealing at $100 \text{ } ^\circ\text{C}$ in N₂ environment [153]. The lowest value reported to date for staggered TFTs is $46.9 \text{ } \Omega\text{cm}$ in BGTC TFTs based single crystals of C₈-DNBDT-NW by virtue of using F₄-TCNQ as a contact dopant to reduce the energetic barrier and reduction of the access resistance by reducing the film thickness to only a bi-layer [81].

There is generally a significant dependence of the measured contact resistance on the semiconductor-layer thickness in staggered geometries, as this layer adds an additional region of high resistance through the semiconductor thin-film that the carriers must traverse after injection from the source contact in order to reach the channel. This issue can be at least partially counteracted by using organic semiconductors which can form laterally-connected films with low nominal thicknesses [154]–[156] or, even better, single-crystalline films of one or only a few monolayers [81], [82], [157], [158]. It has further been shown in BGTC TFTs that the contact resistance can be dependent on the grain size in the semiconductor thin films, with larger contact resistance for, e.g., pentacene thin films with smaller grain sizes being observed [77]. This is often attributed to a higher trap-state density in thin films with a greater number of grain boundaries. In coplanar TFTs, the contact resistance is often higher than in staggered TFTs, since the gate field-assisted charge injection is weakened due to the smaller injection area which is (to a first approximation) limited primarily by the height and width of the contact edge [146]. Perhaps more critical for consideration in real device-fabrication, BC organic TFTs often exhibit a discontinuous coverage and a greater number of grain boundaries in the organic-semiconductor layer along and across the edges of the contacts, which can negatively impact the injection of charge carriers [159]. This occurs because of the crystallization properties of the organic semiconductor thin film on top of the contact material (a reactive metal surface) usually differs profoundly from that of the (inert) gate dielectric,

⁵ Note that the contact resistance was shown to decrease with more negative drain-source voltage in the linear regime, meaning that the lowest reported value in the paper of $21 \text{ } \Omega\text{cm}$ at $V_{DS} = -2.6 \text{ V}$ is likely underestimated when using TLM to evaluate the contact resistance. Therefore, the measurement of $75 \text{ } \Omega\text{cm}$ is the most reliable as it was measured with the V_{DS} closest to 0 V .

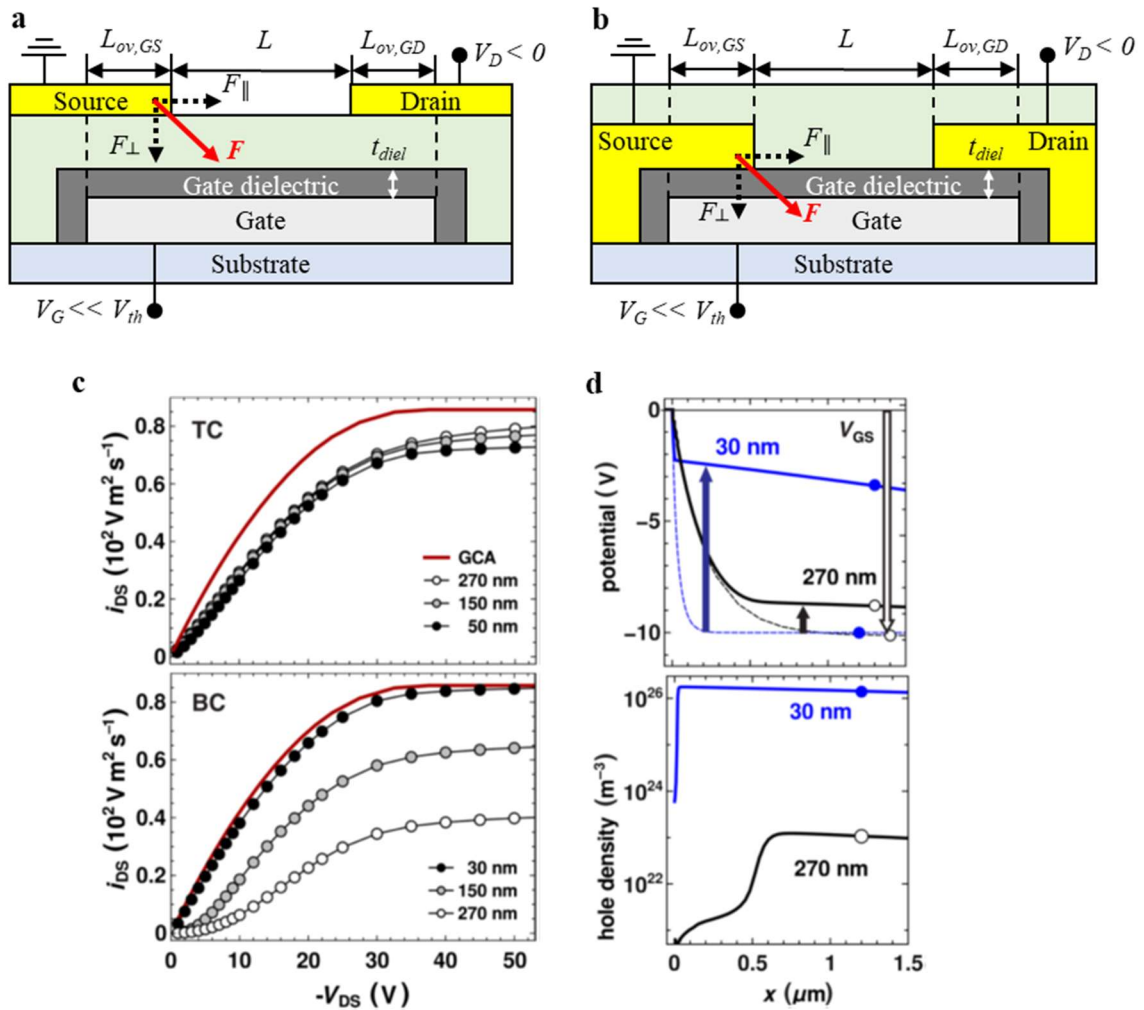


Figure 2.9 Electric field in organic thin-film transistors.

Schematic representation of the components of the applied electric field (F) at the source contact in an organic thin-film transistor with (a) bottom-gate, top-contact (BGTC) and (b) bottom-gate, bottom-contact (BGBC) geometries. c) Normalized output characteristics from drift diffusion-based simulations of BGTC and BGBC TFTs showing the influence of the gate dielectric thickness (t_{diel}) on the charge injection. BGBC shows more ideal characteristics approaching the gradual channel approximation (GCA, red curves) for smaller t_{diel} , due to increased contribution of the lateral field component (F_{\parallel}) in the BGBC architecture, leading to significant differences in the (d) potential and hole density as a function of the distance into the channel region for thin and thick gate dielectrics. From Karin Zojer et al. [18].

resulting in significant difference in the crystal packing arrangements on either surface as a result of differences in the importance of the molecule-molecule van der Waals interactions vs. interactions with the different surfaces [67], [142]. Various approaches have therefore been implemented to improve the wetting behavior of organic semiconductors on metal contacts to promote similar crystallization on the contacts, such as the afore-mentioned UV/ozone

exposure implemented by Stadlober et al. [78], oxygen-plasma treatment [160], [161] and chemisorbed molecular monolayers (CMLs) [162]. The lattermost approach has so far seen the most encouraging results for the reduction of the contact resistance in BC organic TFTs and is a major subject of the experimental investigations presented in this thesis. Despite these extensive efforts to improve the contact-semiconductor interface of BC organic TFTs, up to the end of 2018 their contact resistance was comparatively inferior in most cases to that of TC organic TFTs [81].

A key detail for these trends in the reported contact resistances in organic TFTs was recently elucidated in drift-diffusion-based simulations performed by Karin Zojer et al. which ultimately predicted that coplanar organic TFTs may exhibit lower contact resistances than otherwise equivalent staggered organic TFTs, provided the effective energy barrier (Φ_B) between the source contact and the organic semiconductor is sufficiently low (≤ 0.5 eV) and the gate dielectric is sufficiently thin [17], [18]. The enhancement of the charge injection in the simulated coplanar (BGBC) TFTs with a thin gate dielectric was primarily attributed to the differences in the geometrical configuration of the electric field (F) during transistor operation with respect to the channel and the contacts (Figure 2.9a,b). The vertical component (F_{\perp}) is relatively unaffected by the gate-dielectric thickness and essentially plays no role in the carrier injection in coplanar TFTs other than in forming the channel, whereas it is the predominant contributor to carrier injection in staggered (BGTC) TFTs. Conversely, the lateral component (F_{\parallel}) has a much stronger influence on the carrier injection in coplanar TFTs than in staggered TFTs and, more crucially, has a strong dependence on the gate-dielectric thickness. This is reflected in the simulation results by the relative insensitivity of the output characteristics of the simulated BGTC TFTs to changes in the gate-dielectric thickness from 270 nm to 50 nm (Figure 2.9c). This is in direct contrast to the trend observed for the BGBC TFTs, where a very strong dependence was observed in the output characteristics, such that the simulation results approached the ideal curve determined by the gradual channel approximation (GCA, Figure 2.9c). The dramatic trend was directly attributed to the increased hole density and smaller potential drop at the source contact by virtue of the enhanced F_{\parallel} component (Figure 2.9d). Given the importance of reducing the contact resistance for the static and dynamic performance of organic TFTs [13], [81], this is a potentially critical finding, but an experimental study to confirm the impact of the gate-dielectric thickness on the contact resistance had to the author's knowledge not been performed, despite a number of investigations into the effects of the gate-

dielectric thickness on other organic-TFT-performance parameters [128], [154], [163], [164]. A systematic investigation of the effects of the TFT architecture and gate-dielectric thickness is presented in Chapter 5.

2.4 Measuring the contact resistance in TFTs

2.4.1 The gated transmission line method

The gated transmission line method (TLM) was first developed for evaluating the channel resistance and parasitic contact resistance in hydrogenated amorphous silicon (a-Si:H) TFTs [165]. It is by far the most common method for measuring the contact resistance in organic TFTs [124], [166], due to its relatively easy implementation and straight-forward interpretation. The major assumption of the TLM is that the gradual channel approximation (GCA) holds, such that at vanishingly small V_{DS} and for $V_{GS} < V_{th}$ in a p-channel TFT, the total TFT on-state resistance (R) can be simplified to a series connection of the channel resistance (R_{ch}) and the parasitic contact resistance from the source ($R_{C,S}$) and drain ($R_{C,D}$) contacts, which are lumped into one term for the contact resistance (R_C). One important additional stipulation is that these resistances must be considered Ohmic to justify the use of TLM to evaluate the contact resistance [165].

$$R = \left. \frac{\partial V_{DS}}{\partial I_D} \right|_{V_{DS} \rightarrow 0}^{V_{GS}} = R_{ch} + R_C \quad (47)$$

The channel resistance is determined by the sheet resistance (R_{sh}) of the semiconductor thin film in the channel region, which is a function of the charge-carrier density, and therefore V_{GS} .

$$R_{ch} = R_{sh}(V_{GS}) \frac{L}{W} \quad (48)$$

The sheet resistance is then determined according to the charge-sheet model [125] by the inverse of the product of the intrinsic channel mobility (μ_0), the area-normalized gate-dielectric capacitance (C_{diel}) and the gate overdrive voltage ($V_{GS} - V_{th}$).

$$R_{sh} = \frac{1}{\mu_0 C_{diel} (V_{GS} - V_{th})} \quad (49)$$

By combining equations (47), (48) and (49), and normalizing by W , one then obtains the width-normalized total resistance (RW) as a function of L .

$$RW = \frac{1}{\mu_0 C_{diel} (V_{GS} - V_{th})} L + R_C W \quad (50)$$

By measuring the transfer characteristics of TFTs with different channel lengths in the linear regime, it is then possible to extract $R_C W$ and μ_0 at a given gate overdrive voltage by performing a linear fit to the RW vs. L measurement data and extracting the y-intercept ($L = 0$) and the slope, respectively (Figure 2.10). To account for the V_{GS} -dependence of R_C , the formulation used by Luan and Neudeck [165] models R_C into a series connection between a V_{GS} -modulated resistance in the bulk semiconductor region separating the contact interface and the channel region and a gate-voltage-independent minimum contact resistance ($R_{C,0}W$).

$$R_C W = \frac{l_0}{\mu_0 C_{diel} (V_{GS} - V_{th})} + R_{C,0} W \quad (51)$$

Where l_0 is a characteristic length identified empirically in a TLM experiment by the point where the individual RW vs. L fit lines intersect on the negative x-axis at a common value of $RW = R_{C,0}W$. Note, if the V_{GS} -dependence does not follow precisely that described in equation (51), l_0 and thus $R_{C,0}W$ may not be simply extracted in this way.

For staggered TFTs, a so-called transfer length (L_T) defines an area under the contacts through which 63% of the charge injection takes place [110], [149]. L_T can be determined from TLM measurements by extrapolating the fit lines to $RW = 0$, with the point of intersection with the x-axis denoting $2L_T$. If the gate-to-contact overlap is larger than the transfer length ($L_{ov} > L_T$), the charge-exchange area, and thus R_C , is not limited by the contact-overlap dimensions. The dependence of $R_C W$ on L_T and L_{ov} , with a correction factor corresponding to an extended length (L_{ext}) beyond the gate-to-contact overlap in staggered TFTs [167], follows

$$R_C W = 2R_{sh} L_T \coth\left(\frac{L_{ov} + L_{ext}}{L_T}\right) \quad (52)$$

Of course, such a ‘transfer length’ can also be extracted from the TLM analysis of coplanar TFTs. However, the physical meaning behind an L_T in coplanar TFTs is unclear, since in principle there is no charge exchange occurring underneath or (to a first order) above the contacts [17], [146]. This holds also for l_0 , though both quantities may still be extracted and prove to be useful metrics to analyze the charge injection in both TFT architectures.

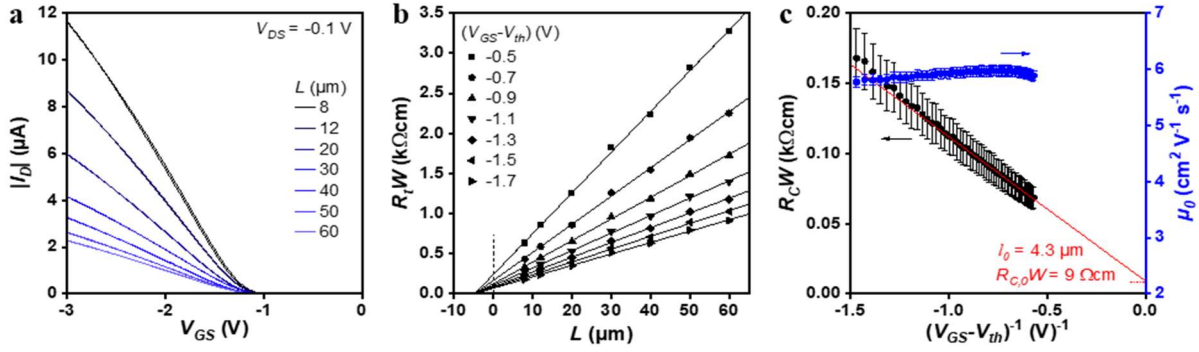


Figure 2.10 Transmission line method analysis of organic-thin film transistors.

a) Transfer characteristics of coplanar TFTs with channel width (W) of 200 μm and channel lengths (L) of 8, 12, 20, 30, 40, 50, and 60 μm measured at a small drain-source voltage (V_{DS}). b) Linear fits to the total width-normalized resistance ($R_W = (V_{DS}/I_D) \cdot W$) as a function of L for several gate overdrive voltages ($V_{GS} - V_{th}$). c) The width-normalized contact resistance ($R_C W$) and intrinsic channel mobility (μ_0) as a function of $(V_{GS} - V_{th})^{-1}$. For ideal TFTs, the fit to $R_C W$ can then be used to extract an effective contact length (l_0) and the gate-voltage-independent minimum contact resistance ($R_{C,0} W$).

In practice, all TFTs used in a TLM-analysis experiment should have been fabricated at the same time and ideally in close proximity to each other on the same substrate so as to avoid sample-to-sample variations as much as possible. The channel lengths of the TFTs should span at least approximately one order of magnitude to improve statistical significance. A consideration should also be given to the magnitude of the resistances in the TFTs. In general, TFTs with smaller channel lengths should be used when the sheet and contact resistances are smaller to reduce the error and improve the statistical weighting of the measurements. The absolute number of TFTs required in the analysis also depends on the variability in the device performances.

2.4.2 Small-signal measurements

In general, the complex impedance of a TFT (Z_{TFT}) is a series combination of the impedances from the contact (Z_C) and the channel (Z_{ch})

$$Z_{TFT} = Z_C + Z_{ch} \quad (53)$$

As with gated TLM, for vanishingly small V_{DS} a transmission line model can also be applied to describe an organic TFT with an equivalent circuit which can be used to evaluate linear-response impedance-spectroscopy measurements (Figure 2.11). While this presents a

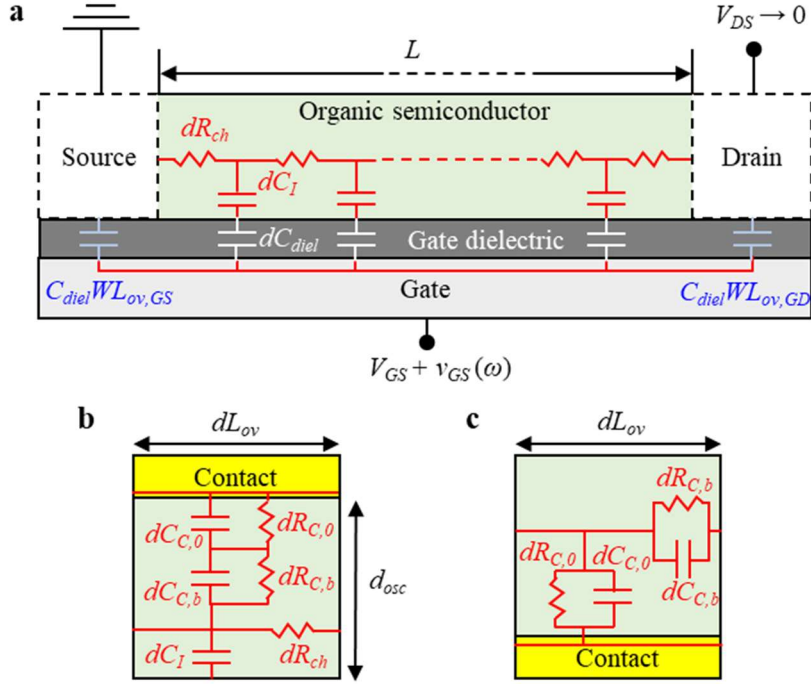


Figure 2.11 Lumped circuit-element model of organic thin-film transistors.

- a) Equivalent circuit model of an organic thin-film transistor where the channel region is described by a transmission line model distributed network. For the contacts, additional circuit blocks are adopted for (b) staggered and (c) coplanar contacts.

potentially powerful method for separating the individual resistive and capacitive components of an electrical device, equivalent-circuit modeling should always be handled with caution, and measurements should be well-controlled to prevent contributions from extrinsic factors (e.g. moisture, bias stress). The models for organic TFTs [132], [168], [169] are typically composed of channel-resistance elements ($dR_{ch} = (R_{sh}/W)*dL$) determined by the point of operation and the dimensions of the channel region, interface capacitance (C_I) accounting for trap states, and the gate-dielectric capacitance (C_{diel}). The channel impedance is then described analytically by

$$Z_{ch} = \frac{1}{j\omega WLC'} \lambda \coth \lambda \quad \lambda = \sqrt{\frac{j\omega C' R_{sh} L^2}{4}} \quad (54)$$

Where ω is the angular frequency and C' is a series connection of the gate-dielectric and interface capacitances related to trap states at the organic semiconductor-gate dielectric interface

$$C' = \frac{C_{diel} C_I}{C_{diel} + C_I} \quad (55)$$

The contact impedance is modeled well in many cases by an additional parallel RC circuit element for the source and drain contacts that captures the charge injection and the transport physics relating to the contacts (R_C, C_C)

$$Z_C = \frac{jR_C}{j - \omega R_C C_C} \quad (56)$$

More detailed models have also been adopted to account for individual contributions to Z_C from e. g. the metal-semiconductor interface including a depletion region [168] and the Schottky barrier (denoted by $R_{C,0}, C_{C,0}$), and from contributions related to the device architecture [132], [150]. For staggered TFTs, the thickness of the semiconductor film separating the contacts from the channel region (t_{osc}) as well as the effects of current crowding are essential ($R_{C,b}, C_{C,b}$) and depend on the gate-to-contact overlap area (WL_{ov}) (Figure 2.11b). These bulk contributions are less significant in coplanar TFTs, and the parasitic overlap capacitance is also simplified to $WL_{ov}C_{diel}$ (Figure 2.11c, see also the experimental Section 5.2.7).

2.4.3 Extraction from measurements of the transit frequency

A fundamental flaw of the above methods which both rely on a transmission line model for analyzing the contact resistance is that the underlying assumptions of a continuous charge-carrier density along the channel region and a V_{DS} close to zero make them unsuitable for the saturation regime, where the channel region is discontinuous. A measurement of the contact resistance in the saturation regime is desirable in order to fully characterize and model the TFTs. Here, a convenient method is proposed in which this can be accomplished through an evaluation of the transit frequency (f_T) of several TFTs with different channel lengths (L). Simply by combining equations (33) and (45), provided the accuracy of the Meyer capacitance model [170], an expression for the transit frequency which depends on the contact resistance is obtained:

$$f_T = \frac{\mu_0(V_{GS} - V_{th})}{2\pi \left(L + \frac{1}{2}\mu_0 C_{diel} R_C W (V_{GS} - V_{th}) \right) \left(2L_{ov} + \frac{2}{3}L \right)} \quad (57)$$

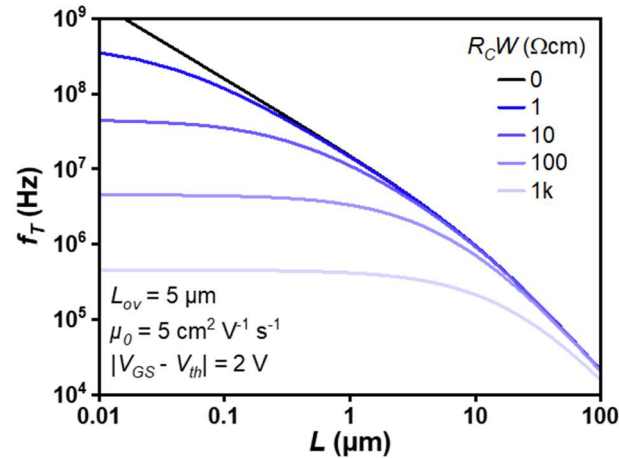


Figure 2.12 Dependence of transit frequency on channel length and contact resistance.

Calculations illustrating the effect of the channel-width-normalized contact resistance (R_CW) on the transit frequency (f_T) for some typical parameters found in the organic thin-film transistors presented in the experimental portions of this thesis.

Using this expression, the transit frequency versus channel length data can, in principle, be fit using R_CW and μ_0 as free fitting parameters, similar to the TLM. As an illustration, the detrimental effects of R_CW are shown in several calculations of f_T vs. L using equation (57) and $L_{ov} = 5 \mu\text{m}$, $C_{diel} = 0.7 \mu\text{F cm}^{-2}$, and $\mu_0 = 5 \text{ cm}^2 \text{ V}^{-1} \text{ s}^{-1}$ in Figure 2.12. In Section 5.2.6 it is demonstrated how this method can be applied to experimental data from high-frequency flexible organic TFTs. Note that for staggered TFTs, equation (57) requires an additional factor (β) which takes into account the organic semiconductor bulk between the contact and the gate dielectric. This primarily contributes to the parasitic capacitance on the drain side of the TFT and is discussed in more detail in Chapter 5.

2.4.4 Other single-device extraction methods

A drawback of the above methods for contact-resistance extraction is that they require several transistors and many time-consuming measurements, ultimately providing only an average measurement of the contact resistance. In addition, none of the above methods provide a separation of the source and drain resistances. There are several other methods requiring only a single device for contact-resistance extraction, and these are summarized in Table 2.1 with their various advantages and disadvantages.

Table 2.1: Methods for extracting the contact resistance using single devices.

Method	Device	Advantages	Disadvantages
<i>Y-function</i> [144]	TFT	Requires only a single TFT with no special device structures.	Assumes a gate-voltage independent contact resistance. Only applicable to the linear regime.
<i>Kelvin probe force microscopy</i> [171], [172]	TFT	Requires only a single TFT with no special device structures. Capable of separating the source and drain contact resistances.	Requires special measurement equipment. Measurement can be very time-consuming and accurate data can be difficult to obtain. Cannot measure very low contact resistances. Large channel length required.
<i>Gated four probe</i> [173]	TFT with two additional terminals in the channel	Capable of separating the source and drain contact resistances.	Special structure requiring additional probes in the channel mostly limits analysis to relatively long-channel devices. Cannot measure very low contact resistances. Can only be performed in the linear regime.
<i>Gated van der Pauw</i> [174]	Van der Pauw structured TFT	Capable of separating the source and drain contact resistances.	Special structure requiring large channel dimensions. Long measurement times and complicated data analysis.

3 The functional interfaces in organic thin-film transistors

The interface is the device.

- Herbert Kroemer, 2000 Nobel Laureate

In organic TFTs, there are usually two interfaces of paramount importance which determine the transistor functionality: (1) the organic semiconductor-gate dielectric interface and (2) the organic semiconductor-contact interface. A significant portion of the device engineering and materials science research on organic TFTs is therefore devoted to understanding and optimizing these interfaces [20], [46], [48]. The organic semiconductor-gate dielectric interface plays a critical role in the channel characteristics such as the charge coupling between the gate electrode and the semiconductor layer and the intrinsic channel mobility (μ_0) of an organic TFT. The organic semiconductor-contact interface mostly determines the charge injection/extraction characteristics, and by extension the contact resistance (R_C) in organic TFTs. In recent years, this second interface has been the more-limiting in the development of high-frequency organic TFTs, due to the limitations on the transistor performance as a result of the contact resistance. Some common features hold for both interfaces. Both depend critically on the morphology of the organic-semiconductor thin film in the vicinity of the interface with the adjacent layer. As discussed at length in Section 1.2, the morphology of the organic semiconductor in this region depends on various parameters including the method by which the semiconductor layer is deposited, the precise order in which the layers of the organic TFT are fabricated (e.g. metal on semiconductor or vice versa) and the chemistry of the surface on which the film is formed. In particular, the surface roughness and the terminal groups of the substrate material (gate dielectric or contacts) can influence the organic-semiconductor layer formation. In most of the relevant cases for organic TFTs, the organic molecules deposited onto a surface are only weakly physisorbed or chemisorbed, but in some cases stronger chemisorption occurs such as in F₄-TCNQ on Au [64] or organic molecules with a reactive end group like in chemisorbed molecular monolayers (CMLs, see Section 3.3.2) [175]. In this chapter, the discussion will proceed with focus on the key aspects that are most relevant to organic TFTs and will place special emphasis on some common approaches to interface modification that are also employed in the experimental investigations of this thesis.

3.1 The organic semiconductor-contact interface

3.1.1 Energy-level alignment at interfaces between organic semiconductors and metals

In general, when two materials are brought into contact, charge rearrangement occurs across the interface to bring the system to thermal equilibrium and establish a common Fermi energy (E_F) [176]. The resulting equilibrium arrangement of the energy levels across this junction will then to a first degree determine the charge-transport processes across the interface during device operation. The most crucial quantity to consider for charge injection from a metal to a semiconductor is the potential energy barrier (Φ_B) that forms at the interface. Several models have been proposed to describe the details of the interface-equilibration process in terms of the energy levels and charge transfer within the semiconductor thin film, in any intervening regions, and at the metal surface in order predict the height of Φ_B . In the simplest model originally developed for metal contacts to inorganic semiconductors, known as the Schottky-Mott limit, the energetic barrier across the contact metal-semiconductor interface for electron or hole transport ($\Phi_{B,n}$ and $\Phi_{B,p}$, respectively) is simply estimated by the difference in the work function of the contact metal (ϕ_m , defined as the difference in energy between the vacuum level (E_{vac}) and the metal Fermi energy) and the semiconductor transport levels (ionization energy (IE) for the hole-injection barrier or electron affinity (EA) for the electron-injection barrier) of

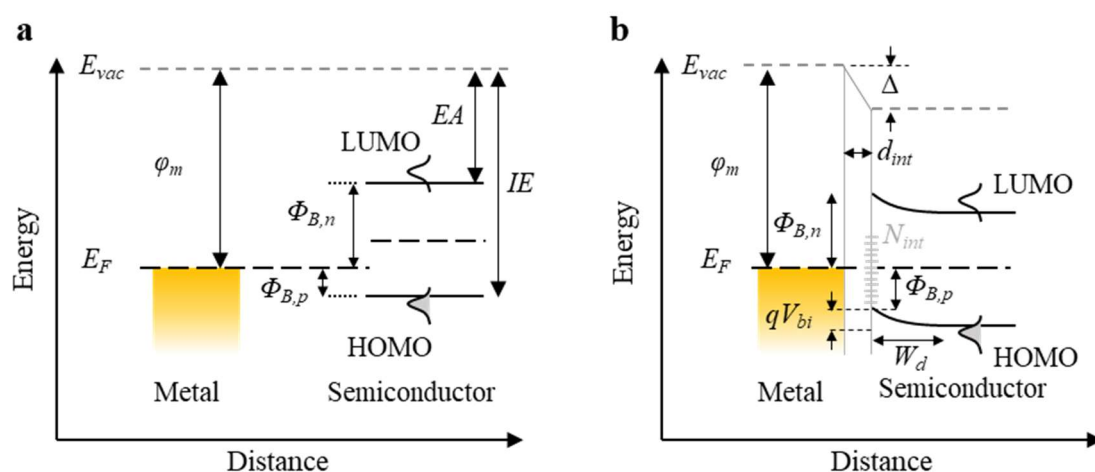


Figure 3.1 Metal-organic semiconductor contact.

Schematic energy diagrams of the formation of the contact-semiconductor interface. a) Isolated contact and semiconductor. b) Metal and semiconductor in contact after equilibration. Adapted from Sze and Ng [176].

the isolated materials (Figure 3.1b) [92], [177]. For organic semiconductors, one may analogously estimate the expected energy barriers for charge injection according to the positions of LUMO and HOMO with respect to φ_m . More efficient injection for electrons (holes) is expected in organic semiconductor-metal contacts for a φ_m that is closer to the LUMO (HOMO). However, this simplification has been shown to be quite inaccurate for precisely predicting Φ_B or for describing the charge-injection properties in real devices [92]. In fact, to date no fabricated contact-semiconductor systems have ever been reported which show precisely this behavior, even for the inorganic semiconductor-metal interfaces for which this model was first developed. The source of the discrepancy in contacts to organic semiconductors is the deviation from vacuum-level alignment due to the formation of an interface dipole (Δ) within the first few molecular layers of the organic semiconductor away from the contact with the metal surface (d_{int} , Figure 3.1b) [92]. This changes the effective work function of the contact (φ_C) such that it no longer coincides with φ_m .

$$\varphi_C = \varphi_m + \Delta, \quad \Phi_B = IE, EA - \varphi_C \quad (58)$$

There are various possible contributors to Δ , which depend on the contact metal and the organic semiconductor as well as extrinsic factors such as the chemical purity of both the metal surface and the organic semiconductor (Figure 3.2) [140], [178]. These include charge transfer across the interface which forms a surface sheet charge on the metal and organic semiconductor, strong chemical reactions between the adsorbate molecule and the metal, variations in the molecular orientations on the surface, presence of an intrinsic dipole moment within the adsorbate species, and reduction of the metal work function by the interaction of the π -electron clouds of a physisorbed organic layer with the metal electron tail states (referred to as the ‘pillow’ or ‘push-back’ effect, Figure 3.2) [140], [178], [179]. The redistribution and accumulation of charges in the semiconductor leads to band-bending (Figure 3.1b) and is typically quantified by the width of the region over which band-bending extends into the semiconductor away from the contact interface [178], [180].

$$W_d = \sqrt{\frac{2\varepsilon_{osc}}{qp} \left(V_{bi} - V - \frac{kT}{q} \right)} \quad (59)$$

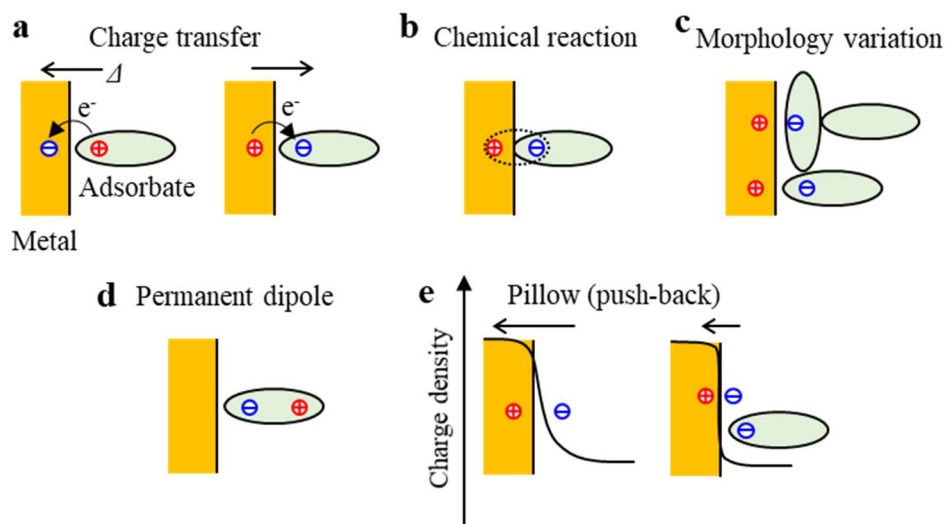


Figure 3.2 Origins of the interface dipole.

Possible contributors to the interface dipole (Δ) which forms at an organic semiconductor-metal interface. Physisorption is denoted by a small space separating the adsorbate from the metal surface and the arrows denote the sign of Δ . a) Charge transfer results in either cation or anion formation. b) Strong chemical reaction through hybridization of metal and semiconductor orbitals, with Δ of both signs possible. c) Semiconductor morphology variations can contribute to the magnitude of Δ . d) Adsorbates with in which the molecule of functional groups have intrinsic dipole moments. e) Suppression (push-back) of the electron cloud extending away from the metal surface by the electron density of the adsorbate. Figure adapted from Ishii et al. [178] and Natali et al. [140].

Where the concentration of free carriers (p), the built-in voltage (V_{bi}), the temperature (T), and the applied voltage (V) partially determine (along with Φ_B) the charge-injection mechanism that dominates across the interface (see Section 3.1.3). The width of this region depends on the density of trap states of the organic semiconductor, which is both strongly affected by the semiconductor morphology and the doping concentration. This also then determines the mean free path of mobile charge carriers that are injected into the semiconductor. In organic semiconductors, the mean free path is often very small leading to diffusion-limited transport [180], [181].

In general, real interfaces in organic semiconductor devices never conform to the sharp interfaces conveyed in the cartoons in Figure 3.2. The sharpness of this interface can be strongly dependent on extrinsic factors including the fabrication conditions, e.g., whether the organic semiconductor is deposited on top of a metal film or vice versa, and whether a small molecule or polymer semiconductor is utilized. By extension, the magnitude of Δ and W_d and the subsequent efficiency of charge-carrier injection and transport depend strongly on the

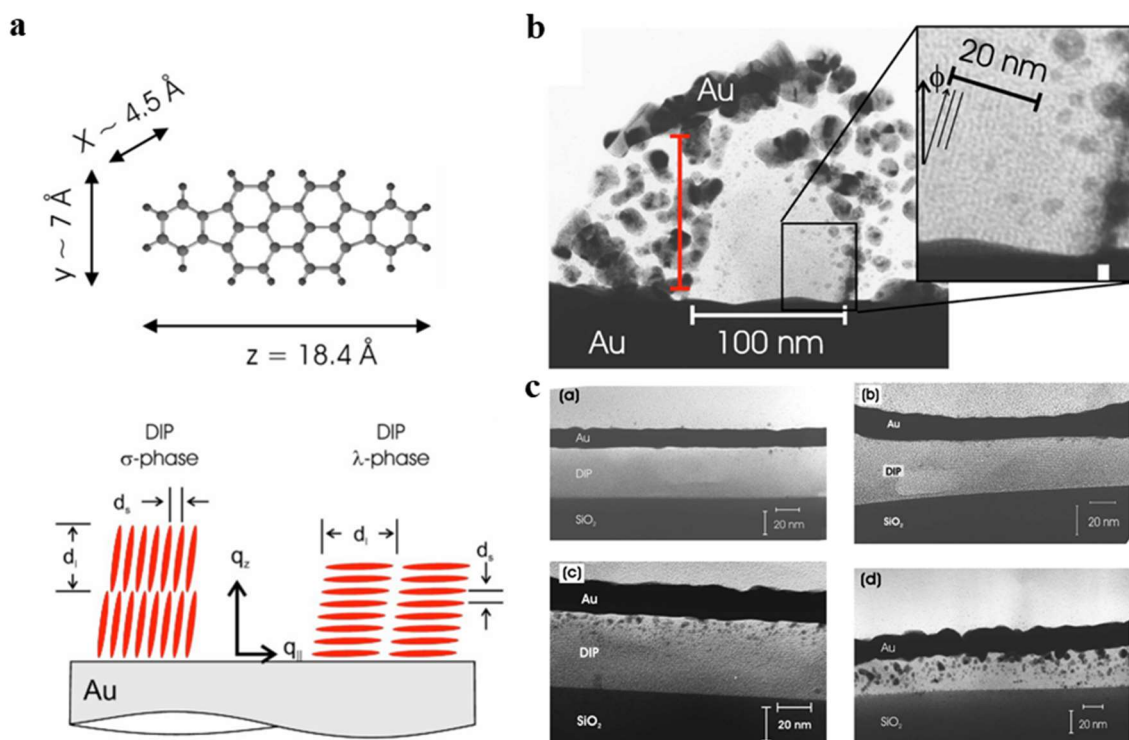


Figure 3.3 Organic semiconductor-metal interfaces.

Example studies from Dürr et al. [182, 183] investigating interfaces formed between diindenoperylene (DIP) and Au. a) DIP chemical structure and schematic diagrams for different crystal phases that can form on the surface. b) Cross-sectional TEM of λ -phase DIP layer on Au with additional Au layer deposited on top of the DIP. c) Au-DIP (σ -phase)-SiO₂ stacks wherein the Au layer was deposited with different conditions (substrate temperature, T_{sub} , deposition rate, R_{dep}): (a) (-120 °C, 23 Å/min), (b) (-120 °C, 0.35 Å/min), (c) (70 °C, 23 Å/min), and (d) (70 °C, 0.35 Å/min).

morphological characteristics of the interface of the fabricated organic semiconductor-metal contacts. A particularly illustrative pair of studies investigating metal interfaces with physisorbed small-molecule organic semiconductors was published by Dürr et al. [182], [183] in which they investigated the morphological and electronic characteristics of diindenoperylene (DIP)-Au interfaces (Figure 3.3). DIP is a highly-conjugated planar perylene derivative which can be vacuum-processed into highly-ordered thin films in a layered herringbone structure on SiO₂, with the DIP molecules standing nearly upright on the surface with their long axis aligned along the surface normal and having a typical separation distance between adjacent layers of DIP molecules in the (001) direction of 16.6 Å. The authors analyzed multiple samples composed of stacks of Au-DIP (Au deposited onto DIP) and DIP-Au (DIP deposited onto Au) on either Au/Cr/SiO₂/Si(100) substrates [182] or on SiO₂/Si(100) substrates [183] with the objective to elucidate the relationship between morphological and electrical properties. In the

DIP-Au samples, a high density of individual 100-nm-wide crystallite islands were observed in which the DIP molecules stacked ‘face down’ with the (010) face of the DIP molecules oriented normal to the Au surface (‘ λ -phase’ in the publication, Figure 3.3b), which resulted in a very rough thin film of DIP. Ultraviolet photoemission spectroscopy (UPS) measurements of the HOMO binding energy of the DIP layers with various thicknesses on Au yielded a large total hole-injection barrier ($\Phi_{B,p}$) of 1.45 eV, i.e., much larger than the difference between the work function of a cleaned sputtered Au substrate (5.4 eV) and the HOMO level of DIP determined at the maximum layer thickness of 30 nm (5.8 eV). From this data, it was found that the Δ forming within the first few adsorbed DIP layers was measured to be 1.05 eV. In the concurrent study on Au deposited on upright (σ -phase) DIP thin films on SiO₂, the authors additionally investigated the effects of substrate temperature and deposition rate on the Au-DIP interface morphology (Figure 3.3c). It was generally found that lower substrate temperature and lower deposition rate yielded a sharper interface between Au and DIP, while elevated temperatures and deposition rate yielded significant diffusion of Au nanoclusters into the DIP thin film (Figure 3.3c(d)). This phenomenon was later directly correlated to differences in the contact resistance and trap-state density in pentacene TFTs in a study by Xu et al. [184]. It was observed that higher deposition rates of Au contacts in a top-contact TFT architecture led to higher contact resistances and increased low-frequency noise due to the higher density of metal clusters that penetrated into the pentacene thin film. Important to note for the engineering of organic TFTs in which the source and drain contacts are patterned via shadow-mask lithography, Au nanoclusters can also diffuse laterally into the channel region, potentially causing large off-state currents in short-channel organic TFTs [185]. Idealization of this interface has been investigated extensively, and some of the most common interface-modification approaches that have been developed so far are presented in 3.3.

3.1.2 Fermi-level pinning

The obvious expectation from equation (58) is that in order to reduce Φ_B , the difference between φ_C and Φ_B should be minimized. Moreover, it would be expected that the magnitude of Δ would vary linearly with φ_m . Therefore, Φ_B would also be expected to vary linearly with φ_C such that the slope (S) for the variation in the hole-injection barrier ($\Phi_{B,p}$) and electron-injection barrier ($\Phi_{B,n}$) would follow

$$S = d\Phi_{B,n}/d\varphi_C = -d\Phi_{B,p}/d\varphi_C = 1 \quad (60)$$

This is known as the Schottky-Mott limit [178]. It is a common approach to then purposefully attempt to introduce an interface dipole with favorable polarity in order to shift φ_C to improve hole or electron injection, e.g. introducing an interlayer with a large intrinsic dipole [186] (Section 3.3.2). However, other factors influence the scaling of the injection barrier such that S is not always unity. This is generally attributed to the presence of a density of interfacial mid-gap states (N_{int} , Figure 3.1b) which allow for equilibration of the interface without changing Φ_B . This phenomenon is known as Fermi-level pinning (FLP) [48], [178], [187]–[189]. A hallmark of FLP that can be measured, e.g., via UPS measurements, is a deviation of the semiconductor work function dependence on the substrate work function away from the Schottky-Mott limit at high or low substrate work functions (Figure 3.4) [189]. FLP is already known for many years from studies of metal contacts to inorganic semiconductors, of which GaAs is a notorious example [190]. In this case the Fermi level can become pinned due to the formation of interface states with energies within the band gap that occur due to adatom-induced defects, metal-induced gap states, chemical impurities, and/or crystallographic dislocations at the surface [190].

The practical importance of FLP for engineering organic devices is that it can greatly influence the effectiveness of certain widespread contact-modification strategies where tuning

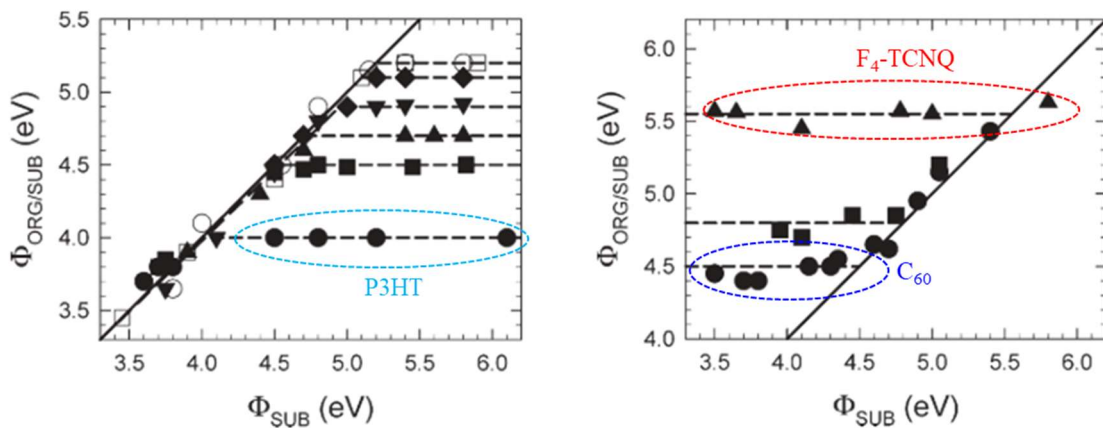


Figure 3.4 Fermi-level pinning at organic semiconductor-metal interfaces.

Survey of UPS measurements of the work function ($\Phi_{ORG/SUB}$) of various organic materials relevant to organic electronics as a function of the substrate work function (Φ_{SUB}). Figure from Braun et al. [189]. Notable materials discussed elsewhere in this thesis are highlighted.

φ_C is the main strategy to reduce Φ_B and realize Ohmic contacts. The precise mechanisms for the occurrence of FLP in organic semiconductors are still somewhat debated [187], [191], [192]. It has been common to attribute the occurrence of FLP in organic semiconductor-metal interfaces to charge transfer between the metal and integer charge-transfer states (ICT) with fixed energy levels for electrons (E_{ICT-}) or holes (E_{ICT+}) upon thermal equilibration [20], [193], resulting in an additional contribution to the interface dipole that leads to a reduction in S . However, Oehzelt et al. [187] and others recently analyzed the pinning behaviors and polaronic-relaxation energies that were observed experimentally, e.g., for pentacene which shows FLP with $S = -0.36$ for $\Phi_{B,p}$ [194]. They showed through their electrostatic model that the presence of an ICT is insufficient to account for the large minimum injection barrier heights that are often observed in interfaces that show FLP, such as Au-pentacene ($\Phi_{B,p} = 0.4$ eV in ref [194]). Instead, it was found that the experimental FLP results for several systems could be better-explained directly from the broad density of states (DOS) distributions that are a characteristic of many organic semiconductors. The universality of this explanation was expounded upon by Yang et al. [191], [192], where it was found that while the presence of a density of tailing gap states into the band gap (DOGS) can contribute to FLP, it can in fact arise also in cases where no gap states are present whatsoever. Instead, the occurrence of FLP and the magnitude of the minimum injection barriers that are possible for a given organic semiconductor-contact system could be predicted based entirely on the standard deviations of the Gaussian HOMO and LUMO distributions of the organic semiconductor layer in weak contact with a metal. These findings have an important implication that the route towards more-Ohmic contacts in organic semiconductor devices necessarily includes the elimination of FLP by narrowing the DOS and minimizing any DOGS. This may then put the elimination of FLP and the development of Ohmic contacts in close alignment with the research and development of organic semiconductors with higher charge-carrier mobilities, since this generally coincides with a narrower DOS [94], [96].

3.1.3 Charge injection physics

The dominant mechanism for charge-carrier transport across the interface between a metal contact and a semiconductor depends on several factors, including the energy levels and distributions of available states in the semiconductor, the height of the Schottky barrier formed at the interface (Φ_B), the presence of interlayers or dopants, the temperature, the interface dipole, and the applied electric field (F) [125], [180], [195], [196]. Classically, charge exchange across the interface between a metal and a semiconductor has been assumed to follow the mechanisms derived for emission of charges from a metal into vacuum. The dominant mechanism depends most critically on W_d (Figure 3.5a). For small p , the majority of charge carriers are injected only after sufficient thermal excitation to overcome the potential barrier (thermionic emission, TE). For intermediate p , some carriers can tunnel through the barrier after some thermal excitation (thermionic field emission, TFE) or be injected via ‘hops’ to intermediate states at the interface, known as gap-state assisted transport [166]. Inorganic semiconductors characterized by highly-delocalized ballistic transport of charges in well-defined energetic bands can be described by these classical models rather well, since the mean free path of the carriers is large, with negligible contributions from diffusion-dominated transport [176]. However, the typically polycrystalline or amorphous thin-film morphology of many organic-semiconductors often leads to a short mean-free path and diffusion-limited

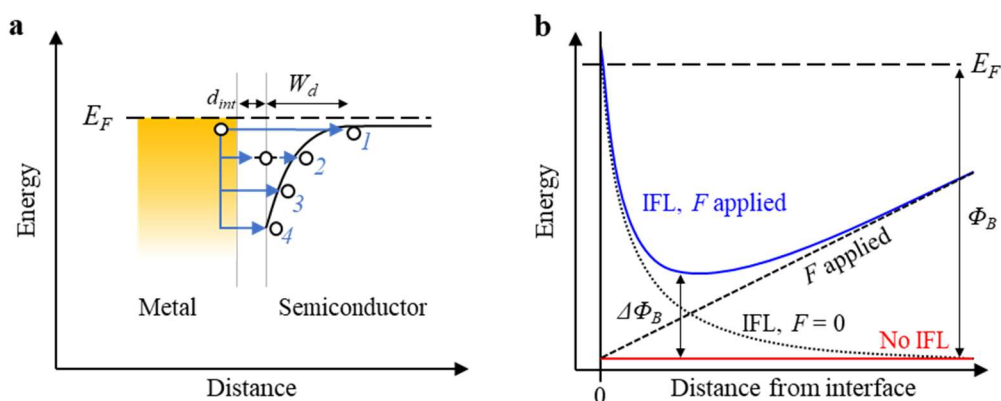


Figure 3.5 Charge-carrier injection from a metal contact into an organic semiconductor.

- a) Schematic energy diagram illustrating the possible charge-carrier injection pathways. 1. Direct tunneling. 2. Gap-state assisted transport. 3. Thermionic-field emission. 4. Thermionic emission.
- b) Schematic diagram of the shape of the Schottky barrier taking into account the effects of image force lowering (IFL) and applied electric field (F) which reduce the effective barrier height by $\Delta\Phi_B$. Adapted from Sze and Ng [176].

hopping transport of the injected charge carriers, with a subsequent heightened dependence of the charge-injection efficiency on the charge-carrier mobility in the organic semiconductor [140], [180]. This was shown to be especially true of many amorphous organic semiconductor polymers where the mobility of the charge carriers tends to be significantly lower and charge recombination rates are higher [180]. In doped and/or more-crystalline organic semiconductors, especially single crystals and liquid crystals, the charge carrier injection from the metal contacts can follow the classical models more closely [197]. The classical formulations for each of the prominent injection theories are outlined in more detail below.

Thermionic emission

The classical expression for the total current density transported across a reverse-biased metal-semiconductor interface by thermionic emission (J_{TE}) into a crystalline semiconductor is

$$J_{TE} = A^* T^2 \exp\left(\frac{-\Phi_B}{k_B T}\right) \left(1 - \exp\left(\frac{\Delta\Phi_B + qV}{k_B T}\right)\right) \quad (61)$$

Where A^* is the effective Richardson constant ($4\pi m^* q k_B^2 / h^3$), T is the temperature, Φ_B is the Schottky-barrier height, k_B is the Boltzmann constant, h is Planck's constant, m^* is the effective mass of the charge carriers, and V is the applied voltage [16], [125]. For charge carriers with short mean-free paths and lower mobilities such as organic semiconductors, the Schottky barrier height can undergo image-force lowering (IFL, Figure 3.5b) due to the Coulombic attractive force between the localized carriers with low mobility in the organic semiconductor and their respective image charges on the metal surface with opposite charge. The magnitude of the barrier lowering ($\Delta\Phi_B$) is derived to be [176]

$$\Delta\Phi_B = \sqrt{\frac{qF}{4\pi\epsilon_0\epsilon_{sc}}} \quad (62)$$

Note that $\Delta\Phi_B$ also depends on the magnitude of the applied electric field (F). For large $F > 10^6$ V cm⁻¹ and typical semiconductor dielectric constants (ϵ_{sc}) between 2 and 4, the barrier can be lowered by several hundred millielectronvolts. To account for these effects, Scott and Malliaras [196] developed a modified version of TE for organic semiconductors-metal contacts, taking into account the Poole-Frenkel effect, charge recombination near the interface, the carrier mobility (μ), the density of states available for hopping transport (N_0) and field-induced barrier-lowering effects (encompassed in the term $4\psi^2$).

$$J_{SM} = 4\Psi^2 N_0 q \mu F \exp\left(\frac{-\left(\Phi_B - \sqrt{q^3 F / 4\pi \epsilon_0 \epsilon_{sc}}\right)}{k_B T}\right) \quad (63)$$

This is similar to the thermionic emission diffusion (TED) model developed by Crowell and Sze [198]. For semiconductors with a higher degree of disorder such as amorphous polymers, Bässler and coworkers published a series of papers [199]–[201] in which a two-step process of (1) tunneling from the metal to a localized state in the semiconductor and (2) transport from that initial state into the bulk was described. An interesting and perhaps counterintuitive aspect is that a larger degree of disorder at the interface can at times enhance the charge-injection efficiency by lowering the effective barrier height in some systems. However, Baldo and Forrest [202] largely disputed this model by noting that the injection of charges may proceed through one or multiple ‘hops’ across the interface and that the presence of a distribution of interface dipoles will induce intermediate states that will alter the effective injection barrier. This is the afore-mentioned gap-state-assisted transport (‘2’ in Figure 3.5a).

Tunneling

For organic semiconductor-metal contacts in which thermionic emission dominates at room temperature, the primary injection mechanism can shift gradually to quantum tunneling at lower temperatures and/or higher electric fields. The temperature range over which this occurs and the type of tunneling depend on Φ_B and the width of the depletion region next to the contact interface (W_d). With small applied fields and at low temperatures, direct tunneling (DT) through the barrier is often the dominant injection mechanism, since the charge carriers no longer have sufficient thermal energy to surmount the barrier. This results in a temperature-independent current density of the form

$$J_{DT} \propto V \exp\left(\frac{-2W_d \sqrt{2m^* \Phi_B}}{\hbar}\right) \quad (64)$$

Where \hbar is the reduced Planck’s constant. If higher electric fields are applied across the interface, the barrier width can be reduced so that more efficient carrier injection results. This is described according to Fowler-Nordheim tunneling (FN) wherein a triangular-shaped barrier is assumed and the injected current density follows

$$J_{FN} \propto V^2 \exp\left(\frac{-4W_d \sqrt{2m^* \Phi_B^3}}{3\hbar qV}\right) \quad (65)$$

This type of tunneling injection is not commonly observed in organic-semiconductor devices, due to the typically rather large W_d that is present. It has been observed in pentacene TFTs with a small channel length ($L = 200$ nm) having contacts composed of conductive networks of single-walled carbon nanotubes operating with $F > 10^6$ V cm⁻¹ [203] but is generally not applicable to the devices discussed in this thesis.

Measurements of the effective injection barrier via I-V measurements

In practice, efforts to separate the temperature dependence of the injected current from the metal to the semiconductor (J_{inj}) from the overall current density measured in an organic-semiconductor device should be undertaken to estimate Φ_B [181]. This can be accomplished by ensuring that the current density measured is significantly dominated by the injecting contacts. Such approaches include measuring contact-limited devices, such as TFTs with very small channel lengths, by relegating the analysis to very high or low electric fields [203], by measuring the contact resistance and intrinsic mobility directly at each temperature using e.g. TLM [161], [173], [204], and/or by restricting the analysis to the subthreshold regime of operation in a TFT where again the current density is primarily limited by the contacts [197]. The specific differential contact resistance (R_{CS}) at zero bias can in principle be determined for any of the above injection processes by evaluating

$$R_{CS} = \left(\frac{dJ_{inj}}{dV}\right)_{V=0}^{-1} \quad (66)$$

For thermionic emission and ignoring field dependence, R_{CS} is therefore

$$R_{CS} = \left(\frac{k_B}{qA^*T}\right) \exp\left(\frac{\Phi_B}{k_B T}\right) \quad (67)$$

This can be implemented, for instance, in the evaluation of temperature-dependent TLM measurements of the contact resistance to extract the Schottky barrier height (Section 5.2.2).

3.2 The organic semiconductor-gate dielectric interface

The performance of organic TFTs depends critically on the use of high-performance gate-dielectric layers that optimize the charge-transport properties of the organic semiconductor [20]. The key requirements for the gate-dielectric layer are mostly the same as for inorganic field-effect transistors, i.e. leakage current through the dielectric layer must be minimized while also promoting efficient charge coupling with the semiconductor layer in contact with the gate dielectric [125]. To a first-order approximation then, the charge coupling of the dielectric with the semiconductor depends primarily on the dielectric constant (ϵ_{diel}) and the dielectric thickness (t_{diel}).

$$C_{diel} = \frac{Q_s}{V_{GS} - V_{th}} = \frac{\epsilon_{diel}\epsilon_0}{t_{diel}} \quad (68)$$

While SiO₂ is a popular choice as the gate dielectric for inorganic transistors and also remains one of the standards for testing new organic semiconductors in organic TFTs, the real target applications in low-power organic electronics have required the implementation and development of alternate dielectric materials [205], [206]. This is because the detailed role of the gate-dielectric for the figures of merit in organic TFTs extends far beyond the simplified view outlined by equation (68). The most prominent source of complexity compared to inorganic semiconductor devices arises due to the weak intermolecular forces between the organic semiconductor molecules, which make the structural and energetic properties of the organic semiconductor layer strongly dependent upon the physicochemical properties of the gate-dielectric surface. This naturally imposes processing requirements as well, such as the particulars of the deposition method for the organic semiconductor layer (i.e. solution vs. vacuum deposition) and the processing temperature and other environmental factors [207].

For organic-semiconductor thin films deposited on top of the gate dielectric (termed ‘bottom-gate’ or ‘inverted’, see the introduction in Chapter 2), the surface chemistry and roughness of the gate dielectric particularly influence the resulting microstructure of the semiconductor thin film [69]. This dependence is partially because the organic molecules are deposited under non-equilibrium conditions (e.g. with high thermal energy as in the case of vacuum-deposition). The impinging molecules then interact with the terminal atoms and functional groups of the surface, as well as with each other, through van der Waals and hydrogen-bonding interactions. These interactions then affect the non-equilibrium nucleation,

wetting, and crystallization processes that occur during thin-film formation [20]. For instance, vacuum-deposited small-molecule semiconductors such as the focus material of this thesis, DNNT, and pentacene generally do not show epitaxial growth, but rather a nucleation-driven crystallization due to the anisotropic structure of the molecules [66]. Therefore, the control of the density of nucleation sites, the rate of nucleation, the growth mode, and preferred molecular orientations on a surface are crucial for formation of high-charge-carrier mobility thin-films in an organic TFT. For such molecules it is often shown that a more hydrophobic, lower-surface energy substrate results in the free-energy orientations of the molecules in a thin film generally being ones where the long axes of the molecules are close to perpendicular to the substrate, leading to the formation of crystal grains with in-plane π -orbital overlap [208]. Beyond the effects on morphology of the semiconductor layer, the hydrophobicity of the surface also can influence the propensity for trap-state formation by water adsorption [104]. This means that direct correlations are observed between the charge-carrier mobility and the surface energy of the gate dielectric, which can be shown by, e.g., contact-angle measurements [206].

The complex interactions between surfaces and organic molecules has led to a wide variety of different materials being utilized as the gate-dielectric layer in organic TFTs, including metal oxides such as Al_2O_3 , polymers such as poly (methyl methacrylate) (PMMA) and polystyrene (PS), and high-permittivity dielectrics such as boron nitride [158]. Of particular interest have been the development of fluoropolymer solution-processed gate dielectrics with high permittivity such as CytopTM [209] and hybrid-gate dielectrics composed of a metal oxide layer passivated with a self-assembled monolayer (SAM) [210]–[212].

3.3 Interface-modification approaches

3.3.1 Interlayers and contact doping to improve charge injection

Doping as described in Section 1.3.4 can be applied to selectively modify the conductivity of the semiconductor region directly adjacent to the contact-semiconductor interface. In inorganic semiconductors, dopants are in the form of atomic interstitial and substitutional defects within the lattice [100]. As such, the doping concentration can be made as large as needed to reduce the width of the insulating region within the semiconductor bulk next to the contact interface. As discussed in Section 3.1.3, depending on the density of mobile carriers, the emission mechanism which dominates across the interface can change due to the reshaping of the Schottky barrier, in some cases transitioning from being dominated by thermionic emission to tunneling [107]. For extremely high charge carrier density, the barrier width can be reduced to effectively zero in inorganic semiconductors, such that the carriers can tunnel directly across the barrier. Thus, in conventional single-crystalline Si or Ge transistors, doping yields Ohmic contacts with a width-normalized contact resistance as low as 10^{-4} Ωcm , since the charge-injection mechanism is by efficient direct tunneling from a metal contact to the heavily doped semiconductor [125], [213], [214]. This also largely combats negative effects from scaling down the contact size [215]. After injection, the charge carriers can be easily transported to the channel, as the contact and the semiconductor are the same material (e.g. Si or Ge with different doping concentrations).

In devices using organic semiconductors, the effectiveness of contact doping is more limited due to the morphological issues discussed so far throughout this thesis and ultimately serves mainly to increase the conductivity of the organic semiconductor near the contact interface by filling trap states [216]. Moreover, because (intentional) dopants usually come in the form of a small molecules or inorganic salts such as FeCl_3 [152], the benefits come only at relatively low concentrations, because the introduction of high concentrations of a dopant can cause increased structural defects [100]. This means that mobile charge-carrier densities of the same degrees that are possible in inorganic semiconductors have so far not been demonstrated in organic semiconductors. Often the optimal doping concentration for improving injection without adversely affecting charge transport is dependent on the organic semiconductor-dopant combination [106].

Various other materials have been used to form insertion layers that are not interspersed within the organic semiconductor to improve charge-carrier injection, usually by modifying the contact work function. These layers also typically do not chemically react with either the metal contacts or the organic semiconductor. For hole injection into p-type organic semiconductors, interlayers with very low-lying electron affinities such as MoO₃ [217], and for electron injection into n-type organic semiconductors, low-work function organic compounds such as polyethyleneimine (PEIE) [218] have been implemented.

While these approaches have also shown merit in improving the charge injection in organic TFTs as well as in other organic electron devices, they have a distinct disadvantage in terms of ease of fabrication of organic TFTs in that both dopants and interlayers must be actively patterned to only modify the contact-semiconductor interface and not the channel region of the TFT. This issue notwithstanding, dopants and interlayer materials tend to diffuse within the semiconductor layer because of the weak intermolecular van der Waals interactions of the semiconductor. This can have undesirable effects, such as increased off-state drain currents, especially when the dimensions of an organic TFT are very small [100], [109], [110]. For practical applications then, self-patterning methods for interface modifications are preferred.

3.3.2 Chemisorbed molecular monolayers and self-assembled monolayers

Molecular self-assembly is a versatile and powerful tool for the fabrication of nano- and micro-scale devices. Through purposeful selection of interface materials and molecules for self-assembly, true direct and precise nanoscale patterning of electronic devices is possible [219]. Molecules which can react with a surface to form a chemisorbed molecular monolayer (CML, Figure 3.6) show particular promise for the modification of both the gate dielectric and the contacts in organic TFTs, because such modifications are area-selective, reproducible and when chosen carefully can enhance the key properties of subsequent layers in the device [123], [166], [220]–[222]. CMLs can be used to modify the surface characteristics of a substrate material, such as the work function of a metal contact and the surface reactivity, depending on the chemistry of the molecules to be assembled on the surface. In a well-known system for metal contacts such as gold and silver [223], molecules with thiol (-SH) anchoring groups bind to the surface through oxidative addition of the S–H bond to the Au surface followed by a

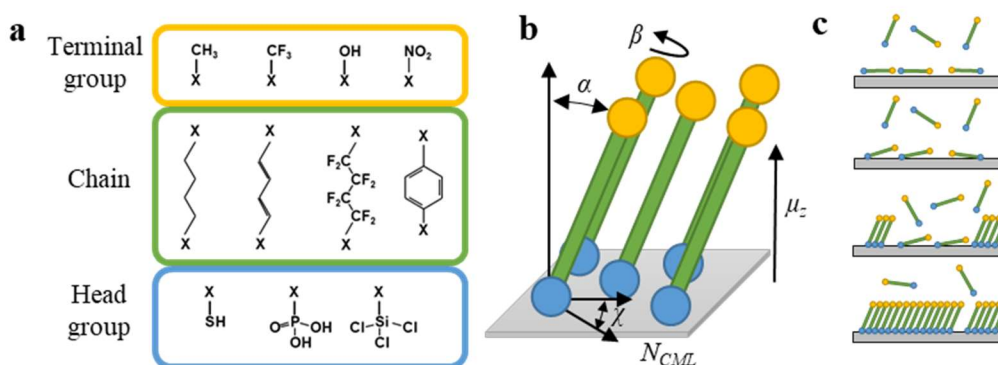


Figure 3.6 Chemisorbed molecular monolayers for interface modification.

a) Adsorbates generally consist of a terminal group, an aliphatic chain, and a head group which reacts with the substrate surface. b) Arrangement of the monolayer and the molecular orientations are determined by the angles (α , β , γ) and the grafting density (N_{CML}). c) Monolayer formation generally occurs through a sequence of steps including (from top to bottom) physisorption, chemisorption, nucleation of standing phases, and completion of long range ordering of standing up phase.

reductive elimination of the hydrogen [224]. Long-chain alkyl thiols are known to commonly form a well-ordered self-assembled monolayer (SAM)⁶ on Au (111) surfaces in a $\sqrt{3} \times \sqrt{3}$ R30° hexagonally symmetric lattice with a nearest neighbor interspacing for 1-decanethiol of 0.5 nm [223]. Molecules with phosphonic acid (-PO(OH)₂, PA) and chlorosilane (-SiCl₃) reactive head groups and long insulating molecular chains have also seen fervent use on gate-dielectric materials such as Al₂O₃ and SiO₂, respectively, due to their ability to also form dense, highly-ordered and stable SAMs. In the case of PA SAMs and Al₂O₃, the molecules predominantly chemisorb through bidentate condensation of the phosphonate onto the Al₂O₃ surface [225], while silanes chemisorb irreversibly to a hydroxylated SiO₂ surface by splitting off the -Cl side groups and forming a strongly-bound Si-O-Si network [226], in both cases forming a highly stable SAM. Using SAMs to functionalize the dielectric surface can introduce several significant benefits. For instance, by implementing a long alkyl chain, the surface can be made to be extremely hydrophobic and chemically inert, thus preventing the formation of trap states within and on the surface of the gate dielectric due to, e.g., water ingress from the ambient air [104], [222].

⁶ In this work, the term ‘self-assembled monolayers’ is restricted to denote the monolayers that are formed by materials that have long aliphatic chains, allowing the formation of extremely dense, stable monolayers through van der Waals packing of the chains [223] (see scheme in Figure 3.6c). They are thus regarded here as a subset of a more-general class of materials that form ‘chemisorbed molecular monolayers’ that do not necessarily form densely packed and stable monolayers. This is contrary to the literature in that the first term is used ubiquitously.

The chain and terminal groups can further affect changes in the thin-film formation and the charge-transport properties of the organic semiconductor layer that is deposited on top of the CML or SAM. For instance, alkylsilane SAMs on SiO₂ were shown to smooth out the surface of the oxide and lower the surface energy, promoting layer by layer growth of pentacene and C₆₀, which yielded high charge carrier mobilities in TFTs [227]. Thiol molecules can be used to form a CML for contact modification to provide both an improvement in the morphology of the organic-semiconductor layer deposited subsequently onto the contacts and across the contact edges to the channel region. On bare-gold contacts, it was shown that pentacene will preferentially adsorb in a ‘flat’ orientation, such that the π -orbitals interact with the predominantly (111) surface of gold thin films. This not only introduces an additional energetic barrier due to an induced surface dipole, but also adversely affects the morphology of pentacene across the contact edges, degrading the performance of the TFT. By including an alkanethiol SAM on the Au contacts, the pentacene molecules instead take the preferred ‘edge-on’ orientation, enhancing the TFT performance [71]. CMLs can also be engineered to alter the charge-coupling or injection behavior between the underlying metal layer and the semiconductor in an organic TFT. For the gate dielectric, low-voltage organic TFTs are enabled by the addition of a SAM with a dipolar character, shifting the threshold voltage closer to 0 V [128], [228], while also reducing leakage current and the subthreshold swing. The threshold voltage shift is actuated by the collective dipole moment of the SAM which imposes a built-in electric field with the electrostatic potential difference corresponding, at least qualitatively, to the Helmholtz equation [128], [166], [229]–[231]. This character can generally be applied to any CML.

$$V_{CML} = \frac{N_{CML}\mu_z}{\epsilon_0\epsilon_{CML}} \quad (69)$$

Where N_{CML} is the areal grafting density of molecules chemisorbed to the surface, μ_z is the collective dipole moment perpendicular to the surface, and ϵ_{CML} is the dielectric constant of the CML. Note that μ_z and ϵ_{CML} contain contributions from both the covalent bond to the surface and the chain and terminal groups of the molecules in the CML as well as the molecular orientation [230].

The dipolar character and the influence on the organic-semiconductor morphology of a CML can also be beneficial for lowering the overall contact resistance in organic TFTs by simultaneously tuning the effective work function of a metal contact (ϕ_C) by up to a few

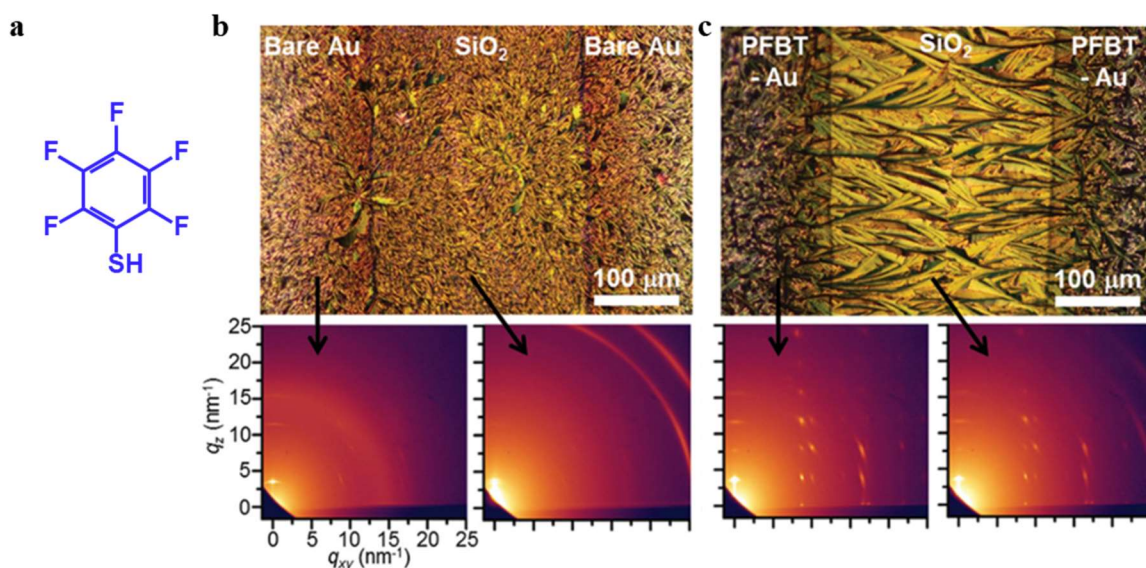


Figure 3.7 Contact modification with pentafluorobenzenethiol.

a) Chemical structure of pentafluorobenzenethiol (PFBT). Polarized optical microscopy of bottom-contact organic TFTs based on diF-TESADT with (b) and without (c) PFBT functionalization of the Au contacts. Corresponding 2D graying-incidence wide-angle x-ray scattering (GIWAXS) patterns for the channel and contact regions are also shown. Figure adapted from Kim et al. [221].

hundred millielectronvolts and improving the organic semiconductor morphology on top of the contacts and into the channel region [186], [232]–[236]. For metal contacts functionalized with a CML, there are generally three steps in the injection process to consider: (1) tunneling through the CML from the metal to the CML-organic semiconductor interface which can be determined, for instance, by the length of the aliphatic chain in an alkyl thiol SAM [70], [237]; (2) injection across the CML-organic semiconductor interface to the organic semiconductor; and (3) transport through the organic-semiconductor film near the interface to the channel region. Therefore, one can surmise that an ideal CML for contact modification to improve the charge injection should be as thin as possible, have a large collective μ_z , and promote the formation of an organic semiconductor thin-film morphology with high charge-carrier mobility.

It is then perhaps no coincidence that the most widely utilized and effective molecule to date for improving the hole injection in p-channel organic TFTs is pentafluorobenzenethiol (PFBT, Figure 3.7a) [76], [159], [221], [235], [238]. Here, a large downward μ_z is created by the high density of fluorine atoms surrounding the benzene ring [230]. On Au, Ag and Cu contacts, a PFBT CML was shown to induce higher crystallinity of diF-TESADT films either

by a templating effect where the molecules conform to the arrangement of the CML molecules on the metal surface [239] or by attraction between the S-groups of diF-TESADT and the F-groups of PFBT [159], [221] (Figure 3.7c). It was additionally observed through density functional theory (DFT) calculations combined with scanning tunneling microscopy (STM) investigations and TFTs based on P3HT, that the work-function shift imposed by PFBT CMLs on Au is relatively unaffected by the precise orientation or ordering of PFBT on the surface of the Au, leading to [240]. The often excellent contact-resistance improvement of p-channel bottom-contact organic TFTs which utilized PFBT as a CML has motivated investigations into other thiol molecules capable of forming CMLs on the metal contacts, particularly those with a large number of fluorine atoms to induce a work-function shift beyond that obtained with PFBT [233], [234]. Other approaches such as using molecules with embedded pyrimidine groups selectively placed within the molecule to induce a μ_z with a downward (upward) polarity have been investigated to improve hole (electron) injection in TFTs based on pentacene (C₆₀) [241]. While using CMLs presents an effective tool for improving injection into some organic semiconductors to achieve contact resistances on the order of a few hundred Ohm centimeters, further reduction of the barrier through the use of molecules with even larger μ_z is likely to be eventually limited by Fermi-level pinning, as discussed in Section 3.1.2 and investigated experimentally in Chapter 6 [48].

4 Experimental

All samples presented in this thesis were fabricated at the Max Planck Institute for Solid State Research either in the Organic Electronics laboratory of Dr. Hagen Klauk (<https://www.fkf.mpg.de/klauk>) or in collaboration with the Nanostructuring Laboratory (NSL) lead by Prof. Jürgen Weis (<https://www.fkf.mpg.de/NSL>).

4.1 Fabrication of TFTs and circuits

Stencil lithography based on high-resolution silicon stencil masks [242] was implemented for the fabrication of organic TFTs and circuits on both rigid and flexible substrates. All metals and organic semiconductor layers were deposited using thermal evaporation/sublimation in vacuum (Figure 4.1). Separate masks were used to pattern the interconnects, gate electrodes,

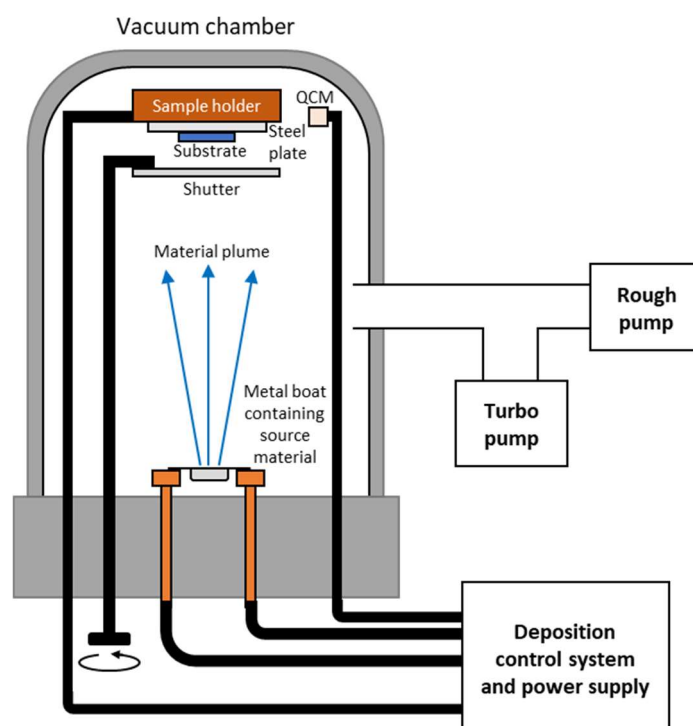


Figure 4.1 Schematic diagram of the apparatus for sample fabrication

Substrates are mounted on a removable steel plate. The sample holder is temperature-controlled to allow deposition of materials at elevated substrate temperatures. The thickness of the deposited layer and the rate of deposition are monitored by a quartz-crystal microbalance (QCM). Materials are deposited from a metal boat which is heated by running large currents from an external power supply. A rotatable shutter allows for initial stabilization of the deposition rate prior to depositing any material onto the substrate.

source and drain contacts, and organic-semiconductor layers. Various parameters including the source and drain contact treatments and gate-dielectric thickness were varied to investigate different aspects of the organic TFT performance. The particular details of fabrication of the samples for each study are outlined in following sections.

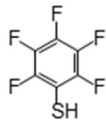
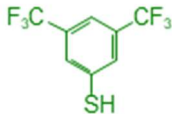


4.1.1 TFTs with different gate-oxide thicknesses and contact treatments on silicon substrates

The TFTs that were used to study the relation between the gate-dielectric thickness and the contact resistance (Chapter 5) were fabricated in the global-back-gate (GBG) architecture on heavily doped silicon wafers (thickness of 525 μm). In this case, the silicon substrate serves as a global gate electrode for all TFTs on the substrate. To reduce the effects of substrate-to-substrate variations, bottom-contact (BC) and top-contact (TC) TFTs with a common gate-dielectric thickness were fabricated on the same substrate in close proximity to each other (separated by about 100 to 200 μm). As the first component of the gate dielectric, stoichiometric aluminum oxide (Al_2O_3) was deposited by atomic layer deposition (ALD, Savannah 100, Cambridge NanoTech Inc.; substrate temperature 250 $^\circ\text{C}$, 10 cycles/nm) with a well-defined thickness ranging between 3 nm to 200 nm. The Al_2O_3 surface was activated by oxygen plasma (Oxford Instruments; oxygen flow rate 30 sccm, partial pressure 10 mTorr, plasma power 200 W, exposure duration 30 s) and then passivated with a self-assembled monolayer (SAM) by immersing the substrate into a 1-mM 2-propanol (VLSI grade) solution of *n*-tetradecylphosphonic acid (TDPA, PCI Synthesis, Newburyport, MA, U.S.A.) for one to two hours [128]. Afterwards, the substrates were rinsed in 2-propanol and dried on a hotplate in ambient air (150 $^\circ\text{C}$, 1 min). The capacitance of these dielectrics was calculated assuming relative dielectric constants (ϵ_r) of 9 for Al_2O_3 and 2.5 for the phosphonic acid SAM [128]. In some experiments, including all of the samples used for comparisons of different contact treatments presented in Chapter 6, an aluminum layer was first deposited onto the silicon substrate and exposed to oxygen plasma (Oxford Instruments, 30 sccm oxygen, 10 mTorr, 200 W, 30-60 s) to form a very thin oxide layer. This layer was similarly passivated with a TDPA SAM, and all the remaining fabrication steps for the TFTs remained the same as described in the following.

For BC TFTs, gold source and drain contacts (30 nm thick) were deposited by thermal evaporation in vacuum onto the surface of the gate dielectric. All source and drain contact pads

have an area of 200 μm x 200 μm and were patterned using a silicon stencil mask (IMS Chips, Stuttgart, Germany) to define channel lengths ranging from 4 to 50 μm [74]. Depending on the purposes of the experiment, the contacts either received no additional treatment steps before proceeding to the deposition of the organic semiconductor or were modified with a chemisorbed molecular monolayer (CML) or self-assembled monolayer (SAM, see Section 3.3.2). In Chapter 5, the bottom contacts were always functionalized with a CML of pentafluorobenzenethiol (PFBT, Santa Cruz Biotechnology, Heidelberg, Germany) by immersing the substrates into a 10-mM solution of PFBT in VLSI-grade 2-propanol or ethanol for at least 30 min. In Chapter 6, the CMLs and SAMs were formed by immersing the substrates after gold deposition into a 10-mM solution of one of the various thiols summarized in the table below for 1-2 hours. In all cases, after a CML/SAM was applied, the substrates were then rinsed with either 2-propanol or ethanol and dried with argon flow.

Table 4.1: Thiols used for the formation of chemisorbed molecular monolayers (CML) and self-assembled monolayers (SAM) on gold contacts in this work.

Chemical name (abbreviation)	Diagram/Formula
pentafluorobenzenethiol (PFBT)	
3,5-bis-trifluoromethylbenzenethiol (BTFMBT)	
4-fluorobenzyl mercaptan (FBM)	
4-nitrothiophenol (NOTP)	
1H,1H,2H,2H-perfluoro-1-decanethiol (PFDT)	$\text{CF}_3(\text{CF}_2)_7\text{CH}_2\text{CH}_2\text{SH}$
1-butanethiol (BT)	$\text{CH}_3(\text{CH}_2)_3\text{SH}$
1-pentanethiol (PT)	$\text{CH}_3(\text{CH}_2)_4\text{SH}$
1-hexanethiol (HT)	$\text{CH}_3(\text{CH}_2)_5\text{SH}$
1-octanethiol (OT)	$\text{CH}_3(\text{CH}_2)_7\text{SH}$
1-decanethiol (DT)	$\text{CH}_3(\text{CH}_2)_9\text{SH}$
1-dodecanethiol (DDT)	$\text{CH}_3(\text{CH}_2)_{11}\text{SH}$

In the gate-dielectric thickness study presented in Chapter 5, a 20-nm-thick layer of 2,9-diphenyl-dinaphtho[2,3-b:2',3'-f]thieno[3,2-b]thiophene (DPh-DNTT; Nippon Kayaku, kindly provided by Koichi Ikeda) was deposited after fabrication of the bottom-contacts by sublimation in vacuum (base pressure 10^{-6} mbar, substrate temperature 90 °C, deposition rate 0.3 \AA s^{-1}) onto all substrates simultaneously in order to minimize substrate-to-substrate variations. In the study focusing on different thiol-based CML/SAM contact treatments presented in Chapter 6, a 40- or 60- nm-thick layer of dinaphtho[2,3-b:2',3'-f]thieno[3,2-b]thiophene (DNTT; Sigma Aldrich) was deposited by sublimation in vacuum (base pressure 10^{-6} mbar, no substrate heating, deposition rate 0.3 \AA s^{-1}). In all cases, prior to electrical measurements, the unpatterned semiconductor layer was scratched away around each set of source and drain contacts using a probe needle to avoid fringe-current effects [243]. To

facilitate comparison to TC TFTs in the experiments presented in Chapter 5, after the electrical measurements to extract I - V curves were performed on the BC TFTs, the substrates were then placed in the evaporator again to deposit the gold top source and drain contacts onto the organic semiconductor layer. The top contacts were deposited in all cases in close proximity to the previously defined bottom contacts according to the procedure outlined above. After this final deposition, electrical measurements were performed on the TC TFTs.

4.1.2 TFTs and circuits on flexible PEN substrates

TFTs with patterned gate electrodes and integrated circuits (Figure 4.2) were fabricated on 125- μm -thick flexible polyethylene naphthalate substrates (Teonex® Q65 PEN; provided by William A. MacDonald, DuPont Teijin Films, Wilton, U.K.) using sets of four silicon stencil masks designed previously by Dr. Reinhold Rödel and Dr. Tarek Zaki (IMS Chips, Stuttgart, Germany) to define interconnects, gate electrodes, source and drain contacts, and the organic semiconductor layer [119], [141], [244]. Prior to device fabrication, the PEN substrates were baked at a temperature of 100 °C for 1 hour and cleaned with 2-propanol to remove any contaminants from the surface. In the first fabrication step, 30-nm-thick gold interconnects and

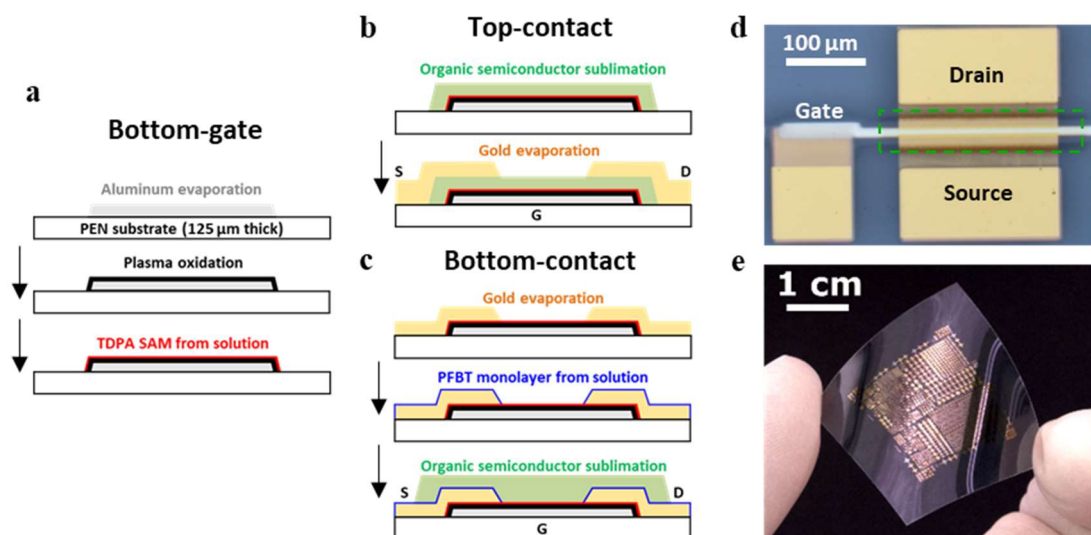


Figure 4.2 Fabrication of flexible organic thin-film transistors

a) Process steps for the fabrication of the gate electrode and the formation of the hybrid gate dielectric. b) Top-contact- and c) bottom-contact-TFT fabrication steps. d) Photograph of a TFT having a channel length of 8 μm , a total gate-to-contact overlap of 4 μm , and a channel width of 200 μm . e) Photograph of organic TFTs and circuits fabricated at a maximum process temperature of 100 °C on a flexible, transparent PEN substrate. Published in [141].

probe pads were deposited through the first stencil mask. This first layer also includes alignment markers to assist with the alignment of the subsequent layers. For the gate electrodes, a 30-nm-thick layer of aluminum was deposited through the second stencil mask. In the case of the TFTs discussed above that were used to evaluate the relation between the gate-dielectric thickness and the contact resistance, the gate oxide was deposited by atomic layer deposition (ALD). ALD has the advantage that the oxide thickness can be easily scaled over a wide range. However, one issue with ALD is that the oxide is not easily deposited selectively, so that subtractive patterning is usually required to create access to the gate electrodes underneath the oxide. For the TFTs discussed above, this issue was avoided by contacting the gate electrode (i.e., the doped silicon substrate) from the backside of the substrate. For devices and circuits on plastic substrates this is clearly not an option. Therefore, for the TFTs and circuits on PEN, plasma oxidation (Oxford Instruments, 30 sccm oxygen, 10 mTorr, 200 W, 30-60 s) was used to form a thin aluminum oxide (AlO_x) layer selectively on the patterned aluminum gate electrodes. The completed gate dielectric is a stack of the thin layer of AlO_x and an *n*-tetradecylphosphonic acid SAM, resulting in a total dielectric thickness of about 5 to 7 nm and unit-area capacitance of $0.7 \mu\text{F cm}^{-2}$ [57]. For all subsequent layers, the fabrication procedure was the same as described above for the TFTs on silicon substrates, with the exception that the semiconductor layer is patterned with a stencil mask.

In the inverters and ring oscillators, the drive TFTs have a channel width of $80 \mu\text{m}$ and the load TFTs have a channel width of $20 \mu\text{m}$. In the two buffer inverters that separate the inverters in the ring from the output node of the ring oscillator the drive TFT has a channel width of $220 \mu\text{m}$ and the load TFT has a channel width of $60 \mu\text{m}$. All of the TFTs in these circuits have channel lengths $L = 1 \mu\text{m}$ and gate-to-contact overlap $L_{ov} = 2 \mu\text{m}$ or $5 \mu\text{m}$.

4.2 Semiconductor thin-film morphology characterization

The thin-film morphology of the organic-semiconductor layer of the TFTs was characterized using tapping-mode atomic force microscopy (AFM) or peak force microscopy (PFM) (both using a Bruker Dimension Icon, Bruker Ltd., Billerica, Massachusetts), scanning electron microscopy (SEM, Zeiss Merlin), and grazing incidence X-ray diffraction (GIXRD, Rigaku SmartLab, Rigaku Co. Ltd., Tokyo). SEM and AFM/PFM characterizations were typically performed on completely processed TFTs. GIXRD required larger uniform sampling areas due to the large spot size required for the measurement. Silicon substrates were thus prepared for the GIXRD measurements. For the samples used in these measurements, the organic semiconductor was deposited on all substrates simultaneously if they are to be directly compared. The X-ray diffractometer is equipped with a 9 kW copper source. The grazing incidence angle was set to 0.15° . The detector moved horizontally at $2\theta = 0.15^\circ$ and $2\theta\chi$ from 15° to 30° in steps of 0.1° . The X-ray beam size was set to 5 mm x 0.1 mm. The diffraction peaks were assigned using the PDXL software with the standard Gaussian distribution method. The GIXRD measurements were done at the University of Hong Kong by Dr. Boyu Peng in the group of Professor Paddy Chan.

4.3 Characterization of chemisorbed molecular monolayers on Au substrates

Contact-angle measurements using a goniometer were performed to assess the surface energy of samples which were functionalized with a chemisorbed molecular monolayer (CML) or self-assembled monolayer (SAM). Changes in the surface energy, especially in the case of enhanced or diminished hydrophobicity, serve as a good method to quickly check the quality of a CML/SAM [186]. For more-detailed information about the thiol monolayers presented in Chapter 6, test samples were characterized using x-ray photoemission spectroscopy (XPS). The spectra were collected with an Al K α (1486.6 eV, $\lambda = 0.83386$ nm) line as the source radiation with an x-ray monochromator and a pass energy of 40 eV for the analyzer, enabling an instrumental resolution of ~ 0.5 eV. Especial attention was given to the binding energies of the S 2p and C 1s orbitals of the CML/SAM on the Au surfaces. Qualitative evaluation of the molecular orientation of the CML/SAM after functionalization on the Au surfaces was obtained using polarization-modulation infrared reflection-absorption spectroscopy (PM-IRRAS, Bruker, PMA50 coupled to a VERTEX 70 spectrometer, equipment courtesy of Professor Dr. Frank Gießelmann at the University of Stuttgart) [245]. Attenuated total reflection (ATR) FTIR spectra of the neat materials were collected for comparison to the PM-IRRAS results. The PM-IRRAS spectra were collected from CMLs/SAMs formed on clean 30-nm-thick gold films thermally deposited on silicon with a 1-nm-thick Ti binding layer. The spectra were measured using *p*-polarized light with a resolution of 4 cm $^{-1}$ at an angle of incidence of 80°. 500 or 1000 scans were collected for all the CMLs/SAMs. The spectral peaks were then analyzed and assigned to likely vibrational modes of the thiols according to standard tables and relevant literature where applicable. All spectra were collected with the assistance of Sherri Liu or Zheyu Wu in the group of Professor Dr. Sabine Ludwigs.

Ultraviolet photoemission spectroscopy (UPS) measurements were used to determine the work function of gold layers modified with the different CMLs/SAMs. In Chapter 6, these measurements were then compared to the work functions measured from DNTT layers deposited on top of each of the modified gold surfaces (see Section 4.1.1 for more details about the different molecules which were used in this study). For the samples used in these measurements, the organic semiconductor was deposited on all substrates simultaneously if they are to be directly compared. The work function was assessed from the data by evaluating

the secondary electron cutoff energy (SEC) and the Fermi level in the UPS spectra. This is generally the standard practice for determining work functions using UPS measurements [246]. The offsets in the binding energies of the spectra were corrected according to a standard of sputter-coated Au film on Si (work function of 5.20 eV, binding energy of 9.07 eV). All UPS and XPS analyses were performed in collaboration with Dr. Florian von Wrochem (Sony, GmbH, Stuttgart: now at Carl Zeiss, GmbH, Oberkochen and the University of Stuttgart).

4.4 DC and AC electrical measurements of organic thin-film transistors and circuits

All electrical measurements were performed in ambient air at room temperature (292 K). The capacitance of the gate dielectrics, the current-voltage characteristics of the TFTs, and the signal propagation delays of the ring oscillators were measured using an Agilent 4156C Semiconductor Parameter Analyzer, a Tektronix TDS1000 oscilloscope, a Femto DPLCA-200 low-noise transimpedance amplifier, and gold-plated tungsten probe tips (EPP GmbH) with a tip radius of 50 or 25 μm for contacting the probe pads. Inverter dynamic measurements were performed using a Picoprobe 19C and 18C-4-20-HV or 18C-4-50-HV probe tips (GGB Industries). The temperature-dependent electrical measurements were performed in a cryostat probe station under high vacuum (LakeShore) in the lab of Professor Dr. R. Thomas Weitz with the assistance of Dr. Jakob Lenz at the Ludwig Maximilian Universität, München.

4.5 Two-port network analysis

Scattering (S) -parameter measurements of organic TFTs on flexible substrates were performed using a N5231A Vector Network Analyzer (Keysight, GmbH, Böblingen) in the lab of Prof. Mario Caironi (IIT, Milano, Italy) with the help of Dr. Michele Giorgio. For these measurements, GS-SG $|Z|$ high-impedance probes (Cascade Microtech, Cascade International Trading Co., Ltd., Beaverton, Oregon) were utilized for making contact to the probe pads of the specially-designed TFTs for these measurements [135], [170]. De-embedding of the probing system was performed using standard silicon calibration samples. Here, a 12-term error correction model was applied to remove non-idealities introduced by the measurement setup and to shift the calibration plane to that of the probe tips [247]. The S-parameter data for the TFTs were collected using a DC bias voltage of -3 V on the gate and drain terminals and an oscillating small-signal probe voltage with amplitude of 0.03 V over a range of frequencies from 300 kHz to 200 MHz. From the raw S-parameter data, both the unity-gain cut-off (transit) frequency (f_T) and individual components of the gate capacitance (C_G) could be determined by implementing standard mathematical transformations as outlined in Section 2.4.2 [138].

5 Analysis of the effects of device architecture on organic thin-film transistors

Two-port network analyses were measured with the assistance of Dr. Michele Giorgio in the group of Professor Mario Caironi at the Center for Nano Science and Technology@PoliMi Milano, Istituto Italiano di Tecnologia, Milan, Italy. Grazing incidence x-ray diffraction (GIXRD) measurements were performed by Dr. Boyu Peng in the group of Professor Paddy K. L. Chan at the Department of Mechanical Engineering, The University of Hong Kong, Pokfulam Road, Hong Kong SAR, China. Portions of this chapter were published in the following:

1. J. W. Borchert, U. Zschieschang, F. Letzkus, M. Giorgio, R. T. Weitz, M. Caironi, J. N. Burghartz, S. Ludwigs, H. Klauk, Flexible low-voltage high-frequency organic thin-film transistors, *Science Advances*, 6 (2020) eaaz5156.
2. J. W. Borchert, B. Peng, F. Letzkus, J. N. Burghartz, P. K. L. Chan, K. Zojer, S. Ludwigs, H. Klauk, Small contact resistance and high-frequency operation of flexible low-voltage inverted coplanar organic transistors, *Nature Communications*, 10 (2019) 1119.
3. J. W. Borchert, U. Zschieschang, F. Letzkus, M. Giorgio, M. Caironi, J. N. Burghartz, S. Ludwigs, H. Klauk, Record static and dynamic performance of flexible organic thin-film transistors, *2018 IEEE International Electron Devices Meeting (IEDM)*, DOI: 10.1109/IEDM.2018.8614641.
4. U. Zschieschang, J. W. Borchert, M. Giorgio, M. Caironi, F. Letzkus, J. N. Burghartz, U. Waizmann, J. Weis, S. Ludwigs, H. Klauk, Roadmap to gigahertz organic transistors, *Advanced Functional Materials*, 30 (2020) 1903812.

Among the most important characteristics that can be affected by the TFT architecture is the contact resistance (R_C) and subsequently the dynamic performance of the TFTs [13]. While there are many aspects that play an additional role that have been investigated extensively [140], [248], [249], a possible key aspect that has so far not been directly investigated experimentally in extensive detail is the role that the thickness of the gate-dielectric layer (t_{diel}) has on the charge injection in organic TFTs with different architectures. In the case of the

inverted (bottom-gate) architectures, the staggered (top-contact; TC) configuration has typically provided smaller contact resistance than the coplanar (bottom-contact; BC) configuration, even for devices comprising the same materials and layer thicknesses [142], [143]. Therefore, in the first of the following sections in this chapter, this aspect is systematically investigated using organic TFTs fabricated with atomic-layer-deposited (ALD) aluminum oxide of different thicknesses passivated with a self-assembled monolayer (SAM) composed of *n*-tetradecylphosphonic acid (TDPA) as the gate dielectric. More details about the fabrication are provided in Section 4.1 and in the following sections. For this and all subsequent investigations of the influence of the device architecture, the primary focus was placed on devices based on the organic semiconductor 2,9-diphenyl-dinaphtho[2,3-b:2',3'-f]thieno[3,2-b]thiophene (DPh-DNTT) [57], [112], [211]. Most of the focus is placed on DPh-DNTT, since top-contact TFTs using this semiconductor have previously shown among the lowest contact resistances in organic TFTs overall, and lower contact resistance than top-contact TFTs using other DNTT derivatives [74]. It is therefore a particularly interesting organic semiconductor for possible application in high-frequency circuits using organic TFTs. For TC TFTs, the lower R_C achieved using DPh-DNTT is primarily attributed to a smaller bulk resistance (R_b) of the semiconductor layer between the contacts and the channel region [74]. This is a particularly beneficial characteristic when considering the test semiconductor in this study, since it will reduce extrinsic factors other than the influence of the gate-dielectric thickness on the R_C , namely the semiconductor-layer thickness (t_{osc}). The morphology of DPh-DNTT on the relevant surfaces for the organic TFTs used in this study (i.e. the gate dielectric and the contacts) is evaluated first with AFM and SEM, and found to not be a major contributing factor to any of the trends in the following TFT results.

Following the direct investigation of the influence of the gate-dielectric thickness, the differences in low-voltage TC and BC TFT performance characteristics for devices fabricated on flexible polyethylene naphthalate (PEN) sheets are examined and compared in Section 5.2. Again, the contact resistance was examined using TLM and the results were compared for the two architectures, and were found to generally agree with the results of the first study. To investigate the extent to which the generally low contact resistances effect the dynamic performance of the TFTs when implemented in circuits, ring oscillators and inverters were evaluated. This is followed by more detailed investigations of the dynamic performance characteristics of individual TFTs using two-port network analysis. Some additional points of

consideration including the reproducibility of high-performance BC TFTs, extension of the results for DPh-DNTT to other organic semiconductors, and bias-stress stability of BC and TC TFTs are discussed in the Appendix, and the final conclusions and remarks on future developments of high-performing organic TFTs can be found in the Conclusions.

5.1 Gate-dielectric thickness and the contact resistance

To maintain the highest possible degree of comparability between the performance of the BC and TC TFTs in this study, multiple measures were taken to render the TFTs to be directly compared as equivalent as possible. This is essential to be able to base the comparison of R_C in the different devices on controlled assumptions.

First, silicon-stencil-mask lithography [250] was used to fabricate the source and drain contacts of the BC and TC TFTs. This enabled the fabrication of the TFTs with well-defined critical dimensions in close proximity to each other on a common doped-silicon substrate that serves as a global-back-gate electrode (Figure 5.1). Therefore, for each sample with a given thickness of the Al_2O_3 layer, the TFTs utilize a common gate dielectric and the same semiconductor layer. Furthermore, direct comparisons are only made between contact resistances that were extracted from TFTs fabricated on the common substrate, i.e., from TFTs sharing the same gate-dielectric thicknesses.

Second, a common nominal thickness of the vacuum-deposited DPh-DNTT layer of $t_{osc} = 20$ nm was implemented for all TFTs in this study. This was determined to be the optimum semiconductor-layer thickness that was previously identified for TC organic TFTs based on DPh-DNTT [57]. It is worth reiterating here that the semiconductor-layer thickness is more relevant in TC TFTs, since a larger semiconductor layer thickness is expected to increase the contact resistance due to usually poorer vertical carrier transport and increased trap-state density relative to a thinner semiconductor layer [121], [150], [204], [251]. The intrinsic charge-carrier mobility in the accumulation region between the contacts and the gate dielectric partially determines the bulk-resistivity component of the contact resistance due to the current-crowding effect [150], so that it is also important to ensure that the semiconductor layer in this region is sufficiently complete to allow the most efficient charge transport possible. This then places a requirement on the minimum nominal thickness for vacuum-deposited semiconductors. To an extent, this effect depends on the particular semiconductor that is utilized, since the film formation characteristics, such as the propensity for 2D or 3D crystal growth, can vary according to the molecular structure [66]. Most crucially for the TC TFTs, a high intrinsic charge-carrier mobility in the accumulation region under the contacts can mitigate the commensurate space-charge limitations on injection that is typical in a staggered TFT [150], [252], [253].

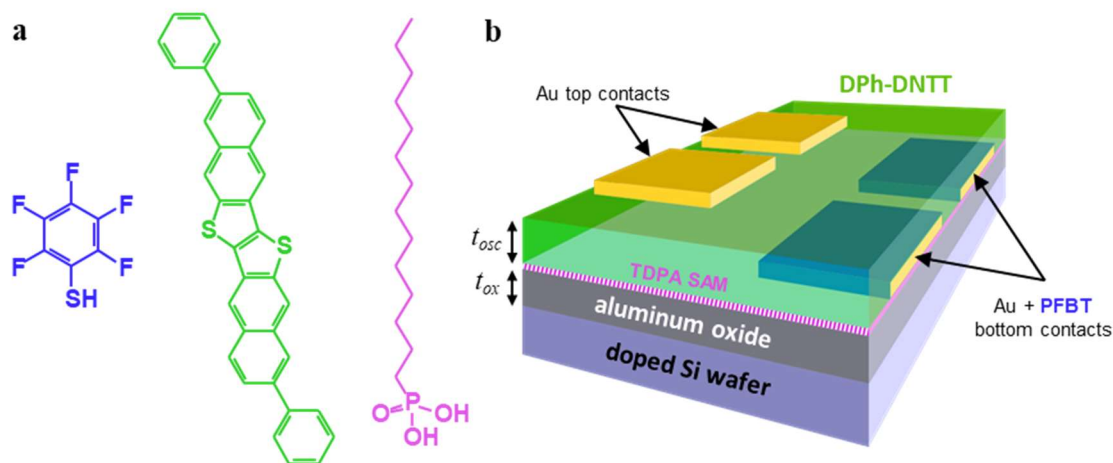


Figure 5.1 Organic thin-film transistors with a global-back-gate electrode in the top-contact and bottom-contact architecture.

a) Chemical structures of pentafluorobenzenethiol (PFBT) used to treat the gold source and drain contacts in the bottom-contact TFTs, the small-molecule semiconductor 2,9-diphenyl-dinaphtho[2,3-b:2',3'-f]thieno[3,2-b]thiophene (DPh-DNTT), and *n*-tetradecylphosphonic acid (TDPA) used to modify the surface of the gate dielectric with a self-assembled monolayer (SAM). b) Schematic cross-section of top-contact and bottom-contact TFTs fabricated on silicon substrates to study the relation between the gate-oxide thickness (t_{ox}) and the TFT performance including the contact resistance. Published in [238].

Third, the use of contact doping for the TFTs in this and all of the subsequent studies was not implemented. While possibly beneficial for reducing contact resistance in staggered TFTs by reducing the number and influence of trap states by filling them with charges generated by the dopant in the semiconductor region directly under the contacts and in parts of the channel region adjacent to the contacts [107], [110], [166], this effect is likely limited in coplanar TFTs due to the relatively smaller injection area that is limited to the edges of the contacts. The application of a contact dopant also adds an unnecessary source of additional variability in the TFTs, since any dopant molecules deposited on top of the contacts in BC TFTs may adversely affect the morphology of the subsequently-deposited organic semiconductor layer.

As a final measure, pentafluorobenzenethiol (PFBT, Figure 3.7a) was used to modify the gold contacts of the BC TFTs. This is primarily necessary as it serves to promote similar semiconductor morphology across the contact-to-channel interface [159], [235], [254]. It should be noted, however, as already discussed in Section 3.3.2, that PFBT has an additional benefit in that it can reduce the nominal charge-injection barrier height by introducing a large, downward dipole which increases the work function of the Au contacts, presumably improving charge injection into p-channel BC TFTs [233]. The PFBT treatment is, however, not

applicable to TC TFTs due to the buried contact-semiconductor interface, but it is nonetheless an acceptable (and necessary) measure for the BC TFTs in this comparative study for several reasons. First, the high surface energy of clean gold contacts compared to the surface of the gate dielectric can cause a significant difference in the semiconductor layer morphology, leading to very large contact resistances [255]. Therefore, the bottom contacts *must* be modified in some way to enable a fair comparison of the contact resistance between TC and BC TFTs at all. Second, by implementing very large contact areas in the TFTs ($200\ \mu\text{m} \times 200\ \mu\text{m}$ for each source and drain contact), this ensures that the largest contributor to the contact resistance in the TC TFTs is the bulk resistance under the contacts and not the interface resistance, which is primarily determined by the energy barrier [149]. Finally, gold contacts were used for the TC TFTs, since the work function of gold ($\sim 5.0\ \text{eV}$) is close to the highest-occupied molecular orbital (HOMO) energy level of DPh-DNTT ($5.3\ \text{eV}$) [75]. It is also noted that penetration of Au nanoclusters into semiconductor films has also been shown to reduce the dipole barrier that can otherwise form at the contact-semiconductor interface, to the benefit of the TC TFTs [256].

The above points notwithstanding, it is noted that while the large perpendicular component of the dipole moment pointing towards the substrate surface in PFBT-treated Au contacts increases the effective work function to around $5.4\ \text{eV}$ [233], [257], it is possible that this has little to no influence by itself on the reduction of the contact resistance in DPh-DNTT TFTs. This is due to the occurrence of Fermi-level pinning (see Chapter 6 for more details). This reiterates that the most crucial aspect of the PFBT treatment is the improvement of the semiconductor morphology on the bottom contacts.

5.1.1 Semiconductor thin-film morphology characterization

AFM and SEM analysis of the DPh-DNTT films deposited on the hybrid $\text{Al}_2\text{O}_3/\text{TDPA}$ gate dielectrics shows a mixture of a characteristic terrace-like microstructure and isolated larger agglomerates distributed in the thin film (Figure 5.2). This thin-film morphology has been observed previously for this molecule when deposited using thermal sublimation in vacuum [57], [74]. AFM analysis of the average step height of each terrace (Δh) (Figure 5.2c,d) corresponds approximately to the length of the long axis of a DPh-DNTT molecule ($2.6\ \text{nm}$), indicating that the molecules in each layer are oriented approximately upright with respect to the gate-dielectric surface [75]. This microstructure is favorable for the promotion of higher mobility in the channel region of a TFT, as it enables more efficient intermolecular in-plane

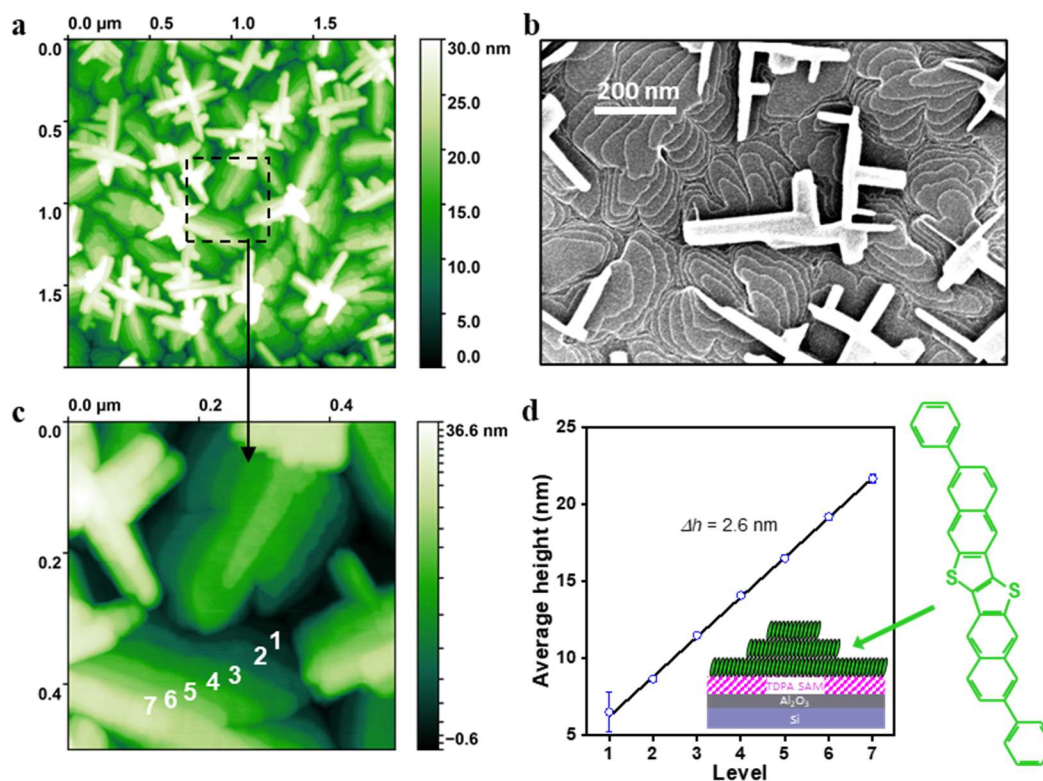


Figure 5.2 AFM and SEM morphological characterization of vacuum-deposited DPh-DNTT films on rigid substrates.

a) AFM topography scan and b) SEM micrograph of a DPh-DNTT layer formed on atomic-layer-deposited Al_2O_3 ($t_{osc} = 3$ nm) passivated with a TDPA SAM. c,d) Analysis of the height differences (Δh) between individual terraces in the area indicated from the AFM scan in (a). The extracted Δh of 2.6 nm corresponds closely to the long axis of a DPh-DNTT molecule, indicating that the molecules in each of the terraces are oriented approximately upright with respect to the gate-dielectric surface (see schematic representation in (d)). Results published in [238].

charge transport due to greater π - π stacking [45], [258]. A key requirement for small contact resistance in BC TFTs is to promote such a similar morphology on top of the source and drain contacts. Due to the greater surface roughness of the gold contacts, an analysis of the semiconductor morphology is problematic using AFM. Likewise using only SEM micrographs, the terrace morphology is clearly apparent in the channel region of a TFT, but is not as easily discernable on top of the contacts due to the low Z-contrast (Figure 5.3b). Thus, to verify the morphological characteristics of the semiconductor on top of the contacts and to examine if the PFBT layer has any effect on the morphology, grazing incidence x-ray diffraction (GIXRD) measurements of DPh-DNTT films deposited onto the hybrid AlO_x /TDPA-SAM gate dielectric, onto bare Au, and onto Au functionalized with PFBT were performed (Figure 5.3c). The DPh-DNTT film on the hybrid gate dielectric shows strong peaks at $2\theta_\chi = 18.5^\circ$, 22.8° ,

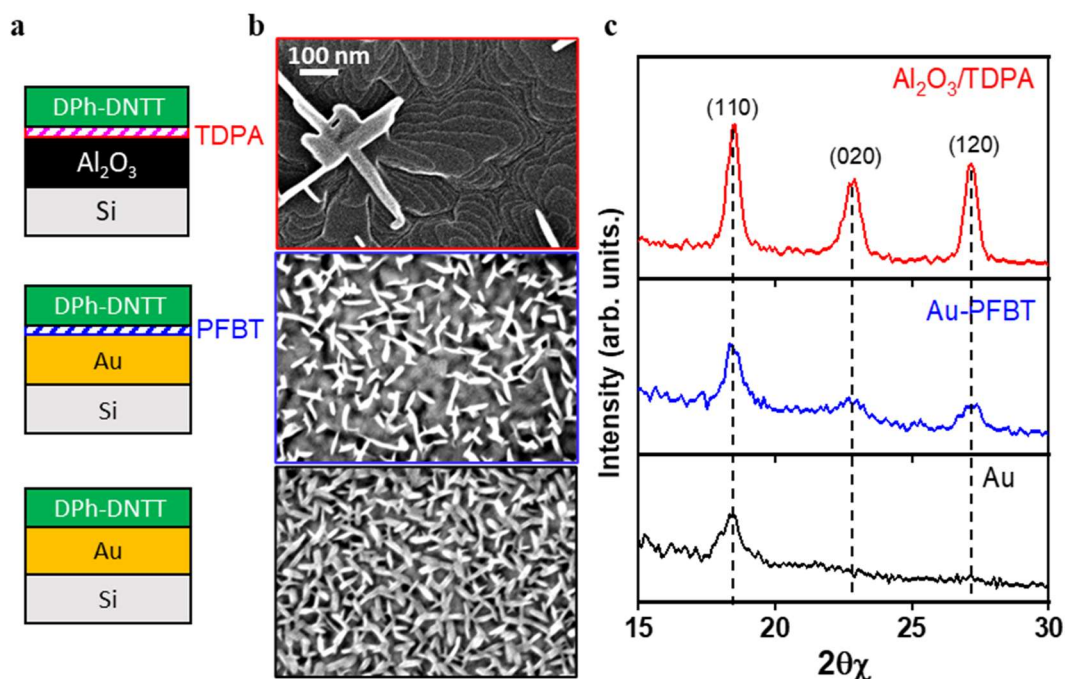


Figure 5.3 Grazing incidence x-ray diffraction characterization of vacuum-deposited DPh-DNTT films on rigid substrates.

a) Schematic diagrams of the samples measured with GIXRD. b) SEM images of 30-nm-thick DPh-DNTT films on bare Au (black outline), PFBT-treated Au (blue outline), and $\text{Al}_2\text{O}_3/\text{TDPA}$ -SAM (red outline). c) Grazing-incidence X-ray diffraction measurements on the DPh-DNTT films on the corresponding surfaces. The (110), (020), and (120) peaks are clearly distinguished in the latter two cases, signifying in-plane π - π stacking, while on bare Au only the (110) peak is present. Results published in [238].

and 27.2° , corresponding respectively to the (110), (020) and (120) crystal-packing directions in the ab -plane of the monoclinic unit cell of a DPh-DNTT single crystal that was determined previously [75]. This along with the AFM and SEM analyses strongly suggest that the DPh-DNTT thin films have a layered, herringbone structure in the channel region of the TFTs, with the c -axis nearly perpendicular to the substrate and with similar to that which was determined from the single-crystal data in that publication. A similar diffraction pattern is present in the film deposited onto Au/PFBT, though the peaks are somewhat broader than on the dielectric surface and reduced in relative intensity compared to the background. This is likely due to the rougher and more highly x-ray reflective underlying Au surface. Conversely, the GIXRD spectrum from DPh-DNTT deposited onto a bare-Au surface shows only the (110) peak, indicating a comparative lack of in-plane π - π stacking and absence of a layered-herringbone structure. This is correlated with a greater density of highly-disconnected needle-like structures that form on the bare-Au surface. This serves to confirm that using an interlayer of PFBT helps

to promote a similar morphology to the one observed on the gate dielectric surface on the surface of the source and drain contacts.

5.1.2 Evaluation of the contact resistance

Four sets of TFTs were fabricated using atomic-layer-deposited (ALD) stoichiometric aluminum oxide with thicknesses (t_{ox}) of 3, 30, 50, and 100 nm as the first part of the hybrid gate dielectrics. Both TC and BC TFTs were fabricated with channel lengths (L) ranging from 6 to 52 μm . The linear transfer characteristics ($V_{DS} = -0.1$ V) of the TFTs with $L = 50$ μm are shown in Figure 5.4. Regardless of the gate-dielectric thickness and the TFT architecture, all TFTs have a threshold voltage (V_{th}) close to zero, a subthreshold swing (SS) smaller than 200 mV/decade, and an on/off current ratio of about 10^6 . To quantify the contact resistance of the

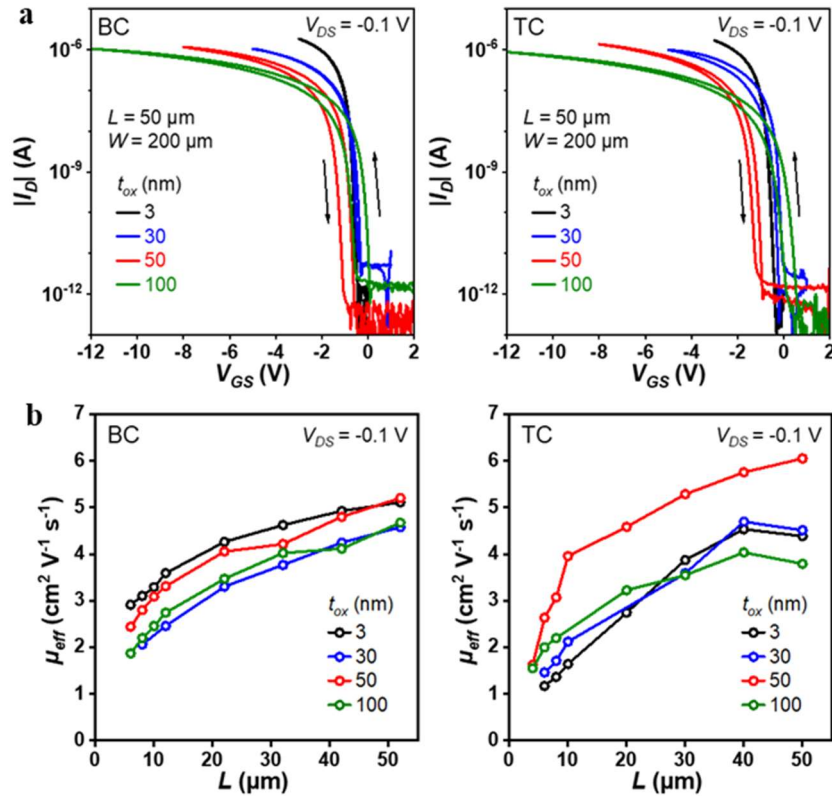


Figure 5.4 Transfer characteristics of organic thin-film transistors with different gate-dielectric thicknesses.

a) Representative transfer characteristics of bottom-contact (BC) and top-contact (TC) DPh-DNTT TFTs with different gate-oxide thicknesses (t_{ox}) measured with drain-source voltage (V_{DS}) of -0.1 V. The TFTs have a channel length (L) of 50 μm and a channel width (W) of 200 μm . b) Effective carrier mobility (μ_{eff}) determined from the transfer curves of the TFTs plotted as a function of the channel length. Results published in [238].

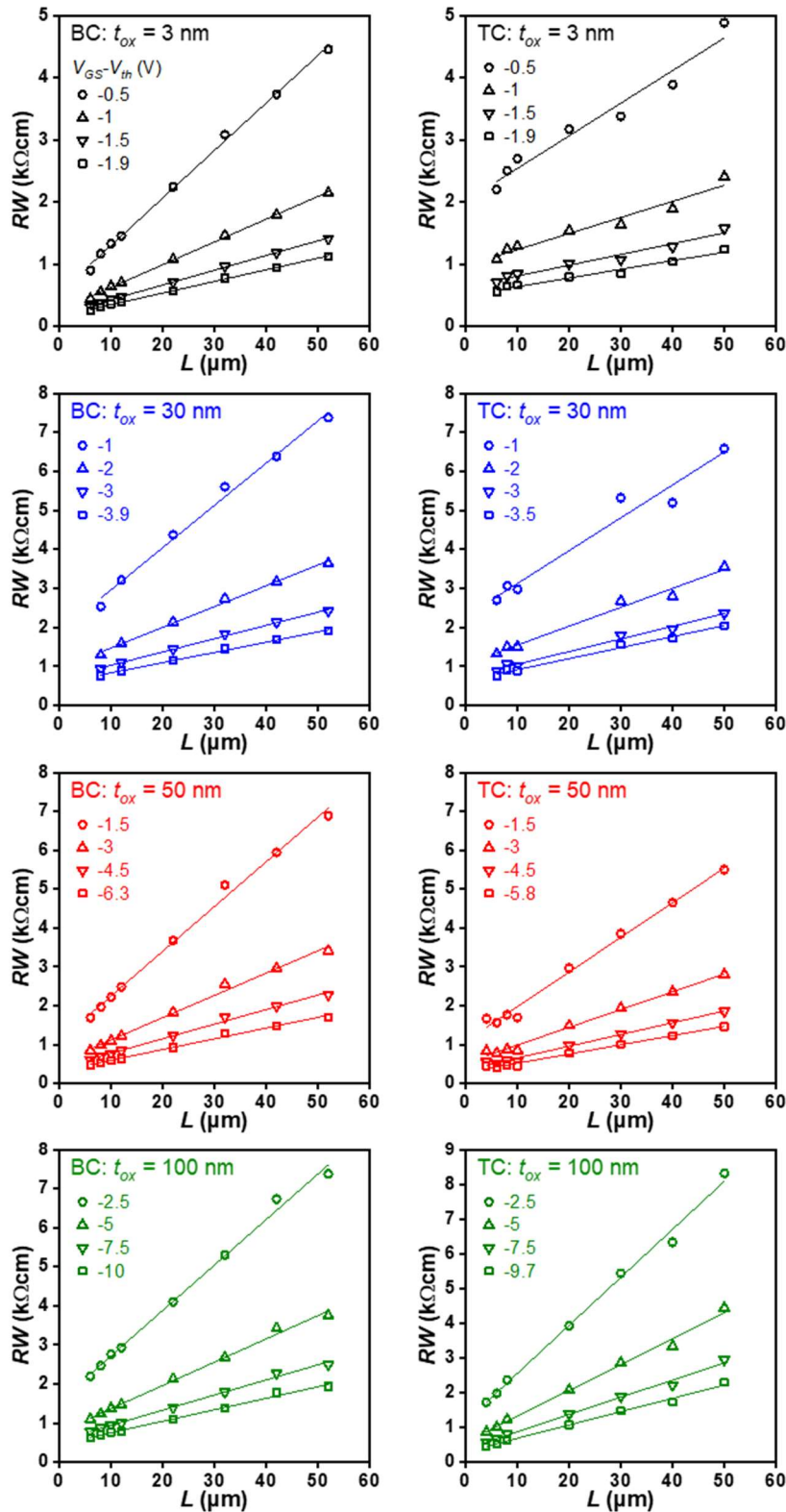


Figure 5.5 Application of the transmission line method (TLM) to organic thin-film transistors with different gate-dielectric thicknesses.

Example linear fits to the width-normalized total resistance (RW) as a function of the channel length (L) for bottom-contact (left column) and top-contact (right column) TFTs. The thicknesses of atomic-layer-deposited Al_2O_3 utilized in the gate dielectric (t_{ox}) are, from the top to bottom row, 3, 30, 50, and 100 nm. Results published in [238].

TFTs, the gated transmission line method (TLM) as described in Section 2.4.1 was employed [165]. The total width-normalized resistance ($RW = (V_{DS}/I_D) \cdot W$) was calculated for each gate overdrive voltage ($V_{GS} - V_{th}$) in the measurements of the linear transfer characteristics. Figure

5.5 shows example fits to the RW vs. L data used to extract the channel-width-normalized contact resistance (R_CW) and intrinsic channel mobility (μ_0) assuming a linear dependence in accordance with the assumptions of TLM. For all sets of devices in the analysis, the fits are of good quality, with adjusted R^2 values > 0.9 . From these fits, R_CW was extracted as a function of $(V_{GS}-V_{th})$ (Figure 5.6). From this representation of the data, it can be readily observed that the relative difference between the contact resistances of the BC and TC TFTs depends on the gate-oxide thickness, in qualitative agreement with the predictions from two-dimensional drift-diffusion simulations reported by Karin Zojer et al., predicting that at sufficiently small gate-dielectric thickness, the R_CW from BC TFTs may be reduced below that of comparative TC TFTs [17], [18]. Indeed, when the gate-oxide thickness is large (> 30 nm), the contact resistance of the TC TFTs is smaller than that of the corresponding BC TFTs over the entire range of $V_{GS}-V_{th}$. In the TFTs with a gate-oxide thickness of 30 nm, the contact resistances are approximately

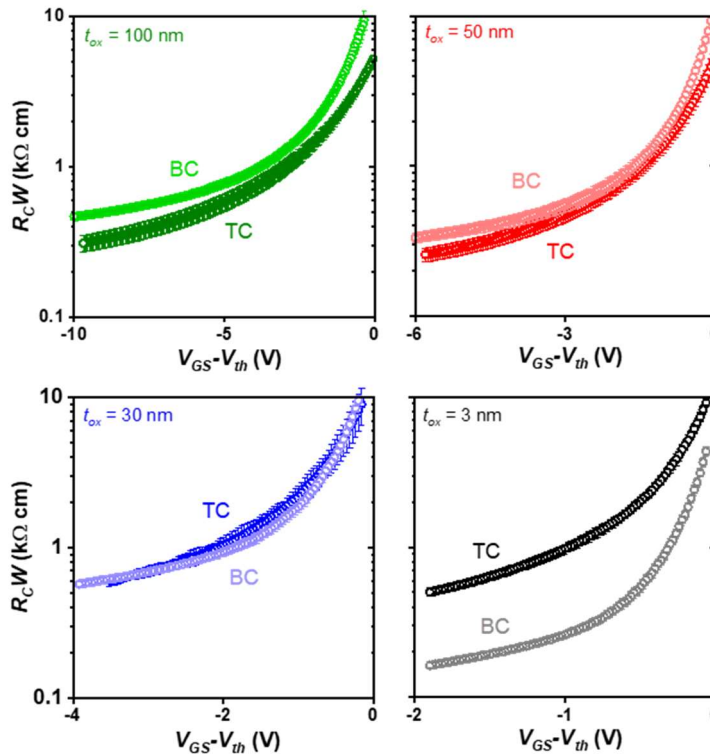


Figure 5.6 Width-normalized contact resistance as a function of the gate overdrive voltage.

Channel-width-normalized contact resistance (R_CW) of TFTs plotted as a function of the gate overdrive voltage ($V_{GS}-V_{th}$), showing the influence of the gate-dielectric thickness on the contact resistance. The contact resistance clearly scales such that with the smallest gate-oxide thickness (t_{ox}) of 3 nm, the contact resistance of the bottom-contact (BC) TFTs is smaller than that of the top-contact (TC) TFTs. Results published in [238].

equal, and for the smallest gate-oxide-thickness of 3 nm, the contact resistance in the BC TFTs is significantly smaller than in the TC TFTs over the entire range of $V_{GS}-V_{th}$.

Further inspection reveals notable differences in the dependence of the contact resistance on the gate overdrive voltage, which are more readily interpreted by examining $R_C W$ as a function of $(V_{GS}-V_{th})^{-1}$ (Figure 5.7). Two regimes can be distinguished according to $V_{GS}-V_{th}$ by a notable change in the slope of the data. In the low $V_{GS}-V_{th}$ regime, the slopes are generally steeper for both device geometries than at high $V_{GS}-V_{th}$. There also appears to be a transition in the relative magnitudes of the slopes between the two geometries as the oxide thickness is reduced, with a larger slope in the data for the BC TFTs for the largest oxide thickness of 100 nm. As the oxide thickness is reduced, the relative differences in the slope are reduced until finally at the lowest oxide thickness of 3 nm, the slope in the $R_C W$ vs. $(V_{GS}-V_{th})^{-1}$ data of the BC TFTs is smaller than that in the TC TFTs. At higher $V_{GS}-V_{th}$, a similar trend is also observed, although the transition to a smaller slope in the data of the BC TFTs appears to occur for a greater thickness of the oxide. As discussed in previous sections, these features are possibly related to the dependence of the contact resistance on two factors whose relative contributions depend on the TFT architecture: (1) the bulk resistance of the semiconductor layer between the contacts and the channel region which depends strongly on the charge carrier density and (2) the architecture-specific electric-field distribution which controls the charge-injection efficiency across the energetic barrier [17], [18]. These two contributions can be quantified using the TLM data by interpreting the contact resistance in terms of a gate-voltage-dependent component ($R_{C,0}$) in series, as outlined by Luan and Neudeck [165]

$$R_C W = \frac{l_0}{\mu_C C_{diel} (V_{GS} - V_{th})} + R_{C,0} W \quad (70)$$

$R_{C,0} W$ can be extracted from the approximately linear relationship between $R_C W$ and $(V_{GS}-V_{th})^{-1}$ in the high $(V_{GS}-V_{th})^{-1}$ regime (see the linear fits in Figure 5.7).

In general, the extracted $R_{C,0} W$ is smaller in the TC TFTs than in the BC TFTs for all oxide thicknesses. This result, in combination with the apparent dependence of $R_C W$ on the oxide thickness, can be understood in the context of the relative contributions from the bulk resistance of the organic-semiconductor layer intervening the contact interface and the channel region and that of the different geometrical components of the electric field modulated by V_{GS} and the gate-dielectric thickness. Both of these aspects are present in the TC and the BC architecture,

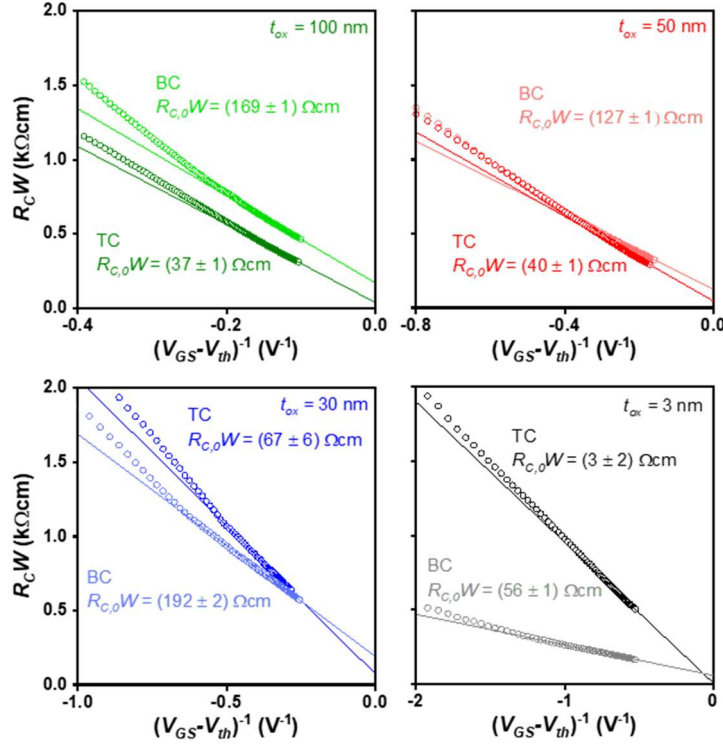


Figure 5.7 Estimation of the interface resistance.

Channel-width-normalized contact resistance ($R_C W$) as a function of the inverse of the gate overdrive voltage ($V_{GS} - V_{th}$). From this representation, the y-intercept can be interpreted as a gate-voltage-independent interface resistance ($R_{C,0}W$) with the slope accounting for the gate-voltage dependence of the contact resistance. Results published in [238].

but their relative contributions to the contact resistance at a given point of operation are different in a few crucial ways.

First it must be considered that the larger volume of the semiconductor through which the injected charges must traverse in staggered (TC) TFTs contributes a resistance component that comprises a significantly greater portion of the contact resistance than in coplanar (BC) TFTs [150], [155]. This contribution is to a first order modulated by the thickness of the semiconductor layer (t_{osc}), wherein a larger t_{osc} results in a larger access resistance to the channel region due to generally poorer intermolecular charge transport between the monolayer terraces of the semiconductor film [157]. The charge density in the semiconductor film in this region changes the magnitude of the access resistance to some extent, and therefore there remains an additional dependence on the gate-source voltage, but with minimal dependence on the gate-dielectric thickness since it is the vertical electric field component that is dominant for this aspect.

The lower overall contact resistance in the BC TFTs for smaller oxide thicknesses (despite the comparatively larger $R_{C,0}W$) can be explained if it is considered that in a coplanar TFT configuration, (1) the volume of semiconductor through which the injected charges from the metal contact must traverse is minimized by the fact that the contacts are now in the same plane as the channel, and (2) the charge-carrier density in the vicinity of the contact interface is now strongly dependent on the lateral (in-plane) component of the electric field created by V_{GS} (and thus also on the thickness of the gate dielectric). For coplanar TFTs, the injection is more strongly dependent on the density of space charges in the semiconductor near the contacts, rather than on an access resistance (so long as the semiconductor morphology is well-controlled across the contact-channel interface) [252]. For larger gate-dielectric thicknesses, the accumulated space-charge density is relatively smaller for a given gate overdrive voltage, since it is primarily the lateral component of the electric field which modulates the charge injection in this device architecture. Therefore, in the TLM analysis the gate-voltage-dependent component of the contact resistance is correspondingly larger for a thicker oxide. For smaller gate-dielectric thicknesses, on the other hand, the relative contribution from the lateral component of the electric field is increased, and thus increases the efficiency of injection from the contact, since the influence on the accumulated charge density is also relatively larger [18], [259], [260]. Provided that the charge-carrier mobility in the channel region adjacent to the contact is large enough and the charge injection is minimally efficient across the contact interface (i.e. $R_{C,0}$ is not overly large due to a high Schottky barrier or poor semiconductor morphology), space charges will not build up near the interface that would inhibit carrier flow away from the region directly adjacent to the source contact in BC TFTs [204], [252]. Hence, with a thinner gate-oxide layer, the contact resistance and its dependence on the gate overdrive voltage are reduced at higher gate overdrive voltages compared to the TC TFTs at sufficiently large carrier densities in the channel.

5.2 Low-voltage transistors on flexible substrates

Keeping the targeted applications for low-voltage flexible circuits in mind, patterned-gate TC and BC TFTs and circuits were also fabricated on flexible polyethylene naphthalate (PEN) substrates (Figure 5.8). Direct comparisons of the contact resistance for the different device architectures was again of interest. For this comparison, TFTs were fabricated with an identical nominal thickness of the semiconductor layer of 20 nm, though in this case the deposition could not be carried out simultaneously as in the previous study, since only one instance of each mask was available for each of the various layers. TLM was used to measure the contact resistance in addition to other electrical characteristics of the TFTs. Here, the dynamic performance was also assessed and compared for the two device architectures implemented in 11-stage unipolar ring oscillators (Section 5.2.4). These were fabricated on the same substrates as the TLM TFTs in order to validate a direct comparison of the contact resistance and the effect that it has on the dynamic performance for the different device architectures.

As before, the thin-film morphology of the DPh-DNTT films deposited on the hybrid gate dielectric fabricated on a flexible PEN substrate was examined (Figure 5.9). Both the SEM and peak force microscopy (PFM) images are similar to those from the rigid substrates presented in the previous section, though GIXRD measurements could not be performed on the flexible substrates. However, the SEM and PFM data, including the extracted average step height of the individual terraces of the DPh-DNTT film (Δh) of 2.6 nm, as well as the electrical

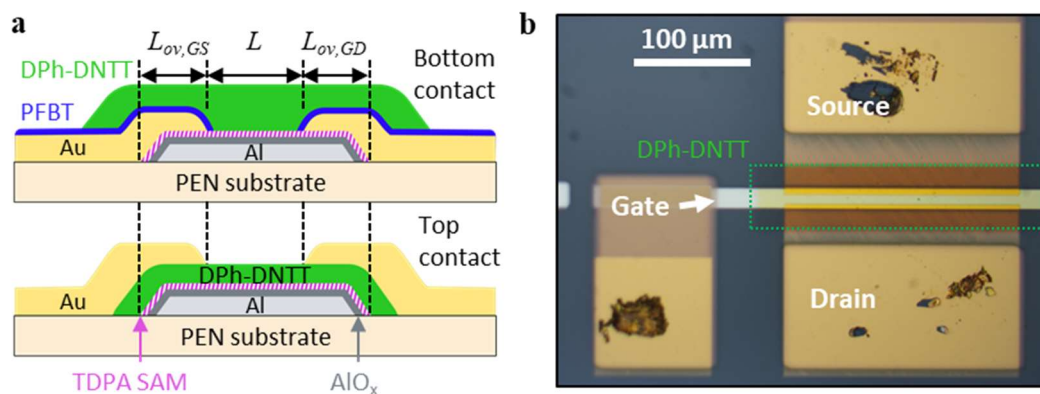


Figure 5.8 Inverted organic thin-film transistors on flexible substrates.

a) Schematic cross-sections of bottom-contact and top-contact organic TFTs fabricated on flexible polyethylene naphthalate substrates. b) Photograph of a bottom-contact organic TFT on PEN. c) SEM micrograph and d) PFM height scan of the a DPh-DNTT layer formed on plasma-grown aluminum oxide (AlO_x) passivated with a TDPA SAM. Published in [238].

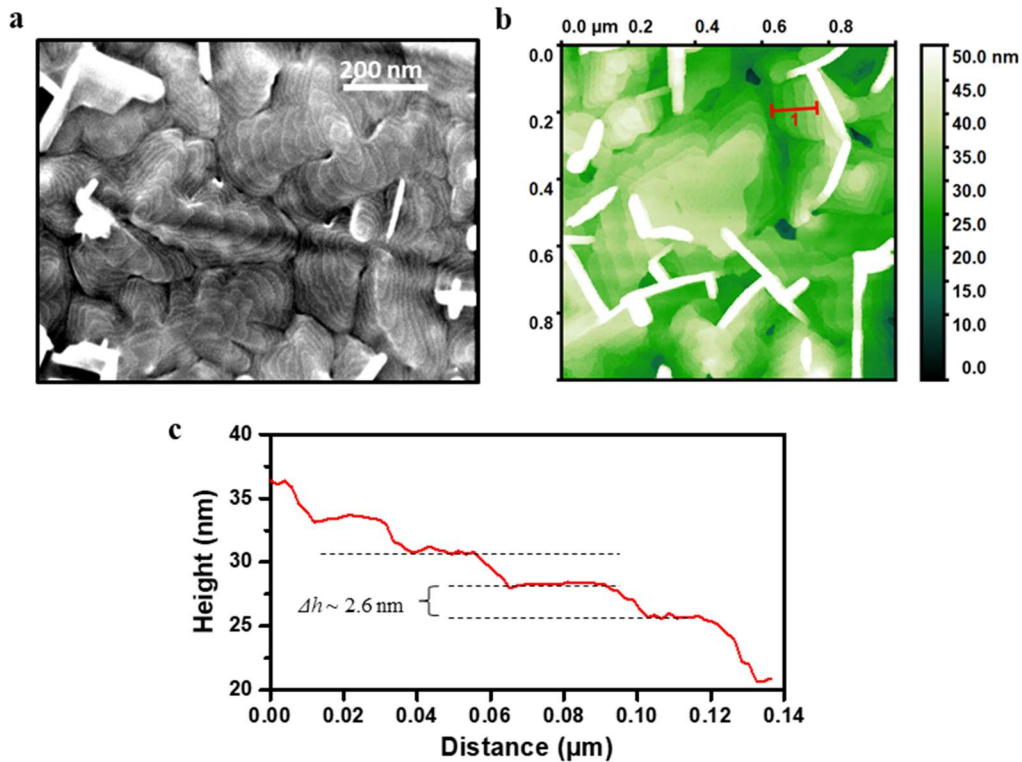


Figure 5.9 Thin-film morphology of DPh-DNTT deposited on flexible substrates.

a) SEM micrograph and b) peak-force microscopy (PFM) height scan of a DPh-DNTT layer formed on plasma-grown aluminum oxide (AlO_x) passivated with a TDPA SAM. c) Line profile from the indicated region in (b). The average step height ($\Delta h \sim 2.6$ nm) between terraces in the thin film corresponds closely to the length of a DPh-DNTT molecule. Results published in [141].

performance data from the TFTs presented in the following sections give us confidence that the crystallography of the DPh-DNTT films is very similar to that obtained on the rigid substrates.

5.2.1 Static electrical performance and contact resistance

Transfer characteristics of BC and TC TFTs with $L_{ov,total} = 10$ μm , $W = 200$ μm , and $L = 8, 12, 20, 30, 40, 50$ and 60 μm were measured at a drain-source voltage (V_{DS}) of -0.1 V and used for TLM analysis (Figure 5.10). The quality of the fits to the RW vs. L data is again excellent, with adjusted $R^2 \geq 0.99$ for all of the fits in the analysis. At a gate overdrive voltage of -2.5 V, the TC TFTs show $R_C W = (56 \pm 14)$ Ωcm , very similar to the lowest contact resistances reported for this device architecture [81], [86], [261]. Remarkably, the BC TFTs have an even smaller $R_C W$ of (29 ± 13) Ωcm , which is the smallest contact resistance yet reported for coplanar

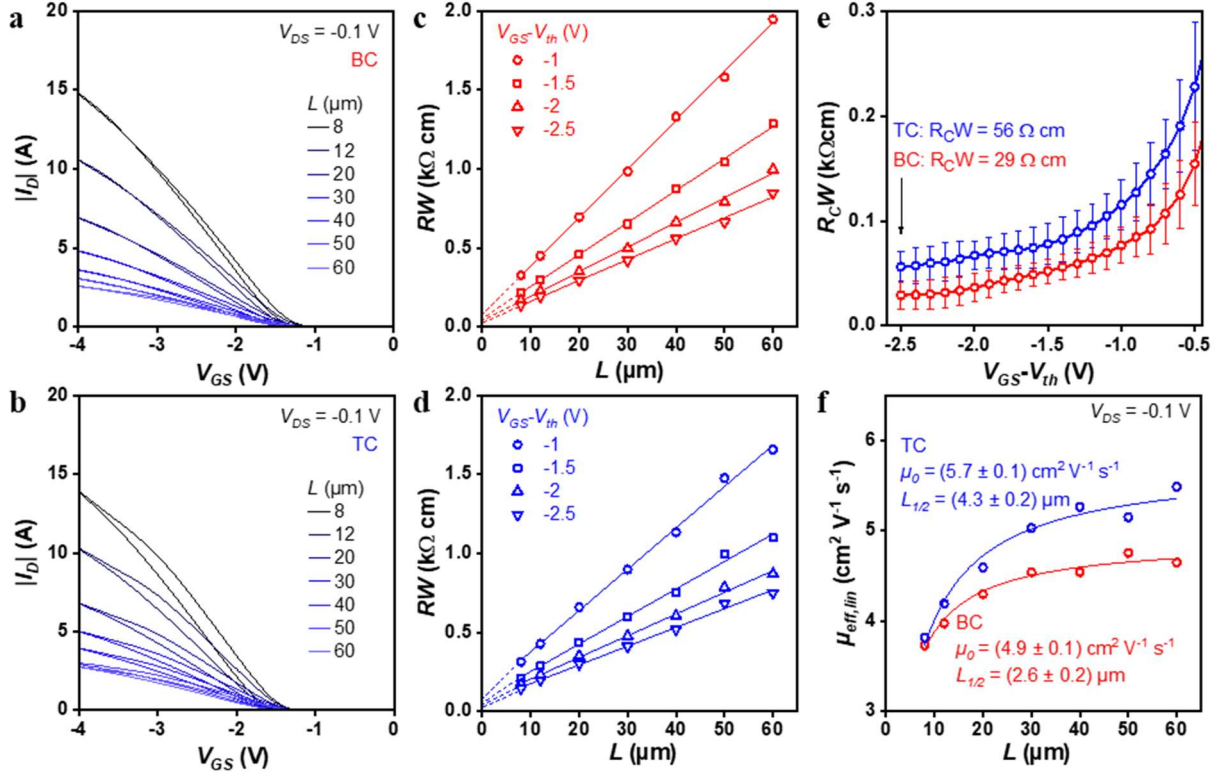


Figure 5.10 Organic thin-film transistors fabricated on flexible PEN substrates employed for the TLM analysis.

The TFTs have channel lengths (L) ranging from 8 to 60 μm , a channel width (W) of 200 μm , and a total gate-to-contact overlap ($L_{ov,total}$) of 10 μm . a) Transfer characteristics of the bottom-contact (BC) TFTs. b) Transfer characteristics of the top-contact (TC) TFTs. c,d) Linear fits to the total width-normalized resistance (RW) at selected gate overdrive voltages ($V_{GS}-V_{th}$). e) Width-normalized contact resistance (R_CW) plotted as a function of the gate overdrive voltage. The error bars correspond to the standard error from the linear regression at each gate overdrive voltage. f) Effective carrier mobility ($\mu_{eff,lin}$) plotted as a function of the channel length. The data are fit to the equation $\mu_{eff,lin} = \mu_0(1+L_{1/2}/L)^{-1}$, where μ_0 is the intrinsic channel mobility and $L_{1/2}$ is the channel length at which $\mu_{eff,lin} = \frac{1}{2} \mu_0$. Results published in [238].

organic TFTs and is within an order of magnitude of the contact resistance achieved in flexible indium gallium zinc oxide (IGZO) TFTs [262]. For comparison, Stadlober et al. reported a contact resistance of 80 Ωcm for bottom-gate, bottom-contact pentacene TFTs in which the surface of the gold source and drain contacts had been exposed to ultraviolet radiation and ozone in order to induce a favorable pentacene morphology on the contacts [78]. Braga et al. reported the smallest contact resistance yet reported for organic TFTs of any architecture in electrolyte-gated top-gate staggered poly(3-hexylthiophene) TFTs in which strong doping of the semiconductor from the electrolyte resulted in a very small contact resistance of 1 Ωcm

[263]. The transfer length (L_T) for the TC TFTs was also extracted from the intersection of the fits with the x-axis, where the intersection point is equivalent to $2L_T$, and is relatively constant over the range of the gate overdrive voltage with a value of about $2.4 \mu\text{m}$. This is significantly smaller than the gate-to-source and gate-to-drain overlaps ($L_{ov,GS}$ and $L_{ov,GD}$), signifying that the charge injection is not severely limited by the contact area [167]. This is important to note so that confidence can be maintained in the comparison to the BC TFTs, whose contact resistance generally has little to no dependence on the contact overlaps. The effective mobility in the linear regime ($\mu_{eff,lin}$) shows a typical dependence on the channel length for TFTs with appreciable contact resistance. From this data, the intrinsic channel mobility (μ_0) and the channel length at which $\mu_{eff,lin}$ is equal to half of μ_0 is extracted using

$$\mu_{eff,lin} = \frac{\mu_0}{1 + \frac{L_{1/2}}{L}} \quad (71)$$

It is notable that the lower contact resistance of the BC TFTs is achieved despite a lower $\mu_0 = (4.9 \pm 0.1) \text{ cm}^2 \text{ V}^{-1} \text{ s}^{-1}$ compared to that in the TC TFTs, $\mu_0 = (5.7 \pm 0.1) \text{ cm}^2 \text{ V}^{-1} \text{ s}^{-1}$.

To highlight some of the other differences in the static performance of TC and BC TFTs, the transfer characteristics of flexible TFTs with $L = 8 \mu\text{m}$ and $L_{ov,total}$ of 4 and 10 μm are shown in Figure 5.11. All TFTs have threshold voltages of about -1 V and on/off current ratios, here defined as the ratio between the drain current at $V_{GS} = -3\text{V}$ and the lowest drain current measured in the transfer curve, between 10^8 and 10^9 . The smaller contact resistance of the BC TFTs results in a larger effective carrier mobility compared to the TC TFTs at this relatively small channel length. All TFTs have subthreshold swings smaller than 100 mV/decade, but those of the BC TFTs are notably steeper (62 to 68 mV/decade) than those of the TC TFTs (92 to 94 mV/decade). This charge-transport behavior suggests that the subthreshold swing is affected not only by the charge-trap density at the interface between the gate dielectric and the semiconductor layer (which is nominally identical in the two device architectures), but also by the charge-trap density in the semiconductor film that separates the top contacts from the gate-induced carrier channel which the carriers have to traverse in the staggered (TC) TFTs. It has now even been observed that bottom-contact DPh-DNTT TFTs (Figure 5.12) can in fact show on/off ratio as high as 10^{10} and can have smaller subthreshold swings as small as 59 mV/decade (within error of theoretical minimum value of 58.6 mV/decade at $T = 292 \text{ K}$), corresponding to an exceptionally low density of interface trap states (N_{it}) on the order of $10^{11} \text{ cm}^{-2}\text{V}^{-1}$ [124].

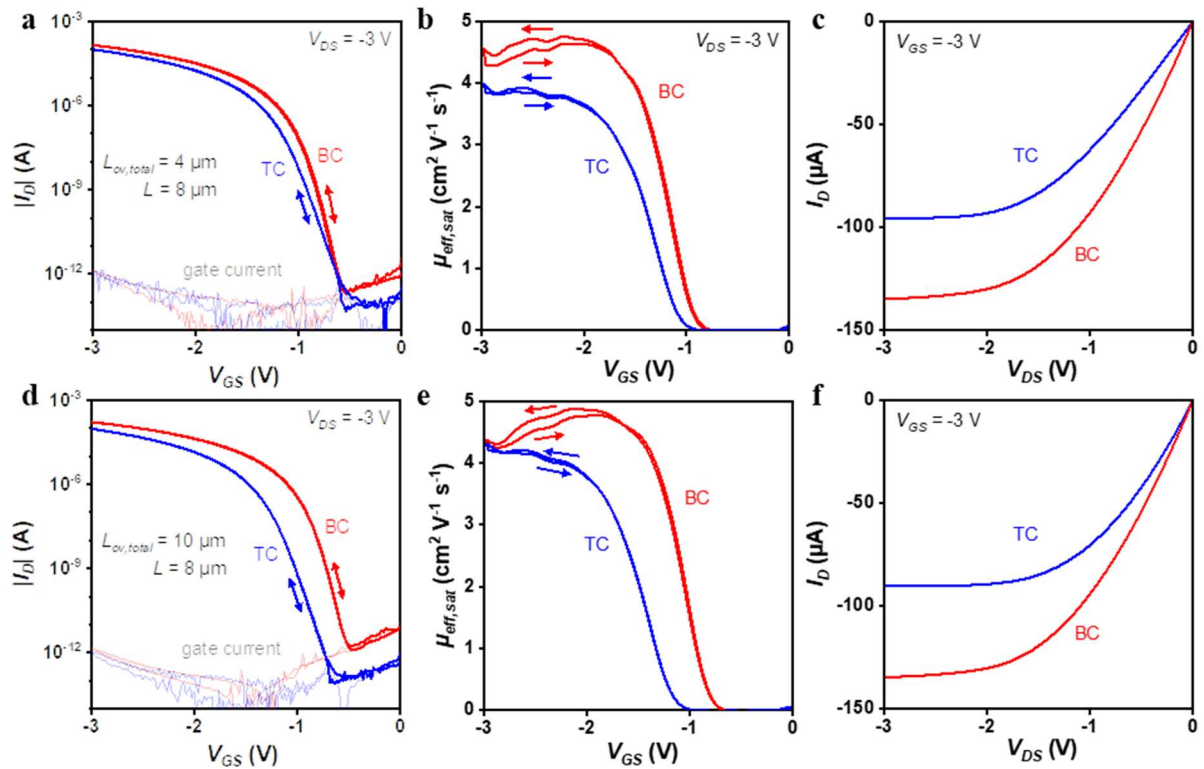


Figure 5.11 Static electrical characteristics of top-contact and bottom-contact organic thin-film transistors on flexible PEN substrates.

The TFTs have a channel length (L) of 8 μm , a channel width (W) of 200 μm , and a total gate-to-contact overlap ($L_{ov,total}$) of 4 μm (a-c) or 10 μm (d-f). a,d) Transfer characteristics measured in the saturation regime ($V_{DS} = -3$ V). b,e) Effective carrier mobility ($\mu_{eff,sat}$) extracted from the transfer characteristics shown in (a) and (d). c,f) Output curves for $V_{GS} = -3$ V. Results published in [238].

To best knowledge of the author, this is the smallest subthreshold swing reported to date for organic TFTs, regardless of the choice of device architecture, gate dielectric, and semiconductor [264]–[267].

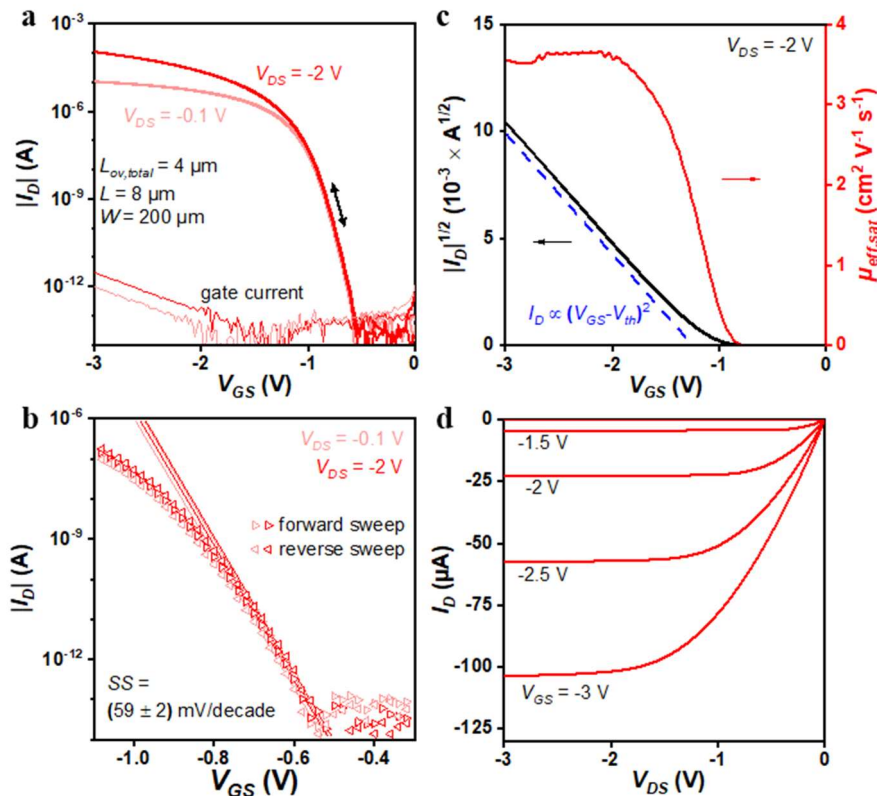


Figure 5.12 Flexible bottom-contact organic thin-film transistor showing record on/off ratio and subthreshold swing.

a) Measured transfer characteristics of a bottom-contact DPh-DNTT TFT fabricated on a PEN substrate having a channel length (L) of 8 μm , a total gate-to-contact overlap ($L_{ov,total}$) of 4 μm and a channel width (W) of 200 μm . b) Square-root of the absolute drain current (I_D) and effective charge-carrier mobility ($\mu_{eff,sat}$) calculated from the transfer characteristics measured at a drain-source voltage (V_{DS}) of -2 V as a function of the gate-source voltage (V_{GS}). The dotted blue line is a guide to the eye, indicating the ideal quadratic dependence of the drain current in the saturation regime on the gate overdrive voltage ($V_{GS}-V_{th}$). c) Extraction of the subthreshold swing (SS) from the forward and reverse sweeps of the transfer curves. The average subthreshold swing of (59 ± 2) mV/decade is within measurement error of the limit set by the thermal voltage at the measurement temperature of 292 K. d) Measured output characteristics of the same TFT. Results published in [141].

5.2.2 Temperature dependence of the electrical characteristics of bottom-contact thin-film transistors based on DPh-DNTT

Additional bottom-contact DPh-DNTT TFTs were fabricated on polyethylene naphthalate (PEN) substrates using Au source and drain contacts functionalized with a chemisorbed monolayer (CML) of pentafluorobenzenethiol (PFBT) according to the same fabrication methods implemented in the previous section. In this case, TFTs with various channel lengths (L) were used for a temperature-dependent TLM analysis of the contact resistance (R_C) and the intrinsic channel mobility (μ_0). Exemplary transfer and output curves of a TFT with $L = 12 \mu\text{m}$ measured at temperatures between 80 and 405 K are shown in Figure 5.13. Increasing the substrate temperature generally leads to a monotonic increase in the magnitude of the drain current ($|I_D|$) in the ‘fully-on’ state at $V_{GS} = -3 \text{ V}$ for low drain-source voltages (V_{DS}). Such a temperature dependence of the drain current is indicative of (predominantly) thermally-activated charge-transport processes in the TFT. While this is not surprising, it is noteworthy that the subthreshold swing (SS) and threshold voltage (V_{th}) show some unexpected dependencies on the temperature. Recalling the equation for the subthreshold swing from Chapter 2, it would be expected to increase proportionally with the temperature:

$$SS = \frac{\partial V_{GS}}{\partial \log(I_D)} = \frac{k_B T}{q} \ln(10) \left(1 + \frac{q N_{it}}{C_{diel}} \right) \quad (72)$$

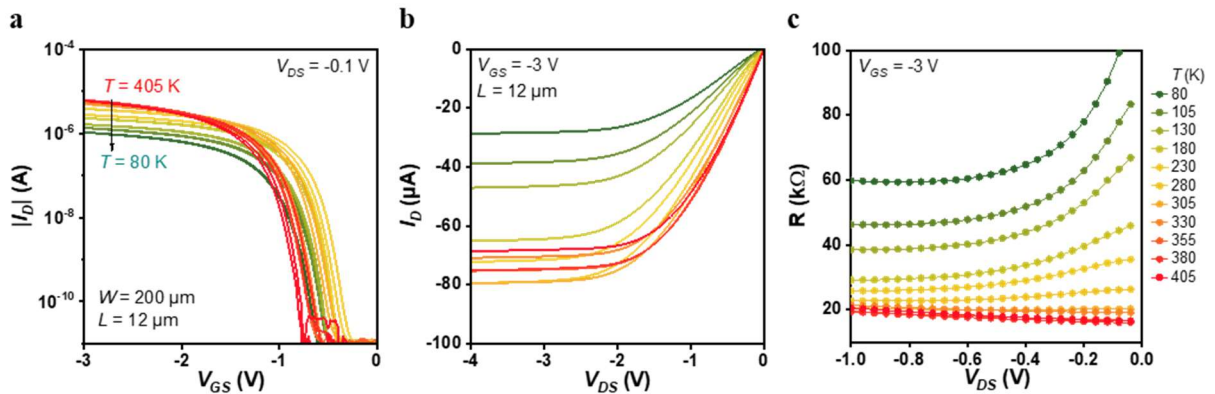


Figure 5.13 Static TFT characteristics at different temperatures.

a) Transfer and b) output curves of a DPh-DNTT TFT with PFBT-functionalized gold bottom contacts having a channel length (L) of $12 \mu\text{m}$ and a channel width (W) of $200 \mu\text{m}$ measured at different temperatures. c) Pointwise total resistance ($R = V_{DS}/I_D$) evaluated from the output curves in (b).

However, from the transfer curves in Figure 5.13a it is shown that S is mostly invariant with the temperature. This is possibly due to an incorrect assumption regarding the density of trap states (N_{it}). In short, in the definition in equation (72) it is assumed that N_{it} is independent of the energy of the trap states [268]. However, it is possible that the trap-state density N_{it} is distributed non-uniformly across a broad energy range separated from the HOMO by an energy of approximately $k_B T$. This is a reasonable assumption, especially in the case of a polycrystalline semiconductor layer as in the present case where structural defects such as grain boundaries can introduce additional traps states [269]. There is also a notable non-monotonic threshold-voltage (V_{th}) shift with the measurement temperature. The most positive threshold voltage of -0.8 V was measured at $T = 280$ K. If the temperature is either increased or decreased, V_{th} shifts towards more negative values. This behavior is evident in all of the other TFTs used in the TLM analysis (transfer curves not shown). Such a shift of V_{th} can be indicative of non-linear (non-ohmic) injection processes in the organic TFTs [172] or differences in trap-state distribution with the temperature [104]. Nonlinear injection is further evidenced by the dependence of the total resistance ($R = V_{DS}/I_D$) on V_{DS} shown in Figure 5.13c, which appears to follow an approximately exponential dependence until between 280 and 305 K. Gomes et al. [270] have also shown that water trapped in the organic-semiconductor film can cause anomalous changes in the charge transport in organic TFTs between 200-300 K.

The temperature-dependent TLM analysis was performed on additional TFTs with $L = 20, 30, 40,$ and $60 \mu\text{m}$. As a reminder, in the TLM analysis the total channel-width-normalized resistance of the TFTs (RW) is modeled at negligible V_{DS} as the series connection of the total combined contact resistances at the source and drain ($R_C W$) and the channel resistance (both normalized to the channel width W). This latter term is in turn related to the intrinsic channel mobility (μ_0), the channel length (L), and the gate-source voltage (V_{GS}) by

$$RW = \frac{1}{\mu_0 C_{diel} (V_{GS} - V_{th})} L + R_C W \quad (73)$$

Where C_{diel} is the area-normalized capacitance of the gate dielectric, and V_{th} is the threshold voltage. Example linear fits to the RW vs. L measurement data at the highest gate overdrive voltage ($V_{GS} - V_{th}$) of -1.5 V over a temperature range of 80 to 405 K are shown in Figure 5.14a. A strong temperature dependence is observed for both the y-intercept and the slope of the fits, implying strongly thermally activated characteristics for both charge injection and transport in

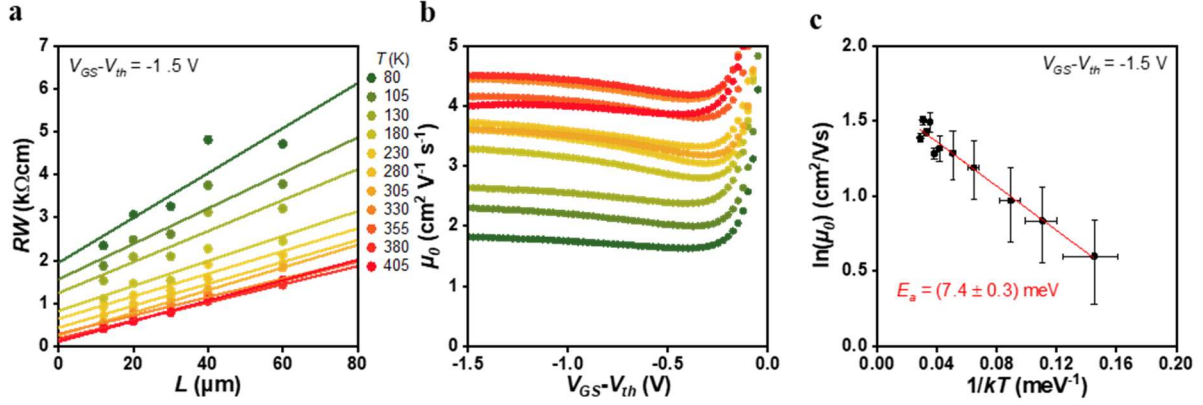


Figure 5.14 Temperature-dependent TLM: Intrinsic-channel mobility.

a) Channel-width-normalized total resistance (RW) of DPh-DNTT TFTs with PFBT-functionalized gold bottom contacts as a function of the channel length (L) measured at different temperatures (T) for a gate-overdrive voltage ($V_{GS}-V_{th}$) of -1.5 V. b) Intrinsic channel mobility (μ_0) at different temperatures. c) Intrinsic channel mobility at $V_{GS}-V_{th} = -1.5$ V. The activation energy (E_a) was extracted using equation (74) (red line).

the channel of the TFTs, respectively. Focusing on transport in the channel first, it is notable that an increase in the temperature generally results in an increase in μ_0 , and for $V_{GS}-V_{th} < -0.3$ V, μ_0 is mostly independent of V_{GS} (Figure 5.14b). This lack of dependence of the intrinsic channel mobility on the gate-source voltage suggests a concomitant lack of dependence on the accumulated charge-carrier density in the channel, indicating that the charge carriers are highly delocalized [93]. This is expected for crystalline or polycrystalline organic semiconductors in the case where the grain sizes are large [89]. An Arrhenius plot of μ_0 extracted at $V_{GS}-V_{th} = -1.5$ V (Figure 5.14c) suggests that the multiple trap and release (MTR) theory may describe the charge transport by an exponential of the form [89]:

$$\mu_0 = \mu_{0,p} \exp\left(\frac{-E_a}{k_B T}\right) \quad (74)$$

where $\mu_{0,p}$ is a temperature-independent pre-factor, E_a is the activation energy separating the transport and the trap-state energy levels (typically attributed to grain boundaries), k_B is the Boltzmann constant, and T is the temperature. A very low $E_a = (7.4 \pm 0.3)$ meV is extracted from the fit of μ_0 vs. $(k_B T)^{-1}$. It is notable that this activation energy is well below $k_B T$ over most of the range of measurement temperatures, and as such this would presumably mean that charge carriers would receive sufficient energy from the thermal bath that the intrinsic channel mobility would saturate for $T \sim 90$ K and above. Such non-physical results for the activation energy when using a simple hopping-transport model like MTR are not unheard of in the

investigation of high-mobility organic semiconductors [98], [173], [204], [271]. It is possible that for such materials as the DPh-DNTT thin-films in these TFTs, other models including e.g. quantum-nuclear tunneling effects [65], a variation in the predominance of hopping transport as a function of temperature [272], and effects related to the vibrations of the crystal lattice using the transient localization (TL) theory [94] must be adopted. This is supported also by the fact that an appreciable finite intrinsic channel mobility of $0.4 \text{ cm}^2/\text{Vs}$ was observed at a temperature of $T = 15 \text{ K}$ (not shown). As one promising example, in TL theory the charge-carrier mobility is described according to

$$\mu = \frac{qL_{tr}^2}{2k_B T \tau_{vib}} \quad (75)$$

Where q is the elementary charge, L_{tr} is the temperature-dependent localization length within the crystal lattice, and τ_{vib} is the timescale of intermolecular vibrations [29]. While this is also not sufficient by itself to describe the mobility in the TFTs due to the increasing intrinsic mobility that was observed with the temperature, it is possible that the concurrent effects described by hopping transport with MTR ($\exp(-E_a/kT)$ dependence) and molecular vibrations in TL (L_{tr}^2/T dependence) might explain the temperature dependence of the intrinsic mobility that was measured. To confirm this will require more extensive charge-transport studies on DPh-DNTT that are beyond the scope of this work. Going forward, the parameter E_a from this part of the analysis is considered only as a convenient semi-quantitative metric to describe the overall temperature dependence of the intrinsic channel mobility in the TFTs.

The contact resistance shows a strong negative correlation with the intrinsic channel mobility (Figure 5.15a), which is not uncommon for organic TFTs when the mobility is low ($< 1 \text{ cm}^2 \text{ V}^{-1} \text{ s}^{-1}$) [51]. An approximate exponential dependence of R_C on μ_0 is observed for $\mu_0 \sim 3.7 \text{ cm}^2 \text{ V}^{-1} \text{ s}^{-1}$ or less, which corresponds to the low-temperature measurement regime ($T < 280 \text{ K}$). Similar to the procedure implemented in other sections, $R_C W$ can be separated into its gate-source-voltage-dependent and independent components:

$$R_C W = \frac{l_0}{\mu_0 C_{diel} (V_{GS} - V_{th})} + R_{C,0} W \quad (76)$$

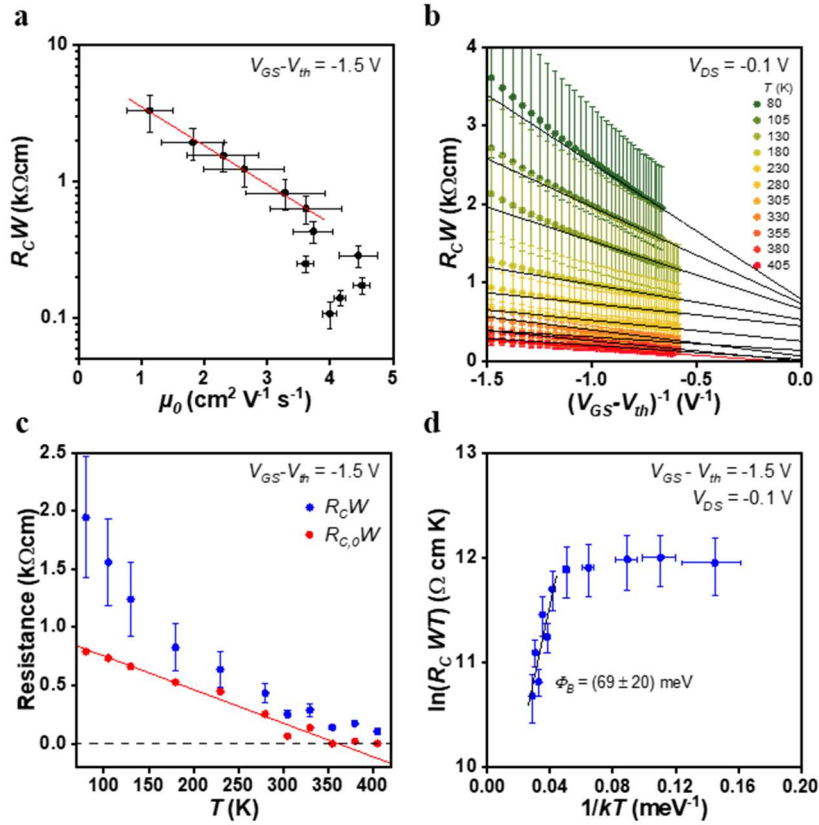


Figure 5.15 Temperature dependent TLM: Contact-resistance modelling.

a) Channel-width-normalized contact resistance ($R_C W$) as a function of the intrinsic channel mobility (μ_0) of DPh-DNTT TFTs with PFBT-functionalized gold bottom contacts at different temperatures. Red line is a guide to the eye showing approximate exponential dependence at low μ_0 . b) Gate-source-voltage dependence of $R_C W$ at different temperatures. Lines are fits to the high-voltage regime to extract the voltage-independent component of the contact resistance ($R_{C,0} W$). c) Temperature dependence of $R_C W$ and $R_{C,0} W$. $R_{C,0} W$ varies linearly with T and is reduced to zero at approximately 355 K. $R_C W$ shows an approximately exponential reduction with the temperature. d) Relation of the contact resistance to $k_B T$, assuming thermionic emission. Fit using equation (79).

$R_{C,0} W$ is again extracted by fitting the high-voltage regime of the $R_C W$ vs. $(V_{GS} - V_{th})^{-1}$ data and extrapolating to the y-intercept (Figure 5.15b,c). This may be interpreted here as the minimum contact resistance that can be realized by fully populating the organic semiconductor with mobile carriers [165]. From a first approximation, $R_C W$ shows a roughly exponential decrease with increasing temperature, while at the same time $R_{C,0} W$ decreases approximately linearly until effectively vanishing at around room temperature (Figure 5.15c, red data). Notice that this roughly coincides with the transition temperature at which the contact resistance shows a markedly reduced dependence on the intrinsic channel mobility (Figure 5.15a). This may hint at a transition in the dominant charge-carrier injection mechanism with the temperature.

When evaluated at zero bias, the specific contact resistance (R_{CS}) taking into account the total charge-injection area is defined by [176]

$$R_{CS} = \left(\frac{dJ}{dV} \right)_{V=0}^{-1} \quad (77)$$

Where J is the current density injected across the contact interface over an area defined by the width and the thickness of the carrier channel, and V is the applied voltage (assumed here to be equivalent to V_{DS}). For semiconductors with low doping density and at moderately high temperatures, thermionic emission (TE) is expected to dominate the charge transport across the interface, such that J will follow

$$J_{TE} = A^* T^2 \exp\left(\frac{-\Phi_B}{k_B T}\right) \left(1 - \exp\left(\frac{\Delta\Phi_B + qV}{k_B T}\right)\right) \quad (78)$$

And thus for evaluation in the low-voltage regime ($V \rightarrow 0$) R_{CS} can be calculated by

$$R_{CS} = \left(\frac{k_B}{qA^*T} \right) \exp\left(\frac{\Phi_B}{k_B T}\right) \quad (79)$$

Where k_B is the Boltzmann constant, q is the elementary charge, and A^* is the reduced effective Richardson constant. A^* depends on many factors, including the effective mass of the charge carriers, the carrier mobility in the semiconductor, and relative contributions from carrier diffusion and carrier drift [166].

Assuming that the thickness of the channel region in the TFTs is independent of the temperature and that the extraction of $R_C W$ at $V_{DS} = -0.1$ V is a valid approximation for low applied fields, the measured $R_C W$ from the TLM measurements at different temperatures can be used to estimate an effective barrier height (Φ_B) from a plot of $\ln(R_C W T)$ as a function of $1/k_B T$ (Figure 5.15d). Two regions are clearly distinguishable in this representation of the contact resistance. First, the high-temperature region above ~ 280 K shows that the injection can be approximately described by thermionic emission using equation (79) with $\Phi_B = (69 \pm 20)$ meV. This effective barrier height is quite low for organic TFTs and is notably smaller than that measured in organic TFTs utilizing pentacene contacted by carbon nanotubes [273], and it is within an order of magnitude of the injection-barrier height reported for two-dimensional semiconductors contacted with graphene electrodes [274]. This low energetic barrier for charge

injection may provide at least a hint of the explanation for why the contact resistance that was measured in the DPh-DNTT TFTs is so much smaller compared to the vast majority of organic TFTs reported in the literature [12], [141]. In the second regime at temperatures below ~ 280 K, the charge injection loses much of the temperature dependence. This most likely denotes a change from thermionic emission to another dominant injection mechanism with reduced temperature dependence. Notably, this transition appears to occur in close accordance with the temperature at which $R_{C,0}W$ decreases to very low values ($T \sim 300$ K, $1/k_B T = 0.039$ meV $^{-1}$) and at which the point-wise total resistance (R) calculated from the output curves at low V_{DS} no longer shows a significant dependence on V_{DS} (Figure 5.13c). Since the dependence of R on V_{DS} in this low-temperature region is more substantial, the assumption required for equation (79) to be valid, namely that $V_{DS} = -0.1$ V is sufficiently small to be negligible, is perhaps no longer valid at such low temperatures. In addition, the TLM analysis may also underestimate R_C in this regime due to the V_{DS} dependence.

In general, tunneling injection or diffusion-limited transport may be more prominent in this temperature range. Pure tunneling is normally characterized by a complete lack of temperature dependence in the classical formulations [166], [176], [181], so some degree of thermally-activated transport must still be present even at low temperatures. Referring back to the notable dependence of the threshold voltage V_{th} on the temperature, it is also possible that trap states in the semiconductor close to the contact interface may play an additional role in the temperature dependence of the injection current and of both R_C and $R_{C,0}$. This could imply that $R_{C,0}$ is strongly trap-limited, with the most impactful factors being the semiconductor morphology (grain boundaries) and the presence of trapped water in the organic-semiconductor layer [270]. At temperatures above ~ 280 K, when the interface traps are mostly filled (or removed) and thus $R_{C,0}$ is effectively eliminated, charge injection is by thermionic emission, since the trap states no longer act as scattering centers for the injected charges.

Finally, it cannot be fully disregarded that the charge transport through the PFBT monolayer that separates the gold contacts from the organic-semiconductor layer may contribute some temperature-dependent charge-transport properties. Previous studies have examined the effect of the temperature on charge transport through alkyl-thiol chemisorbed molecular monolayers (CMLs) on metal contacts in molecular junctions [275]. However, more extensive studies on the temperature dependence of the properties of organic TFTs using PFBT or other thiols in

CMLs are needed, especially in the context of organic TFTs with low contact resistances and high-mobility organic semiconductors as shown here.

5.2.3 Extension to transistors with small channel lengths

A great benefit of stencil lithography using silicon stencil masks is that it enables the fabrication of organic TFTs and circuits with small critical dimensions (channel lengths and contact overlaps $\sim 1 \mu\text{m}$ or smaller) with a high degree of reproducibility [244]. Often when the channel length is reduced to this extent, short-channel effects, such as drain-induced barrier lowering (DIBL) and an increased off-state drain current, can become more prominent [167]. Additional short-channel DPh-DNTT TFTs on PEN substrates to investigate whether or not

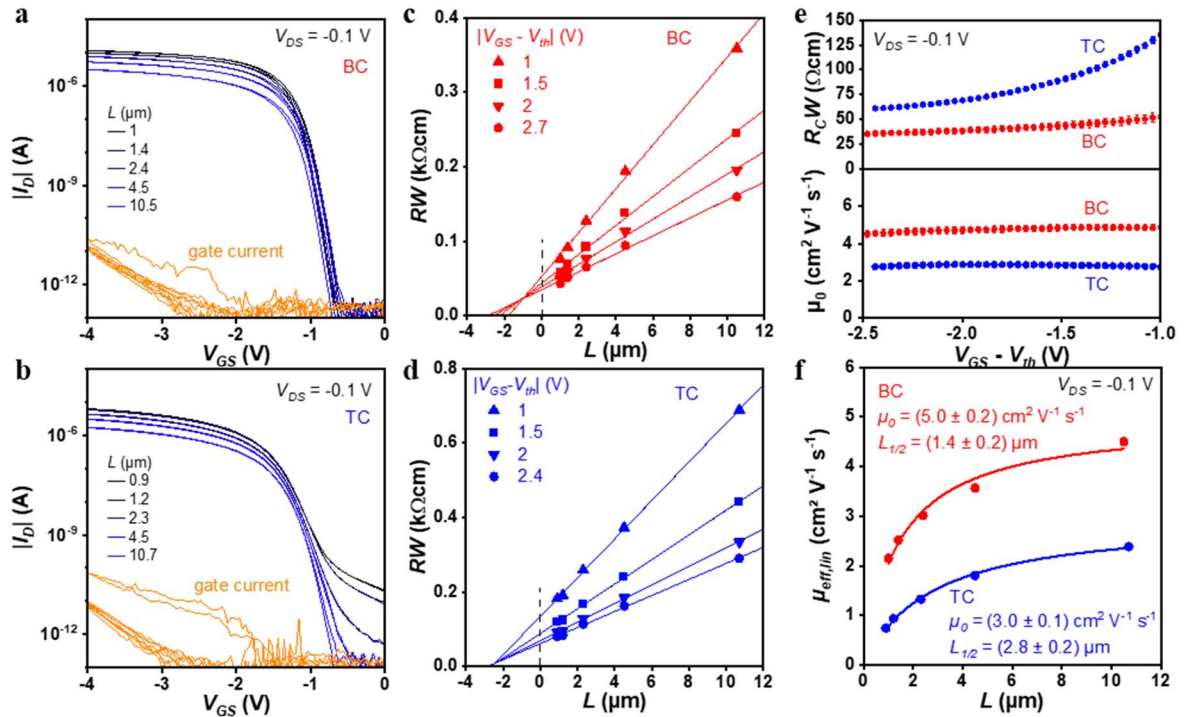


Figure 5.16 TLM analysis of organic thin-film transistors on a flexible PEN substrate with small channel lengths.

All TFTs have a total gate-to-contact overlap ($L_{ov,total}$) of $10 \mu\text{m}$ and channel width (W) of $50 \mu\text{m}$. a,b) Transfer characteristics for $V_{DS} = -0.1 \text{ V}$ of bottom-contact (BC) and top-contact (TC) TFTs, respectively. c,d) Width-normalized total resistance (RW) plotted as a function of channel length (L) at various gate overdrive voltages ($V_{GS} - V_{th}$) corresponding to the transfer curves in (a,b), respectively. e) Results from the fits shown in (c,d) for the width-normalized contact resistance ($R_C W$) and intrinsic channel mobility (μ_0). f) Effective carrier mobility ($\mu_{eff,lin}$) plotted as a function of the channel length. The data are fit to the equation $\mu_{eff,lin} = \mu_0 (1 + L_{1/2}/L)^{-1}$, where μ_0 is the intrinsic channel mobility and $L_{1/2}$ is the channel length at which $\mu_{eff,lin} = 1/2 \mu_0$. Results published in [141].

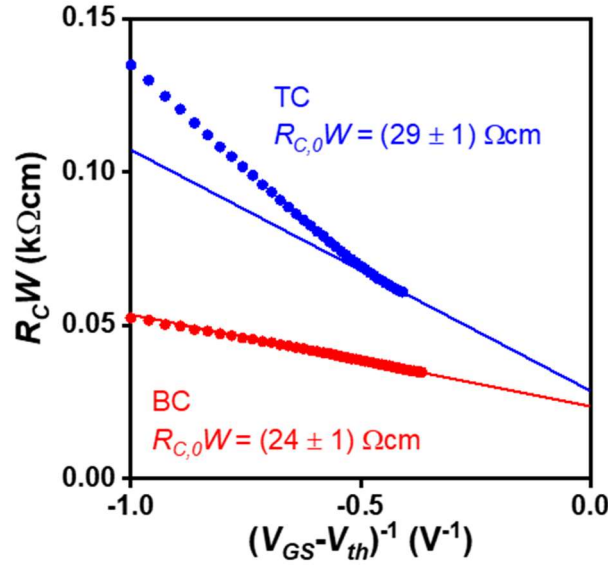


Figure 5.17 Estimation of the interface resistance for TFTs with small channel lengths.

Channel-width-normalized contact resistance ($R_C W$) as a function of the inverse of the gate overdrive voltage ($V_{GS} - V_{th}$). From this representation, the y-intercept can be interpreted as a gate-voltage-independent interface resistance ($R_{C,0} W$), with the slope accounting for the gate-voltage dependence of the contact resistance. Results published in [141].

the flexible TC and BC TFTs show any of these effects for smaller channel lengths. These TFTs have a channel length ranging from 0.9 μm to 10.7 μm (measurements of the channel length using SEM shown in the Appendix), a channel width of 50 μm , and a total gate-to-contact overlap of 10 μm . For the BC TFTs, regardless of the channel length, all TFTs have an on/off current ratio of at least 10^7 (Figure 5.16a) and all TFTs show $\mu_{eff,lin} > 2 \text{ cm}^2 \text{ V}^{-1} \text{ s}^{-1}$ (Figure 5.16f). The TC TFTs on the other hand show a notable increase in the off-state drain current as the channel length is reduced and a lower μ_0 . The TLM analysis again shows a lower $R_C W$ of 35 Ωcm at a gate overdrive voltage of -2.5 V for the BC TFTs compared to the 61 Ωcm at a gate overdrive voltage of -2.4 V for the TC TFTs (Figure 5.16e), in fair agreement with the above-reported results for TFTs with larger channel lengths. The μ_0 varies little from $V_{GS} - V_{th} = -1 \text{ V}$ to -2.5 V for both sets of TFTs, though the overall magnitude of μ_0 in the BC TFTs ($5.0 \text{ cm}^2 \text{ V}^{-1} \text{ s}^{-1}$) is larger than in the TC TFTs ($3.0 \text{ cm}^2 \text{ V}^{-1} \text{ s}^{-1}$). This may partially explain the more noticeable gate dependence of $R_C W$ in the TC TFTs than was observed in the study presented in Section 5.1.2, as the access resistance through the bulk semiconductor film under the source and drain contacts is likely also larger for these TFTs [81]. The transfer length (L_T)

extracted from the TLM analysis of the TC TFTs is nearly constant at 1.4 μm , indicating that the charge-carrier injection is not limited by the gate-to-contact overlap of 5 μm [167]. The contact resistance is again evaluated as a series connection of a gate-voltage-dependent component and minimum contact resistance ($R_{C,0}$) for the TFTs, as was done in Section 5.1.2 (Figure 5.17). From this analysis, it is found that $R_{C,0}$ is similar for both TC and BC TFTs, with a notably more pronounced dependence of the contact resistance on the gate overdrive voltage for the TC TFTs at smaller gate overdrive voltages. This is again possibly a consequence of the lower intrinsic channel mobility as compared to the long-channel length BC TFTs and TC TFTs evaluated previously.

5.2.4 Low-voltage circuit performance characteristics

To demonstrate the benefit of a small contact resistance for the dynamic TFT performance, 11-stage unipolar ring oscillators were fabricated on the same PEN substrates as the TFTs discussed above (Figure 5.10). All TFTs in the ring oscillators have a channel length of 1 μm and a total gate-to-contact overlap of 10 μm . A photograph of a ring oscillator based on BC TFTs is shown in Figure 5.18a. For this channel length and total gate-to-contact overlap, the effective carrier mobilities are 1.3 $\text{cm}^2 \text{V}^{-1} \text{s}^{-1}$ for the TC TFTs and 1.7 $\text{cm}^2 \text{V}^{-1} \text{s}^{-1}$ for the BC TFTs, determined from the transfer characteristics of TFTs with the same dimensions (not shown). The ring oscillators utilize the biased-load inverter design (Figure 5.18b). In this design, the load transistor is always on by applying a bias voltage (V_{bias}), allowing for more rapid discharging of the load transistor and higher dynamic performance than other inverter designs at the expense of greater static power consumption and lower gain [139].

The signal propagation delay (τ) is calculated from the oscillation frequency (f_{osc}) and the number of stages (n) by $\tau = 1/(2nf_{osc})$ [244]. At a supply voltage (V_{DD}) of 3.7 V, the measured signal propagation delay is 178 ns per stage for the ring oscillator based on the TC TFTs and 138 ns per stage for the ring oscillator based on the BC TFTs, corresponding to equivalent frequencies (f_{eq}) of 2.8 MHz and 3.6 MHz, respectively (Figure 5.18d). Noting that typically $f_{eq}/f_T = 0.5$ [15], these correspond to f_T of 5.6 MHz for the TC TFTs and 7.2 MHz for the BC TFTs. With the exception of a later result presented in Section 5.3.3, these signal delays are to the author's knowledge the shortest delays reported to date for organic ring oscillators on flexible substrates [276] and are the shortest delays for organic ring oscillators on any substrate at a supply voltage of less than 50 V [277]. Moreover, when normalized to the supply voltage

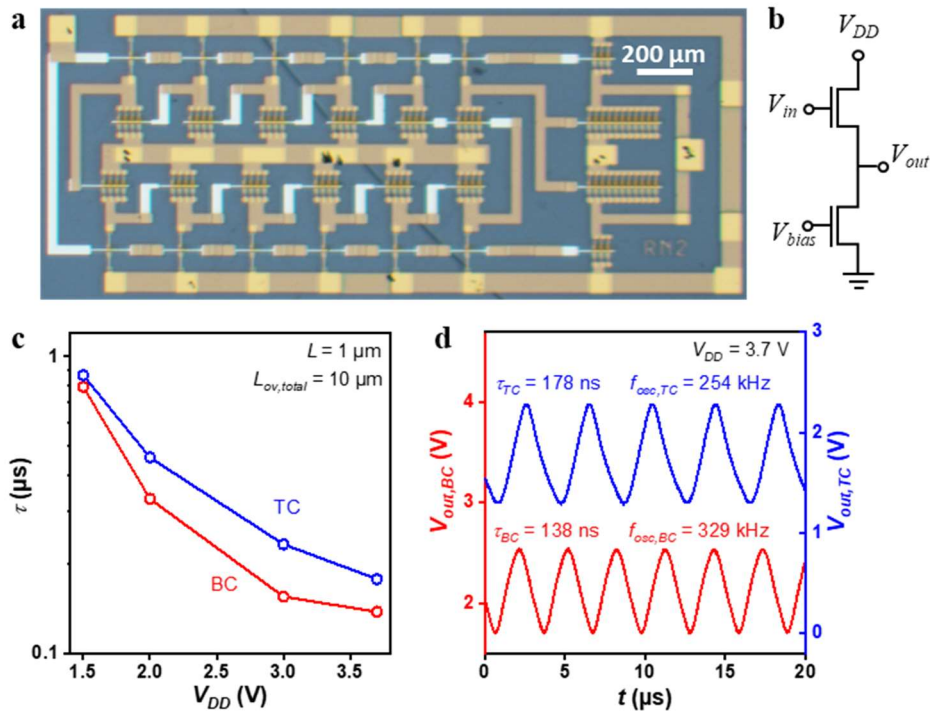


Figure 5.18 Dynamic performance of unipolar ring oscillators on flexible substrates.

a) Photograph of an 11-stage unipolar ring oscillator based on bottom-contact DPh-DNTT TFTs with a channel length (L) of $1 \mu\text{m}$ and a total gate-to-contact overlap ($L_{ov,total}$) of $10 \mu\text{m}$. b) Circuit diagram of the biased-load inverters implemented for the ring oscillators. c) Signal-propagation delay per stage (τ) measured on ring oscillators based on top-contact (TC) and bottom-contact (BC) TFTs plotted as a function of the supply voltage (V_{DD}). d) Output voltage (V_{out}) measured at $V_{DD} = 3.7 \text{ V}$, showing stage delays of 178 ns for the ring oscillator based on TC TFTs and 138 ns for the ring oscillator based on BC TFTs. Depending on V_{DD} , the bias voltage (V_{bias}) is between -1 and -2.5 V . Results published in [238].

of 3.7 V , the BC TFTs show a supply-voltage-normalized transit frequency of 1.95 MHz V^{-1} , which is among the best metrics reported to date for organic transistors. The fact that the ring oscillator based on BC TFTs shows a lower signal delay than the comparable ring oscillator using TC TFTs provides compelling evidence that, from a raw dynamic-performance perspective, the BC TFTs are better-suited for high-frequency circuit applications. While the lower R_C of the BC TFTs certainly contributes to this observation, the differences in contributions linked to the parasitic capacitances from the gate-to-contact overlaps of the TFTs in the circuits must also be considered. As discussed in more detail in the following Section 5.2.7, BC TFTs may actually have a disadvantage from this perspective, since the capacitances from the gate-to-contact overlaps may be higher in BC TFTs than in comparable TC TFTs. In

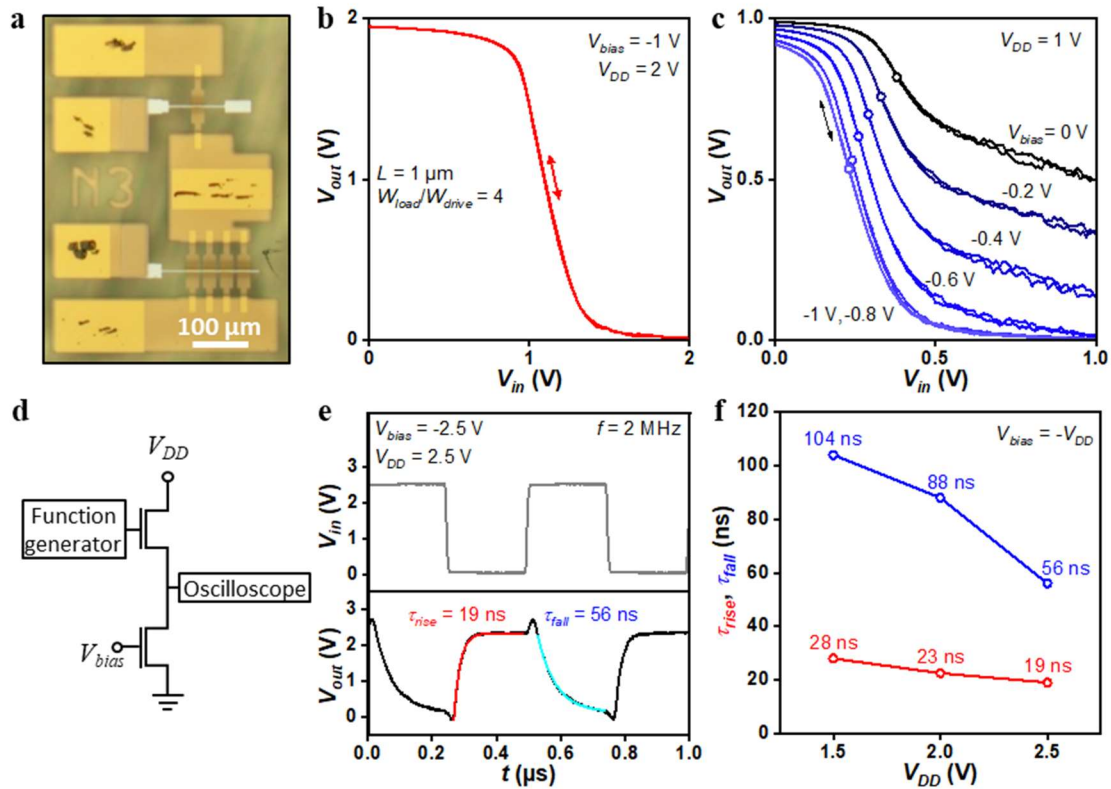


Figure 5.19 Static and dynamic inverter characteristics.

a) Photograph of an inverter based on two bottom-contact DPh-DNTT TFTs in a biased-load circuit design fabricated on a flexible PEN substrate. The TFTs have a channel length (L) of $1\ \mu\text{m}$ and a total gate-to-contact overlap ($L_{ov,total}$) of $4\ \mu\text{m}$. b) Static transfer characteristics of the inverter for a supply voltage (V_{DD}) of $2\ \text{V}$ and bias voltage (V_{bias}) of $-1\ \text{V}$. c) Static transfer characteristics of the same inverter for V_{bias} ranging from -1 to $0\ \text{V}$. The open circles indicate the trip voltage corresponding to the maximum gain in each transfer curve. d) Schematic diagram for the dynamic measurements of the inverter. e) Dynamic characteristics of the inverter in response to a square-wave input signal with a frequency (f) of $2\ \text{MHz}$, a duty cycle of 50% and an amplitude of $2.5\ \text{V}$. Characteristic rise and fall time constants of the switching delays (τ_{rise} , τ_{fall}) were determined by fitting simple exponential functions to the respective regions of the measured output waveform. f) Rise and fall time constants measured for supply voltages (V_{DD}) of 1.5 , 2.0 and $2.5\ \text{V}$. The amplitude of the square-wave input signal was identical to V_{DD} and $V_{bias} = -V_{DD}$ for each measurement. Results published in [141].

short, this is due to the intervening, low-capacitance semiconductor layer between the contact and the channel region in the TC TFTs, which is of course not present in the BC TFTs.

Advantage of the biased-load design for low-voltage flexible circuits

The biased-load inverter design provides a boost in the dynamic performance of unipolar circuits, at the expense of nominally greater static power consumption due to the addition rail

that is needed in the circuit. However, the ability to tune the transconductance of the load TFT also enables an optimization of the circuits to account for process variability and to balance power consumption with dynamic performance [134], [139]. To demonstrate this, a single biased-load inverter based on BC TFTs with $L = 1 \mu\text{m}$ and $L_{ov,total} = 4 \mu\text{m}$ was examined to obtain more information on the low-voltage performance characteristics of the flexible circuits (Figure 5.19). First, note that the V_{GS} of the load TFT can be kept above the threshold voltage at all times, facilitating more rapid discharging of the output node through the load TFT when the output node is switched from the high state (V_{out} near the supply voltage) to the low state (output voltage near 0 V, Figure 5.19b). As a result, the characteristic fall time and thus the total switching delay of biased-load circuits can be shorter than those of unipolar circuits without such an additional power supply. Second, the biased-load design creates the possibility to tune the trip voltage (i.e., the input voltage at which the transition at the output occurs) independent of the supply voltage (V_{DD}). A series of transfer curves of the inverter is shown in Figure 5.19b,c to illustrate this. In Figure 5.19b the transfer curve is measured for $V_{DD} = 2 \text{ V}$ and $V_{bias} = -1 \text{ V}$, i.e., with the load TFT biased slightly above the threshold voltage that is typically observed for the BC TFTs (see for instance the transfer curves in Figure 5.16a). Figure 5.19c shows transfer curves of the same inverter measured for $V_{DD} = 1 \text{ V}$ and at V_{bias} ranging from -1 to 0 V, illustrating that the trip voltage (indicated by open circles) can be tuned over a range of approximately 15% of V_{DD} .

The dynamic performance of the inverter was then evaluated by applying a square-wave signal (V_{in}) from a function generator with a frequency (f) of 2 MHz and an amplitude of 1.5 V, 2.0 V or 2.5 V to the input of the inverter (Figure 5.19d). For each measurement, the supply and bias voltages were adjusted so that $V_{DD} = -V_{bias}$ and with amplitude equivalent to the input signal. The characteristic rise and fall time constants (τ_{rise} , τ_{fall}) of the switching events were determined by fitting simple exponential functions to the measured output-voltage transitions in the corresponding regions. The smallest time constants (19 ns rise and 56 ns fall) were observed for $V_{DD} = 2.5 \text{ V}$ (Figure 5.19e) and they generally decrease with higher V_{DD} .

5.2.5 Two-port network analysis

While the dynamic performance of a ring oscillator or inverter provides a measure of the average switching frequency of the TFTs employed in the circuit, more detailed information about the dynamic properties of individual TFTs can be provided by two-port network analysis

[133]. In particular, scattering-parameter (S -parameter) measurements are attractive for their capability of unambiguously assessing the frequency-dependent characteristics of organic TFTs, even at high frequencies [135], [247]. These measurements can, e. g., provide access to the various contributions to the total gate capacitance (C_G) by converting the S -parameters to admittance (Y) parameters [138] and enable measurement of the unity-current-gain cutoff (or transit) frequency (f_T) of individual TFTs [135]. Using this method, detailed dynamic characterization of TC and BC TFTs (Figure 5.20a,b) with a range of channel lengths fabricated using a silicon stencil mask set designed and implemented previously by Tarek Zaki [170] was utilized. The TFTs here all have a moderate total gate-to-contact overlap ($L_{ov,total}$) of 10 μm . To promote mask stability for the smaller channel lengths, a ‘finger’ structure is implemented in which the total channel width (W) is defined by four sets of source and drain contacts with individual channel widths of 25 μm . The gap between each ‘finger’ is 20 μm . The channel lengths and overlaps of all TFTs were confirmed using SEM micrographs taken after all electrical characterization was completed (see Appendix). Generally, two different aspects were investigated in both TC and BC TFTs:

1. Channel-length dependence using TFTs in which only the channel length was varied, with L ranging from 0.7 to 10.5 μm and $L_{ov,GS} \sim L_{ov,DS}$.
2. Gate-to-contact overlap symmetry dependence using a layout in which the nominal L remained constant for all TFTs (actual L varied between ~ 0.6 and 0.7 μm), but the relative position of the channel region on the gate electrode of successive TFTs was offset by 1 μm . In this way, the gate-to-contact overlaps could be varied in order to study the relative contributions to the overall parasitic capacitance attributed to the gate-to-drain lap ($L_{ov,GD}$) and gate-to-source overlap ($L_{ov,GS}$), and how these contributions may be compared in TC and BC TFTs.

The S -parameters were measured at $V_{GS} = V_{DS} = -3$ V over a measurement frequency (f) range of 0.3 to 200 MHz. The extracted S -parameters were converted to the admittance (Y) parameters and the hybrid parameter corresponding to the gain (h_{21}) using the methods described in Section 2.4.2 (circuit diagram in Figure 5.20b). The gate-drain capacitances (C_{GD}) were evaluated from the Y parameters of the BC TFTs to check whether or not the gate dielectric maintains its insulating properties at high frequencies. This can be done by noting that under saturation conditions, $|Y_{21}| = 2\pi f C_{GD}$ according to the Meyer model (Figure 5.20c,d)

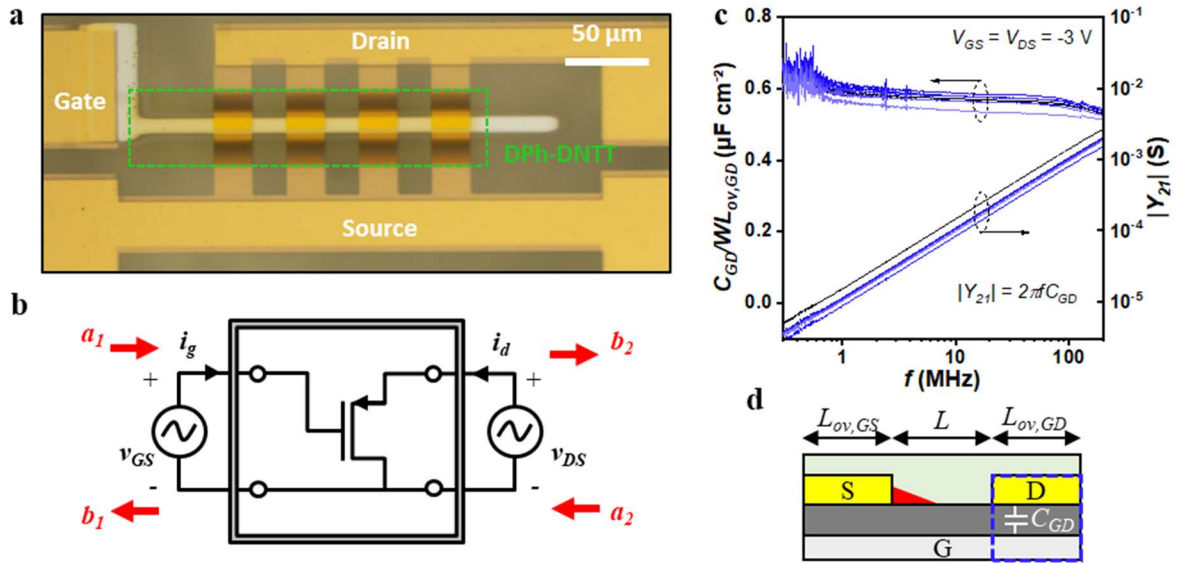


Figure 5.20 Two-port network analysis of flexible organic transistors.

a) Photograph of an organic TFT designed for two-port network analysis fabricated on a PEN substrate. All TFTs used in these analyses have a total gate-to-contact overlap ($L_{ov,total}$) of $10\ \mu\text{m}$ and a nominal channel width (W) of $100\ \mu\text{m}$. b) Circuit diagram of a two-port network with a TFT as the device under test. c) Drain component of the total gate capacitance (C_{GD}) normalized by the gate-to-drain overlap area ($WL_{ov,GD}$) and plotted as a function of the measurement frequency (f) for several bottom-contact TFTs in the two-port network analyses with $V_{GS} = V_{DS} = -3\ \text{V}$. C_{GD} was calculated from the measured admittance parameters, noting that $|Y_{21}| = 2\pi f C_{GD}$. d) Schematic of a bottom-contact TFT operated in the saturation regime, highlighting that C_{GD} is equivalent to the parasitic overlap capacitance only, due to the pinched-off channel (red triangle). Results published in [141].

[133], [278]. In all of the measured TFTs, the area-normalized gate-drain capacitance was found to be relatively invariant with the measurement frequency (with a decrease of $< 20\%$ up to the maximum measurement frequency of $200\ \text{MHz}$). This area-normalized capacitance closely corresponds to the value expected for the unit-area gate-dielectric capacitance (C_{diel}) of 0.6 to $0.7\ \mu\text{F cm}^{-2}$ [278] and is a good indication that the hybrid gate dielectric is stable during these measurements. Measurements of the static transfer characteristics were also performed on the TFTs to extract the transconductance (g_m) which could then be used for comparative analyses to the S -parameter measurements. Finally, it is noted that a comparison of these results can be made to the TLM results presented for small-channel length TFTs in Section 5.2.3, since these were fabricated on the same substrates as the TFTs used for the S -parameter measurements.

5.2.6 Influence of the channel length on dynamic performance

The channel length (L) is the most impactful fabrication parameter for improving the dynamic performance of a TFT technology. Table 5.1 summarizes for each TFT included in the analysis the measurements of L , the peak width-normalized transconductance (g_m), and f_T . Figure 5.21 shows the static characteristics of the TC and BC TFTs with different channel lengths. The drain current and g_m are generally higher for the BC TFTs. The off-state drain current remains very low for the BC TFTs even for very small channel lengths, whereas there is a systematic increase in the off-state drain current for the TC TFTs as the channel length is reduced. However, the output curves show a less-ideal super-linear curvature at low V_{DS} in the BC TFTs which is more extreme with smaller channel lengths. This is indicative of non-Ohmic contacts in which V_{DS} increases the charge injection by providing an additional reduction of the injection barrier at the source contact of the BC TFTs.

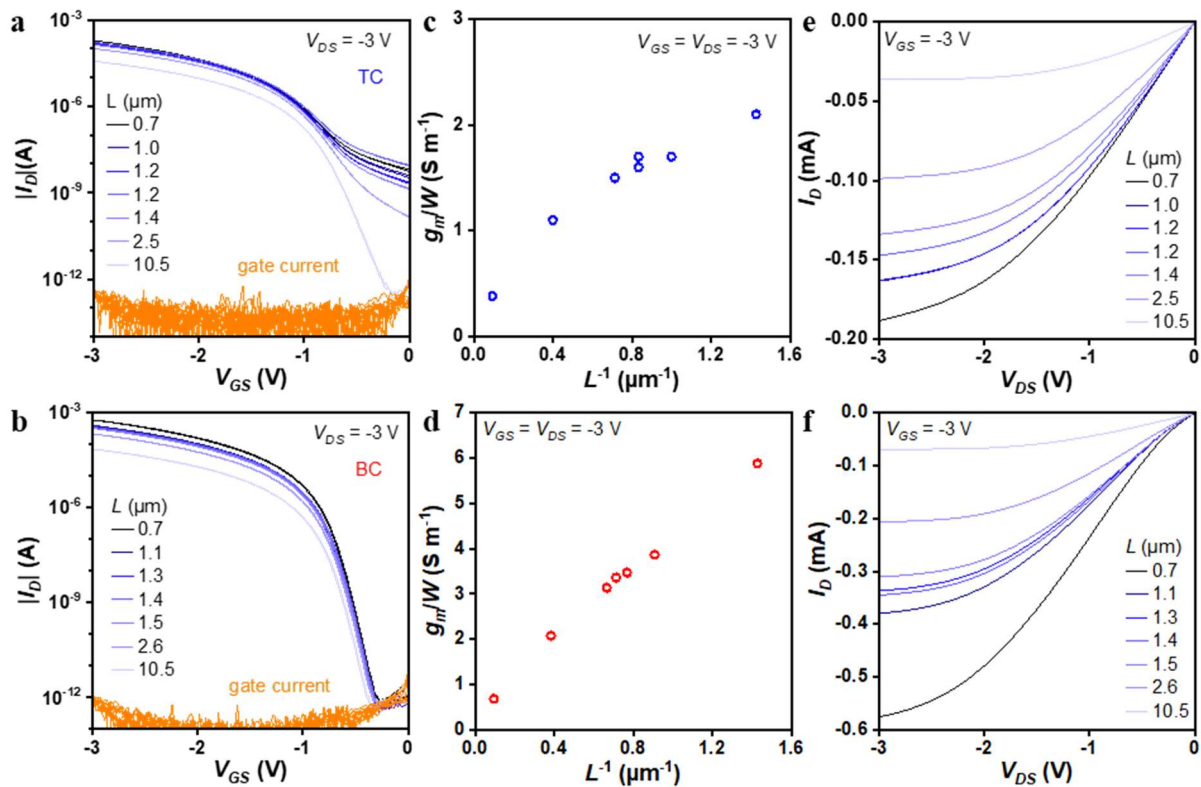


Figure 5.21 Static characteristics of transistors for two-port network analysis with different channel lengths.

a,b) Transfer curves of (a) top-contact (TC) and (b) bottom-contact (BC) TFTs designed for two-port network analysis with different channel lengths (L) fabricated on PEN substrates. c,d) Width-normalized transconductance (g_m/W) evaluated at $V_{GS} = V_{DS} = -3$ V. e,f) Output characteristics measured for $V_{GS} = -3$ V. Results published in [141].

Table 5.1: Width-normalized transconductance and transit frequency of DPh-DNTT TFTs as a function of device geometry and channel length.

Device architecture	L (μm)	g_m/W (S m^{-1})	f_T (MHz)
TC	0.7	2.1	7.4
	1.2	1.7	6
	1	1.7	6
	1.2	1.6	5.2
	1.4	1.5	4.3
	2.5	1.1	2.5
	10.5	0.38	0.3
BC	0.7	5.9	17.8
	1.4	3.9	11.1
	1.1	3.5	12.3
	1.3	3.4	11.1
	1.5	3.1	9.4
	2.6	2.1	5.3
	10.5	0.68	0.7

The results from the S -parameter measurements of the gain ($|h_{21}|$) and the individual component of the gate capacitance (C_{GS} , C_{GD}) are shown in Figure 5.22. In accordance with the expected scaling behavior, the results show that a higher $|h_{21}|$ is achieved for smaller channel lengths in both TFT architectures, resulting in a shift of f_T to higher frequencies for shorter channel lengths. For measurement frequencies between 1 and 20 MHz, $|h_{21}|$ decreases with a slope of between -16 and -20 dB/decade and saturates at a value between -6 and -10 dB at high frequency. Ideally, the slope should be precisely -20 dB/decade at low frequency where $|i_d|/|i_g| > 1$. The slight deviation from this ideality is possibly related to the small window of measurement ($f < 0.3$ MHz was not possible with the vector network analyzer which was used) and/or due to the TFT structure which was implemented here. Namely, the finger structure of the TFTs (see photograph in Figure 5.20a) results in the presence of an organic-semiconductor layer which extends beyond the nominal channel region that can provide additional ‘fringing’ effects whose contributions depend on the measurement frequency (see the following section for more about this aspect) [170]. For all of the BC TFTs, f_T falls clearly within the measurement frequency range and could simply be extracted from the point on each curve where $|h_{21}| = 0$ dB. For all but the longest channel length (10.5 μm) in the TC TFTs, f_T was similarly extracted. For the longest channel length, $f_T = 0.3$ MHz was instead estimated from the data still within the measurement range. The width-normalized contact resistance ($R_C W$)

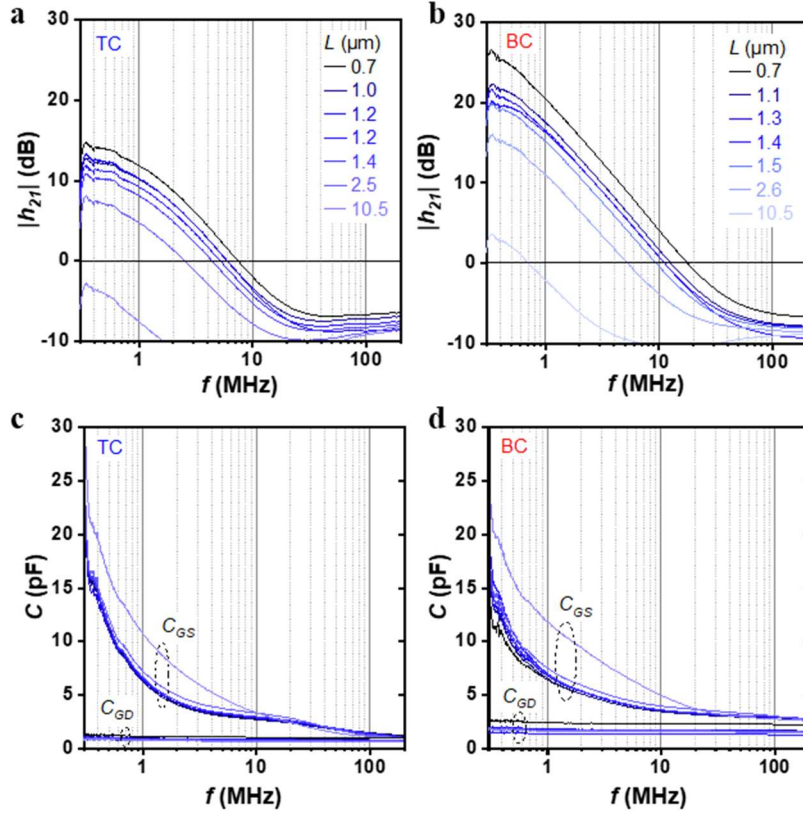


Figure 5.22 Gain and capacitance of organic thin-film transistors with different channel lengths.

a,b) Small-signal current gain $|h_{21}|$ for (a) top-contact (TC) and (b) bottom-contact (BC) TFTs with different channel lengths (L) fabricated on PEN substrates. c,d) Gate-source capacitance (C_{GS}) and gate-drain capacitance (C_{GD}) for (c) TC and (d) BC TFTs. All results evaluated at $V_{GS} = V_{DS} = -3$ V. Results published in [141].

and the intrinsic channel mobility (μ_0) can now be extracted from the dependence of f_T on the channel length

$$f_T = \frac{\mu_0(V_{GS} - V_{th})}{2\pi \left(L + \frac{1}{2}\mu_0 C_{diel} R_C W (V_{GS} - V_{th}) \right) \left(L_{ov,GS} + \beta L_{ov,GD} + \frac{2}{3}L \right)} \quad (80)$$

Where the gate-drain capacitance prefactor (β) is determined by the additional capacitance from the semiconductor layer between the contact and dielectric interface in the staggered architecture (C_{osc}) by

$$\beta = \left(1 + \frac{C_{diel}}{C_{osc}} \right)^{-1} \quad (81)$$

For each set of TFTs, the unit-area gate-dielectric capacitance (C_{diel}) is nominally identical for all TFTs ($\sim 0.6 \mu\text{F cm}^{-2}$ as determined from the measurements of C_{GD} of the BC TFTs). The

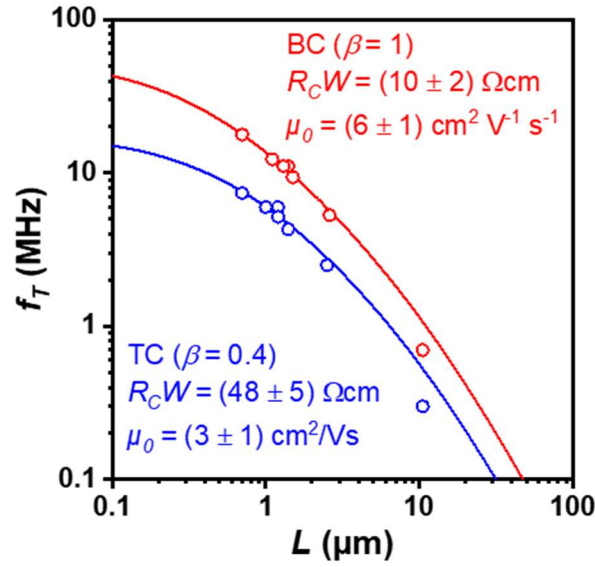


Figure 5.23 Contact-resistance extraction from the channel-length dependence of the transit frequency.

Experimental data and fits of the transit frequency (f_T) plotted as a function of the channel length (L) in top-contact (TC, blue) and bottom-contact (BC, red) TFTs. Results published in [141].

measurements of C_{GD} for the TC TFTs are well-described by $\beta = 0.4$ ($C_{osc} = 0.4 \mu\text{F cm}^{-2}$). The contact resistance and the intrinsic channel mobility can then be extracted by fitting equation (80) to the empirical dependence of the measured transit frequency and the channel length, considering R_CW and μ_0 as free parameters. Figure 5.23 shows that an excellent fit to the experimental data is achieved with $R_CW = (10 \pm 2) \Omega\text{cm}$ and $\mu_0 = (6 \pm 1) \text{cm}^2 \text{V}^{-1} \text{s}^{-1}$ for the BC TFTs and $R_CW = (48 \pm 5) \Omega\text{cm}$ and $\mu_0 = (3 \pm 1) \text{cm}^2 \text{V}^{-1} \text{s}^{-1}$ for the TC TFTs. For both TC and BC TFTs, there is a notable discrepancy between the contact resistance determined using the TLM and the transit frequency method (see Figure 5.16). This discrepancy is likely due to the fact that the lateral electric fields applied in the S -parameter measurements are significantly larger than the fields applied during TLM due to the increased V_{DS} . This effect could generally be caused by various non-idealities of the metal-organic semiconductor interface, such as diffusion-limited charge-carrier injection and image-force barrier lowering [140], [181]. Given that it was shown through temperature-dependent measurements in Section 5.2.2 that the injection is dominated by thermionic emission with a very low estimated Schottky barrier height, it is not surprising that there would be a significant lowering of the injection barrier with modest increase of V_{DS} . Finally, it is noted that the contact resistance is again found to be

smaller in the BC TFTs than in the TC TFTs with a very thin gate dielectric, consistent with the findings throughout this chapter.

5.2.7 Influence of the gate-to-contact overlaps

The transfer curves measured with $V_{DS} = -3$ V of the TC and BC TFTs with a nominally identical channel lengths and varying gate-to-contact overlap asymmetries are shown in Figure 5.24. Similar to the previous section, all of the BC TFTs show low off-state drain current and steep subthreshold swing, whereas the TC TFTs have an increased off-state drain current and larger subthreshold swing. This is perhaps related to the appearance of Au-nanoclusters that appear in the channel region of TC TFTs due to shadowing effects during the fabrication of the source and drain contacts (Figure 5.25). The on-state drain currents and the transconductance (g_m) are also generally higher in the BC TFTs (Figure 5.24c), though there is slightly more

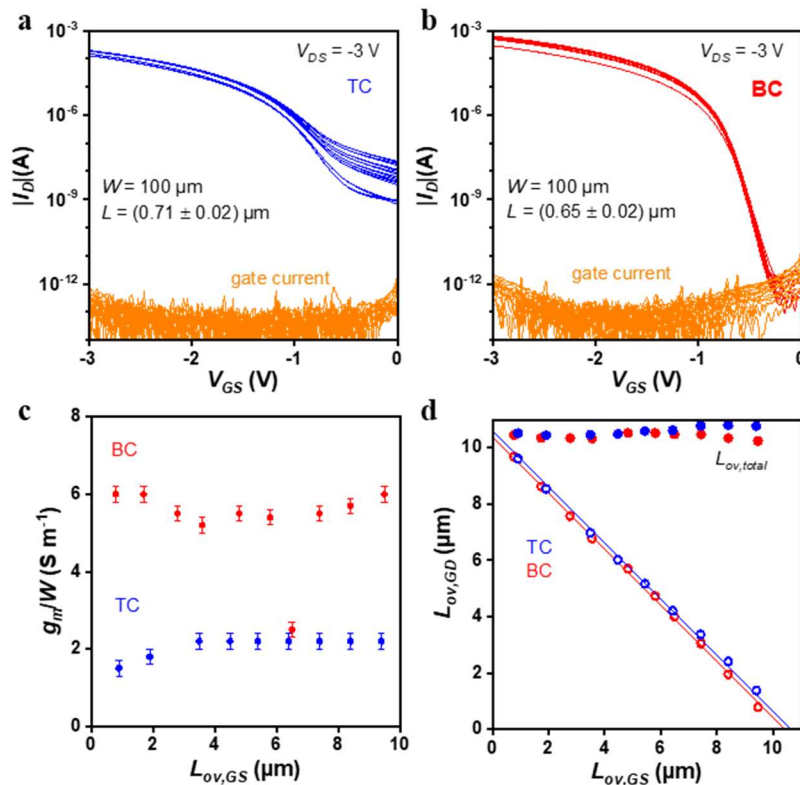


Figure 5.24 Static characteristics of transistors for two-port network analysis with asymmetric gate-to-contact overlaps.

a,b) Transfer curves of (a) top-contact (TC) and (b) bottom-contact (BC) TFTs designed for two-port network analysis with nominally constant channel length (L) and asymmetric gate-to-contact overlaps ($L_{ov,GS}$ and $L_{ov,GD}$) fabricated on PEN substrates. c) Width-normalized transconductance (g_m/W) evaluated at $V_{GS} = V_{DS} = -3$ V as a function of $L_{ov,GS}$. d) Measurements of $L_{ov,GS}$ and $L_{ov,GD}$ using SEM micrographs of the TFTs.

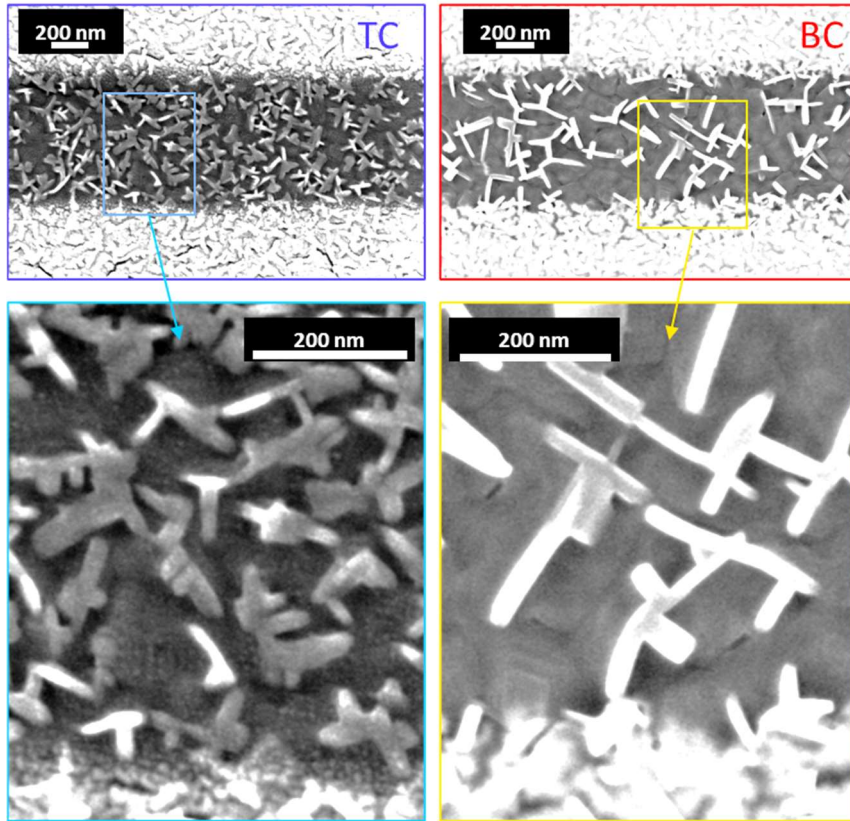


Figure 5.25 Au-nanocluster channel penetration due to shadowing effects in top-contact TFTs.

SEM micrographs of the channel region of short-channel top-contact (TC) and bottom-contact (BC) DPh-DNTT TFTs. The TC TFT shows Au-nanoclusters within the channel region that may be responsible for increased off-state drain current in the TC TFTs compared to BC TFTs, which generally do not show this phenomenon.

variability than in the TC TFTs. The lateral dimensions (L , $L_{ov,GS}$ and $L_{ov,GD}$) were measured using SEM images of the TFTs. A summary of these measurements is shown in Figure 5.24d. The dotted lines in the figure correspond to the expected value for $L_{ov,GD}$ with respect to the average total overlap and the measured $L_{ov,GS}$. These are included to highlight the fact that the dimensions of the TFTs are very well-defined and similar for both the TC and BC TFTs.

The small-signal current gain ($|h_{21}|$) is plotted against the measurement frequency in Figure 5.26. For TFTs with $L_{ov,GS} \geq L_{ov,DS}$, f_T is determined by the zero-gain crossover point of the $|h_{21}|$ vs. $\log(f)$ curve, while for $L_{ov,GS} < L_{ov,DS}$, f_T is determined by fitting the $|h_{21}|$ vs. $\log(f)$ data in the region of the curve where $|h_{21}|$ varies linearly with $\log(f)$ with a slope of approximately -20 dB/decade [135], [170], [247]. As expected, the saturation value of $|h_{21}|$ decreases systematically as approximately $|h_{21}| = L_{ov,GD}/L_{ov,total}$ in each successive TFT as the channel region is moved so that $L_{ov,GS}$ increases and $L_{ov,GD}$ decreases [134]. For asymmetric TFTs with

successively smaller $L_{ov,GS}$, the saturation $|h_{21}|$ approaches 0 dB and the point where $|h_{21}| = 0$ dB shifts to higher frequency. In these cases, f_T was estimated by fitting the linear portion of $|h_{21}|$ at low frequencies and extrapolating to 0 dB. In general, the BC TFTs show higher f_T than the TC TFTs, with an approximately linear dependence with respect to the channel offset (Figure 5.26c). A slope $df_T/dL_{ov,GS}$ of -0.5 MHz/ μm (excluding the outlier at $L_{ov,GS} = 6.5 \mu\text{m}$) was extracted for the BC TFTs from the linear fit shown in the figure. The TC TFTs show smaller f_T than the BC TFTs overall and have a steeper $df_T/dL_{ov,GS} = -1.1 \text{ MHz}/\mu\text{m}$. The highest f_T of 21 MHz was measured for the BC TFT with $L_{ov,GS} = 1.7 \mu\text{m}$. This result is particularly significant, since it represents the highest voltage-normalized transit frequency (7 MHz V^{-1}) measured in any organic transistor [81], [261], [279], [280], an improvement by more than a factor of three over the previous record for flexible organic TFTs [81]. The TFT also shows an effective mobility of $2.7 \text{ cm}^2/\text{Vs}$ (indicating that R_C is again very small), a peak transconductance of 6.4 S m^{-1} and a subthreshold swing of 66 mV dec^{-1} , all of which are records for organic TFTs with $L < 1 \mu\text{m}$.

To better identify the sources of the observed differences between BC and TC TFTs in the frequency scaling of $|h_{21}|$ and f_T , it is informative to examine the admittance (Y) parameters, which allows us to focus on the individual contributions to the total gate capacitance (C_G) in TFTs. Figure 5.26d,e shows the $|Y_{11}|$ parameter as a function of the frequency. This essentially provides a measure of C_G , since $|Y_{11}| = 2\pi f(C_{GS} + C_{GD})$. It be noticed immediately that the capacitance is smaller in the TC TFTs than in the BC TFTs from the slope of the $|Y_{11}|$ curves, and that there is a stronger dependence on the asymmetry of the gate-to-contact overlaps in the TC TFTs, especially at lower frequencies. Interestingly, this would imply that for the same degree of asymmetry and identical transconductance, the TC TFTs could actually still have a higher transit frequency than the BC TFTs. Further separation of the total gate capacitance into the individual source and drain components can be carried out using $|Y_{12}| = 2\pi f C_{GD}$. As done in the previous section, according to the Meyer model C_{GD} can be normalized by the gate-to-drain overlap area ($W \cdot L_{ov,GD}$) (Figure 5.26f). In the BC TFTs, for larger $L_{ov,GD}$ (smaller $L_{ov,GS}$) the normalized capacitance is higher and closer to the expected area-normalized capacitance for the gate dielectric (C_{diel}) of about $0.6 \mu\text{F cm}^{-2}$. A systematic decrease is apparent as $L_{ov,GD}$ ($L_{ov,GS}$) is decreased (increased). This might be attributed to a greater influence on the drain capacitance of the organic semiconductor around the drain contact or it may signify that the effective area is smaller than what is estimated simply by measuring the contacts in the SEM.

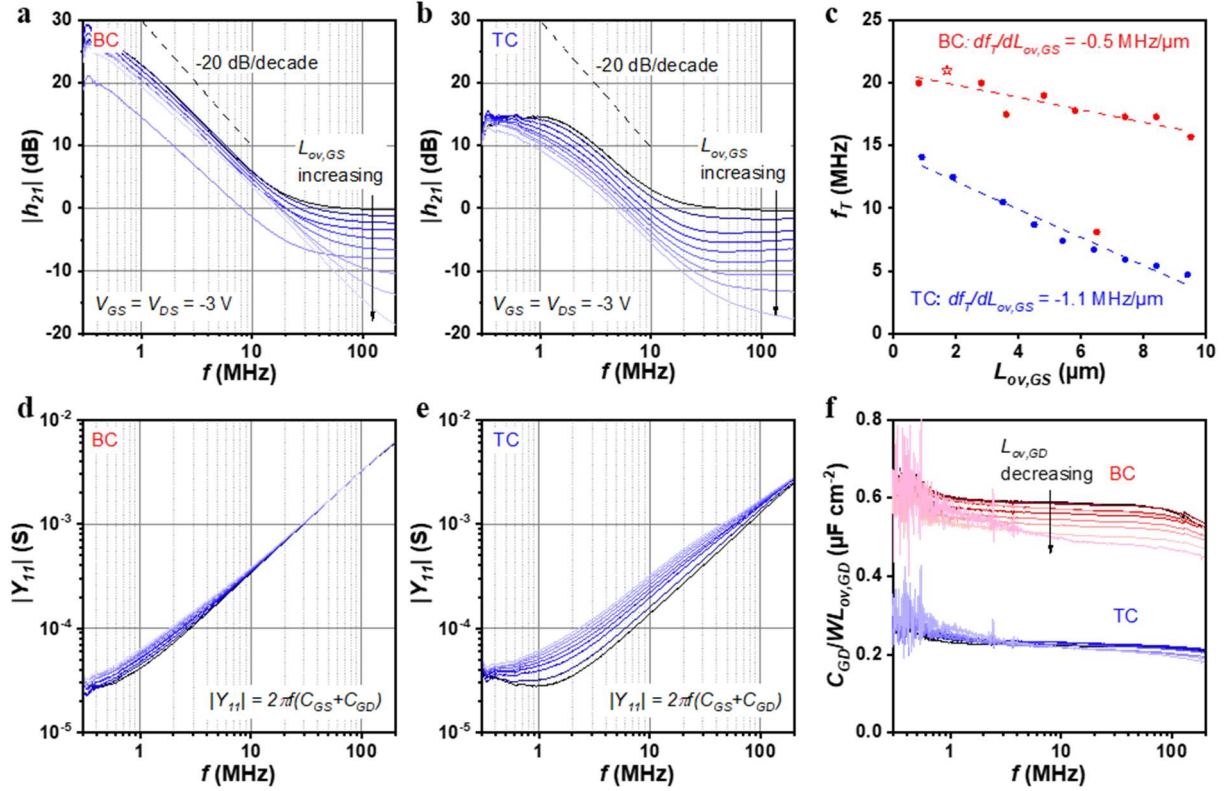


Figure 5.26 Gain, transit frequency and capacitance of organic thin-film transistors with asymmetric overlaps.

a,b) Small-signal current gain $|h_{21}|$ for (a) bottom-contact (BC) and (b) top-contact (TC) TFTs with different degrees of gate-to-contact overlaps (L_{ov}) asymmetry. c) Transit frequency (f_T) as a function of the gate-to-source overlap ($L_{ov,GS}$). d,e) Admittance parameter corresponding to the total gate capacitance ($C_{GS} + C_{GD}$) by $|Y_{11}| = 2\pi f(C_{GS} + C_{GD})$. f) Gate-drain capacitance (C_{GD}) normalized by the overlap area ($WL_{ov,GD}$) for TC and BC TFTs. All results evaluated at $V_{GS} = V_{DS} = -3$ V.

In the TC TFTs, the normalized C_{GD} is generally lower ($\sim 0.22 \mu\text{F cm}^{-2}$) and mostly independent with respect to the contact overlap asymmetry than in the BC TFTs. The lower capacitance in TC TFTs can be understood by taking into account that (a) in the saturation regime virtually all charge carriers are collected at the forward edge of the drain contact (i.e. the transfer length L_T is negligibly small [150]) and (b) the layer of DPh-DNTT under the drain contact introduces its own additional capacitance ($C_{GD,sc}$). Assuming that the bulk-resistance component of the semiconductor layer ($R_{C,sc}$) is very large, the analysis can then proceed by treating the drain side as an MIS capacitor with C_{GD} now described by

$$C_{GD} = \frac{C_{GD,sc} C_{diel} W L_{ov,GD}}{C_{GD,sc} + C_{diel} W L_{ov,GD}} \quad (82)$$

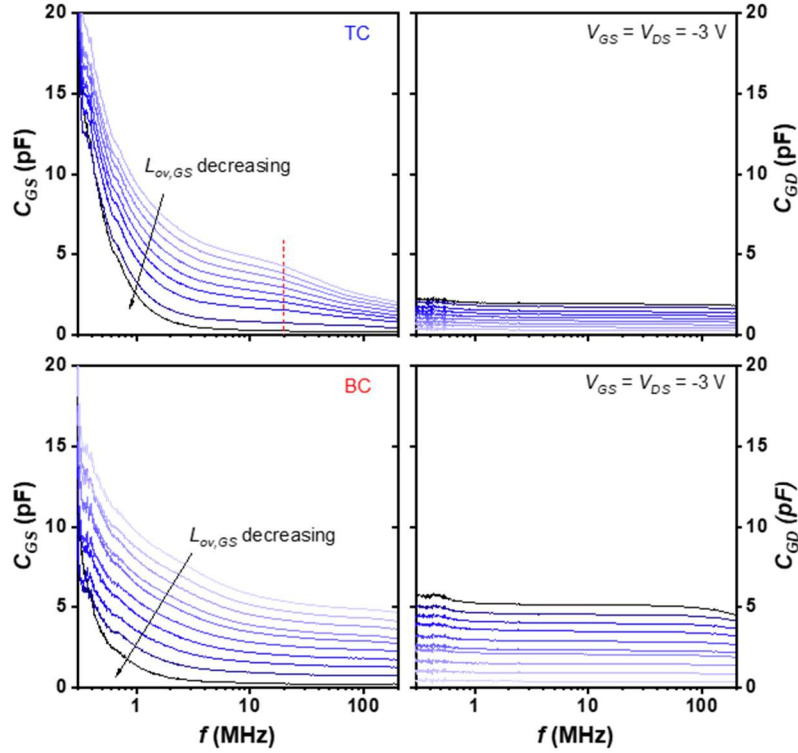


Figure 5.27 Capacitance contributions in organic thin-film transistors with asymmetric gate-to-contact overlaps.

Gate-source capacitance (C_{GS} , left) and gate-drain capacitance (C_{GD} , right) as a function of the measurement frequency (f) for top-contact (TC, top) and bottom-contact (BC, bottom) TFTs. The curves vary according to the asymmetry in the gate-to-contact overlaps (L_{ov}), such that a lower C_{GS} is measured for smaller gate-to-source overlap ($L_{ov,GS}$).

The dielectric constant of DPh-DNTT is not known precisely, but it is likely close to that determined for pentacene ($\epsilon_r = 3.6$) [281]. Assuming that $C_{diel} = 0.6 \mu\text{F cm}^{-2}$ and further assuming a thickness of 20 nm for the DPh-DNTT layer, an area-normalized $C_{GD} = 0.13 \mu\text{F cm}^{-2}$ is obtained. The underestimated C_{GD} in this case likely originates from the assumption that the real thickness of the DPh-DNTT layer in the TC TFTs is identical to the nominal value of 20 nm. Indeed, from the analysis of the thin-film morphology of DPh-DNTT shown in Section 5.2 it is known that a rough polycrystalline layer is formed in the implemented fabrication process (RMS roughness of 6.7 nm), and therefore the effective thickness may be significantly lower than the nominal thickness. If instead an effective thickness of 10 nm is used in the calculation using equation (82), the values measured for C_{GD} are obtained. Another possible explanation is an additional interface capacitance (C_I) as a result of traps created by defects. In particular, interface traps at the metal-semiconductor interface of the TFTs can

hinder the high-frequency response, since trapped carriers cannot respond to the small oscillating voltage due to the additional space-charge region that is formed [168]. The BC TFTs shown here, on the other hand, have a minimal contact area, and the interface with the organic semiconductor is much sharper, so that the density of trap states at this interface is likely reduced.

The source-side contribution to the gate capacitance (C_{GS}) can be extracted by subtracting $|Y_{12}|$ from $|Y_{11}|$ (Figure 5.27; the corresponding C_{GD} is also plotted at right for comparison). The evolution of C_{GS} with the measurement frequency is qualitatively similar for both device architectures. There is an initial steep drop in C_{GS} at lower frequencies which is related to the charge injection and the formation of a channel [282], [283]. The lower initial C_{GS} in the BC TFTs is possibly indicative of more efficient charge injection. Both device architectures show a systematic reduction in C_{GS} as $L_{ov,GS}$ is reduced, due to the reduced contribution of the smaller overlap area defined by $WL_{ov,GS}$. As the measurement frequency approaches the transit frequency of the TFTs, the C_{GS} curves generally saturate to the parasitic capacitance associated with the overlap. This can be plainly seen by noting that the C_{GS} at high frequency is generally of similar value as the C_{GD} measured in TFTs where gate-to-contact overlap lengths are switched (e.g. compare the lightest blue curve for C_{GS} corresponding to the largest $L_{ov,GS}$ to the black curve for C_{GD} corresponding to the largest $L_{ov,GD}$ in Figure 5.27). The precise evolution of C_{GS} is somewhat different between the two device architectures, with a notable change in the slope of the C_{GS} vs. f curves of the TC TFTs that is more significant with larger $L_{ov,GS}$. This may be explained by a reduction of the number of injected charge carriers that can reach the channel through the semiconductor bulk under the contacts as the frequency is increased, until finally resulting in zero carriers reaching the channel region [284]. In this high-frequency regime, the contact again behaves like an MIS capacitor as in the case of the drain side of the TFT. It is possible that a similar change in the capacitance is occurring in the BC TFTs as well, but this occurs at a lower frequency (visible in the light blue C_{GS} vs. f curve between 1 and 10 MHz). The explanation is possibly similar (fewer carriers reaching the channel), but in this case the effective area consists only of the semiconductor regions around the edges of the source contact and contributes a smaller additional capacitance.

5.3 Additional points of consideration and ongoing research

The results presented above give a detailed overlook of organic TFTs based on DPh-DNTT and show that the bottom-contact TFT architecture may be more suitable for high-frequency TFT applications from the viewpoint of the lower contact resistance, leading to a higher transit frequency that is achievable with a thin gate dielectric. However, there are of course some additional open questions of interest and other important aspects to consider for any potential application of a TFT technology. The following sections contain some brief discussions of additional topics and results of interest for the development of organic TFTs in general.

5.3.1 Bias-stress stability

Organic TFTs have long been known to suffer from instability related to bias stress [72 and references therein]. In particular, the threshold voltage (V_{th}) is often prone to shifts after prolonged application of the operating voltages, due to carriers being trapped in the semiconductor, in the gate dielectric, or at the semiconductor-dielectric interface. There has been some investigation into the influence of the TFT device architecture on the bias-stress stability of organic TFTs, with the general result that top-contact TFTs generally show greater stability than bottom-contact TFTs, ostensibly because of the poor morphology of the semiconductor film on the bottom contacts which provides a greater density of possible trapping sites. Figure 5.28 shows the results of bias-stress measurements performed on bottom-contact and top-contact TFTs based on DPh-DNTT. The TFTs were both fabricated on a single

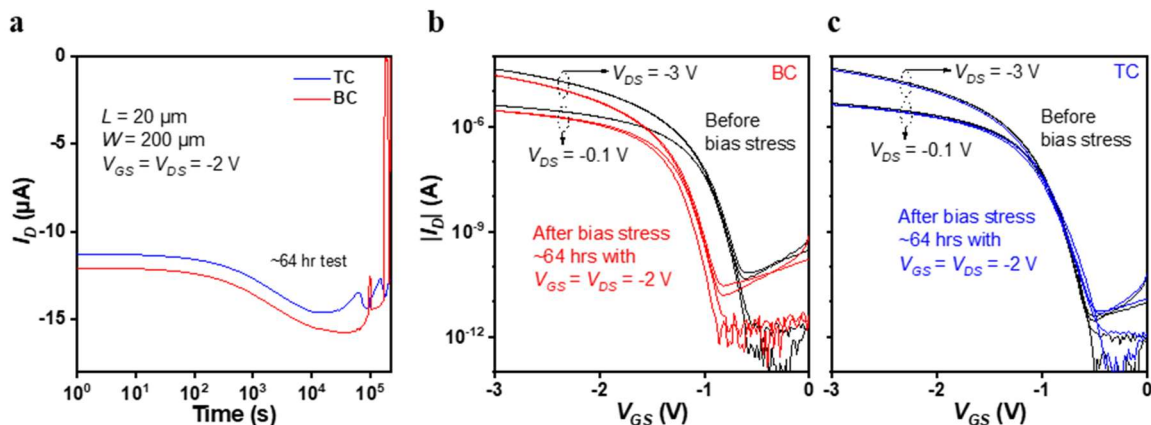


Figure 5.28 Bias-stress stability of bottom-contact and top-contact TFTs.

a) Bias-stress stability of DPh-DNTT TFTs with channel length (L) of $20 \mu\text{m}$ and channel width (W) of $200 \mu\text{m}$. The drain current was continuously measured with a constant bias stress of $V_{GS} = V_{DS} = -2 \text{ V}$. Transfer curves were taken before and after the stress test: (b) bottom-contact and (c) top-contact TFT. Results published in [238].

silicon substrate with a global-back-gate electrode. The gold bottom contacts were treated with PFBT, and the thin gate dielectric was formed similar to the flexible TFTs discussed above with plasma-formed aluminum oxide functionalized with a TDPA SAM. The TFTs were stressed continuously with $V_{GS} = V_{DS} = -2\text{V}$ for about 64 hours. Before and after the bias-stress test, the transfer curves were measured (Figure 5.28b,c). In accordance with expectation from the results in the literature, the top-contact TFTs showed greater stability, whereas the bottom-contact TFTs showed a pronounced shift of the threshold voltage by -0.3 V . The origin for this is unclear at present, since various intrinsic or extrinsic factors can be responsible. For more information, experiments using Kelvin force probe microscopy (KPFM) might be used to investigate the carrier trapping and release dynamics, preferably while also implementing controlled environments to test for possible extrinsic effects, such as oxygen or water ingress into the semiconductor film during bias stress [285]. It would also be beneficial to perform tests on TFTs having smaller channel lengths than the one implemented here ($L = 20\ \mu\text{m}$) as the bias-stress-induced threshold-voltage shifts have been shown to be more pronounced in TFTs with smaller channel lengths, due to smaller grain size of the semiconductor within the channel region.

5.3.2 Reproducibility of the bottom-contact transistors

Reproducibility is an important aspect for any prospective consumer products. To evaluate the reproducibility of short-channel bottom-contact TFTs, 10 DPh-DNTT TFTs were examined with a total gate-to-contact overlap length ($L_{ov,total}$) of $60\ \mu\text{m}$, $L = (1.6 \pm 0.1)\ \mu\text{m}$ and $W = (7.8 \pm 0.1)\ \mu\text{m}$ (Figure 5.29). The statistics for the measurements of the effective carrier mobility, threshold voltage, and subthreshold swing are shown in the figure. Note that in this case, the effective carrier mobility is likely overestimated, since the average W/L is small (4.9), the gate-to-contact overlaps are large, and the semiconductor is not patterned, leading to a significant contribution to the drain current from the fringe regions outside of the channel area defined by the metallurgical channel width [243]. For this reason, the transconductance (g_m) was determined purely by the current-voltage characteristics and was not normalized to the TFT dimensions. The most significant source of variability for the TFTs overall is the threshold voltage (V_{th}), though it is still less than 15%. An even higher degree of reproducibility was

additionally shown for the bottom-contact TFTs with sub-micron channel length in Section 5.2.7, showing that this fabrication approach is promising for larger circuit applications.

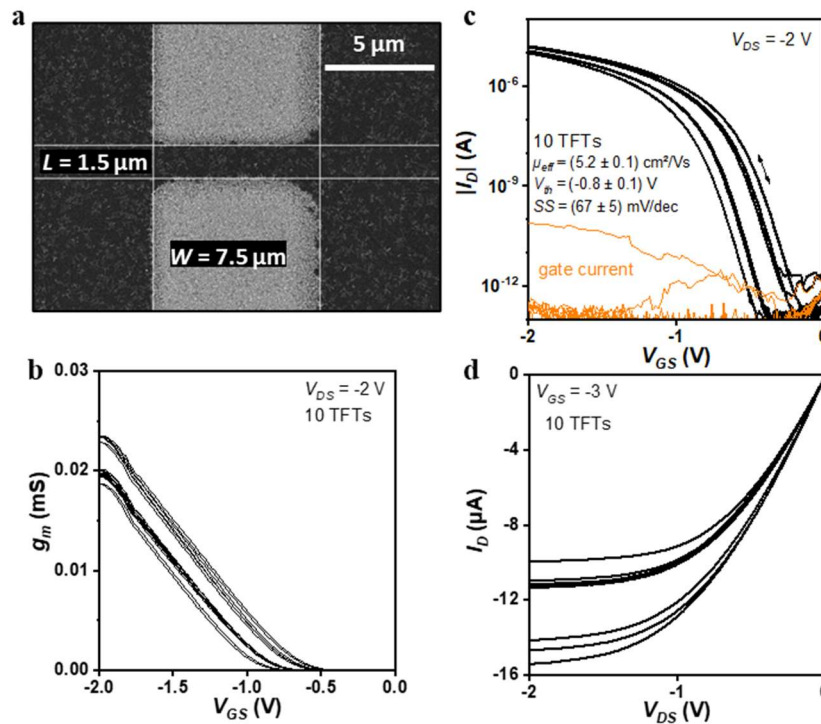


Figure 5.29 Reproducibility of small-channel bottom-contact DPh-DNTT TFTs.

a) SEM micrograph of an individual short-channel TFT with $L_{ov,total} = 60 \mu\text{m}$, $W = 7.5 \mu\text{m}$ (average $7.8 \mu\text{m}$), and $L = 1.5 \mu\text{m}$ (average $1.6 \mu\text{m}$). b) Transfer characteristics measured at $V_{DS} = -2 \text{ V}$. Inset: statistics for the effective carrier mobility (saturation, μ_{eff}), threshold voltage (V_{th}) and subthreshold swing (SS) c) Transconductance (g_m) calculated from the transfer curves in (b) plotted as a function of V_{GS} . d) Output curves measured with $V_{GS} = -2 \text{ V}$. Results published in [141].

5.3.3 Bottom-contact TFTs based on C₁₀-DNNT

In principle, the fabrication approach for flexible organic TFTs and circuits discussed in this section can be implemented using any vacuum-processable organic semiconductor. To demonstrate this, bottom-contact TFTs and circuits based on 2,9-didecyl-dinaphtho-[2,3-b:2,3-f]thieno[3,2-b]thiophene (C₁₀-DNNT) were also fabricated and characterized [85]. Alkylated heteroacenes with extended conjugated core molecules such as C₁₀-DNNT have been of

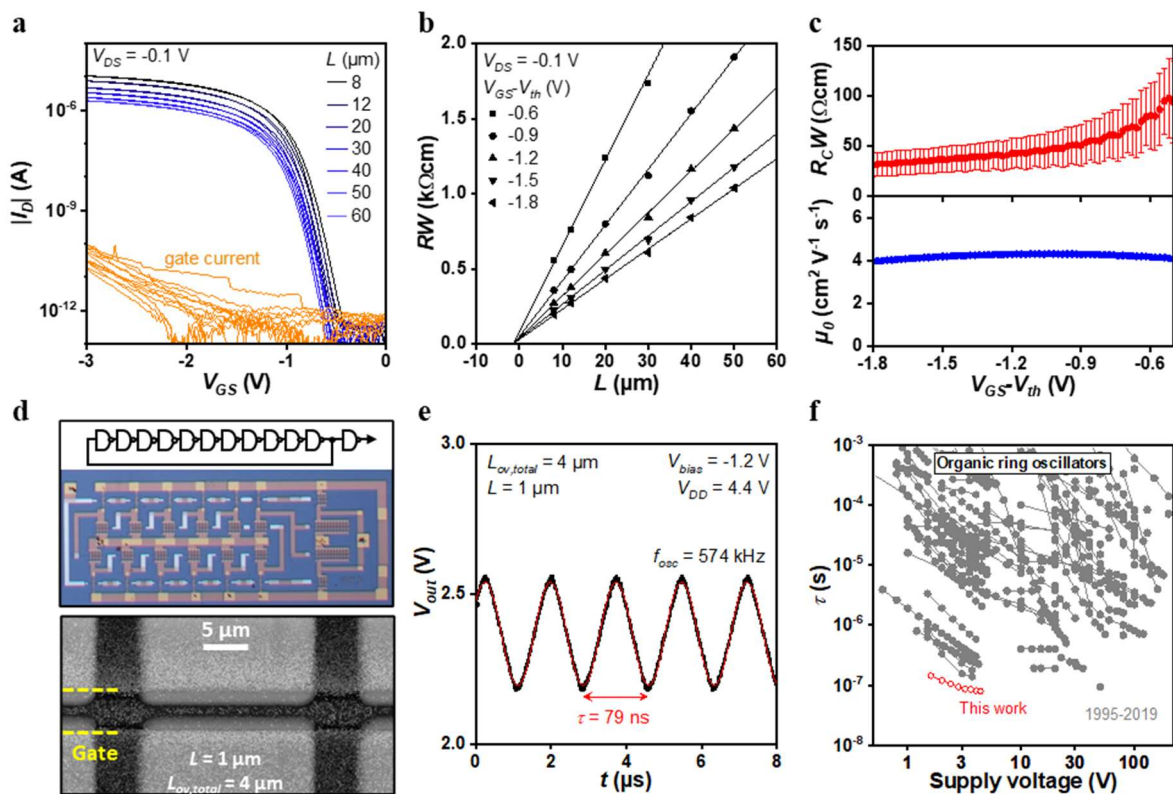


Figure 5.30 Flexible bottom-contact C₁₀-DNNT TFTs and circuits.

a) Transfer curves measured for $V_{DS} = -0.1$ V of C₁₀-DNNT TFTs with several different channel lengths (L) used for TLM. b) Width-normalized resistance (RW) versus L for several different gate overdrive voltages ($V_{GS} - V_{th}$). c) Width-normalized contact resistance (R_CW) and intrinsic channel mobility (μ_0) determined from the fits shown in (b). d) Circuit diagram and photograph of an 11-stage ring oscillator based on biased-load inverters fabricated on a PEN substrate. SEM micrograph is of the channel region of an individual TFT in the ring oscillator. All TFTs in the circuit have $L = 1 \mu\text{m}$ and a total gate-to-contact overlap ($L_{ov,total}$) of $4 \mu\text{m}$. e) Measured output signal of the ring oscillator operated with a supply voltage (V_{DD}) of 4.4 V. A signal-propagation delay per stage (τ) of 79 ns is determined by fitting a sine wave to the output signal. f) Literature review of stage delays of organic-TFT-based ring oscillators as a function of the supply voltage. Results published in [141].

especial interest to the organic TFT community, since the van der Waals interactions between the alkyl side chains can improve the packing density of the molecules through the so-called ‘molecular fastener effect,’ while also rendering them solution processable in some solvents at high temperatures [82], [85]. TFTs based on vacuum-deposited C₁₀-DNNT have previously shown a higher effective carrier mobility than DNNT TFTs, along with a smaller contact resistance in top-contact TFTs [74], [207]. Results of various measurements performed on bottom-contact C₁₀-DNNT TFTs and integrated circuits based on them fabricated on flexible PEN substrates are summarized in Figure 5.30. These TFTs and circuits were fabricated in the same manner as the flexible bottom-contact DPh-DNNT TFTs discussed in the previous sections. Excellent performance characteristics have been obtained for the C₁₀-DNNT TFTs and circuits, most notably the very small signal delay measured in the ring oscillator (Figure 5.30d-f). At 79 ns/stage measured at a supply voltage of 4.4 V, this represents a new record for ring oscillators based on organic TFTs (previous record was 93 ns/stage measured at 50 V [277]), which is most likely due to the combination of low contact resistance ($R_C W = (31 \pm 12) \Omega\text{cm}$ at $V_{GS} - V_{th} = -1.8$ V) and small total gate-to-contact overlaps ($L_{ov,total} = 4 \mu\text{m}$) and channel length ($L = 1 \mu\text{m}$) of the TFTs in the circuit. One issue with C₁₀-DNNT TFTs is that they appear to have poorer long-term stability than DPh-DNNT TFTs, especially concerning the off-state drain current which increases by several orders of magnitude after only a few days, and eventually the TFTs do not turn on at all. This may be related to a ‘delamination effect’ that was observed in the C₁₀-DNNT films (Figure 5.31), wherein the individual monolayers appear to ‘peel up’ from the surface, though this requires further investigation.

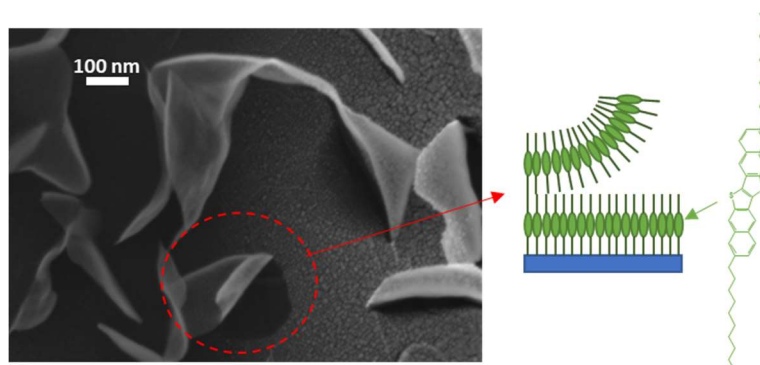


Figure 5.31 Delamination of C₁₀-DNNT over time.

SEM micrograph of the edge of contact in a top-contact C₁₀-DNNT TFT. The Au contact (right side of image) allows to see the delamination of the underlying C₁₀-DNNT monolayer flake over time. The ‘shadow’ left behind is where the flake was laying at the time of the deposition of the Au contacts.

5.3.4 N-channel organic TFTs based on N1100

So far results have only been shown for p-channel TFTs. However, the design and fabrication of low-power complementary circuits requires both n-channel and p-channel TFTs [57], [127]. Therefore, a preliminary study was performed on bottom-contact organic TFTs using the n-channel organic semiconductor Polyera ActivInk™ N1100 (PTCDI-(CN)₂-(CH₂C₃F₇)₂, Figure 5.32) [53]. Here, instead of PFBT, 4-methoxythiophenol (MeOTP) [186] was used to functionalize the gold source and drain contacts, because the electron-donating methoxy group in the para position imposes a dipole moment pointing away from the anchoring thiol, thereby reducing the work function of the MeOTP-functionalized-Au contacts to around 4.24 eV, which is expected to improve electron injection. Unfortunately, the contact resistance in this case was still very high ($R_C W = (26 \pm 1) \text{ k}\Omega\text{cm}$ at $V_{GS} - V_{th} = 2.5 \text{ V}$). It is possible that this was due to the much lower intrinsic carrier mobility of N1100 compared to both DPh-DNTT and C₁₀-DNTT ($\mu_0 = (0.048 \pm 0.001) \text{ cm}^2 \text{ V}^{-1} \text{ s}^{-1}$). It may also be that some optimization of the treatment of the contacts with MeOTP is necessary or that a contact treatment using a different thiol can yield better results for this and other n-channel organic semiconductors.

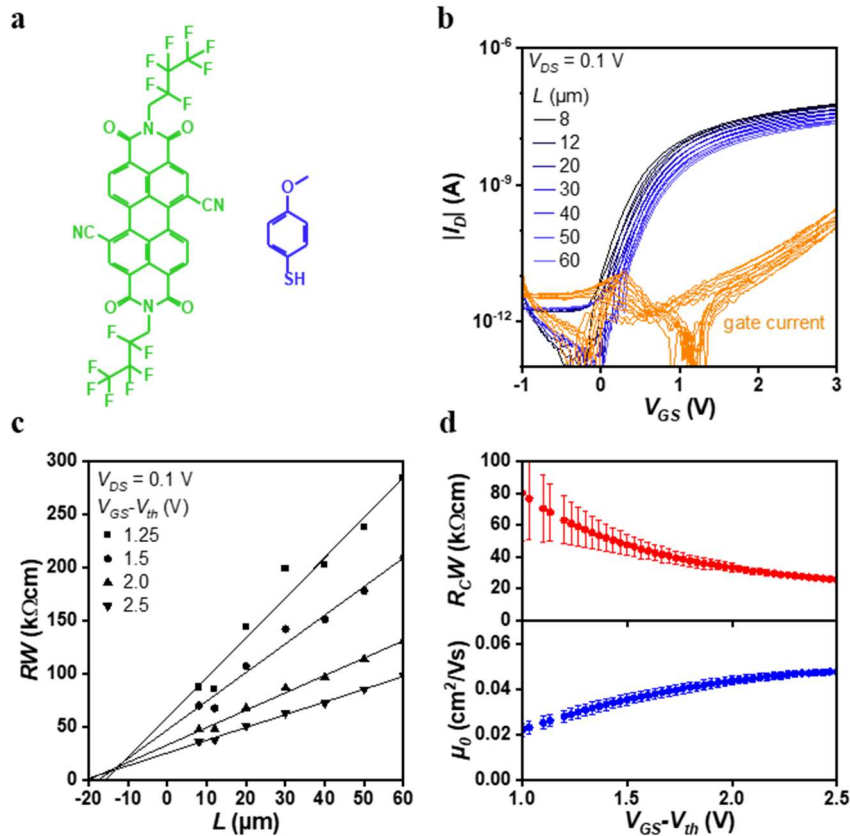


Figure 5.32 Flexible bottom-contact TFTs using the n-channel semiconductor N1100.

a) Chemical structures of the n-channel organic semiconductor N1100 and 4-methoxythiophenol (MeOTP), which was used to functionalize the Au source and drain contacts. b) Transfer curves measured for $V_{DS} = 0.1$ V of N1100 n-channel TFTs with several different channel lengths (L) used for TLM. c) Width-normalized resistance (RW) versus L for several different gate overdrive voltages ($V_{GS} - V_{th}$). d) Width-normalized contact resistance (R_CW) and intrinsic channel mobility (μ_0) determined from the fits shown in (b).

5.4 Conclusions

In this chapter, the effects of the device architecture on several device parameters of organic TFTs were examined, especially in relation to the parasitic contact resistance between the source and drain contacts and the organic-semiconductor layer and how this subsequently affects the dynamic TFT performance. Strong experimental evidence was presented that supports a theoretical prediction by Zojer et al. [17], [18] that in the limit of a very small gate-dielectric thickness, the contact resistance in coplanar (bottom-contact) organic TFTs can be lower than in otherwise comparable staggered (top-contact) TFTs. Indeed, by adopting a bottom-gate, bottom-contact architecture utilizing a very thin hybrid gate dielectric and thiol-based chemisorbed molecular monolayer (CML) to functionalize the source and drain contacts, it was demonstrated that it is possible to fabricate organic TFTs and circuits on flexible substrates with figures of merit that exceed those of comparable bottom-gate, top-contact TFTs.

A novel method for evaluating the contact resistance and intrinsic channel mobility of organic TFTs in the saturation regime was also presented, wherein the channel-length dependence of the unity-current-gain (transit) frequency is examined. It was also found that the general fabrication methods described here lead to organic TFTs and circuits with a high degree of reproducibility and can generally be applied to other vacuum-deposited organic semiconductors such as C₁₀-DNNT and the n-type organic semiconductor small molecule N1100. The most significant device performance results from the flexible low-voltage organic TFTs and circuits are summarized below in Table 5.2. Several of the metrics represent new records for organic TFTs as of the time of writing of this thesis and are denoted in the table.

It was shown that in the DPh-DNNT TFTs in which a CML of pentafluorobenzenethiol (PFBT) was implemented, the charge injection is predominantly a thermally activated process. At temperatures around room temperature, the injection can be modeled quite well by classic thermionic emission theory [176], with a very low Schottky barrier height (Φ_B) of (69 ± 20) meV extracted from temperature-dependent transmission line method (TLM) analysis of the contact resistance. At lower temperatures down to 80 K, the charge injection loses a large portion of its temperature dependence and may be more accurately described by a thermally assisted tunneling or other injection mechanism with different temperature dependence. The intrinsic channel mobility extracted from TLM also showed a pronounced temperature dependence, though an analysis using the typical multiple trap and release theory (MTR)

describing hopping transport of charges yielded an unrealistically low activation energy that was well below kT for most of the temperature range of the measurements. This possibly means that the charge transport in the DPh-DNTT films is characterized by a mixture of hopping transport and another transport mechanism with subdued or negative temperature dependence such as transient localization [29].

Finally, it was also shown that there are significant differences in the parasitic capacitances arising from the gate-to-drain overlaps in bottom-contact and top-contact TFTs. It is predicted that the lower parasitic capacitance of a top-drain contact combined with the lower contact resistance of a bottom-source contact could lead to an improvement of the dynamic performance for similar channel lengths as were tested here.

Table 5.2: Summary of TFT and circuit performance parameters reported in this chapter

Parameter	Device	Critical dimensions	Value
On/off ratio	TFT	$L_{ov,GS}+L_{ov,GD} = 4 \mu\text{m}, W = 200 \mu\text{m}, L = 8 \mu\text{m}$	10^{10} ^a
	TFT (10 duplicates)	$L_{ov,GS}+L_{ov,GD} = 60 \mu\text{m}, W = 7.5 \mu\text{m}, L = 1.5 \mu\text{m}$	10^7 - 10^8
	TFT	$L_{ov,GS} = 1.7 \mu\text{m}, W = 100 \mu\text{m}, L = 0.6 \mu\text{m}$	10^9 ^b
Subthreshold	TFT	$L_{ov,GS}+L_{ov,GD} = 4 \mu\text{m}, W = 200 \mu\text{m}, L = 8 \mu\text{m}$	59 mV/decade ^a
Slope (SS)	TFT (10 duplicates)	$L_{ov,GS}+L_{ov,GD} = 60 \mu\text{m}, W = 7.5 \mu\text{m}, L = 1.5 \mu\text{m}$	(67 ± 5) mV/decade
	TFT	$L_{ov,GS} = 1.7 \mu\text{m}, W = 100 \mu\text{m}, L = 0.6 \mu\text{m}$	66 mV/decade ^b
Contact	TFT (TLM)	$L_{ov,GS}+L_{ov,GD} = 10 \mu\text{m}, W = 200 \mu\text{m}, L = 8 - 60 \mu\text{m}$	$(29 \pm 13) \Omega\text{cm}$ ^a
Resistance ($R_C W$)	TFT (f_T vs. L)	$L_{ov,GS}+L_{ov,GD} = 10 \mu\text{m}, W = 100 \mu\text{m}, L = 0.7 - 10.5 \mu\text{m}$	$(10 \pm 2) \Omega\text{cm}$ ^a
	TFT (TLM)	$L_{ov,GS}+L_{ov,GD} = 10 \mu\text{m}, W = 200 \mu\text{m}, L = 8 - 50 \mu\text{m}$	$(31 \pm 12) \Omega\text{cm}$
Transconductance (g_m/W)	TFT	$L_{ov,GS} = 1.7 \mu\text{m}, W = 100 \mu\text{m}, L = 0.6 \mu\text{m}$	$(6.4) \text{ S m}^{-1}$ ^a
Stage delay (τ)	Inverter	$L_{ov,GS}+L_{ov,GD} = 4 \mu\text{m}, L = 1 \mu\text{m}$	19 ns (rise) ^a
	Ring oscillator	$L_{ov,GS}+L_{ov,GD} = 4 \mu\text{m}, L = 1 \mu\text{m}$	79 ns/stage ^a
	Ring oscillator (BC)	$L_{ov,GS}+L_{ov,GD} = 10 \mu\text{m}, L = 1 \mu\text{m}$	138 ns/stage
	Ring oscillator (TC)	$L_{ov,GS}+L_{ov,GD} = 10 \mu\text{m}, L = 1 \mu\text{m}$	156 ns/stage
Transit frequency (f_T)	TFT (S-parameters)	$L_{ov,GS} = 1.7 \mu\text{m}, W = 100 \mu\text{m}, L = 0.6 \mu\text{m}$	21 MHz ^c
f_T/V	TFT (S-parameters)	$L_{ov,GS} = 1.7 \mu\text{m}, W = 100 \mu\text{m}, L = 0.6 \mu\text{m}$	7 MHz/V ^a
f_{eq}/V	Ring oscillator	$L_{ov,GS}+L_{ov,GD} = 4 \mu\text{m}, L = 1 \mu\text{m}$	1.43 MHz/V

^a Record for all organic transistors

^b Record for organic transistors with channel length less than 1 μm

^c Record for flexible organic transistors

6 Charge injection in bottom-contact organic thin-film transistors using contacts functionalized with thiol-based chemisorbed molecular monolayers

As shown in Chapter 5, organic thin-film transistors (TFTs) fabricated in the bottom-gate, bottom-contact (BC) device architecture show great potential for the realization of organic TFTs for high-frequency flexible electronics applications. However, to improve upon the record metrics for contact resistance ($R_C W$) and transit frequency (f_T) that were presented, a deeper understanding of the charge-injection physics and the interface chemistry in these devices is necessary. In this chapter the physicochemical characteristics of thiol-based chemisorbed molecular monolayers (CML) and self-assembled monolayers (SAM) formed on Au as a method for modifying the contact-organic semiconductor interface is investigated in greater detail. The primary focus of this study is to investigate how the chemical and morphological characteristics of various monolayer chemistries correlate with the electrical properties of in organic TFTs based on dinaphtho[2,3-b:2',3'-f]thieno[3,2-b]thiophene (DNNTT), including most importantly the contact resistance.

The survey starts with the prototypical alkyl-thiol-based SAMs on Au [237]. The focus here is on the effects of interlayer thickness on the charge injection, here controlled by the alkyl chain length. Following this model system, other thiol-based molecules of interest for CMLs chosen based on their molecular dipole moments and terminal groups. The dipolar character of the CMLs directly enables the work function of the functionalized Au contacts to be tuned over a wide range [286]. Various materials characterization methods were implemented to examine each of the different monolayers, including ultraviolet photoemission spectroscopy (UPS) to measure work functions, x-ray photoemission spectroscopy (XPS) to assess the chemical-bonding properties of the CMLs, contact angle measurements to measure the surface energy, polarization-modulation infrared reflection-absorption spectroscopy (PM-IRRAS) to qualitatively evaluate the molecular orientation of the CMLs formed on a gold surface, and grazing incidence x-ray diffraction (GIXRD), atomic force microscopy (AFM) and scanning electron microscopy (SEM) to evaluate the impacts of surface functionalization on the DNNTT layer morphology.

Sets of organic TFTs based on DNNT were fabricated on identically-prepared substrates in which a 30-nm-thick aluminum layer was deposited onto a highly doped silicon wafer which acts as the global-back-gate electrode for all of the TFTs on the substrate. A hybrid gate-dielectric layer was implemented by oxidizing the top few nanometers of the aluminum layer using an oxygen plasma treatment and then functionalizing the surface with a self-assembled monolayer (SAM) of *n*-tetradecylphosphonic acid (TDPA; see Section 4.1 for more details on the formation of the hybrid gate dielectric). The Au source and drain contacts were functionalized with one of several selected thiol molecules for formation of the CML (or SAM in the case of the alkyl-thiols).

Charge-carrier injection across a contact-semiconductor interface in which a chemisorbed interlayer is used to functionalize the metal contact involves three steps: (1) tunneling from the metal through the interlayer, (2) injection into the semiconductor, and (3) transport in the semiconductor to the gate-field-induced carrier channel [70], [166], [237]. The first step in the injection process is examined here by the alkyl-thiol SAMs with different chain lengths to functionalize the surface of the gold bottom contacts. For the two subsequent charge-transport steps (injection into the semiconductor and transport to the channel), the most critical determining factors are the carrier-transport properties of the organic-semiconductor layer at the contact interface and the energy barrier that forms due to the difference between the transport level of the semiconductor and the work function of the contact (ϕ_C). The significance of the last step is determined primarily by the choice of the organic semiconductor and the choice of the transistor architecture (coplanar or staggered). In the coplanar bottom-gate, bottom-contact TFTs examined here, the contacts are located directly on the same plane as the channel region. Therefore, as long as the organic-semiconductor thin-film morphology is well-controlled across the transition from the surface of the contact to the surface of the gate dielectric, the first two steps (tunneling through the CML/SAM and injection) are the limiting steps and therefore the most critical for improving the contact resistance in this device architecture [132].

One of the main questions to be explored is whether or not the relative efficiency of charge injection follows the Schottky-Mott scaling behavior wherein the height of the injection barrier (Φ_B) can be reduced by minimizing the energetic difference between ϕ_C and the HOMO level of DNNT (approximately 5.4 eV [287]). Therefore, the UPS measurements are an ideal method to precisely measure work functions for each of the thiol-functionalized gold contacts [92],

[181] and compare these measurements to the work function of a DNTT film deposited on top of each of the functionalized surfaces (ϕ_{DNTT}). These results were then used to interpret the measurements of the contact resistance of DNTT TFTs using the transmission line method (TLM). From these analyses, strong preliminary evidence was gathered that Fermi-level pinning (FLP) [288] restricts the expected benefits of tuning the work function of the source and drain contacts for improving the contact resistance in the DNTT TFTs.

6.1 Chemisorbed monolayer characterization

For each of the following characterization studies the test samples consisted of Si wafers with 1 nm Ti and 30 nm Au, with the Au surface functionalization with a CML formed from submersion in a solution with 10 mM concentration in ethanol for at least 2 hours. After removal from the solutions, the samples were rinsed copiously with clean ethanol and then dried under a nitrogen flow. Prior to any characterizations, the samples were then stored in an inert environment to prevent degradation from oxygen or moisture.

6.1.1 Contact angle, XPS and UPS measurements

Perhaps the simplest indicative experiment to assess the quality of formation and general surface chemistry of a CML on a surface is to measure the surface energy (γ_s) through contact angle goniometry with one or more test liquids. Here, the surface energy of the functionalized Au surfaces were measured using Owens-Wendt theory [289] which relates the liquid-solid contact angles (θ) to the polar and dispersive components of the surface energy.

$$\frac{\gamma_L(\cos\theta + 1)}{2(\gamma_L^D)^{1/2}} = (\gamma_S^P)^{1/2} \frac{(\gamma_L^P)^{1/2}}{(\gamma_L^D)^{1/2}} + (\gamma_S^D)^{1/2} \quad (83)$$

Figure 6.1a shows the Owens-Wendt analysis for the alkyl-thiol SAMs with different chain lengths (n) obtained from the deionized water, ethylene glycol, and hexadecane static contact angle measurements. From the fits, the polar and dispersive components of the surface energy are evaluated and plotted in Figure 6.1b. All of the SAMs were formed by submerging the Au-coated silicon substrates in 10 mM ethanol solutions for 1 to 2 hours in ambient conditions directly after the deposition of the Au layer. Each of the alkyl-thiol SAMs significantly reduced the surface energy γ_s in comparison to a clean gold surface (45 mJ m^{-2}). This is primarily due to a drastic reduction of the polar component of the surface energy (γ_s^P), which is expected for alkyl monolayers due to the hydrophobic $-\text{CH}_3$ terminal group and the long carbon chains [290]. The 1-dodecanethiol ($n = 12$) SAM produces the lowest surface energy overall (24 mJ m^{-2}), and the surface energy gradually increases with shorter alkyl chains. It is possible that the higher surface energy of the shorter chain-length SAMs is due to incomplete coverage of the gold surface with the monolayer [291] and/or a more disordered SAM [292]. Further evidence for this latter explanation is provided by the PM-IRRAS measurements of the alkyl-thiol SAMs in the following section.

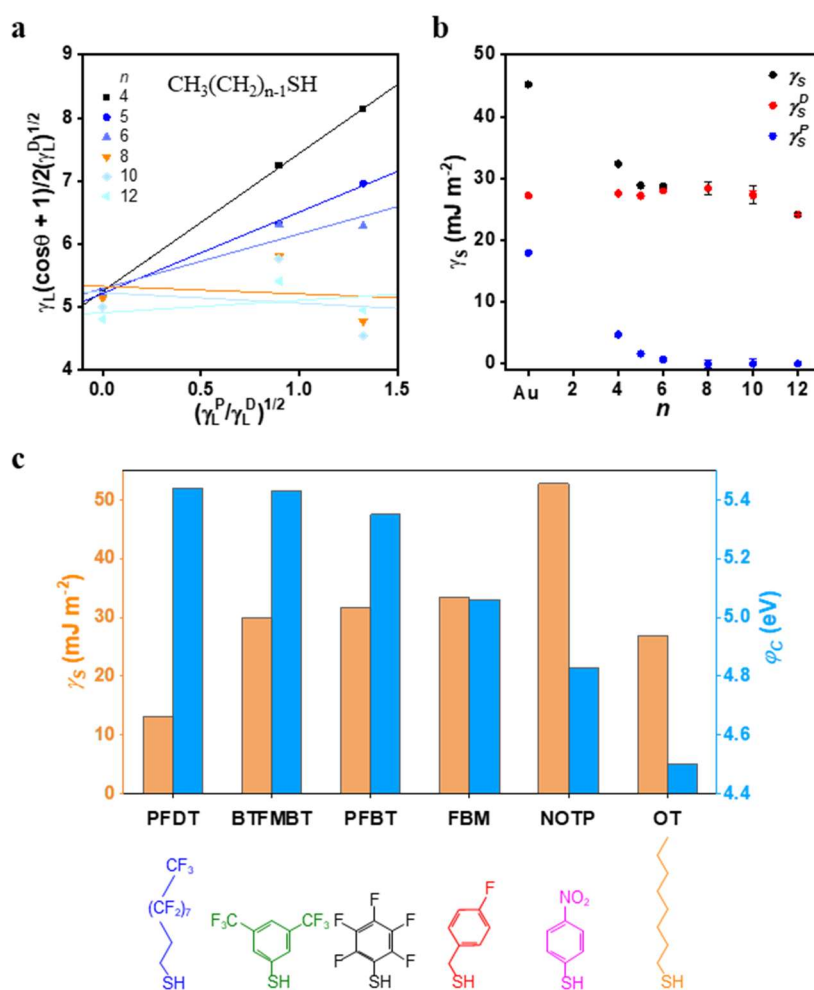


Figure 6.1 Surface energy and work function of various CML/SAM-functionalized Au contacts.

a) Owens-Wendt analysis of the surface energy (γ_S) of alkyl-thiol-functionalized Au. The alkyl chain length is indicated by n . b) Results of the analysis shown in (a) for the polar and dispersive components of the surface energy. c) Surface energy (γ_S) and contact work function (ϕ_C) determined from UPS measurements on Au surfaces functionalized with the indicated chemisorbed monolayers. PFDT: 1H,1H,2H,2H-perfluoro-1-decanethiol, BTFMBT: 3,5-bis-trifluoromethylbenzenethiol, PFBT: pentafluorobenzenethiol, FBM: 4-fluorobenzyl-mercaptan, NOTP: 4-nitrothiophenol, OT: 1-octanethiol.

For the dipolar CMLs, UPS measurements were also implemented to measure the work function of the functionalized Au substrates and are summarized, along with γ_S , in Figure 6.1c. The surface energy ranges between 13.1 mJ m⁻² for 1H,1H,2H,2H-perfluoro-1-decanethiol (PFDT) and 52.8 mJ m⁻² for NOTP. This shows most strongly the influence of the chemical structure and terminal functional groups of the CMLs on the surface energy. In PFDT, the

exceptional hydrophobicity and low surface energy are due to the long carbon chain and the CF_3 terminal group [293], while the central aromatic and the -NO_2 terminal group in 4-nitrothiophenol (NOTP) produce a more hydrophilic surface [186]. Intermediate surface energies are produced by the other CMLs that vary generally according to e.g. the number and position of the fluorine atoms. All work-function measurements were determined from the UPS data by examining the difference between secondary electron cut-off and the Fermi level [186]. The central aromatic motifs of several of the thiols contain different numbers and positions of highly electronegative fluorine atoms, or in the case of NOTP a -NO_2 group in the trans position relative to the thiol anchoring group [186], [294]–[296]. The addition of these functional groups to a central motif allows for fine-tuning of an interface dipole formed by the CML (Δ_{CML}), and thus the contact work function φ_C can be tuned around that of bare gold (~ 5 eV). The measurements of φ_C varied between 4.5 eV for 1-octanethiol (OT) and 5.44 eV for 1H,1H,2H,2H-perfluoro-1-decanethiol (PFDT).

The formation of a thiol-based CML on an Au surface takes place through a thiolate bonding reaction of the anchoring thiol group with Au [222]. Therefore, an indicator for the successful formation of a thiol-based CML or SAM on Au test samples is to examine the shifts in the binding energy of the S 2p core-level orbital [234]. In Figure 6.2a, there is strong evidence of thiolate bonding to Au (binding energies at 162 eV and 163.5 eV). It is notable that all of the monolayers appear to free of oxidized or unbound sulfur species, which would be discernable by peaks at higher binding energies (above approximately 164 eV) [297], [298] or atomic sulfur which would appear at lower binding energies of around 161 eV [223]. These data give strong evidence that for all the investigated molecules, CMLs or SAMs are formed with a high density on the surface of the Au.

From the C 1s spectra (Figure 6.2b), several peaks in the binding energy can be discerned relating to the different chemical structures of the CMLs and SAMs. Strong binding energies for C-C and C-H are located between 284 eV and 285 eV, with a small amount of contamination (~ 20 %) of molecules with incomplete fluorination of the aromatic in PFBT. C-F bonds appear at 286.7 eV for PFBT, 286.8 eV for PFDT, and 286.4 eV for FBM, which also has the lowest intensity as expected due to only the single F atom at the para position with respect to the methylene linker. The peak at 291.9 eV in the BTFMBT spectrum corresponds to the CF_3 groups bonded to the central aromatic ring at the 3 and 5 positions [234]. The peak position in the NOTP C 1s spectrum of 284.4 eV is somewhat shifted to lower binding energy than in

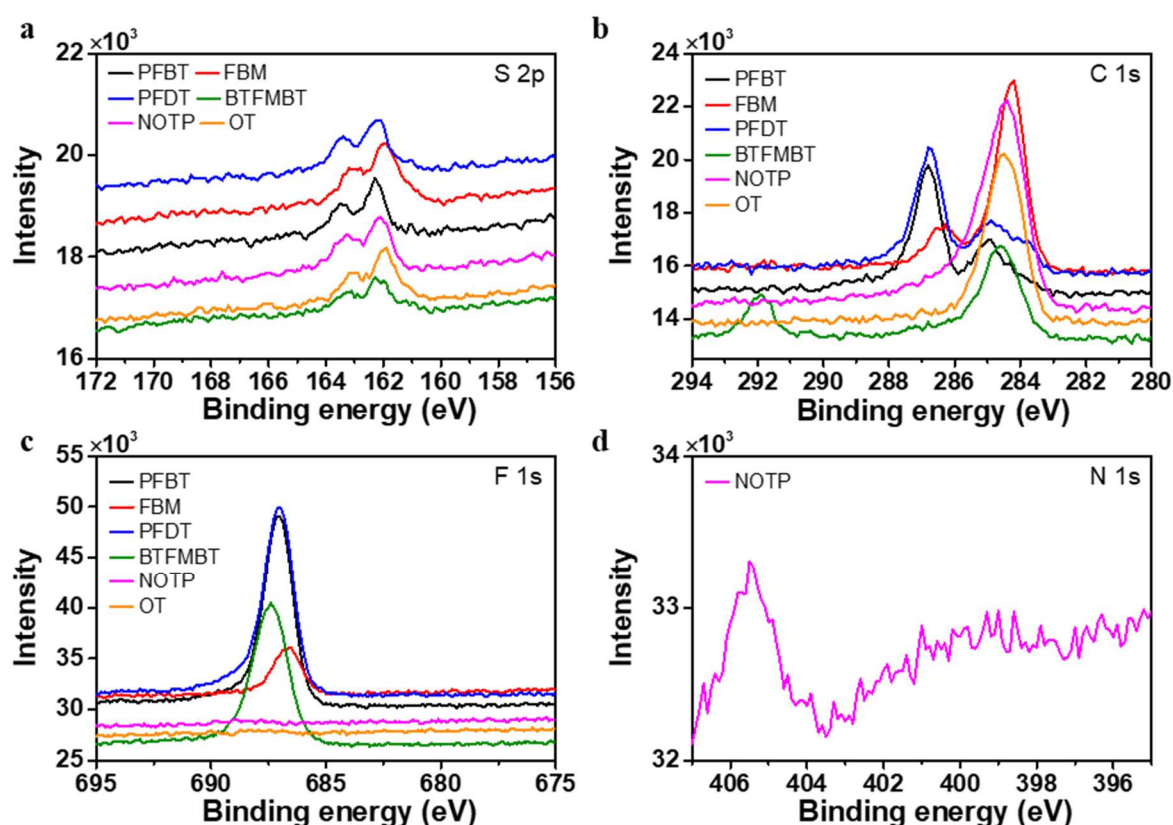


Figure 6.2 X-ray photoemission spectroscopy (XPS) of chemisorbed monolayers on Au.

a) S 2p, b) C 1s, c) F 1s, and d) N 1s core-level shifts for each of the indicated CMLs on Au. The binding energies in (a) at 162 eV and 163 eV are indicative of thiolate bonding to Au without oxidized or physisorbed components.

previous reports of NOTP monolayers on Au (~285.2 eV in [299]). There is also an additional strong peak in the N 1s core-orbital spectrum at 405.5 eV corresponding to NO₂ (Figure 6.2d) [295], [299].

The F 1s spectra (Figure 6.2c) show strong peaks at binding energies of 687.4 eV for BTFMBT, 686.6 eV for FBM, and 687.1 eV for both PFBT and PFDT, corresponding well to the literature for these molecules [234], [300].

6.1.2 Infrared spectroscopy of thiols used to form chemisorbed monolayers on gold

The results from ATR measurements of the bulk thiols on an NaCl background and polarization-modulation infrared reflection absorption spectroscopy (PM-IRRAS) measurements of the CMLs and SAMs formed on Au are analyzed in the following. PM-

IRRAS can provide additional, semi-quantitative information about the formation of thin layers on surfaces, including molecular orientations of chemisorbed species on a surface. This is possible by the selection rules that only vibrational modes having a transition dipole moment (TMD) along the surface normal will be excited by the incident polarized light [245], [301]. While this can provide some molecular orientation information in some cases, PM-IRRAS measurements are typically insufficient to enable unambiguous quantitative information regarding the molecular orientation for arbitrary chemisorbed species or to determine if hybridization with the surface has taken place. They should rather be coupled with rigorous calibration procedures and/or complemented with modeling and other experimental methods such as XPS (to confirm core-level hybridizations as was done in the previous section), scanning tunneling microscopy (STM) [302], sum frequency generation spectroscopy (SFG) [294], or near-edge x-ray absorption fine-structure (NEXAFS) measurements [245], [303]. For the present purposes, PM-IRRAS is mainly used to provide additional supporting evidence that the fabrication methods implemented here produce a dense CML or SAM on the gold surfaces for all of the different thiols that are to be compared in the organic TFTs in the broader goals of this study. Therefore, statements about molecular orientation are only made to the extent that they are warranted by supporting results from the literature or from reasonable assumptions according to the measured spectra and other supporting data that were collected. More crucial for the primary purposes of investigating charge injection in the following bottom-contact DNNT TFTs are measurements of the work function changes induced by the monolayers and the DNNT thin-film morphology when each of the different thiols are used for Au contact functionalization.

Alkyl-thiol self-assembled monolayers

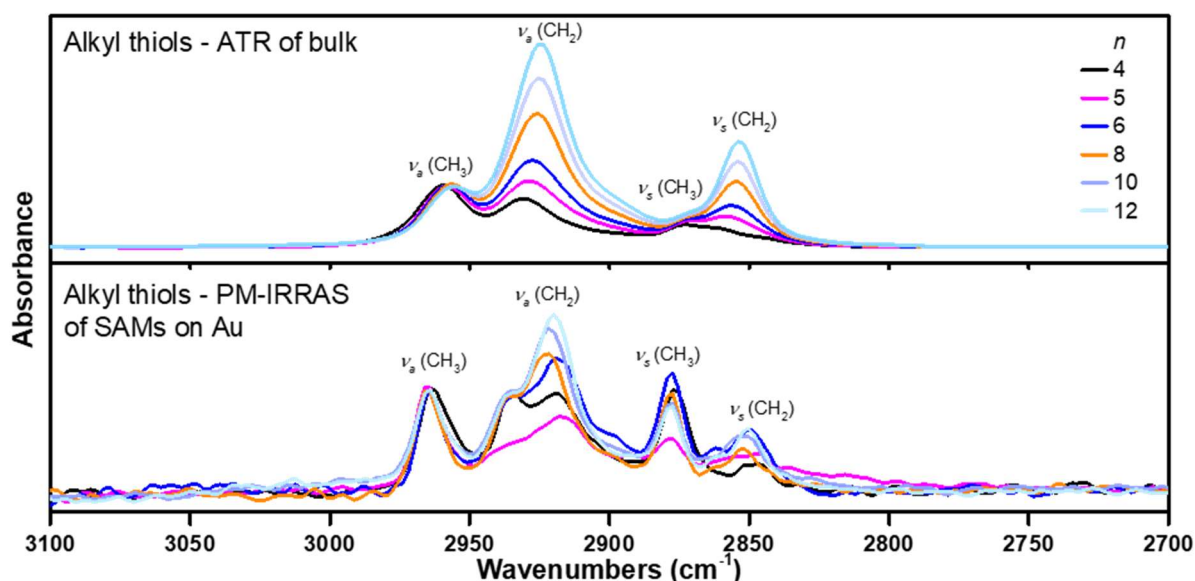


Figure 6.3 Infrared spectroscopy of alkyl thiol SAMs on Au.

High frequency regions of the infrared spectrum for the bulk thiols and as a self-assembled monolayers (SAMs) on Au. Bulk was measured using ATR with a NaCl background. The SAM was measured using polarization-modulation infrared reflection-absorption spectroscopy (PM-IRRAS). Numbered peak assignments are shown in Table 6.1.

Table 6.1: Infrared vibrational assignments for *n*-alkyl-thiol self-assembled monolayers (SAMs) on Au

Peak Assignment*	Wavenumbers (cm ⁻¹), <i>n</i>					
	4	5	6	8	10	12
$\nu_a(\text{CH}_3)$	2964	2965	2964	2965	2965	2965
$\nu_a(\text{CH}_2)$	2918	2916	2919	2923	2922	2920
$\nu_s(\text{CH}_3)$	2877	2877	2878	2878	2878	2877
$\nu_s(\text{CH}_2)$	2848	2850	2850	2852	2852	2850

*From reference [304]

The vibrational modes in the high-energy regime for the alkyl thiol SAMs on Au are shown in Figure 6.3. Strong peaks were observed in the spectra for the bulk thiols and SAMs corresponding to the symmetric (ν_s) and asymmetric (ν_a) vibrational modes for methyl and methylene groups (Table 6.1) [292], [305], [306]. Disorder in the crystalline ordering of the

molecular packing in SAMs with long alkyl chains has been associated with shifts of the methylene antisymmetric stretch at around 2920 cm^{-1} for medium to long alkyl-chain lengths ($n = 8, 10,$ and 12) to higher wavenumbers [292], and the overall intensity reduction of the CH_2 vibrational modes relative to the CH_3 vibrational modes in the SAMs has been related to the orientation of the molecular chain on the surface [307]. Shifts to higher frequencies have been attributed to a less crystalline ordering of the alkyl chains, while shifts to lower frequencies have been attributed to a more liquid state [308]. For chains orientated perfectly perpendicular to the substrate, the CH_2 bands would be expected to disappear entirely, since they would then have TMDs oriented parallel to the substrate surface [309]. From these metrics, it can be inferred from the PM-IRRAS spectra in Figure 6.3 that the molecular orientation of the chains in the SAM is not entirely independent of n , nor does the orientation change in a monotonic manner. For instance, it appears that the 1-pentanethiol ($n = 5$, magenta curve) may have chains that are oriented relatively more upright and have a relatively more crystalline ordering than the 1-butanethiol ($n = 4$, black curve), since the relative intensity and position of the CH_2 asymmetric-stretching peak between them has switched when going from the bulk to the SAM. Likewise, the roughly equal relative intensities of the CH_2 peak for the 1-hexanethiol SAM ($n = 6$, blue curve) and the 1-octanethiol SAM ($n = 8$, orange curve) may indicate a comparatively more upright orientation on average of the 1-octanethiol SAM, but the shift of the peak for $n = 6$ to lower frequency indicates greater crystallinity. These particulars of the molecular orientation and packing are possibly important for a comparison of the charge injection into TFTs utilizing alkyl thiol SAMs on the contacts, since this also varies in principle the thickness of the layer and to a small degree may affect the nucleation of the DNTT films onto the SAMs [70].

Dipolar chemisorbed molecular monolayers for work-function tuning

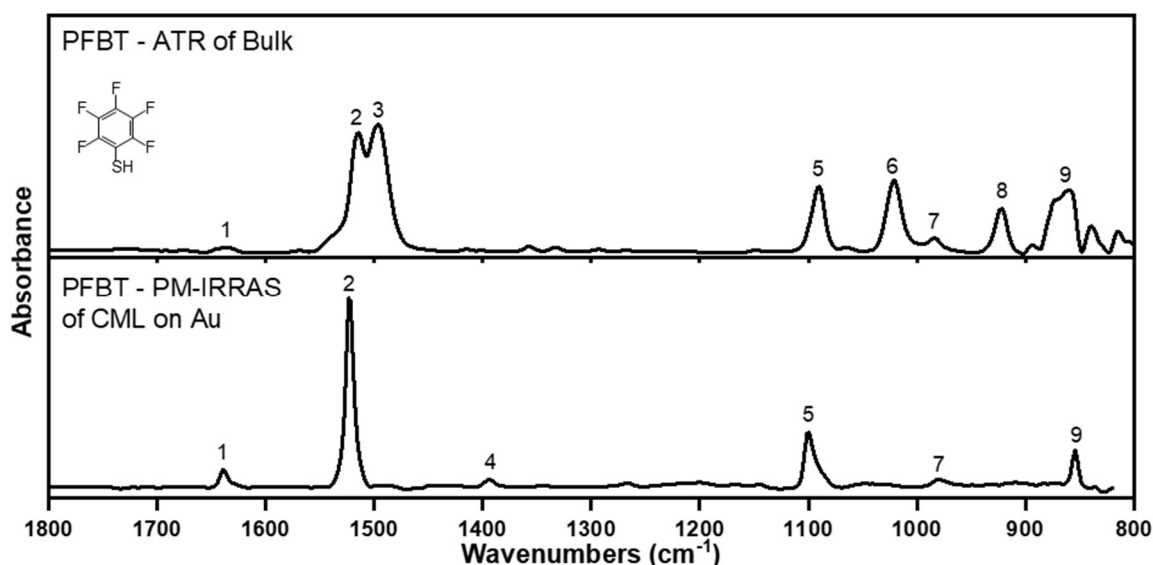


Figure 6.4 Infrared spectroscopy of pentafluorobenzenethiol (PFBT).

Mid-to-low frequency regions of the infrared spectrum for bulk PFBT and as a chemisorbed monolayer (CML) on gold. Bulk was measured using ATR with a NaCl background. The CML was measured using polarization-modulation infrared reflection-absorption spectroscopy (PM-IRRAS). Numbered peak assignments are shown in Table 6.2.

Table 6.2: Infrared vibrational assignments for pentafluorobenzenethiol (PFBT)

Peak number	Bulk (cm ⁻¹)	CML (cm ⁻¹)	Assignment*	Reference
1	1635	1639	(C=C) stretching	[303], [310]
2	1515	1523	(C-F) and (C-C), // 1,4-axis	
3	1496	--	(C-F) and (C-C), // 3,5-axis	
4	--	1394	(S=O) stretch, sulfate	
5	1090	1100	(C-F) and (C-C), // 1,4-axis	[302]
6	1021	--	C-S-H bend	
7	984	980	(C=C) bending, aromatic	
8	922	--	C-S-H bend	
9	860	854	(C-S) stretch, // 1,4-axis	

*Approximated based on standard tables or the indicated references

The IR spectra that were obtained for the PFBT stock and a CML on Au (Figure 6.4) generally show the same peak positions and intensities for the primary vibrational modes as has been previously published in a rigorous study by Azzam et al. [302] on the structural ordering and spectroscopic characteristics of PFBT on Au (111) surfaces. A note is made of some minor peaks that appear in the PM-IRRAS spectrum that are not discussed at length in that publication; a possible (C=C) stretching mode at 1639 cm^{-1} (peak 1), a possible sulfate stretching mode at 1394 cm^{-1} (peak 4), and a possible (C=C) bending mode at 980 cm^{-1} (peak 7) are distinguishable. The appearance of a sulfate peak may be particularly important to note for long-term stability considerations for the CMLs, since oxidization of the sulfur of the thiolate bond may act as a degradation mechanism for the CML and possibly affect the TFT performance over time if PFBT is implemented for source and drain functionalization. Most important to consider for the molecular ordering and orientation of PFBT on the surface are (1) the disappearance in the CML of the (C-F) and (C-C) stretching modes parallel to the 3,5 axis that are very strong in the bulk ATR spectrum, and (2) the intense peaks parallel to the 1,4-axis are present in the PM-IRRAS spectrum. These two features give strong indication that the PFBT molecules are oriented such that the 1,4-axis of the benzene ring is close to perpendicular to the Au surface with little to no rotation with respect to the 1,4 axis.

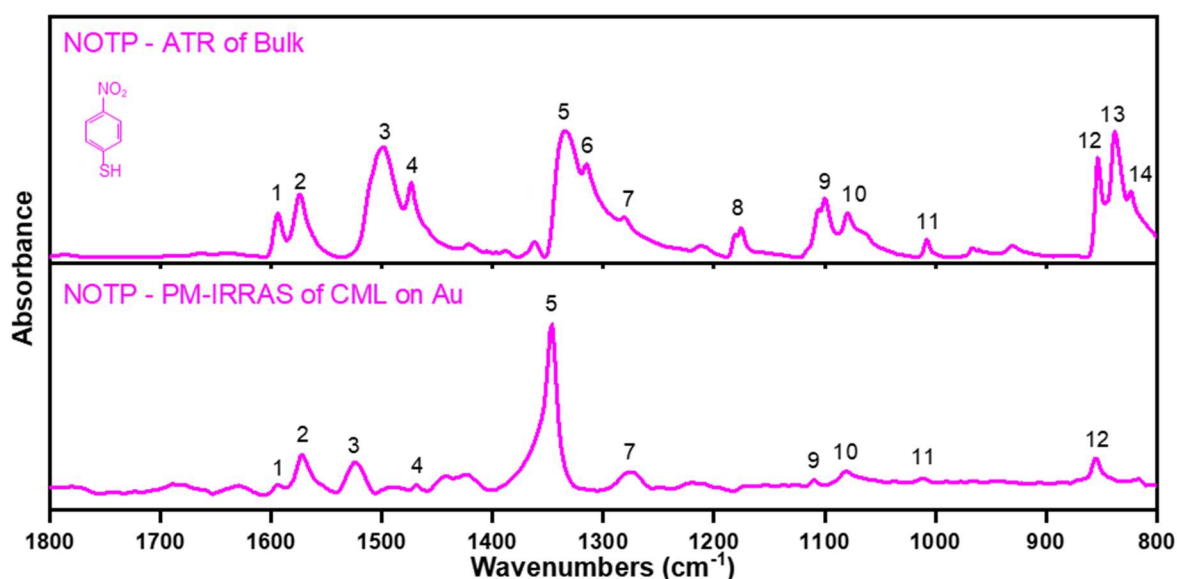


Figure 6.5 Infrared spectroscopy of 4-nitrothiophenol (NOTP).

Mid-to-low frequency regions of the infrared spectrum for bulk NOTP and as a chemisorbed monolayer (CML) on gold. Bulk was measured using ATR with a NaCl background. The CML was measured using polarization-modulation infrared reflection-absorption spectroscopy (PM-IRRAS). Numbered peak assignments are shown in Table 6.3.

Table 6.3: Infrared vibrational assignments for 4-nitrothiophenol (NOTP)

Peak number	Bulk (cm ⁻¹)	CML (cm ⁻¹)	Assignment*	Reference
1	1594	1594	(C-C) stretching; (C-H) bending (in-plane) \perp 1,4-axis	[294]
2	1575	1572	(C-C) stretching; (C-H) bending (in-plane) \perp 1,4-axis	
3	1499	1524	(NO ₂) asymmetric stretching \perp 1,4-axis	
4	1474	1468	(C-H) bending	[294], [296]
5	1335	1346	(NO ₂) symmetric stretching	
6	1316	--	(C-H) bending	[311]
7	1281	1276	(C-N) stretching	
8	1176	--	(S=O) stretching	[311]
9	1100	1110	(C-N) stretching, (C-H) bending	
10	1080	1080	(C-N) stretching, (C-S) stretching	
11	1008	1011	(C=C) bending, aromatic	[311]
12	853	855	(C-H) wagging; (C-S) stretch, // 1,4-axis	
13	838	--	(C=C) bending, aromatic;	[311]
14	823	--	(C-H) wagging	

*Approximated based on standard tables or the indicated references

For molecular orientation of NOTP on gold surfaces, one can refer primarily to Cecchet et al. [294]. In their work, peaks 1 and 3 corresponding to vibrational modes which are perpendicular to the 1,4-axis of the NOTP molecule were utilized with reference to supplementary data from sum frequency generation spectroscopy (SFG) measurements and DFT calculations. From this analysis, it was determined that the NOTP molecules show quite substantial rotational angle of 66° and tilt angle of 60° on gold, implying that the NOTP molecules are close to ‘laying down’ on the surface. The fact that the experimental PM-IRRAS data (Figure 6.5) closely matches the results reported in their work, both in terms of relative intensities and positions of the peaks, leads us to conclude that a similar molecular orientation of NOTP is present for these samples. This is possibly significant for the TFT performance since this could have implications for the molecular orientations of the semiconductor molecules as they arrange into thin films on the surface of the NOTP-functionalized Au contacts.

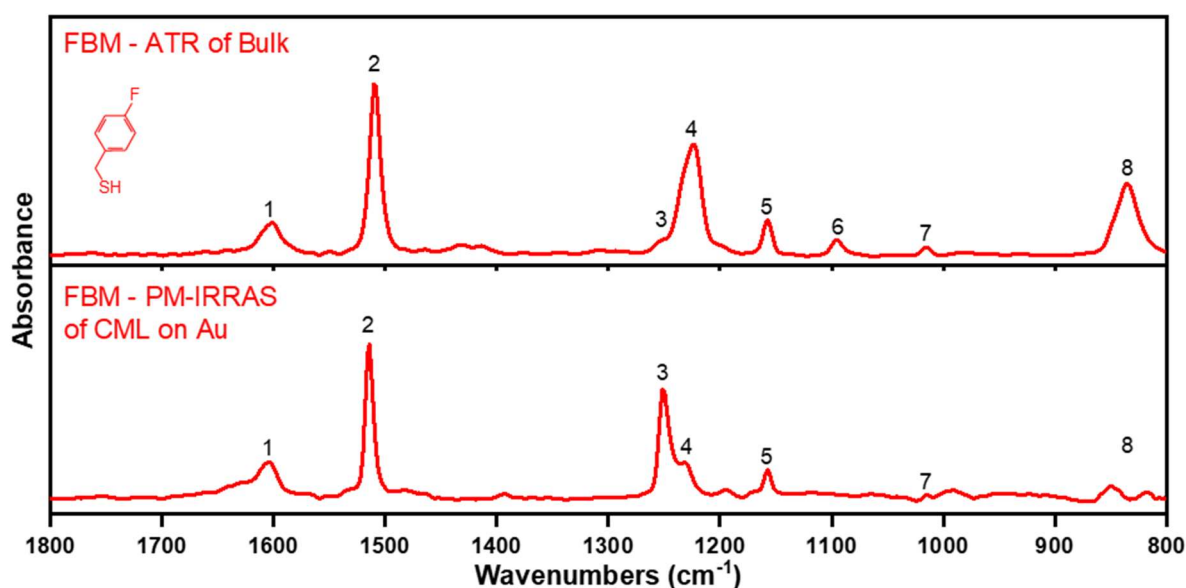


Figure 6.6 Infrared spectroscopy of 4-fluorobenzylmercaptan (FBM)

Mid-to-low frequency regions of the infrared spectrum for bulk FBM and as a chemisorbed monolayer (CML) on gold. Bulk was measured using ATR with a NaCl background. The CML was measured using polarization-modulation infrared reflection-absorption spectroscopy (PM-IRRAS). Numbered peak assignments are shown in Table 6.4.

Table 6.4: Infrared vibrational assignments for 4-fluorobenzylmercaptan (FBM)

Peak number	Bulk (cm ⁻¹)	CML (cm ⁻¹)	Assignment*	Reference
1	1602	1604	(C-C) stretching; (C-H) bending	[303], [310]
2	1510	1515	(C-F) and (C-C), // 1,4-axis	[302]
3	1253	1251	(C-H) deformation; (CH ₂) wagging;	[303], [310]
4	1223	1232	(C-F) stretching	
5	1157	1157	(C-H) deformation; (CH ₂) wagging	[303]
6	1097	--	(S-H) wagging	
7	1016	1014	(C=C) bending	
8	835	849	(S-H) wagging; (C=C) bending, aromatic; (CH ₂) twisting; (C-S) stretching, // 1,4-axis	

*Approximated based on standard tables or the indicated references

To the author's knowledge, there have been no published PM-IRRAS studies of FBM, though there are studies of benzyl mercaptan (BM) and some derivatives thereof [303], [310]. There are notable vibrational modes that were assigned to peaks in the PM-IRRAS data for

FMB (Figure 6.6) according to studies using BM and fluorinated aromatic thiol derivatives like PFBT [302]. For instance, the (C-F) and (C-C) stretching modes parallel to the 1,4-axis of the aromatic that was measured for PFBT (peak 2 in Table 6.2 for a PFBT CML at 1523 cm^{-1}) is very close to peak 2 for the FBM CML at 1515 cm^{-1} . This by itself implies, because of the selection rules of PM-IRRAS, that the FBM is oriented with the 1,4-axis of the benzene ring roughly upright with respect to the surface of the Au substrate. However, a precise orientation cannot be determined without further corroborating experiments such as DFT calculations, especially considering peaks 3 and 4, which could be assigned to several different vibrational modes and show a significant change in relative intensities between the bulk and CML spectra which could not be readily interpreted.

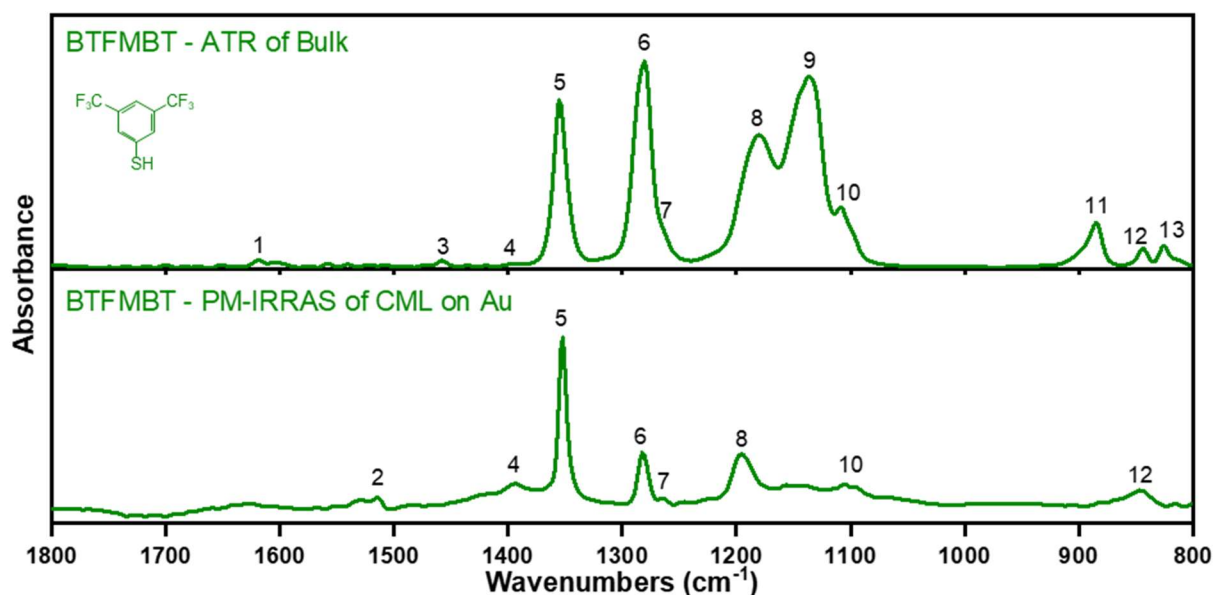


Figure 6.7 Infrared spectroscopy of 3,5-bis-trifluoromethylbenzenethiol (BTFMBT).

Mid-to-low frequency regions of the infrared spectrum for bulk BTFMBT and as a chemisorbed monolayer (CML) on gold. Bulk was measured using ATR with a NaCl background. The CML was measured using polarization-modulation infrared reflection-absorption spectroscopy (PM-IRRAS). Numbered peak assignments are shown in Table 6.5.

Table 6.5: Infrared vibrational assignments for 3,5-bis-trifluoromethylbenzenethiol (BTFMBT)

Peak number	Bulk (cm ⁻¹)	CML (cm ⁻¹)	Assignment*	Reference
1	1617	--	(C-C) stretching; (C-H) bending	[303], [310]
2	--	1514	(C-C) stretching, // 1,4-axis	[302]
3	1457	--	(C-C) stretching, // 3,5-axis	[302]
4	1395	1394	(S=O) stretching, sulfate	
5	1356	1352	(C-F) stretching	
6	1282	1282	(C-H) deformation;	
7	1265	1265	(CH ₂) wagging	[312]
8	1180	1196	(C-F) stretching	
9	1136	--	(C-F) stretching	
10	1109	1103	(C-F) stretching	
11	885	--	(C=C) bending, aromatic;	
12	845	845	(C-S) stretching, // 1,4-axis; C=C bending, aromatic	[302]

*Approximated based on standard tables or the indicated references

The PM-IRRAS spectrum of BTFMBT-functionalized Au (Figure 6.7) shows some significant differences compared to the bulk ATR spectrum, most considerably in terms of the various (C-F) stretching modes. The (C-F) stretching mode at 1352 cm^{-1} (peak 5) maintains a high intensity in the CML, while the intensity of all of the other (C-F) stretching modes (peaks 8-10) and the (C-H) deformation and (CH₂) wagging modes (peaks 6 and 7, respectively) all decrease in intensity. Molecular orientation on the surface again cannot be clearly determined from this data alone. There is possibly a very weak peak for a (C-C) stretching mode parallel to the 1,4-axis at 1514 cm^{-1} (peak 2) which may indicate perpendicular orientation, however this would need to be investigated further with other methods.

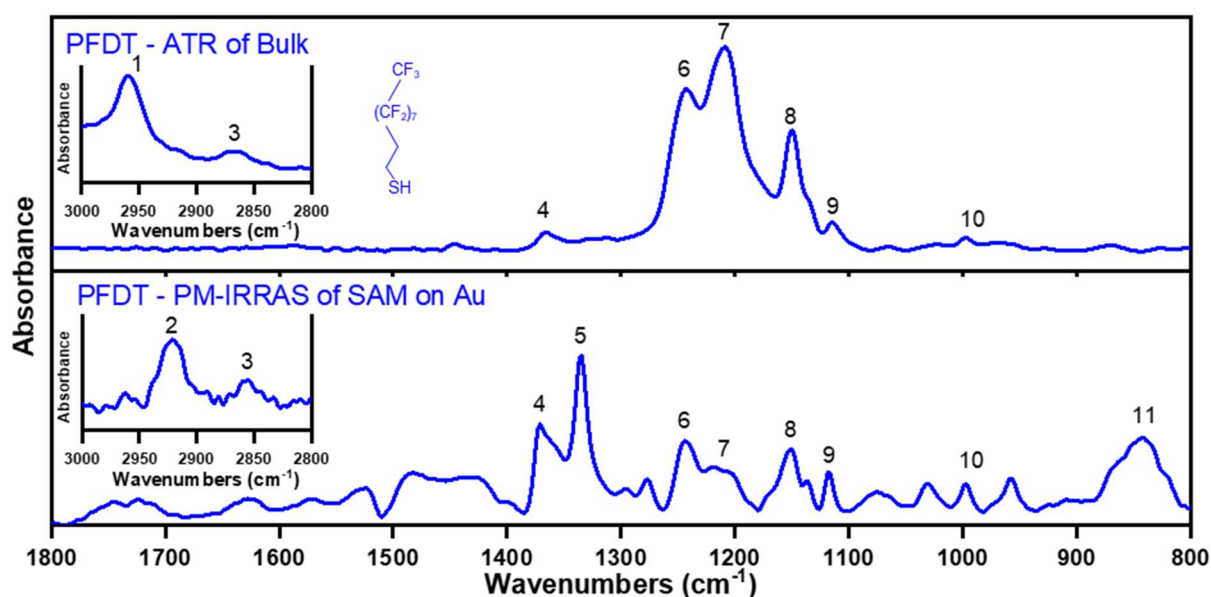


Figure 6.8 Infrared spectroscopy of 1H,1H,2H,2H-perfluoro-1-decanethiol (PFDT).

Infrared spectrum for bulk BTFMBT and as a self-assembled monolayer (SAM) on Au. Bulk was measured using ATR with a NaCl background. The SAM was measured using polarization-modulation infrared reflection-absorption spectroscopy (PM-IRRAS). Numbered peak assignments are shown in Table 6.6. Note that the insets are scaled by approximately 100× for the ATR and 20× in the PM-IRRAS to facilitate analysis of the spectra.

Table 6.6: Infrared vibrational assignments for 1H,1H,2H,2H-perfluoro-1-decanethiol (PFDT)

Peak number	Bulk (cm ⁻¹)	SAM (cm ⁻¹)	Assignment*	Reference
1	2960	--	--	
2	--	2922	ν_a (CH ₂)	
3	2867	2858	ν_s (CH ₂)	
4	1368	1371	ν_{ax} (CF ₂)	[306], [308], [313]–[315]
5	--	1335	ν_{ax} (CF ₂)	
6	1244	1244	ν_{pd} (CF ₂)	
7	1209	1209	ν_{pd} (CF ₂)	
8	1150	1151	ν_s (CF ₂)	
9	1117	1118	(C-F) stretching	[312]
10	997	997	(C-S) stretching	[302]

*Approximated based on standard tables or the indicated references

The PM-IRRAS measurement of the PFDT SAM on Au shows some significant differences in the peak positions and intensity as compared to the ATR measurements of the bulk PFDT (Figure 6.8). Starting with the high frequency region (insets in Figure 6.8), there is a notable anomalous peak (1) at 2960 cm^{-1} in the ATR bulk spectrum that is not typically observed for PFDT [314] and therefore might be attributed to some hydrocarbon contamination. The other peaks in this region correspond to the asymmetric (ν_a , peak 2) and symmetric (ν_s , peak 3) vibrational modes for the short methylene portion of the chains and are both clearly present in the SAM, while peak (2) appears to be hidden by peak (1) in the ATR spectrum. The appearance and high intensity of the axial CF_2 vibrational modes (peaks 4, 5) in comparison to the asymmetric CF_2 vibrational modes (peaks 6-8) in the PM-IRRAS spectrum indicates that there is a high coverage of the surface with PFDT in the form of a densely packed SAM with the chains oriented roughly perpendicular to the surface [316]. This is because the transition dipole moment for the CF_2 asymmetric stretching modes are normal to the PFDT chain axis, whereas the axial stretching modes are all oriented parallel to the chain and are thus far diminished in intensity compared to the bulk ATR spectrum [314]. Following the method from Alt et al. [313], the average polar angle of the PFDT chains (α) can be estimated from the relative absorption intensities of peaks (4) and (8) in the bulk and SAM spectra.

$$\frac{A_{SAM,4}}{A_{SAM,8}} \left(\frac{A_{bulk,4}}{A_{bulk,8}} \right)^{-1} \frac{\nu_8}{\nu_4} = \frac{1}{\tan^2 \alpha} \quad (84)$$

Where ν_8 is the peak position for peak (8) (1150 cm^{-1}), ν_4 is the peak position for peak (4) (1370 cm^{-1}), and A_{SAM} and A_{bulk} are the corresponding absorbance intensities for the indicated peaks in the SAM and bulk, respectively. From this calculation, α is approximately $(18 \pm 2)^\circ$ for the PFDT SAM on Au. This is notably a somewhat larger value in comparison to the results from Alt et al. [313] where the polar angle was estimated to be $(10 \pm 3)^\circ$. It is not entirely clear from where this discrepancy arises, but it may also be notable that the relative intensity of peak (8) in the ATR bulk spectrum appears to be somewhat diminished in comparison to the relative intensity in the publication from Alt et al. [313] and is in rather more agreement with the bulk spectra from Chidsey et al. [314], as well as with their reported tilt angle of $(15-16)^\circ$.

6.2 Dependence of the contact resistance on the thickness (chain length) of an alkyl-thiol monolayer

Chemisorbed alkyl-thiol monolayers on gold contacts are a prototypical example of a self-assembled monolayer (SAM) which can be used to modify the charge injection in organic electronic devices [175], [317]. They also act as an interesting test system for investigating the charge transport across contact-organic semiconductor interfaces in organic TFTs with respect to the influence of the thickness of a SAM, since the length of the alkyl chain (n , the number of C atoms) can be systematically modified to adjust this thickness. The charge injection through alkyl-thiol monolayers with different chain lengths has been investigated previously with other organic semiconductors, most notably pentacene, with the result that the charge-carrier transport should vary approximately exponentially with the number of carbon atoms in the alkyl chain [70], [237]. This result hints that the tunneling through the SAM is a limiting step, since this should depend exponentially on the thickness of the insulating interlayer in a metal-insulator-semiconductor device [176].

To highlight the effects on the thin-film morphology of vacuum-deposited DNTT on gold contacts with and without an alkyl SAM, the AFM amplitude scans of the DNTT films formed across the contact and into the channel region of the TFTs were examined (Figure 6.9a,b). Amplitude scans (as opposed to height scans) are useful for highlighting morphology changes in the DNTT layer across the two interfaces without having to deconvolute the 30-nm-height difference of the Au contact compared to the channel region [318]. One can see from these scans that the morphology of the 40-nm-thick DNTT film across the contact-channel transition region is far less disturbed for the case where the gold contacts were functionalized with an alkyl-thiol SAM (1-decanethiol, Figure 6.9a). The average size of the grains in the DNTT film is also noticeably smaller for the bare-gold contacts both on top of the contacts and well into the channel region. The smaller grain size is likely related to the propensity for acenes and heteroacenes to adsorb ‘face-down’ on the surface of clean Au (111) [301], [318]. This promotes a mixed orientation of the molecules in the thin film that extends up to several microns into the channel region near to the contacts [78], as can be seen in the noticeable change in the DNTT film in the SEM micrographs in Figure 6.9c,d and the AFM height scans

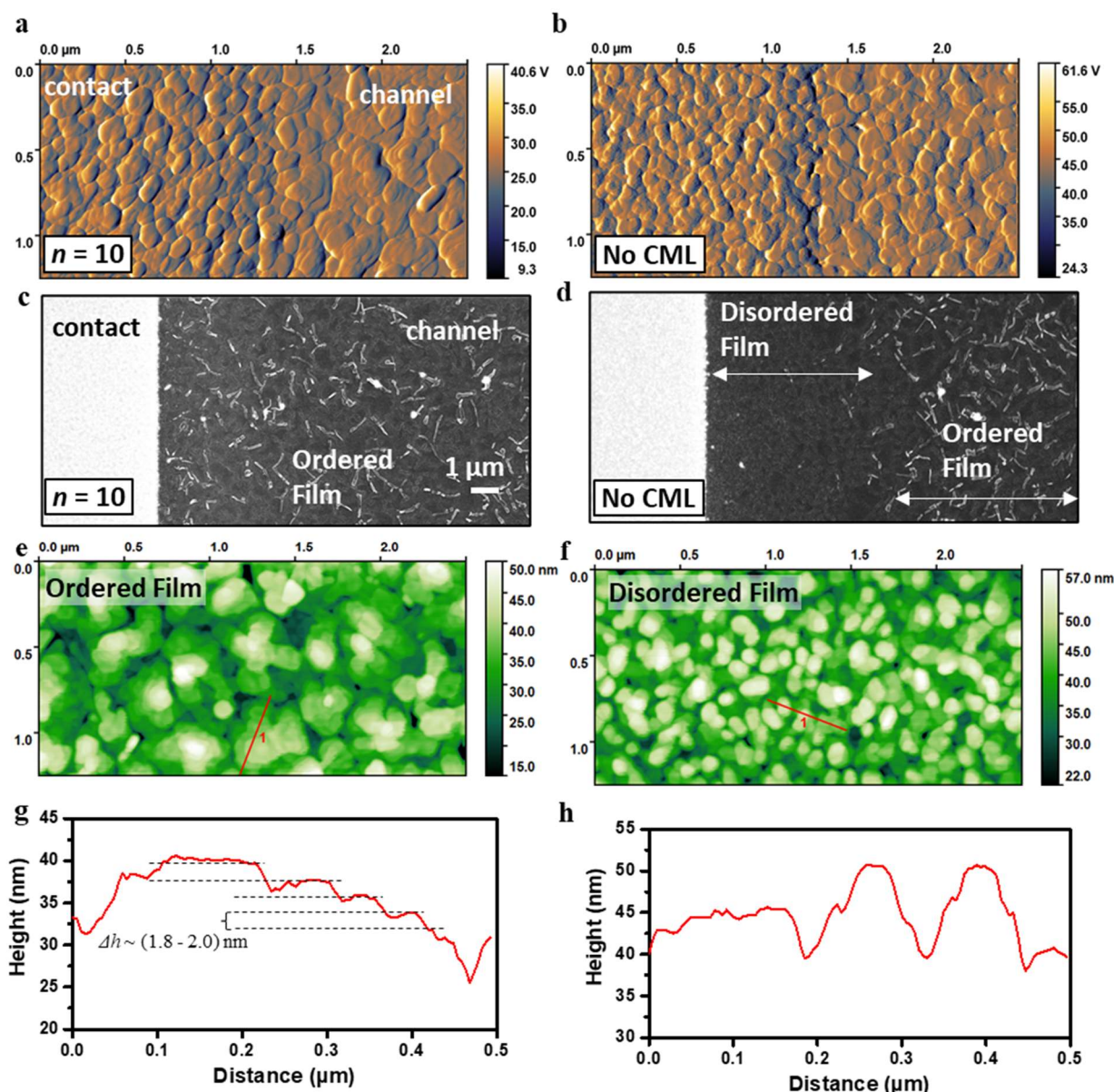


Figure 6.9 Surface morphology of nominally 40-nm-thick DNTT layers deposited by sublimation in vacuum onto gold contacts with and without functionalization with 1-decanethiol.

a,b) AFM amplitude scans of the contact edge in bottom-contact DNTT TFTs. c,d) SEM images of the channel in bottom-contact DNTT TFTs. (a,c) Au contacts functionalized with a monolayer of 1-decanethiol ($n = 10$) SAM. (b,d) Bare Au contacts (without functionalization). e,f) AFM height scans of the ordered and disordered regions of the DNTT films highlighted in (d). g,h) Line profiles from (e,f). The step height (Δh) of (1.8-2.0) nm that is estimated in (g) roughly corresponds to the long axis length of a DNTT molecule (1.6 nm) [45].

of the two regions shown in Figure 6.9e,f. This is important to note going forward as the discussion is shifted to the TFT performances, as this can impose a channel-length dependence

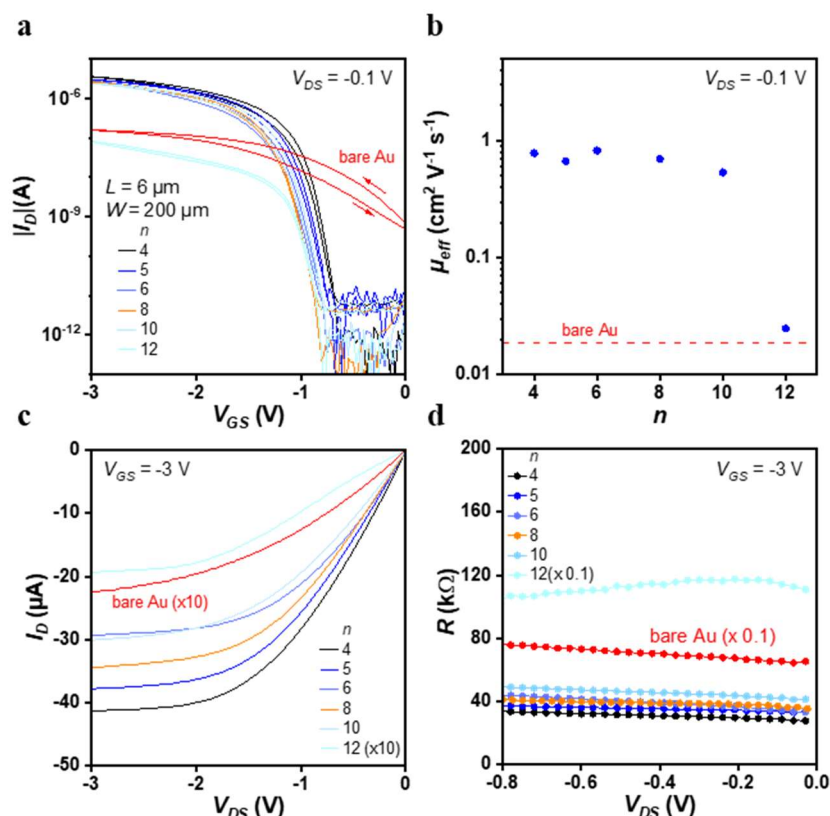


Figure 6.10 Static TFT characteristics: influence of contact functionalization with alkyl-thiols with various chain lengths.

a) Representative transfer curves ($V_{DS} = -0.1$ V) of DNTT TFTs with alkyl-thiol-functionalized Au bottom contacts having a channel length (L) of $6 \mu\text{m}$ and a channel width (W) of $200 \mu\text{m}$. n denotes the number of C atoms in the alkyl chain of the thiol. b) Effective carrier mobility (μ_{eff}) determined from the transfer curves in the linear regime of operation plotted as a function of n . c) Output curves of the same TFTs at $V_{GS} = -3$ V. d) Output resistance ($R = V_{DS}/I_D$) in the linear regime of operation (for $V_{DS} \rightarrow 0$). Red curves are for TFTs using gold source and drain contacts without functionalization with a thiol monolayer.

of the intrinsic channel mobility in the TFTs. For a sufficiently short channel, the disordered DNTT film can extend to the other contact, drastically inhibiting the intrinsic carrier mobility throughout the channel region. This has been observed in similar comparisons with both solution-processed organic semiconductors (e.g. diF-TESADT [319]) and vacuum-deposited organic semiconductors (e.g. pentacene [318]). In general, high degrees of disorder of the molecular orientation of the molecules in the semiconductor layer at any of the functional interfaces in a TFT can adversely affect charge transport in several ways, such as the introduction of a significantly higher density of trap states [269] and interruptions in the in-

plane π -orbital coupling leading to lower charge-carrier mobility and diminished TFT performance.

Figure 6.10 shows representative transfer curves, effective carrier mobility (μ_{eff}) in the linear regime of operation ($V_{DS} = -0.1$ V) and output curves of TFTs with a channel length (L) of 6 μm and a channel width (W) of 200 μm . All of the TFTs in which the gold source and drain contacts were functionalized with an alkyl-thiol monolayer (annotated in the figure by the number of carbon atoms in the alkyl chain, n) show significantly different characteristics compared to the control TFT with bare gold contacts (red curves). In particular, the off-state drain current and subthreshold swing are very high for the control TFT (1 nA and approximately 600 mV/decade, respectively). These are coupled with pronounced drain-current hysteresis between the forward and reverse sweeps of the gate-source voltage (V_{GS}) and a low effective carrier mobility (μ_{eff}) of 0.02 cm^2/Vs . These features are consistent with the disordered morphology of the DNTT film that was observed in the thin-film characterization. The low effective carrier mobility is likely a result of both large contact resistance and a smaller intrinsic channel mobility (μ_0) than is present for longer channel lengths. The modulation of the drain current is significantly improved for the TFTs in which the contacts were functionalized with an alkyl-thiol SAM. In general, the drain current on-off ratios are greater than 10^5 for the functionalized contacts. The off-state drain current is low (<10 pA) and the subthreshold swing is significantly sharper (between 77 and 95 mV/decade). There is also a notable shift in the turn-on voltage and the threshold voltage (V_{th}) towards more negative values as n is increased. This possibly indicates that more trap states form in the SAM and/or that the charge density in the channel needs to be larger for injection to occur for longer chains.

For n up to 10, the effective carrier mobility μ_{eff} is much higher than in the control TFT (Figure 6.10b), with the maximum of 0.82 cm^2/Vs for the TFT in which the contacts were functionalized with a monolayer of 1-hexanethiol ($n = 6$). One can again point to a notable comparison of these results that can be made to those from similar experiments using pentacene TFTs with alkyl-thiol SAMs reported by Stoliar et al. [70]. In their results, an exponential decay of the effective carrier mobility was observed for $n > 8$, wherein the charge transport along the alkyl backbone of the SAM presumably dominates injection. For smaller n , the effective carrier mobility in their TFTs tended to saturate and may in fact decrease for n as small as 3 (1-propanethiol). The results here using DNTT show a markedly lower dependence of μ_{eff} on n up to 1-decanethiol ($n = 10$), before dropping off considerably for 1-dodecanethiol ($n = 12$). In

addition, Stoliar et al. and other researchers [237] have noted a pronounced ‘odd-even’ effect due to the interaction between the HOMO level of pentacene and the angle of the terminal σ bond of the alkyl-thiol SAM that changes depending on the choice of odd or even n . In their pentacene TFTs, this translated to an alternating magnitude of the effective mobility attributed to the differences in injection related to the coupling of the SAM surface with the pentacene film. A similar effect for $n = 4, 5$, and 6 is also possibly seen here, though additional odd- n alkyl-thiol SAMs should be tested to confirm this.

An example of the width-normalized resistance (RW) of the TFTs with an alkyl-thiol SAM are shown in Figure 6.11a (1-butanethiol, $n = 4$). Similar fits were implemented to evaluate the width-normalized contact resistance (RCW) for the other alkyl-thiols. Figure 6.11b shows the results of RCW as a function of the gate overdrive voltage ($V_{GS}-V_{th}$) for all sets of TFTs that were evaluated. The linear fits shown in Figure 6.11b suggest that for all TFTs with thiol-functionalized contacts, the minimum contact resistance ($R_{C,0}$) extracted from the y-intercept is extremely small. The extraction for the TFT with the functionalization using 1-dodecanthiol ($n = 12$) is, however, likely inaccurate due to the larger threshold-voltage shift in those TFTs. The shift prevented the extraction of the contact resistance from a region of adequate charge accumulation where the contact resistance varies linearly with $(V_{GS}-V_{th})^{-1}$ according to the model of Luan and Neudeck [165]. The control TFTs without a SAM show a high estimated

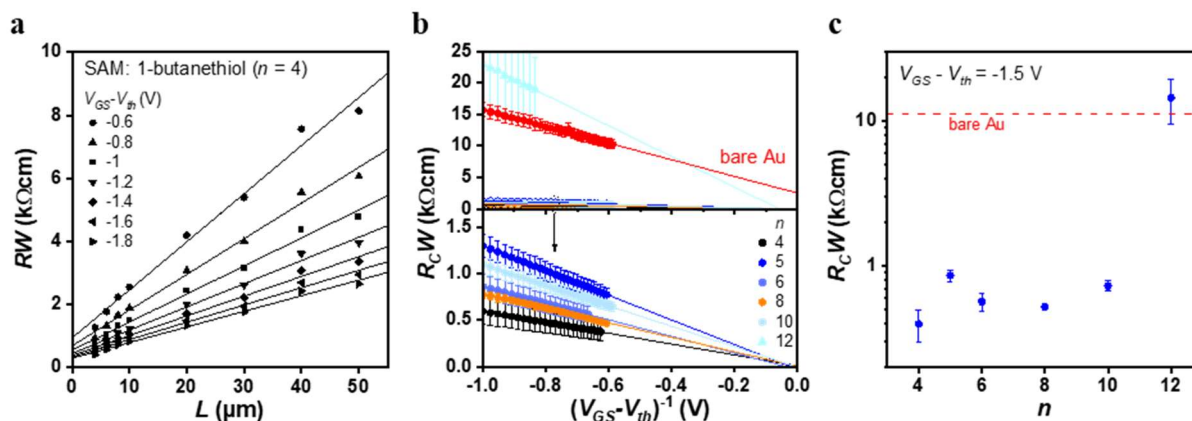


Figure 6.11 TLM analysis: influence of contact modification with alkyl thiols.

a) Channel-width normalized resistance (RW) of DNTT TFTs with Au bottom contacts functionalized with 1-butanethiol ($n = 4$) as a function of the channel length (L) at several gate overdrive voltages ($V_{GS}-V_{th}$). b) Width-normalized contact resistance (RCW). The linear extrapolations were used to evaluate $R_{C,0}$. c) RCW evaluated at $V_{GS}-V_{th} = -1.5$ V as a function of n . Red curves correspond to the control TFT using gold contacts without thiol functionalization.

$R_{C,0}W$ of 2.5 k Ω cm, which likely is attributed to the smaller grains in the DNNT layer on the bare-Au contacts which contributes a large voltage-independent resistance.

At a gate overdrive voltage ($V_{GS}-V_{th}$) of -1.5 V⁷, $R_{C}W$ follows the general trends of the results shown in Figure 6.10b for the effective carrier mobility (Figure 6.11c). This provides strong evidence that the variation in μ_{eff} is indeed a result of the differences in the charge-injection efficiency, i.e., in the contact resistance. On this point, the results are not quite in agreement with the results of Stoliar et al. [70], since they found a simple exponential dependence of the total resistance of the pentacene TFTs which they used as an estimate for the contact resistance. This may imply that for their devices, the static electrical performance was determined primarily by the crystallographic ordering and the intrinsic channel mobility of the pentacene film, which in turn depended strongly on the choice of the molecules for the contact functionalization, whereas here the injection through the SAM is perhaps the deciding factor. However, the results of Stoliar et al. also show a large spread in the measurement data, and they did not perform a more accurate measurement of the contact resistance, and so a comparison between their results and ours cannot yield definitive conclusions about the differences between charge injection in DNNT and pentacene TFTs.

A lingering question from the results of these experiments is why the jump in the contact resistance between $n = 10$ and 12 is so dramatic. No evidence can be seen of highly diminished DNNT morphology that could explain such a drop in the charge-injection efficiency. A possible explanation is that there is a transition from contacts that show Fermi-level pinning (see next section) for $n \leq 10$, to unpinned contacts in the Schottky-Mott regime for $n = 12$. This is possible because the work function of the gold contact is expected to shift to smaller values for large n due to a larger dipole moment. From the results that were shown in this section, one can only conclude that the charge injection cannot be adequately modeled by changes to the tunneling probability alone, since the results do not show an exponential dependence on the alkyl-chain length (assuming this adequately represents the SAM thickness). Instead, one can see an approximately linear dependence for relatively small thicknesses (approximately 1.6 nm based on $n = 10$ [306]) and a minor indication of odd-even chain-length effects for small n . While the results that have been obtained are not completely surprising given the prior art from Stoliar et

⁷ For 1-dodecanethiol ($n = 12$), the contact resistance at $V_{GS}-V_{th} = -1.5$ V could not be extracted directly from the transfer data due to the negative shift of the threshold voltage V_{th} . An estimate was made by assuming an exponential decay of the contact resistance.

al. [70], further experiments, including UPS measurements of the work function for alkyl-thiol SAMs on gold to address the possible Fermi-level pinning of the contacts as it relates to the chain length in alkyl-thiol SAMs in combination with temperature-dependent transport measurements like those which were presented in Section 5.2.2 for DPh-DNTT TFTs may be useful to verify the dominant injection mechanisms.

6.3 Dependence of the contact resistance on work-function tuning using thiols with large dipoles

Two factors which influence the transport of charges from a CML or SAM-functionalized contact to the organic-semiconductor layer are the thin-film morphology of the semiconductor at the interface with the contact and the energetic and spatial properties of the transport level(s) in the semiconductor. As discussed in the previous section, the surface energy of the CML-functionalized contact (γ_s) largely determines the subsequent thin-film morphology of the semiconductor layer and to secondary extent the transport levels [320]. The process of charge exchange between the metal contact and the semiconductor also depends critically on the energetic mismatch between the transport levels and the work function of the contact (ϕ_C). To minimize this mismatch, it is common practice to try to tune the contact work function through the deliberate choice of the metal according to the work function [142] or by functionalizing the metal surface with a thin layer of another material like a CML or SAM [288], [321]. Thiols with different dipole moments were used here to modify the work function of Au contacts in an effort to examine the efficacy of tuning ϕ_C to reduce the contact resistance in bottom-contact DNTT TFTs.

6.3.1 DNTT morphology characterization

To evaluate the DNTT morphology in the TFTs, SEM analysis of the contact-channel transition was performed (Figure 6.12a). For each of the different thiols, similar grain size for DNTT on top of each of the contacts was observed. In addition, the DNTT film on the channel (right side of each image) shows larger grain sizes, as opposed to the smaller grains sizes that were noticeable for a bare gold contact as shown in Figure 6.9 of the previous section on alkyl thiol SAMs. In this case, these purely surface-level analyses were complimented with grazing-incidence x-ray diffraction (GIXRD) measurements of a nominally 60-nm-thick DNTT film on each of the CML-functionalized Au surfaces and on the gate dielectric as part of a collaboration with the group of Prof. Paddy K. L. Chan at the University of Hong Kong. The GIXRD measurements show pronounced diffraction peaks at 18.1 °, 22.7 °, and 26.9 ° are assigned to the (110), (020), and (120) in-plane packing directions, respectively, and are indicative of strong in-plane π -stacking in a layered-herringbone molecular arrangement of the DNTT molecules which has been observed in DNTT single crystals (Figure 6.12b) [117]. It is

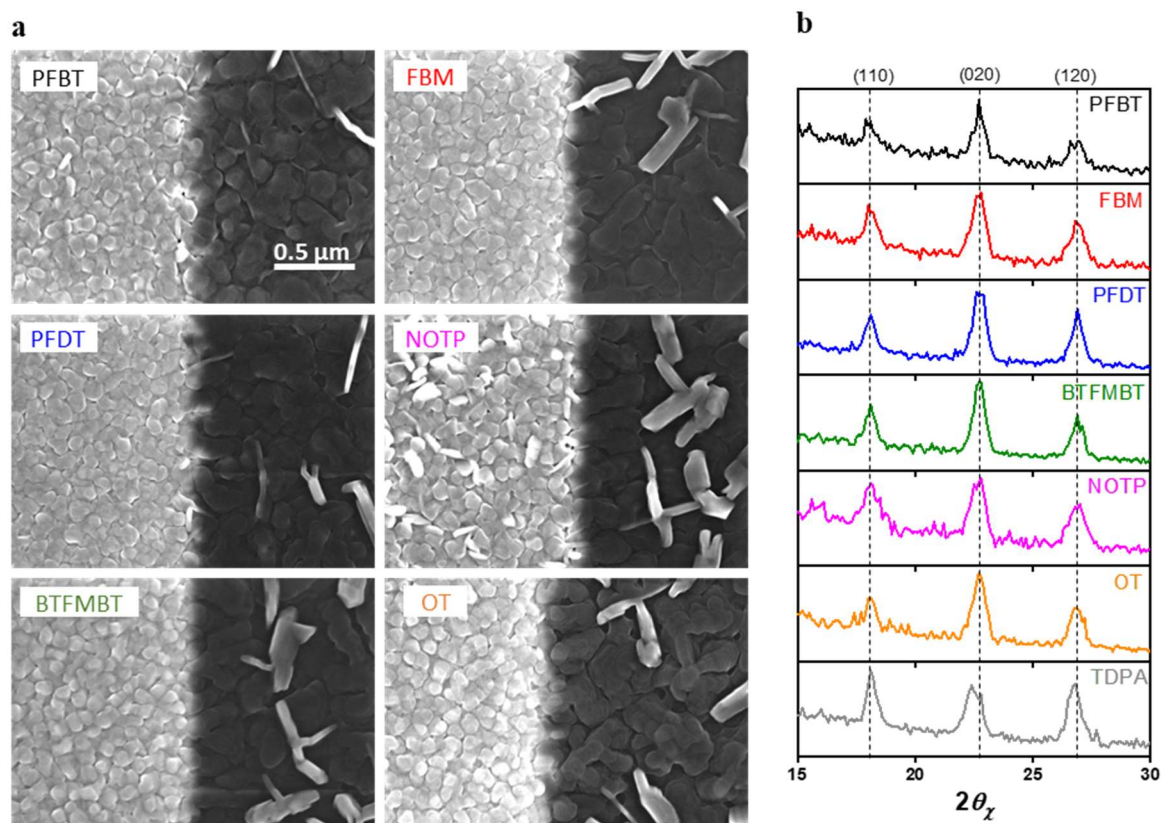


Figure 6.12 Electron microscopy and grazing-incidence x-ray diffraction analyses of DNTT films on Au contacts functionalized with various thiols.

- a) SEM images of the contact-channel transition in bottom-contact DNTT TFTs. Gold contacts (left half of each image) were functionalized with one of six different thiols.
 b) Grazing-incidence x-ray diffraction measurements on nominally 60-nm-thick DNTT films on each of the CMLs. For reference, the GIXRD spectrum of a DNTT film on the gate-dielectric SAM (TDPA) is also included.

notable that the diffraction is essentially the same, regardless of the thiol which was used to functionalize the Au contacts or if the DNTT layer was instead deposited on the AlO_x/TDPA gate dielectric (gray curve in Figure 6.12b). This is generally corroborated by the SEM analyses of the DNTT films on the functionalized contacts of the TFTs, both of which show that the DNTT morphology is minimally disturbed across the contact-channel transition (Figure 6.12a). A notable observation is that the very low surface energy (γ_s) of the NOTP-functionalized Au contacts does not appear to drastically affect the morphology of the DNTT film in either the SEM or GIXRD analyses. This goes somewhat counter to the expectation that DNTT would form a more disordered layer on low- γ_s surfaces (e.g. the bare gold contacts in Figure 6.9). This is perhaps due to the fact that the temperature of the substrate during the DNTT deposition

can greatly determine the strength of the interactions of the surface with the DNTT molecules, thereby influencing the nucleation and growth of DNTT crystals on the contacts [322]. This can be better illustrated by the results from another set of experiments wherein a nominally 30-nm-thick DNTT film was deposited at a substrate temperature of 60 °C onto bare Au and NOTP- and PFBT-functionalized Au contacts (Figure 6.13). In this case with additional substrate heating, there is a much more pronounced difference in the DNTT morphology on the different contacts, since the increased thermal energy enables the DNTT molecules to be more mobile on the surface, such that there is a greater driving force for film formation that promotes minimal interaction with the hydrophilic surface of either bare gold or NOTP-functionalized gold. This also results in marked differences in the electrical characteristics of the TFTs, as indicated by the transfer and output curves shown in Figure 6.13b-d.

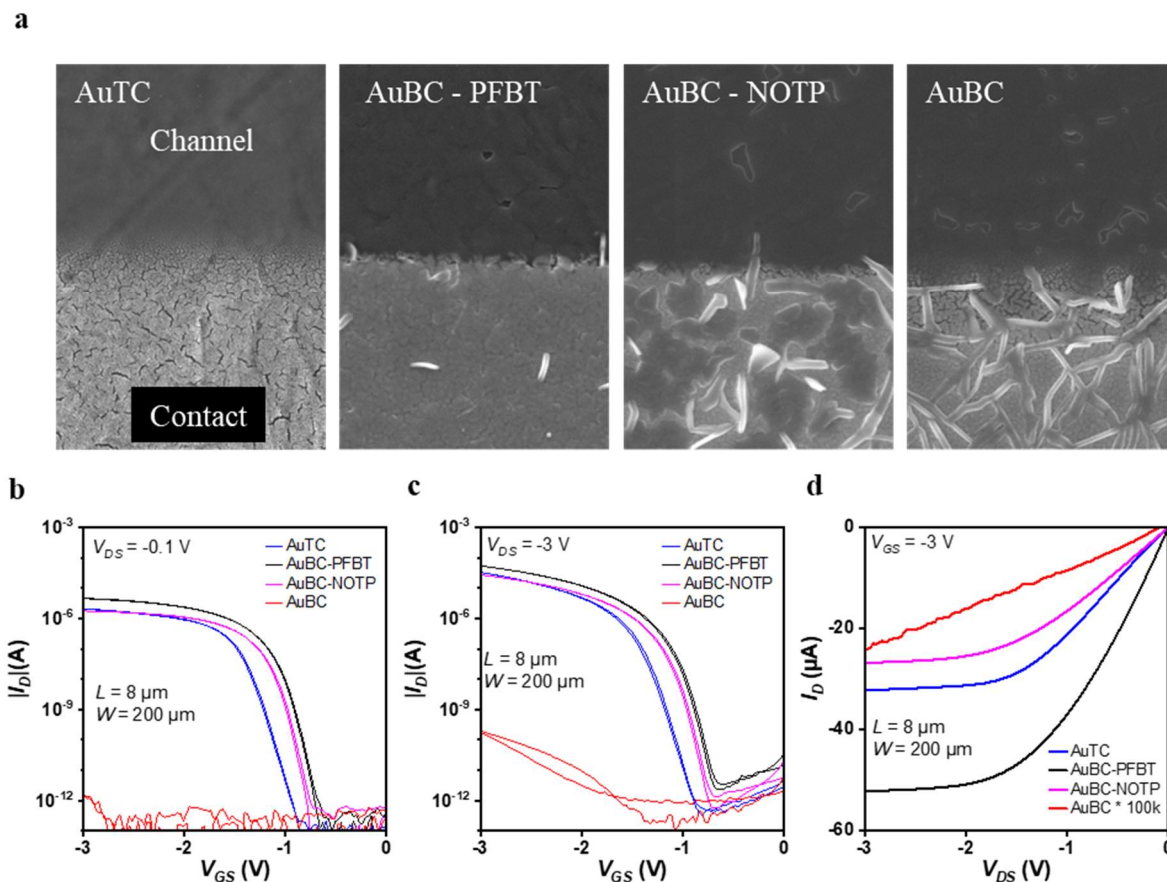


Figure 6.13 Flexible DNTT thin-film transistors with various contacts.

a) SEM micrographs of the contact-channel edge for gold top-contacts (AuTC), gold bottom contacts treated with functionalized with pentafluorobenzenethiol (PFBT), gold bottom contacts functionalized with 4-nitrothiophenol (NOTP), and gold bottom contacts with no additional treatments (AuBC). b-d) Transfer and output curves from TFTs with a channel length (L) of $8 \mu\text{m}$ and channel width (W) of $200 \mu\text{m}$. The substrate was heated to $60 \text{ }^\circ\text{C}$ during the DNTT deposition, which improves the in-plane π -stacking in the channel region, but also enhances the detrimental effects of the surface energy of the contacts on the DNTT thin-film morphology. PFBT functionalized contacts have the lowest surface energy of all bottom contacts, leading to good DNTT coverage and excellent electrical characteristics due to low contact resistance.

6.3.2 UPS measurements of DNTT on substrates with different work functions

For the UPS measurements of ϕ_{DNTT} , a 60-nm-thick DNTT film was deposited on separate test samples with each of the thiol-functionalized Au surfaces. Here, the thicker DNTT film was deposited without additional substrate heating. This proves to be beneficial in that it minimizes the differences in the DNTT thin-film morphology for the various surfaces as was shown in Figure 6.12 and therefore the results of the subsequent analyses of the contact resistance can primarily be attributed to differences in the contact work function ϕ_C . In addition

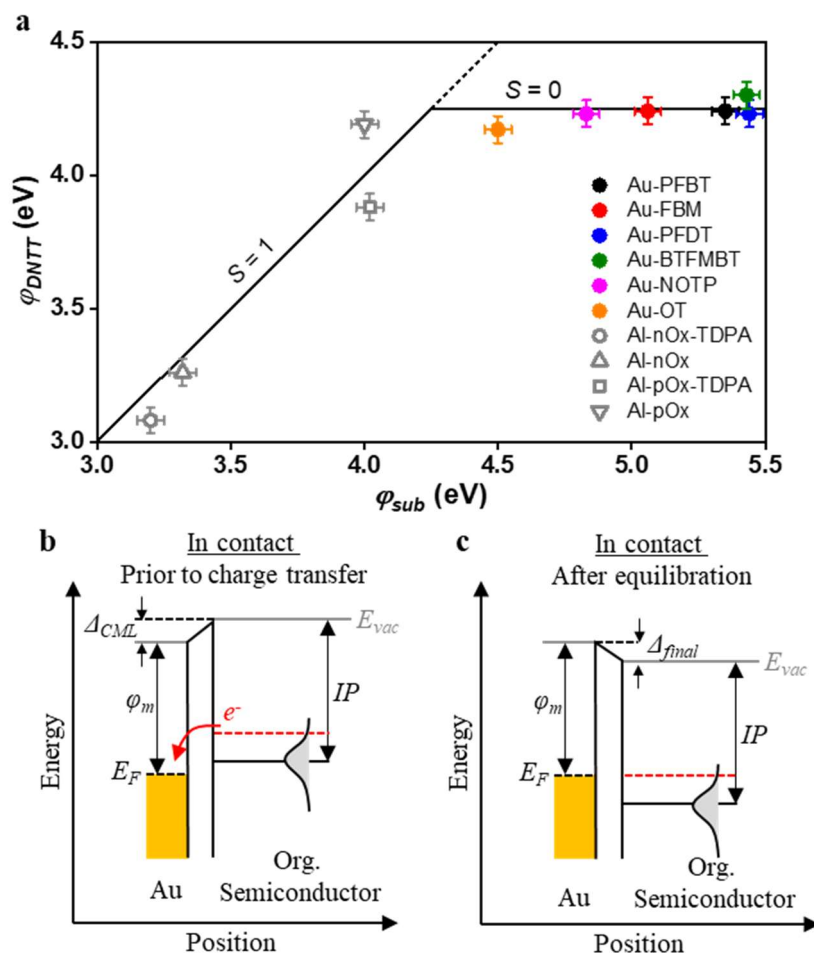


Figure 6.14 Evidence of Fermi-level pinning in DNTT.

a) UPS measurements of the work function of a DNTT film (ϕ_{DNTT}) deposited onto each of the substrates with corresponding work function (ϕ_{sub}). A deviation from the Schottky-Mott limit ($S=1$) to strong Fermi-level pinning ($S=0$) is observed at a work function of 4.2 eV. b) Schematic diagram of the CML-functionalized gold contact and DNTT film immediately after formation of the contact. c) Charge exchange across the interface leads to Fermi-level pinning.

to the gold surfaces functionalized with each of the different thiols, low-work-function substrates were also prepared using aluminum covered with either a native or a plasma-grown aluminum-oxide layer functionalized with an *n*-tetradecylphosphonic acid (TDPA) SAM or were left without any further functionalization (grey data points in Figure 6.14), similar to the gate dielectric typically employed in the TFTs. In Figure 6.14, ϕ_{DNTT} is then plotted against the various substrate work functions (ϕ_{sub}).

It can be clearly seen that ϕ_{DNTT} does not scale according to the Schottky-Mott limit ($S = 1$, dotted line in Figure 6.14), but rather the Fermi level is pinned for work functions above ~ 4.2 eV [188]. The pinning level is notably closer to the vacuum energy than is the HOMO expected for DNTT thin-films (5.44 eV) [45]. This suggests that there is possibly a preponderance of interface states likely related to the morphology of the polycrystalline DNTT film on the contacts and/or that the distribution of the occupied states is very broad and extends well into the bandgap (shown schematically in Figure 6.14b,c) [187], [188]. This has the important practical consequence that each of the CMLs or SAMs utilized here to improve the contact resistance produces a contact work function that is well within the pinning regime and that the injection barrier (Φ_B) cannot be reduced by further increasing the contact work function (ϕ_C) alone. The effects that this and the other features related to the choice of the functionalization layer have on the TFT performance, especially with respect to the contact resistance, are apparent in the TFT analyses (vide infra).

6.3.3 Static electrical performance of the DNTT TFTs

Each of the transfer and output characteristics shown in Figure 6.15 are from TFTs with an identical channel length (L) of 6 μm and width (W) of 200 μm . The only variable is the thiol that was used to functionalize the gold source and drain contacts, as indicated in the legend. The dependence of the drain current on the gate-source voltage (V_{GS}) is similar in terms of the threshold voltage (V_{th}) and the magnitude of the on-state drain current in both the linear and saturation regimes (Figure 6.15a,c, respectively). Except for the TFT in which the contacts were functionalized with 1-octanethiol (OT; orange curve), the dependence of the drain current on the gate-source voltage (V_{GS}) for a drain-source voltage (V_{DS}) of -0.1 V (Figure 6.15a) is highly nonlinear, which is indicative of the drain current being suppressed by the large contact resistance. This is most pronounced for the TFTs in which the contacts were functionalized

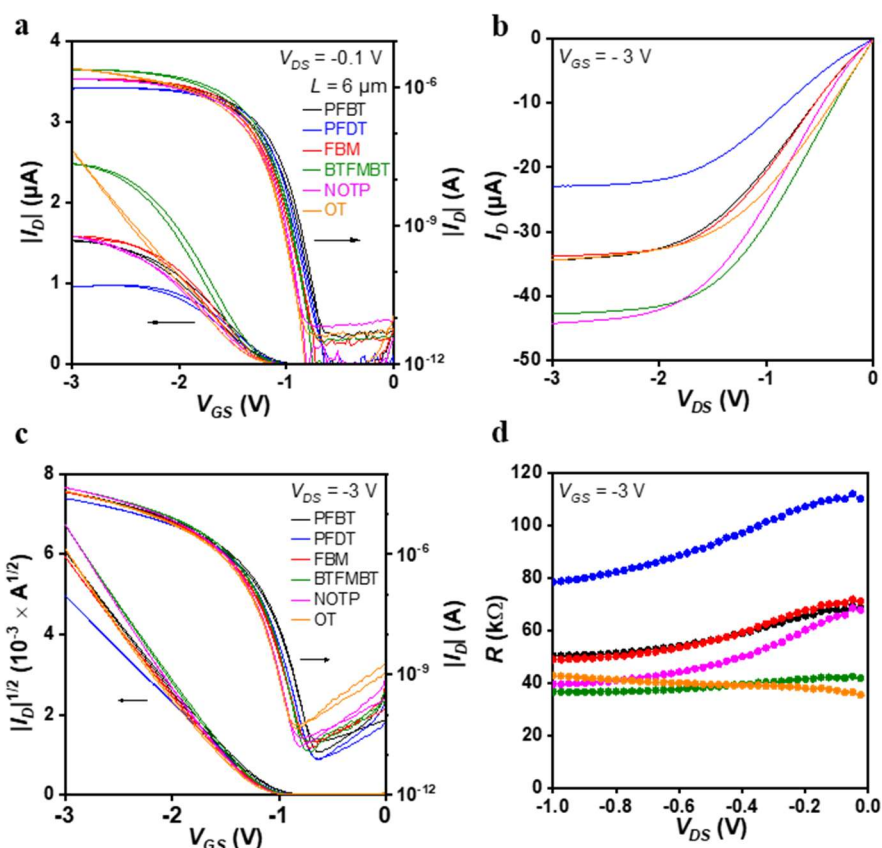


Figure 6.15 Static TFT characteristics: tuning the contact work function with different thiols

a) Transfer curves ($V_{DS} = -0.1 \text{ V}$) of DNTT TFTs with Au bottom contacts functionalized with various thiols having a channel length (L) of $6 \mu\text{m}$ and a channel width (W) of $200 \mu\text{m}$. b) Output curves at $V_{GS} = -3 \text{ V}$. c) Transfer curves ($V_{DS} = -3 \text{ V}$). d) Total output resistance ($R = V_{DS}/I_D$) from the output curves shown in (b).

with 1H,1H,2H,2H-perfluoro-1-decanethiol (PFDT; blue curve). This deviation of the measured transfer curves from the ideal scenario (in which the drain current is not limited by the contact resistance) is less pronounced when the transfer curves are measured with a larger drain-source voltage ($V_{DS} = -3 \text{ V}$; Figure 6.15c), which suggests that the contact resistance is strongly dependent on the applied drain-source voltage [323]. The dependence of the drain current on the drain-source voltage is apparent also in the output curves measured at $V_{GS} = -3 \text{ V}$ (Figure 6.15b) and in the point-wise total resistance ($R = V_{DS}/I_D$) (Figure 6.15d). A contact resistance independent of the drain-source voltage (Ohmic contact resistance) is observed only for the TFTs in which the contacts were functionalized using OT (orange curves) or 3,5-bis-trifluoromethylbenzenethiol (BTFMBT; green curves; Figure 6.15d). The pronounced suppression of the drain current by the contact resistance seen in Figure 6.15 for all but the

TFTs in which the contacts were functionalized with OT and BTFMBT is similar to what was observed for the TFTs in which the contacts were functionalized with 1-dodecanethiol, though the drain current is at least an order of magnitude higher in Figure 6.15 than in Figure 6.10.

An informative comparison can be made between PFDT and 1-decanethiol (DT) which have the same chain length, so that the thickness of the (in this case) SAMs can be assumed to be similar. The large dipole moment pointing towards the highly electronegative fluorine atoms of PFDT [324] results in a significant shift of the contact work function ϕ_C (5.44 eV in the presented UPS measurements, in agreement with ref. [325]), whereas a dipole moment pointing towards the substrate in the DT CML leads to a ϕ_C that is smaller (4.22 eV from ref.[326]) than that of bare Au. Despite this, DT clearly gives the better performance characteristics in the TFTs, including a higher drain current and Ohmic resistance at small V_{DS} . This is notably in direct contrast to other reported comparisons between these two thiols in organic TFTs [327]. The discrepancies in the presented results are likely linked to multiple factors that are apparently different from the other reported studies in which organic semiconductors other than DNTT were used. Most significantly, Fermi-level pinning likely nullifies any expected benefit of the higher contact work function ϕ_C for the TFTs utilizing a PFDT SAM. This then evidently eliminates the only advantage that the PFDT SAM would have over the more well-ordered DT SAM on the gold contacts, explaining the better charge injection in the TFTs which used DT for the contact functionalization [314], [326], [328].

6.3.4 Contact resistance analysis

The contact resistance and intrinsic channel mobility of the TFTs fabricated using the different CMLs is obtained through TLM analysis (Figure 6.16). The dependence of $R_C W$ and μ_0 on the gate-source voltage V_{GS} are shown in Figure 6.16a. As with the previous study on TFTs with alkyl-thiol CMLs, μ_0 is relatively constant above a certain gate overdrive voltage and is between 1 and 2 cm² V⁻¹ s⁻¹. $R_C W$ shows some variation in its dependence on V_{GS} for the different thiols. For 1-octanethiol (OT), again extrapolation of the contact resistance $R_C W$ yields a minimum resistance ($R_{C,0}$) that is near 0 Ω . For the other CMLs, $R_C W$ actually starts to *increase* as V_{GS} is made more negative beyond $V_{GS}-V_{th} \sim -1.4$ V. This is unusual, since one would normally expect the contact resistance to decrease with increasing gate-source voltage. It is possible that this increase in $R_C W$ at higher V_{GS} occurs because of bias-stress effects wherein the threshold voltage shifts towards more negative values during the measurement (see

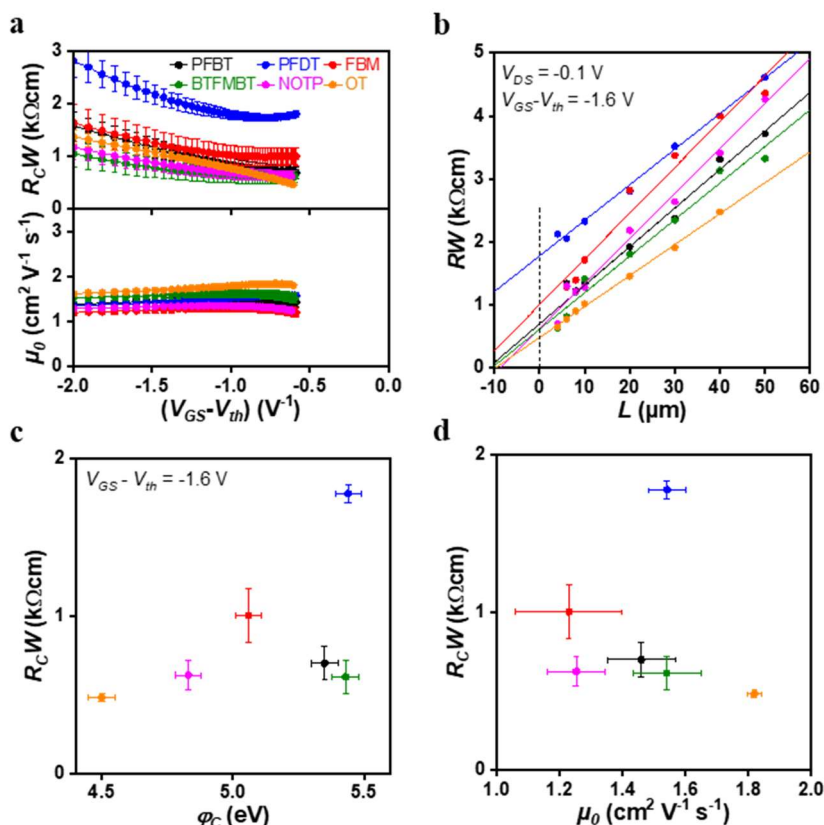


Figure 6.16 TLM analysis results for TFTs with various contact work functions.

a) Channel-width-normalized contact resistance (R_CW) and intrinsic channel mobility (μ_0) as a function of the inverse of the gate overdrive voltage ($V_{GS}-V_{th}$) of DNTT TFTs with Au bottom contacts functionalized with various thiols. b) Example fits of the total width-normalized resistance (RW) versus the channel length (L) at $V_{GS}-V_{th} = -1.6$ V. c) R_CW as a function of the contact work function (ϕ_C) and (d) μ_0 .

for instance Section 5.3.1 with a PFBT CML in DPh-DNTT TFTs). Nonetheless, a comparison of R_CW with respect to other parameters, such as the contact work function (Figure 6.16c) and the intrinsic channel mobility (Figure 6.16d) can be made. It can readily be seen that R_CW does not show a decrease with the contact work function ϕ_C that might be expected for Schottky-Mott scaling [186]. In fact, the highest R_CW of 1.8 k Ω cm is measured for the PFDT CML, which has the highest $\phi_C = 5.44$ eV of any of the CMLs utilized in this study. This result is most likely a direct consequence of the pinned Fermi level which effectively fixes the barrier height at the source contact in the TFTs [257]. There are inclinations to associate some of the variability in R_CW between the different CMLs with the differences in the thickness of the CML, as has also been reported for the alkyl-thiol SAMs in Section 5.2. See for instance the larger R_CW of the TFTs which have a CML composed of 4-fluorobenzyl-mercaptan (FBM, red

data points), which is expected to have a slightly larger thickness than either PFBT, NOTP, or BTFMBT. However, the slightly lower intrinsic channel mobility of the DNNT layer may also contribute to the higher R_CW (Figure 6.16d) [78]. Curiously, the OT SAM, which has nominally the second largest thickness and the smallest work function, results in the lowest R_CW of the different CMLs in this part of the study. The reason for this is not currently clear, but the explanations may lay in the differences between implementing a dense SAM vs. a possibly less-densely packed CML as the functionalization layer.

6.4 Conclusions

In this chapter, the charge injection properties in bottom-gate, bottom-contact organic TFTs utilizing chemisorbed molecular monolayers (CML) and self-assembled monolayers (SAM) to improve the contact interface have been investigated. The most notable preliminary findings were that the dependence of the contact resistance on the chain length of alkyl-thiol SAMs (i.e. the thickness) was far subdued compared to a similar study from Stoliar et al. [70] that focused on charge transport in pentacene bottom-gate, bottom-contact TFTs. This study was followed up with an investigation of the effects of using other thiol CMLs with different dipole moments to tune the work function of the gold source and drain contacts (ϕ_C). It was found that the work function of DNTT (ϕ_{DNTT}) did not show the expected Schottky-Mott scaling ($S = d\phi_{DNTT}/d\phi_C = 1$), but rather that the Fermi level is evidently strongly pinned to a mid-gap level around 4.2 eV, which is more than 1 eV in difference to the HOMO level of DNTT (5.4 eV). It can be reasonably predicted that this is the reason that the contact resistance that was measured in the corresponding DNTT TFTs was essentially independent of the contact work function. The charge injection in these TFTs is apparently more dependent on the CML thickness and likely on the molecular ordering of the adsorbed molecules in the CML based on the analyses of both the TFTs and the surface and spectral analyses of the DNTT layers and CMLs on gold. A further discussion of the significance of these results for the future progress in eliminating the contact resistance in organic TFTs can be found in the Final Conclusions and Remarks chapter of this thesis.

7 Final conclusions and remarks

After several decades of cumulative research efforts from many groups, organic transistors are beginning to achieve performance levels that may enable them to be used in low-power high-frequency commercial electronics applications such as active-matrix organic light-emitting diode (AMOLED) displays [81], [141], [279]. This is primarily owing to the development of more-effective fabrication methods to reduce the critical dimensions (channel length and parasitic overlaps) coupled with improvements to the charge-carrier mobility and reduction of the contact resistance. A key result for organic thin-film transistors (TFTs) that was shown in this thesis was the experimental validation for previous theoretical results by Karin Zojer et al. [17], [18] that predicted that a coplanar TFT geometry combined with a very thin gate dielectric can yield lower contact resistance than comparable staggered TFTs (Chapter 4 and refs. [141], [238]). This ultimately led to a new record for the supply-voltage-normalized transit frequency of organic TFTs (21 MHz at 3 V). In fact, transit frequencies in excess of 100 MHz may already be achievable using the silicon stencil mask lithography approach by noting that the minimum gate electrode width that has been demonstrated is about 3 μm [134] and the minimum channel length in an organic TFT using silicon stencil masks is that has been demonstrated is 0.3 μm [329]. Using these dimensions and the metrics reported in Section 5.2.6 for the intrinsic channel mobility ($6 \text{ cm}^2 \text{ V}^{-1} \text{ s}^{-1}$) and contact resistance (10 Ωcm), a transit frequency slightly above 100 MHz would be expected; more than twice the current record metric for any organic transistor technology (40 MHz at 8.6 V, shown in a vertical organic permeable-base transistor [279]). This would also match the state-of-the-art for flexible indium gallium zinc oxide (IGZO) TFTs [262] and expand the possible applications of organic TFTs.

While a transit frequency of 100 MHz would indeed be an exciting milestone from an electrical engineering perspective for organic transistors, further progress to increase the transit frequency to 1 GHz and beyond is not likely to be realized without the use of fabrication approaches that are capable of more aggressive scaling of the dimensions of the TFTs. This includes e.g. electron-beam lithography [330] or nanoimprint lithography [331], [332]. The realization that bottom-gate, bottom-contact TFTs with low contact resistance could be produced has motivated a pursuit towards gigahertz organic TFTs fabricated using electron-beam lithography within the Organic Electronics group in collaboration with the Nanostructuring Laboratory at the Max Planck Institute [15]. As of the writing of this thesis the results have so far not yielded new records for the transit frequency, primarily because of

high contact resistance (typically around 1 k Ω cm, see Figure A1.4 in the Appendix). This is most likely occurring due to residues left on the contacts after the polymer resist is dissolved and/or the sharper edges of the contacts, which can disrupt the crystal morphology of the organic-semiconductor layer. Therefore, it remains critical for concurrent research efforts to focus on understanding and improving the organic semiconductor-contact interface from both an engineering and materials science perspective.

Temperature-dependent measurements of the contact resistance were shown in Section 5.2.2 that indicate that hole injection into the organic semiconductor DPh-DNTT is mostly a thermally activated process, even in the more-ideal case of a thin gate dielectric and functionalization of the source and drain contacts to increase the work function. This means that charge injection is still most-strictly determined by the effective height of the Schottky barrier that forms at the organic semiconductor-contact interface. Unfortunately, it was also shown that the near ubiquitous method of using chemisorbed molecular monolayers (CMLs) or self-assembled monolayers (SAMs), ostensibly to reduce the height of the Schottky barrier by modifying the work function of the contact metal, may be strictly limited by the occurrence of Fermi-level pinning. This effectively prevents the Schottky-barrier height from being reduced beyond a certain level that is determined by the semiconductor, regardless of the contact work function. For DNTT, it was shown that Fermi-level pinning occurs at around 4.2 eV, meaning that the Schottky barrier may be as high as 1.2 eV, since the HOMO level of DNTT is around 5.4 eV. This also resulted in a disappointing minimum contact resistance for bottom-contact DNTT TFTs of about 0.4 k Ω cm attained for a 1-butanethiol SAM, an order of magnitude higher than what was demonstrated in analogous DPh-DNTT TFTs.

The root cause of Fermi-level pinning is typically assigned to mid-gap states that form at the interface once the contact is fabricated. These can be attributed to various culprits including a more disordered semiconductor morphology near the interface or quite irrevocably to the distribution of the density of states inherent to the semiconductor [187], [191]. While contact doping with strong acceptors may help to alleviate the effects of disorder, such as trap states at the interface, increasing the mobile carrier density and improving the contact resistance [107], [121], the wide distribution of the density of states of the host semiconductor may represent a permanent roadblock for efficient injection into some organic semiconductors. It therefore remains to be seen if any interlayer approach can be expected to further improve carrier injection without also changing the organic semiconductor. The contact-resistance question

notwithstanding, an important practical note must be made clear: any non-self-patterning approach to modify the contact-organic semiconductor interface (and only the interface), such as contact doping or oxide interlayers, will likely remain very challenging to apply to organic TFTs with the extremely small lateral dimensions required for high-frequency operation.

In such times where the path forward to further improvement is not readily apparent, some hints may be gleaned from other materials systems and fields of research. One such source of insight may lay in the body of research on field-effect transistors (FET) based on two-dimensional (2D) semiconductors [16]. For instance, in 2D FETs based on transition-metal dichalcogenides (TMD) such as MoS₂ the contact resistance also tends to be relatively high if careful control of the fabrication of the contacts is not heeded. The main issues that determine the contact resistance in 2D FETs are generally the same: Fermi-level pinning and high energy barriers for charge injection [16]. Naturally, there are also some very crucial differences between most organic TFTs and 2D FETs that must also be appreciated. Of initial practical importance is that there are far fewer materials to choose from in 2D FETs as compared to the uncountable possible variations for organic semiconductors. This is intimately coupled with the advantage that the high degree of structural ordering of 2D materials facilitates far simpler and more accurate modelling compared to organic materials, especially with respect to interfaces and the wide variation of crystal morphologies that are possible [66], [333]. These factors have certainly enabled a much more controlled systematic approach for research into and the rapid reduction of the achievable contact resistances in 2D FETs [16]. Another major difference is that the semiconductor in 2D FETs is usually an ultrathin and single-crystalline layer with a much narrower density of states and a higher carrier mobility than what is achieved in even the best organic-semiconductor single-crystals [94]. While it can be plainly demonstrated that the carrier mobility in the channel region is irrelevant for enhancing the dynamic transistor performance if the contact resistance is too high [13], the mobility of the semiconductor in the vicinity of the interface can influence various aspects of the charge injection, including image-force lowering and diffusion-limited transport [176], [181]. Indeed, higher carrier mobility along with a narrower density of states are likely contributing reasons that the ultrathin, single-crystalline organic-semiconductor layers implemented by some other groups have yielded impressive contact resistances below 100 Ωcm [81], [86]. It should, however, be noted that using semiconductors with high in-plane mobility and a narrow density of states is evidently not a catch-all solution, as shown in transistors using other highly-

crystalline organic-semiconductor layers such as 2-decyl-7-phenyl[1]-benzothieno[3;2-b][1]benzothiophene (Ph-BTBT-C₁₀) [157] and rubrene [334], as well as in some 2D materials [335]. This is often because the in-plane charge-carrier mobility is generally much higher than the out-of-plane mobility, leading to high contact resistance especially in staggered transistor geometries that are so far necessary for such devices [16]. This is then a reason to use the thinnest layer possible, making contact resistance almost entirely an interface problem.

So what attributes of the interface are still to be addressed? A well-known issue for contacts in 2D FETs that is analogous for organic TFTs is that there often exists a van der Waals (vdW) gap between the metal contact and the top-most semiconductor layer. This imposes an additional tunneling barrier that reduces the efficiency of charge transport from the metal to the semiconductor [16]. Both the vdW gap and a typically low out-of-plane mobility have been partially circumvented in 2D FETs by forming so-called edge contacts where the metal contact is fabricated so that charges are injected at the in-plane edge of the semiconductor crystal. Edge contacts might also be implementable in organic transistors, especially in the case of highly-crystalline monolayers [81], [86]. However, since the molecular crystals are formed by vdW interactions between molecules in the monolayer, edge contacts may not be feasible for organic TFTs. Also, for practical contacts where an out-of-plane contribution to charge injection is inevitable, the vdW gap should ideally be eliminated entirely by hybridization of the metal with the first surface layer of the semiconductor to minimize this contribution to the injection barrier. This is achieved in TMD FETs by careful selection of the contact metal and the semiconductor with additional steps to remove surface contaminants. A drawback is that hybridization of the metal with the TMD is not always beneficial [336], and this approach often requires subsequent high-temperature annealing processes to complete the reaction at the interface.

For organic transistors, a low-temperature process would need to be developed to form similarly intimate contact interfaces. This might be achieved by including a reactive functional group on the organic semiconductor molecule that can facilitate hybridization with the contact (e.g. a thiol for metals). For bottom contacts, this might then simply be a chemisorbed molecular monolayer which includes the intended semiconductor motif as the tail group (SC-CML). Likely, the main challenge would be attempting to implement a well-ordered layer across the contact-to-channel interface, which would most likely have different surface chemistries and reactivities (metals, oxides, or other organics). In addition, a hybridized interface does not necessarily do anything to help with Fermi-level pinning. De-pinning

approaches such as the use of a buffer interlayer are also mutually exclusive in principle to the hybridization approach for removing the vdW gap. However, some special examples do exist in 2D FETs, such as MoTe₂ FETs with scandium contacts, where a single-atom-thick layer of hexagonal boron nitride can be inserted to prevent Fermi-level pinning and the (in this case) detrimental reaction of the first few layers of MoTe₂ with the scandium [336]. In this case there is a minimal vdW gap and the Fermi level is effectively de-pinned to yield extremely low contact resistance (0.1 Ωcm). In bottom-contact organic TFTs, it may be possible to implement a similar strategy with a donor (acceptor) molecule that forms a single-atom-thick chemisorbed layer on gold contacts to improve electron (hole) injection [64]. Another route might be to engineer a ‘de-pinning layer’ directly into the SC-CML molecules themselves simply by the addition of an insulating functional group that separates the semiconductor from the contact, rather than having to rely on a separately-formed interlayer. It is possible that this is already a reason that lower contact resistance is achieved in C₁₀-DNNT and DPh-DNNT than in DNNT in the TFTs that were shown in this work.

In closing, some of the results presented in this thesis can be considered the state-of-the-art for organic TFTs by several metrics, none more critical than the contact resistance. However, when taken in context with the accumulated research efforts focusing on charge injection into organic semiconductors over the last several decades [12], [20], especially with respect to other reports of similarly-low contact resistances in organic TFTs [81], [86], the contact resistance results also appear to indicate that a plateau has been reached at around 10-100 Ωcm. This hypothesis is based on both the current fundamental understanding of the contact-organic semiconductor interface and the approaches that have so far been developed for improving charge injection. It is unlikely that this roadblock will be overcome without the development of new, or at least more-nuanced, approaches for engineering the contact interface. These generally must take into account and address the deeper fundamental reasons, at the interface level, for high contact resistance such as Fermi-level pinning and a vdW gap.

Symbols and Abbreviations

Symbol/Abbreviation	Definition/Meaning	Units
[RuCp*(mes)] ₂	Ruthenium(pentamethylcyclopentadienyl)(1,3,5-trimethylbenzene)	
$\langle x^2 \rangle$	Mean free path of charge carriers	m
μ	Mobility	m ² V ⁻¹ s ⁻¹
μ_0	Intrinsic channel mobility (such as in an organic TFT)	m ² V ⁻¹ s ⁻¹
$\mu_{0,C}$	Characteristic electron mobility of a material	m ² V ⁻¹ s ⁻¹
$\mu_{0,p}$	Temperature-independent mobility pre-factor	m ² V ⁻¹ s ⁻¹
μ_{eff}	Effective mobility	m ² V ⁻¹ s ⁻¹
μ_z	Collective dipole moment perpendicular to a surface	C m
A^*	Effective Richardson constant	A m ⁻² K ⁻²
a, b	Incident and reflected power waves	
A_{bulk}	Absorbance (bulk)	
AFM	Atomic force microscopy	
AFM	Atomic force microscopy	
ALD	Atomic layer deposition	
AlO _x	Aluminum oxide (unknown stoichiometry)	
Alq ₃	Tris(8-hydroxyquinolino)aluminum	
AMLCD	Active-matrix liquid crystal displays	
AMOLED	Active-matrix organic light-emitting diode	
A_{SAM}	Absorbance (self-assembled monolayer)	
a-Si:H	Hydrogenated amorphous silicon	
ATR	Attenuated total reflection	
BC	Bottom contact	
BGBC	Bottom gate - bottom contact	
BGTC	Bottom gate - top contact	
BT	1-butanethiol	
BTBT	Benzothieno[3,2-b]benzothiophene	
BTFMBT	3,5-bis-trifluoromethylbenzenethiol	
C	Capacitance	F
C'	Series capacitance of the gate-dielectric and interface capacitances	F
C ₁₀ -DNTT	2,9-didecyldinaphtho- [2,3-b:2,3-f]thieno[3,2-b]thiophene	
C ₆₀	Buckminster fullerene	
C ₈ -DNBDT-NW	3,11-dioctyl-dinaphtho[2,3-d:2',3'-d']benzo[1,2-b:4,5-b']dithiophene	
CB	Conduction band	
C_C	Contact capacitance	F
C_{ch}	Channel capacitance	F

C_{diel}	Area-normalized capacitance of the gate-dielectric layer	$F\ m^{-2}$
C_G	Total gate capacitance	F
C_{GD}	Capacitance attributed to the gate-to-drain overlap area	F
$C_{GD,ov}$	Parasitic capacitance from the gate-to-drain overlap in a TFT	F
C_{GS}	Capacitance attributed to the gate-to-source overlap area	F
$C_{GS,ov}$	Parasitic capacitance from the gate-to-source overlap in a TFT	F
C_I	Interface trap state capacitance	F
CML	Chemisorbed molecular monolayer	
CuPc	Copper phthalocyanine	
D	Diffusion coefficient	$m^2\ s^{-1}$
d	Layer thickness between parallel planar electrodes	m
$D(E)$	Diffusivity as a function of energy	$m^2\ s^{-1}\ eV^{-1}$
DDT	1-dodecanethiol	
diF-TESADT	2,8-difluoro-5,11-bis (triethylsilylethynyl)anthradithiophene	
d_{int}	Width of the interfacial region in a metal-semiconductor contact	m
DNTT	Dinaphtho[2,3-b:2',3'-f]thieno[3,2-b]thiophene	
DOGS	Density of tailing gap states	
DOS	Density of states	
DPh-DNTT	2,9-diphenyl-dinaphtho[2,3-b:2',3'-f]thieno[3,2-b]thiophene	
DT	1-decanethiol	
E_0	Energy around which the density of states is centered	eV
EA	Electron affinity	eV
E_A	Acceptor energy level	eV
E_{act}	Activation energy	eV
E_F	Fermi level	eV
E_{HOMO}	HOMO energy	eV
E_{ICT}	Integer charge-transfer state energy level	eV
E_{LUMO}	LUMO energy	eV
$E_{T,n}$	Discrete trap state energies in MTR theory	eV
E_{vac}	Vacuum energy	eV
f	Frequency of oscillation	Hz
F	Applied electric field	$V\ m^{-1}$
F_{\parallel}	Lateral component of the electric field imposed by the gate-source voltage in a TFT	$V\ m^{-1}$
F_{\perp}	Vertical component of the electric field imposed by the gate-source voltage in a TFT	$V\ m^{-1}$
F ₄ -TCNQ	Tetrafluoro-tetracyanoquinodimethane	
FBM	4-fluorobenzyl mercaptan	
f_{eq}	Average equivalent frequency oscillation of the inverter stages in a ring oscillator	Hz
FET	Field-effect transistor	

FLP	Fermi-level pinning	
f_{osc}	Oscillation output signal frequency of a ring oscillator	Hz
f_T	Unity-current gain (transit) frequency	Hz
FTIR	Fourier transform infrared	
GCA	Gradual channel approximation	
GER	Generalized Einstein relation	
GIXRD	Grazing incidence x-ray diffraction	
g_m	Channel transconductance in a TFT	S
h	Planck's constant	eV s
\hbar	Reduced Planck's constant	eV s
h_{21}	Ratio of the small signal drain and gate currents in a TFT	dB
HOMO	Highest occupied molecular orbital	
HT	1-hexanethiol	
i_D	Small signal drain current	A
I_D	Drain current	A
IDTBT	Poly(indacenodithiophene-benzothiadiazole)	
IE	Ionization energy	eV
IFL	Image force lowering	
i_G	Small signal gate current	A
I_G	Gate current	A
IGZO	Indium gallium zinc oxide	
ITO	Indium-doped tin oxide	
J_{DT}	Total current density transported across metal-semiconductor interface by direct tunneling	A m ⁻²
J_{FN}	Total current density transported across metal-semiconductor interface by Fowler-Nordheim tunneling	A m ⁻²
J_{inj}	Injected current density from metal to semiconductor	A m ⁻²
J_{SM}	Total current density transported across metal-semiconductor interface (Scott-Malliaras model)	A m ⁻²
J_{TE}	Total current density transported across a reverse-biased metal-semiconductor interface by thermionic emission	A m ⁻²
J_{tr}	Transfer integral	eV
k_B	Boltzmann constant	eV K ⁻¹
L	Channel length of a TFT	m
l_0	Characteristic contact length	m
$L_{1/2}$	Channel length at which the effective mobility is half of the intrinsic channel mobility	m
L_{ext}	Extended contact length	m
L_{ov}	Gate-to-contact overlap length of a TFT	m
$L_{ov,GD}$	Gate-to-drain overlap length of a TFT	m
$L_{ov,GS}$	Gate-to-source overlap length of a TFT	m
L_T	Transfer length	m
LTPS	Low-temperature polysilicon	
L_{tr}	Temperature-dependent transient localization length	m
LUMO	Lowest unoccupied molecular orbital	
m^*	Effective mass	kg
MISM	Metal-insulator-semiconductor-metal	

MOSFET	Metal-oxide-semiconductor field-effect transistor	
MR	Molar ratio	
MTR	Multiple trapping and release	
$N(E)$	Density of states within an organic semiconductor layer as a function of energy	$\text{m}^{-3} \text{eV}^{-1}$
N_0	Density of states available for hopping transport in the Scott-Malliaras model	m^{-2}
N1100	N,N'-bis(2,2,3,3,4,4,4) heptafluorobutyl-1,7-dicyano-perylene-(3,4:9,10)-tetracarboxylic diimide	
N_A	Neutral dopant density	m^{-3}
N_A^-	Ionized dopant density	m^{-3}
n_C	Total carrier concentration	m^{-3}
N_C	Characteristic carrier concentration	m^{-3}
N_{CML}	Grafting density of molecules chemisorbed to a surface	m^{-2}
NDI	Naphthalene diimide	
N_{int}	Density of interface mid-gap states in a metal-semiconductor contact	$\text{eV}^{-1} \text{m}^{-2}$
N_{it}	Density of trap states of in the organic semiconductor layer near the interface with the dielectric in a TFT	$\text{eV}^{-1} \text{m}^{-2}$
NOTP	4-nitrothiophenol	
N_t	Characteristic band density of states	m^{-3}
OLED	Organic light-emitting diode	
OPV	Organic photovoltaic	
OT	1-octanethiol	
p	Free carrier density	m^{-3}
P(NDI2OD-T2) or N2200	{[N,N'-bis(2-octyldodecyl)-naphthalene-1,4,5,8-bis(dicarboximide)-2,6-diyl]-alt-5,5'-(2,2'-bithiophene)}	
P3HT	Poly (3-hexylthiophene)	
pBTTT	Poly (2,5-bis(3-alkylthiophen-2-yl) thieno[3,2- <i>b</i>]thiophene)	
PDI1MPCN2	N,N'-di((S)-1-methylpentyl)-1,7(6)-dicyano-perylene-3,4:9,10-bis(dicarboximide)	
PEDOT	Poly (3,4-ethylenedioxythiophene)	
PEIE	Polyethyleneimine	
PEN	Polyethylene naphthalate	
PFBT	Pentafluorobenzenethiol	
PFDT	1H,1H,2H,2H-perfluoro-1-decanethiol	
PFM	Peak force microscopy	
Ph-BTBT-C ₁₀	2-decyl-7-phenyl-benzothieno[3,2- <i>b</i>]benzothiophene	
PI	Polyimide	
PM-IRRAS	Polarization-modulation infrared reflection-absorption spectroscopy	
PMMA	Poly (methyl methacrylate)	
PS	Polystyrene	
PSS	Polystyrene sulfonate	
PT	1-pentanethiol	
q	Elementary charge	C
QCM	Quartz crystal microbalance	

Q_s	Areal density of mobile charge carriers in the channel region	C m^{-2}
$Q_{s,diel}$	Areal density of charged states in the gate dielectric	C m^{-2}
R	Resistance	Ω
r_0	Output resistance	Ω
R_C	Contact resistance	Ω
$R_{C,0}$	Minimum contact resistance	Ω
R_{ch}	Channel resistance in a TFT	Ω
R_{CS}	Specific contact resistance at zero bias	$\Omega \text{ m}^{-2}$
R_{dep}	Deposition rate	\AA s^{-1}
RO	Ring oscillator	
R_{sh}	Sheet resistance	Ω/\square
S	Derivative of the Schottky barrier height with respect to the contact work function	
SAM	Self-assembled monolayer	
SCLC	Space-charge limited current	
SEC	Secondary electron cutoff energy	eV
SEM	Scanning electron microscopy	
S_{ij}	Element of the S-parameter matrix	
SS	Subthreshold swing	V decade^{-1}
STM	Scanning tunneling microscopy	
T	Absolute temperature	K
TC	Top contact	
t_{diel}	Thickness of the dielectric layer in a parallel plate capacitor or TFT	m
TDPA	<i>N</i> -tetradecylphosphonic acid	
TE	Thermionic emission	
TFE	Thermionic field emission	
TFT	Thin-film transistor	
TGBC	Top gate - bottom contact	
TGTC	Top gate - top contact	
TIPS pentacene	6,13-bis(triisopropylsilyl)ethynylpentacene	
TLM	Transmission line method	
TMD	Transition-metal dichalcogenide	
t_{osc}	Thickness of the organic semiconductor layer in a TFT	m
t_{ox}	Oxide thickness	m
T_{sub}	Substrate temperature	$^{\circ}\text{C}$
UPS	Ultraviolet photoemission spectroscopy	
V	Applied voltage	V
VB	Valence band	
V_{bi}	Built-in voltage	V
V_{bias}	Bias voltage of an inverter/ring oscillator	V
V_C	Contact voltage drop at the source and drain contacts in a TFT	V
V_{CML}	Electrostatic potential difference induced by a chemisorbed molecular monolayer	V
v_d	Charge-carrier velocity	m s^{-1}

V_{DD}	Supply voltage of an inverter/ring oscillator	V
V_{DS}	Drain-source voltage	V
v_{ds}	Small-signal drain-source voltage	V
V_{FB}	Flat-band voltage	V
V_{GS}	Gate-source voltage	V
v_{gs}	Small-signal gate-source voltage	V
V_{in}	Input voltage	V
V_{out}	Output voltage of an inverter/ring oscillator	V
VRH	Variable range hopping	
V_{th}	Threshold voltage	V
W	Channel width of a TFT	m
W_d	Width of the band-bending region extending into the semiconductor from the contact interface	m
XPS	X-ray photoelectron spectroscopy	
Y_{ij}	Element of the admittance parameter matrix	S
Z_C	Complex contact impedance of a TFT	Ω
Z_{ch}	Complex channel impedance of a TFT	Ω
Z_{TFT}	Complex impedance of a TFT	Ω
α	Polar angle with respect to the surface and the primary axis of a molecule chemisorbed to the surface	$^\circ$
β	Meyer model correction factor for staggered TFTs	
γ_L	Surface energy of a liquid surface	$J m^{-2}$
γ_L^D	Dispersive component of the surface energy of a liquid surface	$J m^{-2}$
γ_L^P	Polar component of the surface energy of a liquid surface	$J m^{-2}$
γ_s	Surface energy of a solid surface	$J m^{-2}$
γ_s^D	Dispersive component of the surface energy of a solid surface	$J m^{-2}$
γ_s^P	Polar component of the surface energy of a solid surface	$J m^{-2}$
Δ	Interface dipole	eV
ΔD	Degree of delocalization of charge carriers in a material	
ΔE	Energy level variance	eV
Δh	Step height measured from AFM or PFM measurements of semiconductor thin films	m
ϵ_0	Permittivity in vacuum	$F m^{-1}$
ϵ_{CML}	Relative permittivity of a chemisorbed molecular monolayer	
ϵ_{diel}	Relative permittivity of the dielectric layer in a parallel plate capacitor or TFT	
ϵ_{osc}	Organic semiconductor relative permittivity	
ϵ_r	Relative permittivity in a material	
ϵ_{sc}	Semiconductor relative permittivity	
θ	Liquid contact angle	$^\circ$
ν_a	Asymmetric vibrational mode	cm^{-1}
ν_{ax}	Axial vibrational mode (PFDT)	cm^{-1}
ν_{pd}	Perpendicular vibrational mode (PFDT)	cm^{-1}
ν_s	Symmetric vibrational mode	cm^{-1}
σ	Conductivity	$S m^{-1}$

σ'	Energy-dependent microscopic conductivity of electronic states	$\text{S m}^{-1} \text{ eV}^{-1}$
$\sigma_{0,C}$	Characteristic conductivity of a material	S m^{-1}
σ_{ch}	Channel conductivity in a TFT	S m^{-1}
τ	Average signal delay time of an individual inverter stage in a ring oscillator	s
τ_{rise}, τ_{fall}	Time delay constants of an inverter	s
τ_{vib}	Timescale of intermolecular vibrations	s
Φ_B	Potential energy barrier formed at a metal-semiconductor contact interface (Schottky barrier)	eV
φ_C	Effective work function of the contacts in a TFT	eV
φ_{DNTT}	Work function of a DNTT thin film	eV
φ_m	Contact metal work function	eV
$\varphi_{m,G}$	Work function of the gate-electrode material	eV
φ_{osc}	Work function of the organic semiconductor	eV
Φ_{PF}	Energy barrier for bound (trapped) charges (Poole-Frenkel effect)	eV
φ_{sub}	Work function of a substrate	eV
χ	Azimuthal angle with respect to the surface and the primary axis of a molecule chemisorbed to the surface	°
Ψ	Term accounting for field-induced barrier-lowering effects in the Scott-Malliaras model	
ω	Angular frequency	rad s^{-1}

Appendix

A.1 SEM micrographs of bottom-contact organic TFTs presented in Chapter 5

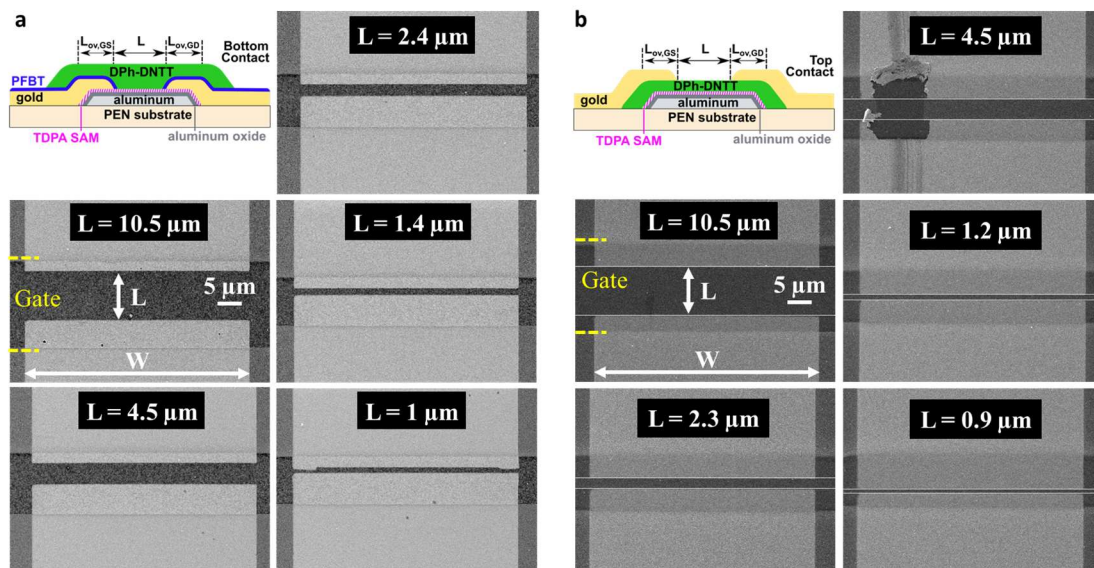


Figure A1.1 Small-channel length TFTs used for TLM analysis shown in Figure 5.16.

a) Bottom contact and (b) top contact TFT schematic diagrams and SEM micrographs of the channel region of each of the TFTs. The channel width (W) is $50\ \mu\text{m}$ for all TFTs. Note that the scratching damage to the TC TFT with channel length $L = 4.5\ \mu\text{m}$ occurred after electrical characterization, and so it did not affect the TLM analysis results. Results published in [141].

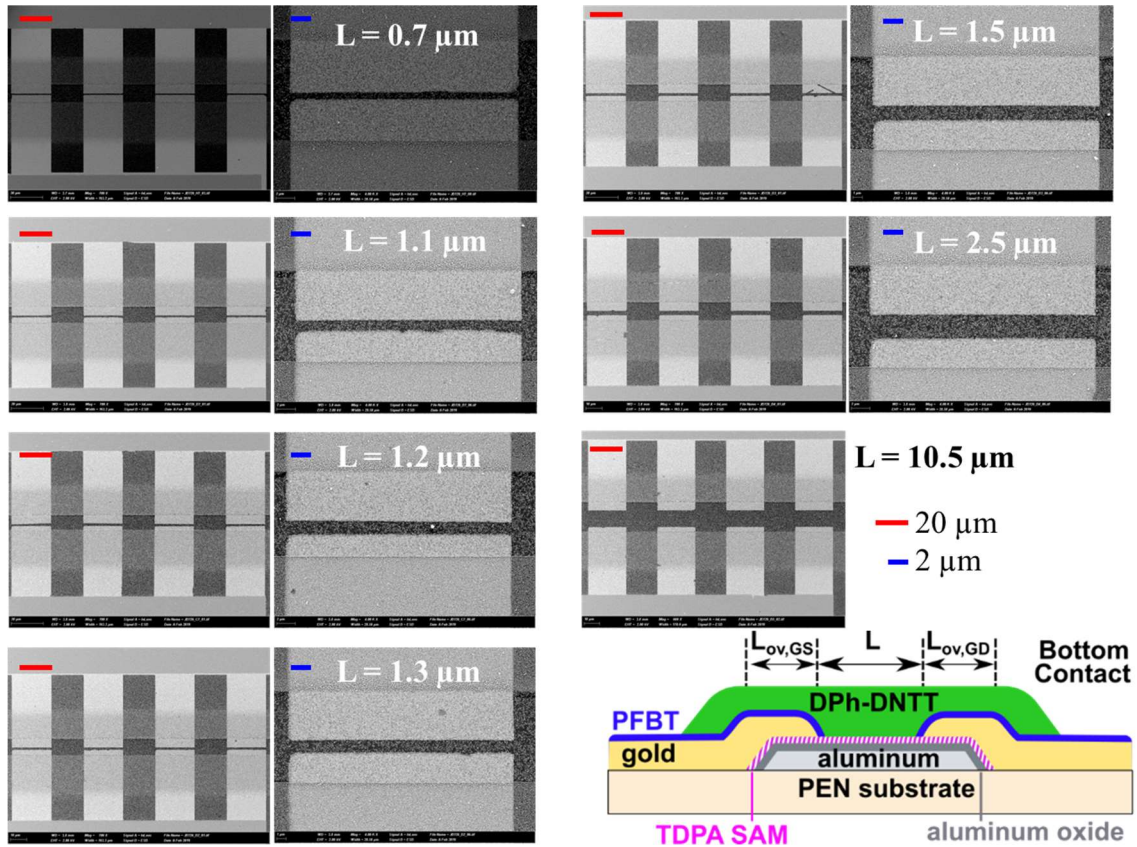


Figure A1.2 Small-channel length bottom-contact TFTs used for two-port network analysis shown in Figure 5.21.

Bottom contact TFT schematic diagrams and SEM micrographs of the channel region of each of the TFTs. The channel width (W) is $100 \mu\text{m}$ for all TFTs. Results published in [141].

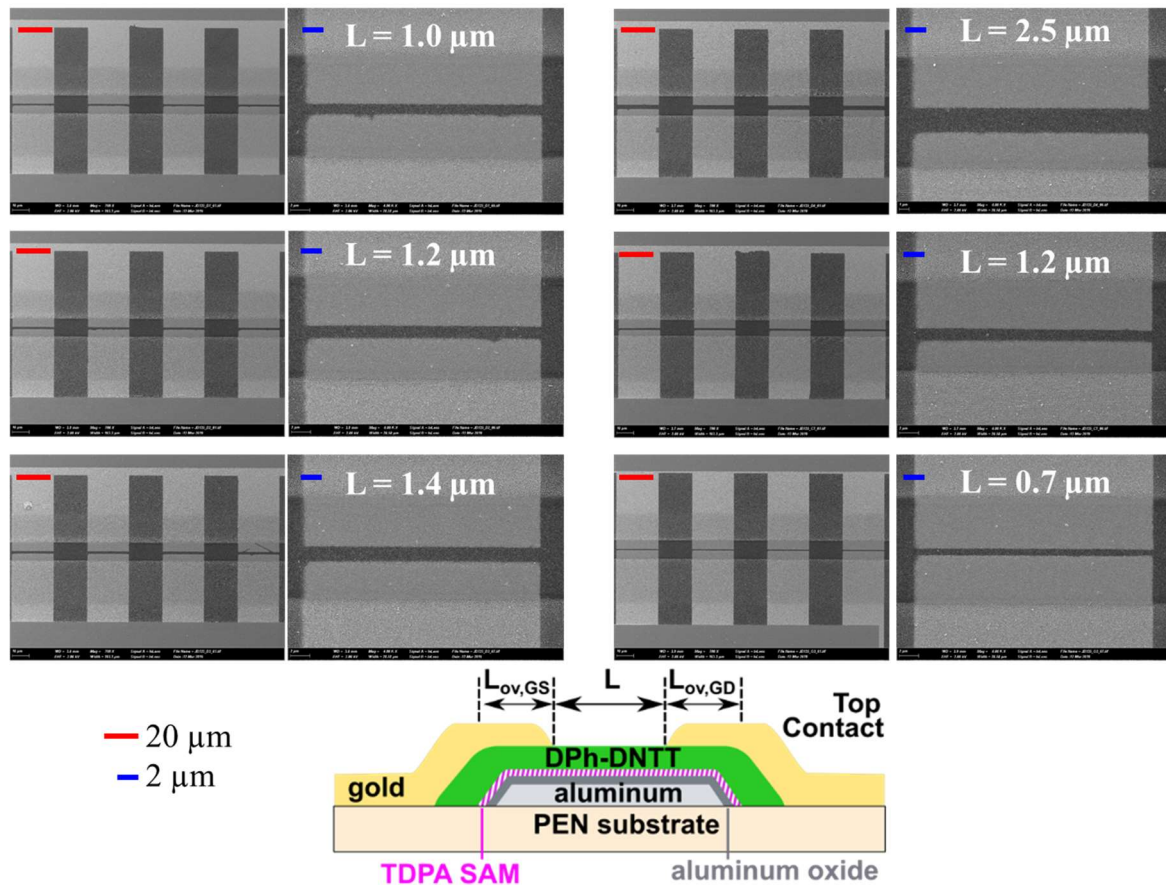


Figure A1.3 Small-channel length top-contact TFTs used for two-port network analysis shown in Figure 5.21.

Top contact TFT schematic diagrams and SEM micrographs of the channel region of each of the TFTs. The channel width (W) is $100 \mu\text{m}$ for all TFTs. Diagram adapted from [238].

A.2 Additional measurements of organic TFTs

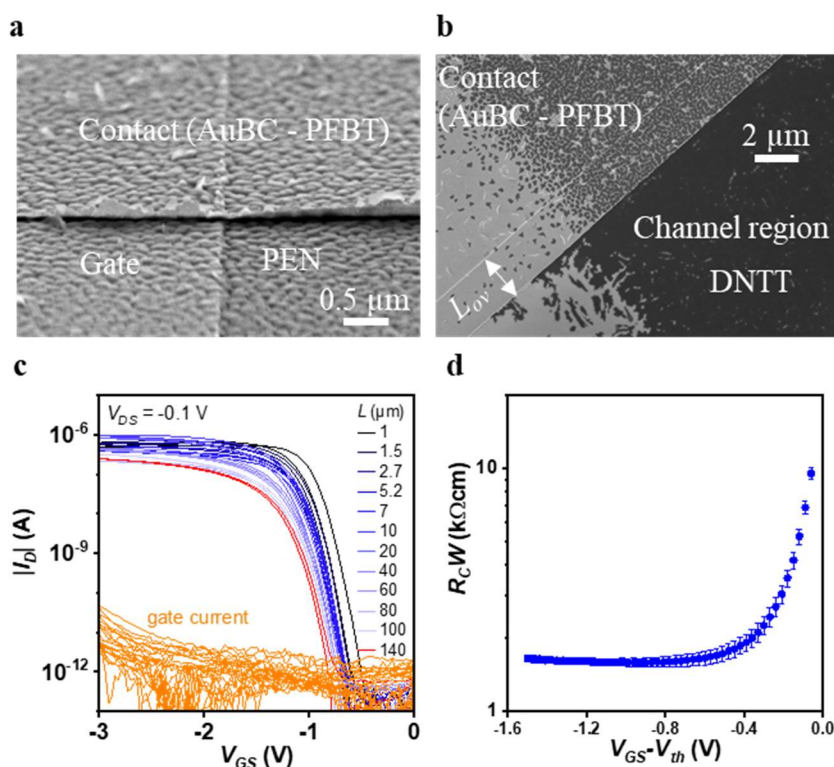


Figure A1.4 Bottom-contact DNTT transistors fabricated with electron-beam lithography

a) SEM micrograph taken at viewing angle of 60° relative to the normal of the sample surface. This allows examination of the edges of the layers in the TFT. Here, the transition region where the contact overlaps with the gate electrode is highlighted. The raised edges of the contact are due to the liftoff process. b) SEM micrograph of a similarly fabricated TFT showing the detrimental effects of the sharp, raised edges of the contact. The DNTT film crystallizes along the contact edge rather than over the contact leading to poor charge injection. This is highlighted by the TLM analysis (c,d). c) Transfer curves of e-beam DNTT TFTs used for TLM analysis of the contact resistance. d) Channel-width-normalized contact resistance ($R_C W$) as a function of the gate overdrive voltage.

A.3 Literature overview of contact resistance in organic thin-film transistors

Table A.1: Channel-width-normalized contact resistance (R_cW) reported for the maximum reported gate overdrive voltage or gate voltage.

Year	R_cW (Ωcm)	Semiconductor	Charge carriers (n/p)	Contact	Geometry	Reference
1999	80000	Sexithiophene	p	Au	BGTC	[337]
2000	30000	Sexithiophene	p	Au	BGBC	[338]
2002	8000000	F8T2	p	Au	BGBC	[339]
2003	1390	Pentacene	p	Au	BGTC	[340]
2003	62000	Pentacene	p	Au	BGBC	
2003	10000	P3HT	p	Au	BGBC	[341]
2003	40000	Pentacene	p	Au	BGBC	[342]
2003	5000	Pentacene	p	Au	BGBC	[343]
2003	13000	Pentacene	p	Pd	BGBC	[145]
2003	1000	Pentacene	p	Pd	BGTC	
2003	3000	Pentacene	p	Au	BGTC	[344]
2003	2000	Pentacene	p	Au	BGTC	
2004	13000	Pentacene	p	DNNSA-PANI/SWNT	BGBC	[345]
2004	35000	PTCDI-C5	n	Ag	BGTC	[346]
2004	44000	PTCDI-C5	n	Au	BGTC	
2004	620	Pentacene	p	3-Mercapto-propyl-trimethoxy silane/Au	BGBC	[347]
2004	1100	P3HT	p	Au/O ₂ plasma	BGBC	[161]
2004	9600	P3HT	p	Au/O ₂ plasma	BGBC	
2004	11000	P3HT	p	Au/O ₂ plasma	BGBC	[173]
2004	1300	Pentacene	p	Au	BGTC	
2004	4000	Pentacene	p	Pt	BGTC	
2004	5500	Pentacene	p	Ag	BGTC	
2004	85000	Pentacene	p	Ca	BGTC	
2004	700	Pentacene	p	Au	BGTC	
2005	3000	Pentacene	p	Au	BGTC	[348]
2006	100	Rubrene	p	Ni/NiO	BGBC	[334]
2006	3000	Pentacene	p	Pd	BGBC	[142]
2006	2800	Pentacene	p	Au	BGTC	
2006	6000	Pentacene	p	Au	BGBC	[77]
2006	1800	Pentacene	p	Au	BGTC	
2006	5000	Pentacene	p	Au/DDSH	BGBC	[349]
2006	1800	Pentacene	p	Au/4-methoxythiophenol	BGBC	
2007	80	Pentacene	p	UV-Ozone treated Au	BGBC	[78]

2007	250	Rubrene	p	Ni/NiO	BGBC	[350]	
2007	18100	Pentacene	p	Au	BGTC	[351]	
2007	23000	Pentacene	p	Au/F4TCNQ	BGTC	[352]	
2007	90000	F8T2	p	Au	TGBC	[149]	
2008	8800	P3HT	p	Au/PFBT	BGBC	[168]	
2008	20000	Pentacene	p	Au/MoOx	BGBC	[353]	
2008	400	Pentacene	p	Au	BGBC	[354]	
2009	2300	Rubrene	p	Au	BGBC	[355]	
2009	47000	Pentacene	p	Ag	BGTC	[356]	
2009	99000	Pentacene	p	Ag	BGBC		
2009	187	C60	n	Au/DABT	BGBC	[49]	
2010	1	P3HT	p	Au	TGBC	[263]	
2010	500	Pentacene	p	Au/Mo(tdf)3	BGTC	[357]	
2010	3400	Pentacene	p	Au	BGTC		
2010	8000	diF- TESADT:PTAA	p	Au/PFBT	TGBC	[358]	
2010	21000	TIPS Pentacene	p	Au/PFDT	TGBC	[186]	
2010	93000	N1400	n	Au/MeTP	TGBC		
2010	200000	TFB		Au/PFOT	TGBC		
2010	408	Pentacene	p	Au/PFBT	BGBC	[359]	
2010	2800	Pentacene	p	Au	BGTC	[144]	
2010	3100	Pentacene	p	Au	BGTC		
2010	3400	Pentacene	p	Au	BGTC		
2010	56000	Pentacene	p	Au/MoO3	BGBC		
2010	110000	Pentacene	p	Au/MoO3	BGBC		
2010	160000	Pentacene	p	Au/MoO3	BGBC		
2010	3500	DH7T	p	Au	BGBC		[360]
2010	250000	perylene diimide derivative	n	Au	TGBC		[361]
2010	900000	poly-triarylamine derivative	p	Au	TGBC		
2010	5600	Pentacene	p	Au	BGTC	[362]	
2011	4500	P3HT	p	Au/BTFMBT	BGBC	[234]	
2011	90000	pBTTT	p	Au/PFDT	TGBC	[363]	
2011	700	Pentacene	p	Ag/OPA	BGBC	[220]	
2011	6500	Pentacene	p	Ag/DDPA	BGBC		
2011	500000	Pentacene	p	Ag/ODPA	BGBC		
2011	850	C60	n	Ag/OPA	BGBC		
2011	57000	C60	n	Ag/DDPA	BGBC		
2011	1000000 0	C60	n	Ag/ODPA	BGBC		
2011	940	C60	n	Au(DABT	BGBC	[137]	
2011	3000	Pentacene	p	Au/PFBT	BGBC		
2011	390	DNTT	p	Au/NDP-9	BGTC	[110]	
2012	100	C ₈ -BTBT	p	Au/FeCl3	TGBC	[271]	

2012	200	C ₈ -BTBT	p	Au/FeCl ₃	TGTC	
2012	600	DNTT	p	Au	BGTC	[167]
2012	8800	C ₈ -BTBT	p	Au/FeCl ₃	BGTC	[107]
2012	31000	PDI-8CN2	n	Au/4-chlorobenzene methanethiol	BGBC	[364]
2013	90	DNTT	p	Au/F6TNAP	BGTC	[121]
2013	110	C ₁₀ -DNTT	p	Au/F6TNAP	BGTC	
2013	290	C ₁₀ -DNTT	p	Au/PFBT	BGBC	[365]
2013	330	C ₁₀ -DNTT	p	Au	BGTC	[207]
2013	1600	Pentacene	p	Au/Be	BGTC	[366]
2013	5500	C60	n	Au/rhodocene-dimer	BGTC	[367]
2013	10000	C ₈ -BTBT	p	Au/FeCl ₃	BGTC	[164]
2013	100000	Pentacene	p	Au	BGBC	[259]
2013	25000	Pentacene	p	Au	BGTC	[251]
2014	200	C ₁₀ -DNTT	p	Au	BGTC	[368]
2014	200	DNTT	p	Au	BGTC	[278]
2014	480	C ₁₀ -DNTT	p	Au	BGTC-split gate	[369]
2014	1800	Lisicon-S1200	n	Au/Lisicon-M001(SAM)	BGBC	[370]
2014	11000	PDPP-TVT	p	Au	TGBC	[371]
2014	3000	Rubrene	p	Au (air exposed)	BGBC	[372]
2015	123	C ₁₀ -DNBDT	p	Au	BGTC	[373]
2015	1300	BASF-GSID-104-031-1	p	Au/TTF	BGTC	
2015	156	Ph-BTBT-C ₁₀	p	Au/PFBT	BGBC	[83]
2015	160	DPh-DNTT	p	Au	BGTC	[57]
2015	300	DNTT	p	Au	BGTC	
2015	470	C ₁₀ -DNTT	p	Au	BGTC	
2015	15000	N1100	n	Au	BGTC	
2015	300	P3HT	p	Au/PFBT	BGBC	[240]
2015	1400	Pentacene	p	Au	BGTC	[374]
2015	1500	Tetraceno[2,3-b]thiophene	p	Au	BGTC	
2015	80000	diF-TESADT	p	Au/PFBT	BGBC	[221]
2015	300000	diF-TESADT	P	Ag/PFBT	BGBC	
2015	2.00E+06	diF-TESADT	P	Cu/PFBT	BGBC	
2016	131	DNTT	p	Au	BGTC	[375]
2016	200	C ₁₀ -DNTT	p	Au	BGTC	[376]
2016	240	DPh-DNTT	p	Au	BGTC	[74]
2016	460	DNTT	p	Au	BGTC	
2016	490	C ₁₀ -DNTT	p	Au	BGTC	
2016	1400	Pentacene	p	Au	BGTC	
2016	351000	TIPS-Pentacene	p	Au	TGBC	[257]

2016	65000	TIPS Pentacene	p	Au/PFBT	TGBC	
2016	13000	TIPS Pentacene	p	Au/Mo(tdf)3	TGBC	
2016	11000	TIPS Pentacene	p	Au/MoO3	TGBC	
2017	75	C ₁₀ -DNNT	p	Au/PFBT	BGBC	[153]
2017	100	C ₈ -BTBT	p	Au	BGTC	[158]
2017	200	DNTT	p	Au	BGTC	[139]
2017	19300	diF-TESADT	p	Au	TGBC	[233]
2017	5600	diF-TESADT	p	Au/PFBT	TGBC	
2017	2500	diF-TESADT	p	Au/TFBT	TGBC	
2017	4000	diF-TESADT	p	Au/TTFP	TGBC	
2017	390	Ph-BTBT-C ₁₀	p	Au	BGTC	[157]
2017	1.14E+06	TIPS Pentacene	P	Au	BGBC	[377]
2017	270000	TIPS Pentacene	P	Au	BGBC	
2017	140	C ₁₀ -DNNT	p	Au/F4TCNQ	BGTC	[155]
2017	100	C ₁₀ -DNNT	p	Au/F6TNAP	BGTC	
2017	145000	C ₈ -BTBT	p	Au	BGTC	
2017	3440000	C ₈ -BTBT	p	Ag	BGTC	
2017	6670	C ₈ -BTBT	p	MoOx/Au	BGTC	
2017	850	C ₁₀ -DNBDT	p	Au	BGTC	
2017	330	C ₁₀ -DNNT	p	Au	BGTC	[174]
2017	960	DPh-DNNT	p	Au	BGTC	
2017	1350	DNTT	p	MoOx/Au	BGTC	
2017	28800	NDI-cy6	n	Ca/Ag	BGTC	
2017	13800	Pentacene	p	Au	BGTC	
2018	47	C ₈ -DNBDT-NW	p	Au/F4TCNQ	BGTC	[81]
2018	200	IDTBT	p	Au/PFBT	TGBC	[76]
2018	500	diF-TESADT	p	Au/PFBT	TGBC	
2018	5500	Pentacene	p	Au/TP1-down	BGBC	[241]
2018	2400	Pentacene	p	Au/BP0-down	BGBC	
2018	400	Pentacene	p	Au/BP0-down	BGBC	
2018	3000	C60	n	Au/BP0-up	BGBC	
2018	580	Pentacene	p	Au/BP0-down	BGBC	
2018	220	TIPS Pentacene	p	Au	TGBC	[277]
2018	8700	NDI2HD	n	Au	BGBC	[378]
2018	7700	NDI2OD	n	Au	BGBC	
2018	500	NDI2HD	n	Au	BGTC	
2018	18000	NDI2OD	n	Au	BGTC	
2019	29	DPh-DNNT	p	Au/PFBT	BGBC	This work [238]
2019	56	DPh-DNNT	p	Au	BGTC	
2019	430	DNTT	p	Au	BGTC	[56]
2019	1770	HTEB	p	Au	BGTC	[379]
2019	26900	HTEB	p	Au	BGTC	
2019	5150000	HTEB	p	Au	BGTC	

2019	540	HTEB	p	Au	BGTC	
2019	12000	P-90	n	Au/4-methylbenzenethiol	TGBC	[380]
2020	10	DPh-DNTT	p	Au/PFBT	BGBC	This work
2020	35	DPh-DNTT	p	Au/PFBT	BGBC	[141]

Bibliography

- [1] R. K. Cavin, P. Lugli, and V. V. Zhirnov, "Science and engineering beyond moore's law," *Proc. IEEE*, vol. 100, pp. 1720–1749, 2012.
- [2] I. L. Markov, "Limits on fundamental limits to computation," *Nature*, vol. 512, no. 7513, pp. 147–154, 2014.
- [3] K. Nomura, H. Ohta, A. Takagi, T. Kamiya, M. Hirano, and H. Hosono, "Room-temperature fabrication of transparent flexible thin-film transistors using amorphous oxide semiconductors," *Nature*, vol. 432–492, no. November, p. 488, 2004.
- [4] D. Hsieh, "Flat panel display market & technology outlook," 2017.
- [5] K. Myny, "The development of flexible integrated circuits based on thin-film transistors," *Nat. Electron.*, vol. 1, no. 1, pp. 30–39, 2018.
- [6] G. Schweicher, G. Garbay, R. Jouclas, F. Vibert, F. Devaux, and Y. H. Geerts, "Molecular semiconductors for logic operations: Dead-end or bright future?," *Adv. Mater.*, vol. 32, no. 10, p. 1905909, 2020.
- [7] U. Zschieschang and H. Klauk, "Organic transistors on paper: A brief review," *J. Mater. Chem. C*, vol. 7, no. 19, pp. 5522–5533, 2019.
- [8] J. W. Ward, Z. A. Lamport, and O. D. Jurchescu, "Versatile organic transistors by solution processing," *ChemPhysChem*, vol. 16, no. 6, pp. 1118–1132, 2015.
- [9] B. Geffroy, P. le Roy, and C. Prat, "Organic light-emitting diode (OLED) technology: Materials, devices and display technologies," *Polym. Int.*, vol. 55, no. 6, pp. 572–582, 2006.
- [10] L. Meng *et al.*, "Organic and solution-processed tandem solar cells with 17.3% efficiency," *Science*, vol. 1098, no. September, pp. 1094–1098, 2018.
- [11] X. Guo *et al.*, "Current status and opportunities of organic thin-film transistor technologies," *IEEE Trans. Electron Devices*, vol. 64, no. 5, pp. 1906–1921, 2017.
- [12] M. Waldrip, O. D. Jurchescu, D. J. Gundlach, and E. G. Bittle, "Contact resistance in organic field-effect transistors: Conquering the barrier," *Adv. Funct. Mater.*, vol. 30, p. 1904576, 2019.
- [13] H. Klauk, "Will we see gigahertz organic transistors?," *Adv. Electron. Mater.*, vol. 4, no. 10, p. 1700474, 2018.
- [14] H.-W. Chen, J.-H. Lee, B.-Y. Lin, S. Chen, and S.-T. Wu, "Liquid crystal display and organic light-emitting diode display: present status and future perspectives," *Light Sci. Appl.*, vol. 7, no. 3, pp. 17168–17168, 2018.
- [15] U. Zschieschang *et al.*, "Roadmap to Gigahertz Organic Transistors," *Adv. Funct. Mater.*, vol. 30, no. 20, p. 1903812, 2020.
- [16] A. Allain, J. Kang, K. Banerjee, and A. Kis, "Electrical contacts to two-dimensional semiconductors," *Nat. Mater.*, vol. 14, no. 12, pp. 1195–1205, 2015.
- [17] M. Gruber *et al.*, "Impact of materials versus geometric parameters on the contact resistance in organic thin-film transistors," *Adv. Funct. Mater.*, vol. 23, no. 23, pp. 2941–2952, 2013.
- [18] K. Zojer, E. Zojer, A. F. Fernandez, and M. Gruber, "Impact of the capacitance of the dielectric on the contact resistance of organic thin-film transistors," *Phys. Rev. Appl.*, vol. 4, no. 4, p. 044002, 2015.
- [19] G. Horowitz, "Organic Transistors," in *Organic Electronics*, 1st ed., H. Klauk, Ed. Weinheim, Germany: Wiley-VCH, 2006, pp. 3–32.
- [20] M. Fahlman, S. Fabiano, V. Gueskine, D. Simon, M. Berggren, and X. Crispin, "Interfaces in organic electronics," *Nat. Rev. Mater.*, vol. 4, pp. 627–650, 2019.

-
- [21] S. C. Rasmussen, "The Early History of Polyaniline: Discovery and Origins," *An Int. J. Hist. Chem. Subst.*, vol. 1, no. 12, pp. 99–109, 2017.
- [22] R. D. McCullough, S. Tristram-Nagle, S. P. Williams, R. D. Lowe, and M. Jayaraman, "Self-orienting head-to-tail poly(3-alkylthiophenes): new insights on structure-property relationships in conducting polymers," *J. Am. Chem. Soc.*, vol. 115, no. 11, pp. 4910–4911, 1993.
- [23] Z. Bao, A. Dodabalapur, and A. J. Lovinger, "Soluble and processable regioregular poly(3-hexylthiophene) for thin film field-effect transistor applications with high mobility," *Appl. Phys. Lett.*, vol. 69, no. 26, pp. 4108–4110, 1996.
- [24] H. Shirakawa, E. J. Louis, A. G. MacDiarmid, C. K. Chiang, and A. J. Heeger, "Synthesis of electrically conducting organic polymers: Halogen derivatives of polyacetylene, (CH)_x," *J. Chem. Soc. Chem. Commun.*, no. 16, pp. 578–580, 1977.
- [25] F. Jonas, B. Ag, and Z. B. Zentrale, "Conductive Modifications of Polymers with Polypyrroles and Polythiophenes," *Synth. Met.*, vol. 43, pp. 831–836, 1991.
- [26] L. Groenendaal, F. Jonas, D. Freitag, H. Pielartzik, and J. R. Reynolds, "Poly(3,4-ethylenedioxythiophene) and its derivatives: past, present, and future," *Adv. Mater.*, vol. 12, no. 7, pp. 481–494, 2000.
- [27] X. Crispin *et al.*, "The Origin of the High Conductivity of (PEDOT–PSS) Plastic Electrodes," *Chem. Mater.*, vol. 18, no. 4, pp. 4354–4360, 2006.
- [28] Y. H. Kim, C. Sachse, M. L. MacHala, C. May, L. Müller-Meskamp, and K. Leo, "Highly conductive PEDOT:PSS electrode with optimized solvent and thermal post-treatment for ITO-free organic solar cells," *Adv. Funct. Mater.*, vol. 21, no. 6, pp. 1076–1081, 2011.
- [29] S. Fratini, M. Nikolka, A. Salleo, G. Schweicher, and H. Sirringhaus, "Charge transport in high-mobility conjugated polymers and molecular semiconductors," *Nat. Mater.*, vol. 19, no. May, pp. 491–502, 2020.
- [30] M. Kim *et al.*, "Donor–Acceptor-Conjugated Polymer for High-Performance Organic Field-Effect Transistors: A Progress Report," *Adv. Funct. Mater.*, vol. 30, no. 20, p. 1904545, 2020.
- [31] W. Zhang *et al.*, "Indacenodithiophene semiconducting polymers for high-performance, air-stable transistors," *J. Am. Chem. Soc.*, vol. 132, no. 33, pp. 11437–11439, 2010.
- [32] I. McCulloch *et al.*, "Liquid-crystalline semiconducting polymers with high charge-carrier mobility," *Nat. Mater.*, vol. 5, no. 4, pp. 328–333, 2006.
- [33] D. Venkateshvaran *et al.*, "Approaching disorder-free transport in high-mobility conjugated polymers," *Nature*, vol. 515, no. 7527, pp. 384–388, 2014.
- [34] Y. Y. Lin *et al.*, "High-Mobility Pentacene Organic Thin Film Transistors," in *Dig. 54th Device Research Conf.*, 1996, pp. 80–81.
- [35] Y.-Y. Lin, D. J. Gundlach, S. F. Nelson, and T. N. Jackson, "Stacked pentacene layer organic thin-film transistors with improved characteristics," *IEEE Electron Device Lett.*, vol. 18, no. 12, pp. 606–608, 1997.
- [36] D. J. Gundlach, Y. Y. Lin, T. N. Jackson, S. F. Nelson, and D. G. Schlom, "Pentacene Organic Thin-Film Transistors — Molecular Ordering and Mobility," *IEEE Electron Device Lett.*, vol. 18, no. 3, pp. 87–89, 1997.
- [37] C. D. Sheraw, T. N. Jackson, D. L. Eaton, and J. E. Anthony, "Functionalized pentacene active layer organic thin-film transistors," *Adv. Mater.*, vol. 15, no. 23, pp. 2009–2011, 2003.
- [38] C. Reese and Z. Bao, "Organic single-crystal field-effect transistors," *Mater. Today*,
-

- vol. 10, no. 3, pp. 20–27, 2007.
- [39] V. Podzorov, S. E. Sysoev, E. Logina, V. M. Pudalov, and M. E. Gershenson, “Single-crystal organic field effect transistors with the hole mobility $\sim 8 \text{ cm}^2/\text{Vs}$,” *Appl. Phys. Lett.*, vol. 83, no. 17, pp. 3504–3506, 2003.
- [40] R. W. I. de Boer, M. Gershenson, A. F. Morpurgo, and V. Podzorov, “Organic single-crystal field-effect transistors,” *Phys. Status Solidi A*, vol. 201, no. 6, pp. 1302–1331, 2004.
- [41] J. Takeya *et al.*, “Very high-mobility organic single-crystal transistors with in-crystal conduction channels,” *Appl. Phys. Lett.*, vol. 90, no. 10, 2007.
- [42] M. D. Halls and H. B. Schlegel, “Molecular orbital study of the first excited state of the OLED material tris(8-hydroxyquinoline)aluminum(III),” *Chem. Mater.*, vol. 13, no. 8, pp. 2632–2640, 2001.
- [43] O. A. Melville, B. H. Lessard, and T. P. Bender, “Phthalocyanine-Based Organic Thin-Film Transistors: A Review of Recent Advances,” *ACS Appl. Mater. Interfaces*, vol. 7, no. 24, pp. 13105–13118, 2015.
- [44] A. Maliakal, K. Raghavachari, H. Katz, E. Chandross, and T. Siegrist, “Photochemical stability of pentacene and a substituted pentacene in solution and in thin films,” *Chem. Mater.*, vol. 16, no. 24, pp. 4980–4986, 2004.
- [45] T. Yamamoto and K. Takimiya, “Facile synthesis of highly π -extended heteroarenes, dinaphtho[2,3-b: 2',3'-f]chalcogenopheno[3,2-b]chalcogenophenes, and their application to field-effect transistors,” *J. Am. Chem. Soc.*, vol. 129, no. 8, pp. 2224–2225, 2007.
- [46] N. Koch, “Organic electronic devices and their functional interfaces,” *ChemPhysChem*, vol. 8, no. 10, pp. 1438–1455, 2007.
- [47] H. Ma, H. L. Yip, F. Huang, and A. K. Y. Jen, “Interface engineering for organic electronics,” *Adv. Funct. Mater.*, vol. 20, no. 9, pp. 1371–1388, 2010.
- [48] J. Hwang, A. Wan, and A. Kahn, “Energetics of metal-organic interfaces: New experiments and assessment of the field,” *Mater. Sci. Eng. R Reports*, vol. 64, no. 1–2, pp. 1–31, 2009.
- [49] M. Kitamura and Y. Arakawa, “Current-gain cutoff frequencies above 10 MHz for organic thin-film transistors with high mobility and low parasitic capacitance,” *Appl. Phys. Lett.*, vol. 95, no. 2, pp. 2007–2010, 2009.
- [50] J. E. Anthony, A. Facchetti, M. Heeney, and S. R. Marder, “n-Type Organic Semiconductors in Organic Electronics,” *Adv. Mater.*, vol. 22, no. 34, pp. 3876–3892, 2010.
- [51] A. F. Paterson *et al.*, “Recent progress in high-mobility organic transistors: A reality check,” *Adv. Mater.*, vol. 30, no. 36, p. 1801079, 2018.
- [52] B. A. Jones, A. Facchetti, M. R. Wasielewski, and T. J. Marks, “Tuning orbital energetics in arylene diimide semiconductors. Materials design for ambient stability of n-type charge transport,” *J. Am. Chem. Soc.*, vol. 129, no. 49, pp. 15259–15278, 2007.
- [53] B. A. Jones, M. J. Ahrens, M. H. Yoon, A. Facchetti, T. J. Marks, and M. R. Wasielewski, “High-mobility air-stable n-type semiconductors with processing versatility: Dicyanoperylene-3,4:9,10-bis(dicarboximides),” *Angew. Chemie - Int. Ed.*, vol. 43, no. 46, pp. 6363–6366, 2004.
- [54] H. Yan *et al.*, “A high-mobility electron-transporting polymer for printed transistors,” *Nature*, vol. 457, no. 7230, pp. 679–686, 2009.
- [55] F. Jones, F. Léonard, A. A. Talin, and N. S. Bell, “Electrical conduction and photoluminescence properties of solution-grown ZnO nanowires,” *J. Appl. Phys.*, vol.

- 102, no. 1, p. 014305, 2007.
- [56] U. Kraft *et al.*, “Low-voltage, high-Frequency organic transistors and unipolar and complementary ring oscillators on paper,” *Adv. Electron. Mater.*, vol. 5, no. 2, p. 1800453, 2019.
- [57] U. Kraft *et al.*, “Flexible low-voltage organic complementary circuits: Finding the optimum combination of semiconductors and monolayer gate dielectrics,” *Adv. Mater.*, vol. 27, no. 2, pp. 207–214, 2015.
- [58] J. Rivnay, S. C. B. Mannsfeld, C. E. Miller, A. Salleo, and M. F. Toney, “Quantitative Determination of Organic Semiconductor Microstructure from the Molecular to Device Scale,” *Chem. Rev.*, vol. 112, pp. 5488–5519, 2012.
- [59] B. J. Worfolk, S. C. Andrews, S. Park, J. Reinspach, N. Liu, and M. F. Toney, “Ultrahigh electrical conductivity in solution-sheared polymeric transparent films,” *Proc. Natl. Acad. Sci. U. S. A.*, vol. 112, p. 14138, 2015.
- [60] G. Giri *et al.*, “Effect of Solution Shearing Method on Packing and Disorder of Organic Semiconductor Polymers,” *Chem. Mater.*, vol. 27, pp. 2350–2359, 2015.
- [61] A. Böker *et al.*, “Microscopic mechanisms of electric-field-induced alignment of block copolymer microdomains,” *Phys. Rev. Lett.*, vol. 89, no. 13, p. 135502, 2002.
- [62] E. J. W. Crossland, K. Rahimi, G. Reiter, U. Steiner, and S. Ludwigs, “Systematic Control of Nucleation Density in Poly (3-Hexylthiophene) Thin Films,” *Adv. Funct. Mater.*, vol. 21, no. 3, pp. 518–524, 2011.
- [63] R. Noriega *et al.*, “A general relationship between disorder, aggregation and charge transport in conjugated polymers,” *Nat. Mater.*, vol. 12, pp. 1038–1044, 2013.
- [64] D. Gerbert, O. T. Hofmann, and P. Tegeder, “Formation of Occupied and Unoccupied Hybrid Bands at Interfaces between Metals and Organic Donors/Acceptors,” *J. Phys. Chem. C*, vol. 122, no. 48, pp. 27554–27560, 2018.
- [65] V. Coropceanu, J. Cornil, D. A. da Silva Filho, Y. Olivier, R. Silbey, and J.-L. Brédas, “Charge transport in organic semiconductors,” *Chem. Rev.*, vol. 107, no. 4, pp. 926–952, 2007.
- [66] A. A. Virkar, S. Mannsfeld, Z. Bao, and N. Stingelin, “Organic semiconductor growth and morphology considerations for organic thin-film transistors,” *Adv. Mater.*, vol. 22, no. 34, pp. 3857–3875, 2010.
- [67] R. Ruiz *et al.*, “Pentacene thin film growth,” *Chem. Mater.*, vol. 16, no. 23, pp. 4497–4508, 2004.
- [68] M. D. Curtis, J. Cao, and J. W. Kampf, “Solid-State Packing of Conjugated Oligomers: From π -Stacks to the Herringbone Structure,” *J. Am. Chem. Soc.*, vol. 126, no. 13, pp. 4318–4328, 2004.
- [69] J. E. Anthony, “Functionalized acenes and heteroacenes for organic electronics,” *Chem. Rev.*, vol. 106, no. 12, pp. 5028–5048, 2006.
- [70] P. Stolar *et al.*, “Charge injection across self-assembly monolayers in organic field-effect transistors: Odd-even effects,” *J. Am. Chem. Soc.*, vol. 129, no. 20, pp. 6477–6484, 2007.
- [71] D. Käfer, L. Ruppel, and G. Witte, “Growth of pentacene on clean and modified gold surfaces,” *Phys. Rev. B*, vol. 75, no. 8, pp. 1–14, 2007.
- [72] S. Verlaak, S. Steudel, P. Heremans, D. Janssen, and M. Deleuze, “Nucleation of organic semiconductors on inert substrates,” *Phys. Rev. B*, vol. 68, no. 19, p. 195409, 2003.
- [73] S. Schiefer, M. Huth, A. Dobrinevski, and B. Nickel, “Determination of the crystal structure of substrate-induced pentacene polymorphs in fiber structured thin films,” *J.*

- Am. Chem. Soc.*, vol. 129, no. 34, pp. 10316–10317, 2007.
- [74] U. Kraft *et al.*, “Detailed analysis and contact properties of low-voltage organic thin-film transistors based on dinaphtho[2,3-b:2',3'-f]thieno[3,2-b]thiophene (DNNT) and its didecyl and diphenyl derivatives,” *Org. Electron.*, vol. 35, pp. 33–40, 2016.
- [75] M. J. Kang, E. Miyazaki, I. Osaka, K. Takimiya, and A. Nakao, “Diphenyl derivatives of dinaphtho[2,3-b:2',3'-f]thieno[3,2-b]thiophene: Organic semiconductors for thermally stable thin-film transistors,” *ACS Appl. Mater. Interfaces*, vol. 5, no. 7, pp. 2331–2336, 2013.
- [76] Z. A. Lampion *et al.*, “A simple and robust approach to reducing contact resistance in organic transistors,” *Nat. Commun.*, vol. 9, no. 1, p. 5130, 2018.
- [77] S. H. Jin, K. D. Jung, H. Shin, B.-G. Park, and J. D. Lee, “Grain size effects on contact resistance of top-contact pentacene TFTs,” *Synth. Met.*, vol. 156, no. 2–4, pp. 196–201, 2006.
- [78] B. Stadlober *et al.*, “Orders-of-magnitude reduction of the contact resistance in short-channel hot embossed organic thin film transistors by oxidative treatment of Au-electrodes,” *Adv. Funct. Mater.*, vol. 17, no. 15, pp. 2687–2692, 2007.
- [79] O. D. Jurchescu *et al.*, “Correlation between microstructure, electronic properties and flicker noise in organic thin film transistors,” *Appl. Phys. Lett.*, vol. 92, no. 13, p. 132103, 2008.
- [80] H. Iino and J. I. Hanna, “Liquid crystalline organic semiconductors for organic transistor applications,” *Polym. J.*, vol. 49, no. 1, pp. 23–30, 2017.
- [81] A. Yamamura *et al.*, “Wafer-scale, layer-controlled organic single crystals for high-speed circuit operation,” *Sci. Adv.*, vol. 4, no. 2, p. eaao5758, 2018.
- [82] B. Peng, Z. Wang, and P. K. L. Chan, “A simulation-assisted solution-processing method for a large-area, high-performance C10-DNNT organic semiconductor crystal,” *J. Mater. Chem. C*, vol. 4, no. 37, pp. 8628–8633, 2016.
- [83] H. Iino, T. Usui, and J. Hanna, “Liquid crystals for organic thin-film transistors,” *Nat. Commun.*, vol. 6, p. 6828, 2015.
- [84] T. Hamai, S. Inoue, S. Arai, and T. Hasegawa, “Trap-state suppression and band-like transport in bilayer-type organic semiconductor ultrathin single crystals,” *Phys. Rev. Mater.*, vol. 4, no. 7, p. 074601, 2020.
- [85] M. J. Kang *et al.*, “Alkylated dinaphtho[2,3-b:2',3'-f]thieno[3,2-b]thiophenes (Cn-DNNTs): Organic semiconductors for high-performance thin-film transistors,” *Adv. Mater.*, vol. 23, no. 10, pp. 1222–1225, 2011.
- [86] B. Peng, H. Yuen Lau, M. Chen, and P. K. L. Chan, “Realization of Ohmic-contact and velocity saturation in organic field-effect transistors by crystallized monolayer,” *Arxiv*, p. 1908.01032, 2019.
- [87] L. S. Schaffroth, J. Lenz, V. Giegold, M. Kögl, A. Hartschuh, and R. T. Weitz, “Freely Suspended, van der Waals Bound Organic Nanometer-Thin Functional Films: Mechanical and Electronic Characterization,” *Adv. Mater.*, vol. 31, no. 16, p. 1808309, 2019.
- [88] M. Schwoerer and H. C. Wolf, “Organic Semiconductors,” in *Organic Molecular Solids*, Wiley-VCH, 2007, pp. 217–304.
- [89] G. Horowitz, “Organic Field-Effect Transistors,” *Adv. Mater.*, vol. 10, no. 5, pp. 365–377, 1998.
- [90] S. Jeong, D. Kim, S. Lee, B. K. Park, and J. Moon, “Organic-inorganic hybrid dielectrics with low leakage current for organic thin-film transistors,” *Appl. Phys. Lett.*, vol. 89, no. 9, p. 092101, 2006.

-
- [91] R. M. Hill, "Variable-range hopping," *Phys. Status Solidi A*, vol. 34, no. 2, pp. 601–613, 1976.
- [92] A. Kahn, N. Koch, and W. Gao, "Electronic structure and electrical properties of interfaces between metals and p-conjugated molecular films," *J. Polym. Sci. Part B Polym. Phys.*, vol. 41, no. 21, pp. 2529–2548, 2003.
- [93] C. Liu *et al.*, "A unified understanding of charge transport in organic semiconductors: The importance of attenuated delocalization for the carriers," *Mater. Horizons*, vol. 4, no. 4, pp. 608–618, 2017.
- [94] S. Fratini, S. Ciuchi, D. Mayou, G. T. De Laissardière, and A. Troisi, "A map of high-mobility molecular semiconductors," *Nat. Mater.*, vol. 16, no. 10, pp. 998–1002, 2017.
- [95] Y. Roichman and N. Tessler, "Generalized Einstein relation for disordered semiconductors - Implications for device performance," *Appl. Phys. Lett.*, vol. 80, no. 11, pp. 1948–1950, 2002.
- [96] S. Ciuchi, S. Fratini, and D. Mayou, "Transient localization in crystalline organic semiconductors," *Phys. Rev. B*, vol. 83, no. 8, p. 081202(R), 2011.
- [97] S. Fratini, D. Mayou, and S. Ciuchi, "The transient localization scenario for charge transport in crystalline organic materials," *Adv. Funct. Mater.*, vol. 26, no. 14, pp. 2292–2315, 2016.
- [98] A. Troisi, "The speed limit for sequential charge hopping in molecular materials," *Org. Electron.*, vol. 12, no. 12, pp. 1988–1991, 2011.
- [99] B. Lüssem, M. Riede, and K. Leo, "Doping of organic semiconductors," *Phys. Status Solidi A*, vol. 210, no. 1, pp. 9–43, 2013.
- [100] I. E. Jacobs and A. J. Moulé, "Controlling Molecular Doping in Organic Semiconductors," *Adv. Mater.*, vol. 29, no. 42, p. 1703063, Sep. 2017.
- [101] K. Walzer *et al.*, "Highly Efficient Organic Devices Based on Electrically Doped Transport Layers," *Chem. Rev.*, vol. 107, no. 4, pp. 1233–1271, 2007.
- [102] S. Tanaka *et al.*, "Doping effect of tetrathianaphthacene molecule in organic semiconductors on their interfacial electronic structures studied by UV photoemission spectroscopy," *Jpn. J. Appl. Phys.*, vol. 44, no. 6 A, pp. 3760–3763, 2005.
- [103] Y. Qi, S. K. Mohapatra, S. B. Kim, S. Barlow, S. R. Marder, and A. Kahn, "Solution doping of organic semiconductors using air-stable n-dopants," *Appl. Phys. Lett.*, vol. 100, no. 8, p. 083305, 2012.
- [104] H. Sirringhaus, "Reliability of organic field-effect transistors," *Adv. Mater.*, vol. 21, pp. 3859–3873, 2009.
- [105] M. L. Tietze *et al.*, "Elementary steps in electrical doping of organic semiconductors," *Nat. Commun.*, vol. 9, p. 1182, 2018.
- [106] S. Olthof *et al.*, "Ultralow doping in organic semiconductors: Evidence of trap filling," *Phys. Rev. Lett.*, vol. 109, no. 17, p. 176601, 2012.
- [107] T. Minari, P. Darmawan, C. Liu, Y. Li, Y. Xu, and K. Tsukagoshi, "Highly enhanced charge injection in thienoacene-based organic field-effect transistors with chemically doped contact," *Appl. Phys. Lett.*, vol. 100, no. 9, p. 93303, 2012.
- [108] S. Olthof, W. Tress, R. Meerheim, B. Lüssem, and K. Leo, "Photoelectron spectroscopy study of systematically varied doping concentrations in an organic semiconductor layer using a molecular p-dopant," *J. Appl. Phys.*, vol. 106, no. 10, 2009.
- [109] L. Müller *et al.*, "Electric-Field-Controlled Dopant Distribution in Organic Semiconductors," *Adv. Mater.*, vol. 29, no. 30, p. 1701466, 2017.
- [110] F. Ante *et al.*, "Contact doping and ultrathin gate dielectrics for nanoscale organic thin-
-

- film transistors,” *Small*, vol. 7, no. 9, pp. 1186–1191, 2011.
- [111] K. Takimiya, S. Shinamura, I. Osaka, and E. Miyazaki, “Thienoacene-based organic semiconductors,” *Adv. Mater.*, vol. 23, no. 38, pp. 4347–4370, 2011.
- [112] K. Niimi, M. J. Kang, E. Miyazaki, I. Osaka, and K. Takimiya, “General synthesis of dinaphtho[2,3-b:2',3'-f]thieno[3,2-b]thiophene (DNTT) derivatives,” *Org. Lett.*, vol. 13, no. 13, pp. 3430–3433, 2011.
- [113] R. S. Sánchez-Carrera, S. Atahan, J. Schrier, and A. Aspuru-Guzik, “Theoretical Characterization of the Air-Stable, High-Mobility Dinaphtho[2,3-b:2'3'-f]thieno[3,2-b]-thiophene Organic Semiconductor,” *J. Phys. Chem. C*, vol. 114, pp. 2334–2340, 2010.
- [114] M. Uno *et al.*, “Moderately anisotropic field-effect mobility in dinaphtho [2,3-b: 2', 3'-f] thiopheno [3,2-b] thiophenes single-crystal transistors,” *Appl. Phys. Lett.*, vol. 94, p. 223308, 2009.
- [115] J. Y. Lee, S. Roth, and Y. W. Park, “Anisotropic field effect mobility in single crystal pentacene,” *Appl. Phys. Lett.*, vol. 88, no. 25, p. 252106, 2006.
- [116] M. Sugiyama *et al.*, “An ultraflexible organic differential amplifier for recording electrocardiograms,” *Nat. Electron.*, vol. 2, pp. 351–360, 2019.
- [117] K. Kuribara *et al.*, “Organic transistors with high thermal stability for medical applications,” *Nat. Commun.*, vol. 3, pp. 723–727, 2012.
- [118] T. Sekitani, U. Zschieschang, H. Klauk, and T. Someya, “Flexible organic transistors and circuits with extreme bending stability,” *Nat. Mater.*, vol. 9, no. 12, pp. 1015–1022, 2010.
- [119] T. Zaki *et al.*, “Digital-to-analog converter using organic p-type thin-film transistors on glass,” *IEEE J. Solid-State Circuits*, vol. 47, no. 1, pp. 292–300, 2012.
- [120] U. Zschieschang *et al.*, “Dinaphtho[2,3-b:2',3'-f]thieno[3,2-b]thiophene (DNTT) thin-film transistors with improved performance and stability,” *Org. Electron.*, vol. 12, no. 8, pp. 1370–1375, 2011.
- [121] T. Matsumoto, W. Ou-Yang, K. Miyake, T. Uemura, and J. Takeya, “Study of contact resistance of high-mobility organic transistors through comparisons,” *Org. Electron.*, vol. 14, no. 10, pp. 2590–2595, 2013.
- [122] H. Koezuka, A. Tsumura, and T. Ando, “Field-effect transistor with polythiophene thin film,” *Synth. Met.*, vol. 18, pp. 699–704, 1987.
- [123] Y.-Y. Lin, D. J. Gundlach, S. F. Nelson, and T. N. Jackson, “Stacked pentacene layer organic thin-film transistors with improved characteristics,” *IEEE Electron Device Lett.*, vol. 18, no. 12, pp. 606–608, 1997.
- [124] H. Klauk, “Organic thin-film transistors,” *Chem. Soc. Rev.*, vol. 39, no. 7, pp. 2643–2666, 2010.
- [125] S. M. Sze and K. K. Ng, *Semiconductor Devices: Physics and Technology*, 3rd ed. Hoboken: John Wiley & Sons, Inc., 2007.
- [126] M. Kitamura, Y. Kuzumoto, S. Aomori, M. Kamura, J. H. Na, and Y. Arakawa, “Threshold voltage control of bottom-contact n-channel organic thin-film transistors using modified drain/source electrodes,” *Appl. Phys. Lett.*, vol. 94, no. 8, p. 083310, 2009.
- [127] U. Zschieschang, V. P. Bader, and H. Klauk, “Below-one-volt organic thin-film transistors with large on/off current ratios,” *Org. Electron. physics, Mater. Appl.*, vol. 49, pp. 179–186, 2017.
- [128] M. Aghamohammadi *et al.*, “Threshold-Voltage Shifts in Organic Transistors Due to Self-Assembled Monolayers at the Dielectric: Evidence for Electronic Coupling and

- Dipolar Effects,” *ACS Appl. Mater. Interfaces*, vol. 7, no. 41, pp. 22775–22785, 2015.
- [129] S. G. J. Mathijssen *et al.*, “Charge trapping at the dielectric of organic transistors visualized in real time and space,” *Adv. Mater.*, vol. 20, no. 5, pp. 975–979, 2008.
- [130] M. Weis, “Gradual channel approximation models for organic field-effect transistors: The space-charge field effect,” *J. Appl. Phys.*, vol. 111, p. 054506, 2012.
- [131] A. Fischer *et al.*, “Self-heating, bistability, and thermal switching in organic semiconductors,” *Phys. Rev. Lett.*, vol. 110, no. 12, p. 126601, 2013.
- [132] E. G. Bittle, J. I. Basham, T. N. Jackson, O. D. Jurchescu, and D. J. Gundlach, “Mobility overestimation due to gated contacts in organic field-effect transistors,” *Nat. Commun.*, vol. 7, p. 10908, 2016.
- [133] A. Perinot, M. Giorgio, and M. Caironi, “Development of organic field-effect transistors for operation at high frequency,” in *Flexible carbon-based electronics*, 1st ed., V. Palermo and P. Samori, Eds. Weinheim, Germany: Wiley-VCH, 2018, pp. 71–94.
- [134] T. Zaki, *Short-Channel Organic Thin-Film Transistors*. 2015.
- [135] T. Zaki *et al.*, “S-parameter characterization of submicrometer low-voltage organic thin-film transistors,” *IEEE Electron Device Lett.*, vol. 34, no. 4, pp. 520–522, 2013.
- [136] A. Perinot, P. Kshirsagar, M. A. Malvindi, P. P. Pompa, R. Fiammengo, and M. Caironi, “Direct-written polymer field-effect transistors operating at 20 MHz,” *Sci. Rep.*, vol. 6, p. 38941, 2016.
- [137] M. Kitamura and Y. Arakawa, “High current-gain cutoff frequencies above 10 MHz in n-channel C60 and p-channel pentacene thin-film transistors,” *Jpn. J. Appl. Phys.*, vol. 50, p. 01BC01, 2011.
- [138] D. A. Frickey, “Conversions between S, Z, Y, h, ABCD, and T parameters which are valid for complex source and load impedances,” *IEEE Trans. Microw. Theory Tech.*, vol. 42, no. 2, pp. 205–211, 1994.
- [139] M. Elsobky *et al.*, “A digital library for a flexible low-voltage organic thin-film transistor technology,” *Org. Electron.*, vol. 50, pp. 491–498, 2017.
- [140] D. Natali and M. Caironi, “Charge injection in solution-processed organic field-effect transistors: Physics, models and characterization methods,” *Adv. Mater.*, vol. 24, no. 11, pp. 1357–1387, 2012.
- [141] J. W. Borchert *et al.*, “Flexible low-voltage high-frequency organic thin-film transistors,” *Sci. Adv.*, vol. 6, p. eaaz5156, 2020.
- [142] D. J. Gundlach, L. Zhou, J. A. Nichols, T. N. Jackson, P. V. Necliudov, and M. S. Shur, “An experimental study of contact effects in organic thin film transistors,” *J. Appl. Phys.*, vol. 100, no. 2, p. 024509, 2006.
- [143] C. H. Kim, Y. Bonnassieux, and G. Horowitz, “Fundamental benefits of the staggered geometry for organic field-effect transistors,” *IEEE Electron Device Lett.*, vol. 32, no. 9, pp. 1302–1304, 2011.
- [144] Y. Xu, T. Minari, K. Tsukagoshi, J. A. Chroboczek, and G. Ghibaudo, “Direct evaluation of low-field mobility and access resistance in pentacene field-effect transistors,” *J. Appl. Phys.*, vol. 107, no. 11, pp. 1–7, 2010.
- [145] P. V. Necliudov, M. S. Shur, D. J. Gundlach, and T. N. Jackson, “Contact resistance extraction in pentacene thin film transistors,” *Solid. State. Electron.*, vol. 47, no. 2, pp. 259–262, 2003.
- [146] C.-H. Shim, F. Maruoka, and R. Hattori, “Structural Analysis on Organic Thin-Film Transistor With Device Simulation,” *IEEE Trans. Electron Devices*, vol. 57, no. 1, pp. 195–200, 2010.

-
- [147] C. H. Kim, Y. Bonnassieux, and G. Horowitz, "Compact DC Modeling of Organic Field-Effect Transistors: Review and Perspectives," *IEEE Trans. Electron Devices*, vol. 61, no. 2, pp. 278–287, 2014.
- [148] D. Gupta, M. Katiyar, and D. Gupta, "An analysis of the difference in behavior of top and bottom contact organic thin film transistors using device simulation," *Org. Electron.*, vol. 10, no. 5, pp. 775–784, 2009.
- [149] T. J. Richards and H. Sirringhaus, "Analysis of the contact resistance in staggered, top-gate organic field-effect transistors," *J. Appl. Phys.*, vol. 102, no. 9, p. 094510, 2007.
- [150] A. Fischer *et al.*, "Nonlinear contact effects in staggered thin-film transistors," *Phys. Rev. Appl.*, vol. 8, no. 5, p. 054012, 2017.
- [151] D. Braga and G. Horowitz, "High-Performance organic field-effect transistors," *Adv. Mater.*, vol. 21, no. 14–15, pp. 1473–1486, 2009.
- [152] R. Schroeder, L. A. Majewski, and M. Grell, "Improving organic transistor performance with Schottky contacts," *Appl. Phys. Lett.*, vol. 84, no. 6, pp. 1004–1006, 2004.
- [153] M. Kitamura, "Organic transistor for logic circuit application," *Oyo Buturi*, vol. 86, no. 2, pp. 122–126, 2017.
- [154] K. Tsukagoshi, F. Fujimori, T. Minari, T. Miyadera, T. Hamano, and Y. Aoyagi, "Suppression of short channel effect in organic thin film transistors," *Appl. Phys. Lett.*, vol. 91, no. 11, p. 113508, 2007.
- [155] J. Li, W. Ou-Yang, and M. Weis, "Electric-field enhanced thermionic emission model for carrier injection mechanism of organic field-effect transistors: Understanding of contact resistance," *J. Phys. D. Appl. Phys.*, vol. 50, no. 3, p. 035101, 2017.
- [156] F. Ante, "Contact Effects in Organic Transistors," École Polytechnique Fédérale de Lausanne, 2010.
- [157] T. Hamai, S. Arai, H. Minemawari, S. Inoue, R. Kumai, and T. Hasegawa, "Tunneling and Origin of Large Access Resistance in Layered-Crystal Organic Transistors," *Phys. Rev. Appl.*, vol. 8, no. 5, p. 054011, 2017.
- [158] D. He *et al.*, "Ultrahigh mobility and efficient charge injection in monolayer organic thin-film transistors on boron nitride," *Sci. Adv.*, vol. 3, p. e1701186, 2017.
- [159] D. J. Gundlach *et al.*, "Contact-induced crystallinity for high-performance soluble acene-based transistors and circuits," *Nat. Mater.*, vol. 7, no. 3, pp. 216–221, 2008.
- [160] W. K. Kim, K. Hong, and J. L. Lee, "Enhancement of hole injection in pentacene organic thin-film transistor of O₂ plasma-treated Au electrodes," *Appl. Phys. Lett.*, vol. 89, no. 14, p. 142117, 2006.
- [161] B. H. Hamadani and D. Natelson, "Temperature-dependent contact resistances in high-quality polymer field-effect transistors," *Appl. Phys. Lett.*, vol. 84, no. 3, pp. 443–445, 2004.
- [162] D. J. Gundlach, L. Jia, and T. N. Jackson, "Pentacene TFT With Improved Linear Region Characteristics Using Chemically Modified Source and Drain Electrodes," *IEEE Electron Device Lett.*, vol. 22, no. 12, pp. 571–573, 2001.
- [163] R. P. Ortiz, A. Facchetti, and T. J. Marks, "High- k Organic, Inorganic, and Hybrid Dielectrics for Low-Voltage Organic Field-Effect Transistors," *Chem. Rev.*, vol. 110, no. 1, pp. 205–239, 2010.
- [164] C. Liu, Y. Xu, Y. Li, W. Scheideler, and T. Minari, "Critical impact of gate dielectric interfaces on the contact resistance of high-performance organic field-effect transistors," *J. Phys. Chem. C*, vol. 117, no. 23, pp. 12337–12345, 2013.
- [165] S. Luan and G. W. Neudeck, "An experimental study of the source/drain parasitic
-

- resistance effects in amorphous silicon thin film transistors,” *J. Appl. Phys.*, vol. 72, no. 2, pp. 766–772, 1992.
- [166] C. Liu, Y. Xu, and Y. Y. Noh, “Contact engineering in organic field-effect transistors,” *Mater. Today*, vol. 18, no. 2, pp. 79–96, 2015.
- [167] F. Ante *et al.*, “Contact resistance and megahertz operation of aggressively scaled organic transistors,” *Small*, vol. 8, no. 1, pp. 73–79, 2012.
- [168] B. H. Hamadani, C. A. Richter, J. S. Suehle, and D. J. Gundlach, “Insights into the characterization of polymer-based organic thin-film transistors using capacitance-voltage analysis,” *Appl. Phys. Lett.*, vol. 92, no. 20, pp. 2006–2009, 2008.
- [169] J. Lin, M. Weis, D. Taguchi, T. Manaka, and M. Iwamoto, “Carrier injection and transport in organic field-effect transistor investigated by impedance spectroscopy,” *Thin Solid Films*, vol. 518, no. 2, pp. 448–451, 2009.
- [170] T. Zaki *et al.*, “AC characterization of organic thin-film transistors with asymmetric gate-to-source and gate-to-drain overlaps,” *Org. Electron.*, vol. 14, no. 5, pp. 1318–1322, 2013.
- [171] T. Kimura, K. Kobayashi, and H. Yamada, “Direct investigations of the interface impedance of organic field-effect transistors with self-assembled-monolayer-modified electrodes,” *Org. Electron.*, vol. 38, pp. 74–78, 2016.
- [172] L. Giraudet and O. Simonetti, “Threshold voltage and turn-on voltage in organic transistors: Sensitivity to contact parasitics,” *Org. Electron.*, vol. 12, no. 1, pp. 219–225, 2011.
- [173] P. V. Pesavento, R. J. Chesterfield, C. R. Newman, and C. D. Frisble, “Gated four-probe measurements on pentacene thin-film transistors: Contact resistance as a function of gate voltage and temperature,” *J. Appl. Phys.*, vol. 96, no. 12, pp. 7312–7324, 2004.
- [174] C. Rolin, E. Kang, J. H. Lee, G. Borghs, P. Heremans, and J. Genoe, “Charge carrier mobility in thin films of organic semiconductors by the gated van der Pauw method,” *Nat. Commun.*, vol. 8, p. 14975, 2017.
- [175] L. Miozzo, A. Yassar, and G. Horowitz, “Surface engineering for high performance organic electronic devices: the chemical approach,” *J. Mater. Chem.*, vol. 20, no. 13, p. 2513, 2010.
- [176] S. M. Sze and K. N. Kwok, “Physics of Semiconductor Devices, 3rd Edition,” *John Wiley Sons, Inc*, p. 138, 2007.
- [177] S. Winkler *et al.*, “The impact of local work function variations on Fermi level pinning of organic semiconductors,” *J. Phys. Chem. C*, vol. 117, no. 43, pp. 22285–22289, 2013.
- [178] H. S. Ishii, K. Ito, E. Seki, K. Seki, “Energy level alignment and interfacial electronic structures at organic metal and organic organic interfaces,” *Adv. Mater.*, vol. 11, no. 8, pp. 605–625, 1999.
- [179] F. Amy, C. Chan, and A. Kahn, “Polarization at the gold/pentacene interface,” *Org. Electron.*, vol. 6, no. 2, pp. 85–91, 2005.
- [180] C. Liu *et al.*, “Universal diffusion-limited injection and the hook effect in organic thin-film transistors,” *Sci. Rep.*, vol. 6, no. July, p. 29811, 2016.
- [181] J. C. Scott, “Metal–organic interface and charge injection in organic electronic devices,” *J. Vac. Sci. Technol. A*, vol. 21, no. 3, pp. 521–531, 2003.
- [182] A. C. Dürr *et al.*, “Interplay between morphology, structure, and electronic properties at diindenoperylene-gold interfaces,” *Phys. Rev. B*, vol. 68, no. 11, p. 115428, 2003.
- [183] A. C. Dürr, F. Schreiber, M. Kelsch, H. D. Carstanjen, H. Dosch, and O. H. Seeck,

- “Morphology and interdiffusion behavior of evaporated metal films on crystalline diindenoperylene thin films,” *J. Appl. Phys.*, vol. 93, no. 9, pp. 5201–5209, 2003.
- [184] Y. Xu *et al.*, “Metal evaporation dependent charge injection in organic transistors,” *Org. Electron.*, vol. 15, no. 8, pp. 1738–1744, 2014.
- [185] W. Qin and H. Goebel, “Understanding the dependence of the ohmic drain-source leakage current on gold deposition rate in top-contact pentacene-based thin film transistors,” *Microelectron. Eng.*, vol. 162, pp. 96–99, 2016.
- [186] D. Boudinet *et al.*, “Modification of gold source and drain electrodes by self-assembled monolayer in staggered n- and p-channel organic thin film transistors,” *Org. Electron.*, vol. 11, no. 2, pp. 227–237, 2010.
- [187] M. Oehzelt, N. Koch, and G. Heimel, “Organic semiconductor density of states controls the energy level alignment at electrode interfaces,” *Nat. Commun.*, vol. 5, p. 4174, 2014.
- [188] S. Yogev, R. Matsubara, M. Nakamura, U. Zschieschang, H. Klauk, and Y. Rosenwaks, “Fermi level pinning by gap states in organic semiconductors,” *Phys. Rev. Lett.*, vol. 110, no. 3, p. 036803, 2013.
- [189] S. Braun, W. R. Salaneck, and M. Fahlman, “Energy-level alignment at organic/metal and organic/organic interfaces,” *Adv. Mater.*, vol. 21, no. 14–15, pp. 1450–1472, 2009.
- [190] J. M. Woodall, G. D. Pettit, T. N. Jackson, C. Lanza, K. L. Kavanagh, and J. W. Mayer, “Fermi-level pinning by misfit dislocations at GaAs interfaces,” *Phys. Rev. Lett.*, vol. 51, no. 19, pp. 1783–1786, 1983.
- [191] J. P. Yang *et al.*, “Fermi-level pinning appears upon weak electrode-organic contact without gap states: A universal phenomenon,” *Org. Electron.*, vol. 48, pp. 172–178, 2017.
- [192] J. P. Yang, F. Bussolotti, S. Kera, and N. Ueno, “Origin and role of gap states in organic semiconductor studied by UPS: As the nature of organic molecular crystals,” *J. Phys. D: Appl. Phys.*, vol. 50, p. 423002, 2017.
- [193] L. Lindell, D. Çakır, G. Brocks, M. Fahlman, and S. Braun, “Role of intrinsic molecular dipole in energy level alignment at organic interfaces,” *Appl. Phys. Lett.*, vol. 102, no. 22, p. 223301, 2013.
- [194] B. Jaeckel, J. B. Sambur, and B. A. Parkinson, “The influence of metal work function on the barrier heights of metal/pentacene junctions,” *J. Appl. Phys.*, vol. 103, p. 063719, 2008.
- [195] E. H. Rhoderick and R. H. Williams, “Metal-Semiconductor Contacts,” *IEE Rev.*, 1988.
- [196] J. C. Scott and G. G. Malliaras, “Charge injection and recombination at the metal-organic interface,” *Chem. Phys. Lett.*, vol. 299, no. 2, pp. 115–119, 1999.
- [197] C. Jiang, H. W. Choi, X. Cheng, H. Ma, D. Hasko, and A. Nathan, “Printed subthreshold organic transistors operating at high gain and ultralow power,” *Science*, vol. 363, pp. 719–723, 2019.
- [198] C. R. Crowell and S. M. Sze, “Current transport in metal-semiconductor barriers,” *Solid State Electron.*, vol. 9, no. 11–12, pp. 1035–1048, 1966.
- [199] V. I. Arkhipov, E. V. Emelianova, Y. H. Tak, and H. Bässler, “Charge injection into light-emitting diodes: Theory and experiment,” *J. Appl. Phys.*, vol. 84, no. 2, pp. 848–856, 1998.
- [200] U. Wolf, V. I. Arkhipov, and H. Bässler, “Current injection from a metal to a disordered hopping system. I. Monte carlo simulation,” *Phys. Rev. B*, vol. 59, no. 11, pp. 7507–7513, 1999.

-
- [201] V. I. Arkhipov, U. Wolf, and H. Bässler, “Current injection from a metal to a disordered hopping system. II. Comparison between analytic theory and simulation,” *Phys. Rev. B*, vol. 59, no. 11, pp. 7514–7520, 1999.
- [202] M. A. Baldo and S. R. Forrest, “Interface-limited injection in amorphous organic semiconductors,” *Phys. Rev. B*, vol. 64, p. 085201, 2001.
- [203] B. K. Sarker and S. I. Khondaker, “Thermionic emission and tunneling at carbon nanotube-organic semiconductor interface,” *ACS Nano*, vol. 6, no. 6, pp. 4993–4999, 2012.
- [204] P. V. Pesavento, K. P. Puntambekar, C. D. Frisbie, J. C. McKeen, and P. P. Ruden, “Film and contact resistance in pentacene thin-film transistors: Dependence on film thickness, electrode geometry, and correlation with hole mobility,” *J. Appl. Phys.*, vol. 99, no. 9, p. 094504, 2006.
- [205] A. Facchetti, M. H. Yoon, and T. J. Marks, “Gate dielectrics for organic field-effect transistors: New opportunities for organic electronics,” *Adv. Mater.*, vol. 17, no. 14, pp. 1705–1725, 2005.
- [206] J. Veres, S. Ogier, G. Lloyd, and D. De Leeuw, “Gate insulators in organic field-effect transistors,” *Chem. Mater.*, vol. 16, no. 23, pp. 4543–4555, 2004.
- [207] R. Hofmockel *et al.*, “High-mobility organic thin-film transistors based on a small-molecule semiconductor deposited in vacuum and by solution shearing,” *Org. Electron.*, vol. 14, no. 12, pp. 3213–3221, 2013.
- [208] D. J. Gundlach, C.-C. S. Kuo, C. D. Sheraw, J. A. Nichols, and T. N. Jackson, “Improved organic thin film transistor performance using chemically modified gate dielectrics,” *Proc. SPIE*, vol. 4466, no. December 2001, pp. 54–64, 2001.
- [209] M. H. Yoon, C. Kim, A. Facchetti, and T. J. Marks, “Gate dielectric chemical structure-organic field-effect transistor performance correlations for electron, hole, and ambipolar organic semiconductors,” *J. Am. Chem. Soc.*, vol. 128, no. 39, pp. 12851–12869, 2006.
- [210] H. Klauk, U. Zschieschang, J. Pflaum, and M. Halik, “Ultralow-power organic complementary circuits,” *Nature*, vol. 445, no. 7129, pp. 745–748, 2007.
- [211] T. Yokota *et al.*, “Flexible low-voltage organic transistors with high thermal stability at 250 °C,” *Adv. Mater.*, vol. 25, no. 27, pp. 3639–3644, 2013.
- [212] O. Acton, G. G. Ting, P. J. Shamberger, F. S. Ohuchi, H. Ma, and A. K. Y. Jen, “Dielectric surface-controlled low-voltage organic transistors via n-alkyl phosphonic acid self-assembled monolayers on high-k metal oxide,” *ACS Appl. Mater. Interfaces*, vol. 2, no. 2, pp. 511–520, 2010.
- [213] Z. Zhang *et al.*, “Ultra low contact resistivities for CMOS beyond 10-nm node,” *IEEE Electron Device Lett.*, vol. 34, no. 6, pp. 723–725, 2013.
- [214] Y. Wu *et al.*, “Ultra-low specific contact resistivity ($1.4 \times 10^{-9} \Omega \cdot \text{cm}^2$) for metal contacts on in-situ Ga-doped Ge_{0.95}Sn_{0.05} film,” *J. Appl. Phys.*, vol. 122, no. 22, p. 224503, 2017.
- [215] A. Risteska, K. Myny, S. Steudel, M. Nakamura, and D. Knipp, “Scaling limits of organic digital circuits,” *Org. Electron.*, vol. 15, no. 2, pp. 461–469, 2014.
- [216] D. K. Schroder, “Contact resistance and schottky barriers,” *Semicond. Mater. Device Charact.*, pp. 127–184, 2006.
- [217] M. Kröger, S. Hamwi, J. Meyer, T. Riedl, W. Kowalsky, and A. Kahn, “Role of the deep-lying electronic states of MoO₃ in the enhancement of hole-injection in organic thin films,” *Appl. Phys. Lett.*, vol. 95, no. 12, p. 123301, 2009.
- [218] X. Peng, L. Hu, F. Qin, Y. Zhou, and P. K. Chu, “Low Work Function Surface
-

- Modifiers for Solution-Processed Electronics: A Review,” *Adv. Mater. Interfaces*, vol. 5, p. 1701404, 2018.
- [219] Y. Y. Noh, N. Zhao, M. Caironi, and H. Sirringhaus, “Downscaling of self-aligned, all-printed polymer thin-film transistors,” *Nat. Nanotechnol.*, vol. 2, no. 12, pp. 784–789, 2007.
- [220] O. Acton *et al.*, “Simultaneous modification of bottom-contact electrode and dielectric surfaces for organic thin-film transistors through single-component spin-cast monolayers,” *Adv. Funct. Mater.*, vol. 21, no. 8, pp. 1476–1488, 2011.
- [221] C. H. Kim *et al.*, “Decoupling the Effects of Self-Assembled Monolayers on Gold, Silver, and Copper Organic Transistor Contacts,” *Adv. Mater. Interfaces*, vol. 2, no. 2, p. 1400384, 2015.
- [222] S. Casalini, C. A. Bortolotti, F. Leonardi, and F. Biscarini, “Self-assembled monolayers in organic electronics,” *Chem. Soc. Rev.*, vol. 46, pp. 40–71, 2017.
- [223] C. Vericat, M. E. Vela, G. Benitez, P. Carro, and R. C. Salvarezza, “Self-assembled monolayers of thiols and dithiols on gold: New challenges for a well-known system,” *Chem. Soc. Rev.*, vol. 39, no. 5, pp. 1805–1834, 2010.
- [224] M. Singh, N. Kaur, and E. Comini, “The role of self-assembled monolayers in electronic devices,” *J. Mater. Chem. C*, vol. 8, no. 12, pp. 3938–3955, 2020.
- [225] P. Thissen, M. Valtiner, and G. Grundmeier, “Stability of phosphonic acid self-assembled monolayers on amorphous and Single-crystalline aluminum oxide surfaces in aqueous solution,” *Langmuir*, vol. 26, no. 1, pp. 156–164, 2010.
- [226] F. Schreiber, “Self-assembled monolayers: From ‘simple’ model systems to biofunctionalized interfaces,” *J. Phys. Condens. Matter*, vol. 16, no. 28, pp. 881–900, 2004.
- [227] Y. Ito *et al.*, “Crystalline ultrasmooth self-assembled monolayers of alkylsilanes for organic field-effect transistors,” *J. Am. Chem. Soc.*, vol. 131, no. 26, pp. 9396–9404, 2009.
- [228] R. Acharya, B. Peng, P. K. L. Chan, G. Schmitz, and H. Klauk, “Achieving Ultralow Turn-On Voltages in Organic Thin-Film Transistors: Investigating Fluoroalkylphosphonic Acid Self-Assembled Monolayer Hybrid Dielectrics,” *ACS Appl. Mater. Interfaces*, vol. 11, no. 30, pp. 27104–27111, 2019.
- [229] F. Abraham, W. E. Ford, F. Scholz, G. Nelles, G. Sandford, and F. Von Wrochem, “Surface Energy and Work Function Control of AlO_x/Al Surfaces by Fluorinated Benzylphosphonic Acids,” *ACS Appl. Mater. Interfaces*, vol. 8, no. 18, pp. 11857–11867, 2016.
- [230] B. De Boer, A. Hadipour, M. M. Mandoc, T. Van Woudenberg, and P. W. M. Blom, “Tuning of metal work functions with self-assembled monolayers,” *Adv. Mater.*, vol. 17, no. 5, pp. 621–625, 2005.
- [231] M. Salinas *et al.*, “The relationship between threshold voltage and dipolar character of self-assembled monolayers in organic thin-film transistors,” *J. Am. Chem. Soc.*, vol. 134, no. 30, pp. 12648–12652, 2012.
- [232] D. Liu and Q. Miao, “Recent progress in interface engineering of organic thin film transistors with self-assembled monolayers,” *Mater. Chem. Front.*, vol. 2, pp. 11–21, 2017.
- [233] Y. Mei *et al.*, “Interface engineering to enhance charge injection and transport in solution-deposited organic transistors,” *Org. Electron.*, vol. 50, pp. 100–105, 2017.
- [234] K. A. Singh *et al.*, “Effect of self-assembled monolayers on charge injection and transport in poly(3-hexylthiophene)-based field-effect transistors at different channel

- length scales,” *ACS Appl. Mater. Interfaces*, vol. 3, no. 8, pp. 2973–2978, 2011.
- [235] M. R. Niazi *et al.*, “Contact-induced nucleation in high-performance bottom-contact organic thin film transistors manufactured by large-area compatible solution processing,” *Adv. Funct. Mater.*, vol. 26, no. 14, pp. 2371–2378, 2016.
- [236] A. Risteska, S. Steudel, M. Nakamura, and D. Knipp, “Structural ordering versus energy band alignment: Effects of self-assembled monolayers on the metal/semiconductor interfaces of small molecule organic thin-film transistors,” *Org. Electron.*, vol. 15, no. 12, pp. 3723–3728, 2014.
- [237] M. M. Thuo *et al.*, “Odd-even effects in charge transport across self-assembled monolayers,” *J. Am. Chem. Soc.*, vol. 133, no. 9, pp. 2962–2975, 2011.
- [238] J. W. Borchert *et al.*, “Small contact resistance and high-frequency operation of flexible low-voltage inverted coplanar organic transistors,” *Nat. Commun.*, vol. 10, no. 1, p. 1119, 2019.
- [239] C. H. Kim, H. Hlaing, F. Carta, Y. Bonnassieux, G. Horowitz, and I. Kyymissis, “Templating and charge injection from copper electrodes into solution-processed organic field-effect transistors,” *ACS Appl. Mater. Interfaces*, vol. 5, no. 9, pp. 3716–3721, 2013.
- [240] O. Fenwick *et al.*, “Modulating the charge injection in organic field-effect transistors: Fluorinated oligophenyl self-assembled monolayers for high work function electrodes,” *J. Mater. Chem. C*, vol. 3, no. 13, pp. 3007–3015, 2015.
- [241] A. Petritz *et al.*, “Embedded Dipole Self-Assembled Monolayers for Contact Resistance Tuning in p-Type and n-Type Organic Thin Film Transistors and Flexible Electronic Circuits,” *Adv. Funct. Mater.*, vol. 28, no. 45, p. 1804462, 2018.
- [242] F. Letzkus *et al.*, “Dry etch improvements in the SOI wafer flow process for IPL stencil mask fabrication,” *Microelectron. Eng.*, vol. 53, no. 1, pp. 609–612, 2000.
- [243] K. Pei, M. Chen, Z. Zhou, H. Li, and P. K. L. Chan, “Overestimation of carrier mobility in organic thin film transistors due to unaccounted fringe currents,” *ACS Appl. Electron. Mater.*, vol. 1, no. 3, pp. 379–388, 2019.
- [244] U. Zschieschang *et al.*, “Megahertz operation of flexible low-voltage organic thin-film transistors,” *Org. Electron.*, vol. 14, no. 6, pp. 1516–1520, 2013.
- [245] A. Ramin *et al.*, “PM-IRRAS investigation of self-assembled monolayers grafted onto SiO₂/Au substrates,” *Langmuir*, vol. 27, no. 10, pp. 6076–6084, 2011.
- [246] N. Koch, “Energy levels at interfaces between metals and conjugated organic molecules,” *J. Phys. Condens. Matter*, vol. 20, no. 18, p. 184008, 2008.
- [247] M. Giorgio and M. Caironi, “Radio-frequency polymer field-effect transistors characterized by S-parameters,” *IEEE Electron Device Lett.*, vol. 40, no. 6, pp. 953–956, 2019.
- [248] Z. Liu, M. Kobayashi, B. C. Paul, Z. Bao, and Y. Nishi, “Contact engineering for organic semiconductor devices via Fermi level depinning at the metal-organic interface,” *Phys. Rev. B*, vol. 82, no. 3, p. 035311, 2010.
- [249] C. Liu *et al.*, “Device physics of contact issues for the overestimation and underestimation of carrier mobility in field-effect transistors,” *Phys. Rev. Appl.*, vol. 8, no. 3, p. 034020, 2017.
- [250] F. Ante *et al.*, “Submicron low-voltage organic transistors and circuits enabled by high-resolution silicon stencil masks,” *Tech. Dig. - Int. Electron Devices Meet. IEDM*, pp. 516–519, 2010.
- [251] Y. Xu *et al.*, “Understanding thickness-dependent charge transport in pentacene transistors by low-frequency noise,” *IEEE Electron Device Lett.*, vol. 34, no. 10, pp.

- 1298–1300, 2013.
- [252] L. Mercas, R. F. de Oliveira, H. L. Gomes, and C. C. Bof Bufon, “The role of the electrode configuration on the electrical properties of small-molecule semiconductor thin-films,” *Org. Electron.*, vol. 49, pp. 107–113, 2017.
- [253] Y. Yuan *et al.*, “Ultra-high mobility transparent organic thin film transistors grown by an off-centre spin-coating method,” *Nat. Commun.*, vol. 5, p. 3005, 2014.
- [254] G. Heimel, I. Salzmann, S. Duhm, and N. Koch, “Design of organic semiconductors from molecular electrostatics,” *Chem. Mater.*, vol. 23, no. 3, pp. 359–377, 2011.
- [255] C. Bock, D. V. Pham, U. Kunze, D. Käfer, G. Witte, and C. Wöll, “Improved morphology and charge carrier injection in pentacene field-effect transistors with thiol-treated electrodes,” *J. Appl. Phys.*, vol. 100, no. 11, p. 114517, 2006.
- [256] G. Horowitz, “Organic thin film transistors: From theory to real devices,” *J. Mater. Res.*, vol. 19, no. 07, pp. 1946–1962, 2004.
- [257] S. Choi *et al.*, “A Study on Reducing Contact Resistance in Solution-Processed Organic Field-Effect Transistors,” *ACS Appl. Mater. Interfaces*, vol. 8, no. 37, pp. 24744–24752, 2016.
- [258] S. E. Fritz, S. M. Martin, C. D. Frisbie, M. D. Ward, and M. F. Toney, “Structural Characterization of a Pentacene Monolayer on an Amorphous SiO₂ Substrate with Grazing Incidence X-ray Diffraction,” *J. Am. Chem. Soc.*, vol. 126, no. 13, pp. 4084–4085, 2004.
- [259] C. H. Kim, Y. Bonnassieux, G. Horowitz, and S. Member, “Charge Distribution and Contact Resistance Model for Coplanar Organic Field-Effect Transistors,” *IEEE Trans. Electron Devices*, vol. 60, no. 1, pp. 280–287, 2013.
- [260] J. J. Brondijk, F. Torricelli, E. C. P. P. Smits, P. W. M. M. Blom, and D. M. De Leeuw, “Gate-bias assisted charge injection in organic field-effect transistors,” *Org. Electron.*, vol. 13, no. 9, pp. 1526–1531, 2012.
- [261] A. Yamamura *et al.*, “High-Speed Organic Single-Crystal Transistor Responding to Very High Frequency Band,” *Adv. Funct. Mater.*, vol. 30, no. 11, p. 1909501, 2020.
- [262] N. Münzenrieder *et al.*, “Contact resistance and overlapping capacitance in flexible sub-micron long oxide thin-film transistors for above 100 MHz operation,” *Appl. Phys. Lett.*, vol. 105, no. 26, p. 263504, 2014.
- [263] D. Braga, M. Ha, W. Xie, and C. D. Frisbie, “Ultralow contact resistance in electrolyte-gated organic thin film transistors,” *Appl. Phys. Lett.*, vol. 97, no. 19, p. 193311, 2010.
- [264] U. Zschieschang *et al.*, “Flexible low-voltage organic thin-film transistors and circuits based on C₁₀-DNTT,” *J. Mater. Chem.*, vol. 22, no. 10, pp. 4273–4277, 2012.
- [265] B. Blülle, R. Häusermann, and B. Batlogg, “Approaching the trap-free limit in organic single-crystal field-effect transistors,” *Phys. Rev. Appl.*, vol. 1, no. 3, p. 034006, 2014.
- [266] W. Xu, F. Wang, and S.-W. Rhee, “Quasi-ordering in spontaneously associated surface dipoles: an intrinsic interfacial factor for high-k-polymer insulated organic field-effect transistors,” *J. Mater. Chem.*, vol. 22, no. 4, pp. 1482–1488, 2012.
- [267] J. Zhao, W. Tang, Q. Li, W. Liu, and X. Guo, “Fully Solution Processed Bottom-Gate Organic Field-Effect Transistor with Steep Subthreshold Swing Approaching the Theoretical Limit,” *IEEE Electron Device Lett.*, vol. 38, no. 10, pp. 1465–1468, 2017.
- [268] W. L. Kalb and B. Batlogg, “Calculating the trap density of states in organic field-effect transistors from experiment: A comparison of different methods,” *Phys. Rev. B*, vol. 81, no. 3, p. 035327, 2010.
- [269] H. F. Haneef, A. M. Zeidell, and O. D. Jurchescu, “Charge carrier traps in organic

- semiconductors: A review on the underlying physics and impact on electronic devices,” *J. Mater. Chem. C*, vol. 8, pp. 759–787, 2020.
- [270] H. L. Gomes, P. Stallinga, M. Cölle, D. M. De Leeuw, and F. Biscarini, “Electrical instabilities in organic semiconductors caused by trapped supercooled water,” *Appl. Phys. Lett.*, vol. 88, no. 8, p. 082101, 2006.
- [271] P. Darmawan *et al.*, “Optimal structure for high-performance and low-contact-resistance organic field-effect transistors using contact-doped coplanar and pseudo-staggered device architectures,” *Adv. Funct. Mater.*, vol. 22, no. 21, pp. 4577–4583, 2012.
- [272] Y. Jiang, H. Geng, W. Li, and Z. Shuai, “Understanding carrier transport in organic semiconductors: Computation of charge mobility considering quantum nuclear tunneling and delocalization effects,” *J. Chem. Theory Comput.*, vol. 15, no. 3, pp. 1477–1491, 2019.
- [273] I. Valitova *et al.*, “Carbon nanotube electrodes in organic transistors,” *Nanoscale*, vol. 5, no. 11, pp. 4638–4646, 2013.
- [274] J. Yoon *et al.*, “Highly flexible and transparent multilayer MoS₂ transistors with graphene electrodes,” *Small*, vol. 9, no. 19, pp. 3295–3300, 2013.
- [275] W. Wang *et al.*, “Mechanism of electron conduction in self-assembled alkanethiol monolayer devices,” *Phys. Rev. B*, vol. 68, no. 3, p. 035416, 2003.
- [276] P. Heremans *et al.*, “Thin-film transistors and circuits on plastic foil,” *2009 IEEE Int. Electron Devices Meet.*, pp. 371–374, 2009.
- [277] S. D. Ogier *et al.*, “Uniform, high performance, solution processed organic thin-film transistors integrated in 1 MHz frequency ring oscillators,” *Org. Electron.*, vol. 54, pp. 40–47, 2018.
- [278] T. Zaki *et al.*, “Accurate capacitance modeling and characterization of organic thin-film transistors,” *IEEE Trans. Electron Devices*, vol. 61, no. 1, pp. 98–104, 2014.
- [279] B. Kheradmand-Boroujeni, M. P. Klinger, A. Fischer, H. Kleemann, K. Leo, and F. Ellinger, “A Pulse-Biasing Small-Signal Measurement Technique Enabling 40 MHz Operation of Vertical Organic Transistors,” *Sci. Rep.*, vol. 8, no. 1, p. 7643, 2018.
- [280] A. Perinot and M. Caironi, “Accessing MHz Operation at 2 V with Field-Effect Transistors Based on Printed Polymers on Plastic,” *Adv. Sci.*, vol. 6, no. 4, p. 1801566, 2019.
- [281] S. Refaely-Abramson, S. Sharifzadeh, M. Jain, R. Baer, J. B. Neaton, and L. Kronik, “Gap renormalization of molecular crystals from density-functional theory,” *Phys. Rev. B*, vol. 88, no. 8, p. 081204(R), 2013.
- [282] J. Jang *et al.*, “Extraction of the sub-bandgap density-of-states in polymer thin-film transistors with the multi-frequency capacitance-voltage spectroscopy,” *Appl. Phys. Lett.*, vol. 100, no. 13, p. 133506, 2012.
- [283] T. Miyadera, T. Minari, K. Tsukagoshi, H. Ito, and Y. Aoyagi, “Frequency response analysis of pentacene thin-film transistors with low impedance contact by interface molecular doping,” *Appl. Phys. Lett.*, vol. 91, no. 1, p. 013512, 2007.
- [284] L. Zhang, D. Taguchi, H. Masada, T. Manaka, and M. Iwamoto, “Channel formation as an interface charging process in a pentacene field effect transistor investigated by time-resolved second harmonic generation and impedance spectroscopy,” *Jpn. J. Appl. Phys.*, vol. 51, no. 2 PART 2, p. 02BK08, 2012.
- [285] S. J. Zilker, C. Detcheverry, E. Cantatore, and D. M. De Leeuw, “Bias stress in organic thin-film transistors and logic gates,” *Appl. Phys. Lett.*, vol. 79, no. 8, pp. 1124–1126, 2001.

-
- [286] Y. Kuzumoto and M. Kitamura, "Work function of gold surfaces modified using substituted benzenethiols: Reaction time dependence and thermal stability," *Appl. Phys. Express*, vol. 7, no. 3, p. 035701, 2014.
- [287] W. Xie *et al.*, "Temperature-independent transport in high-mobility dinaphtho-thienothiophene (DNNT) single crystal transistors," *Adv. Mater.*, vol. 25, no. 25, pp. 3478–3484, 2013.
- [288] V. Diez-Cabanes, S. R. Gonzalez, S. Osella, D. Cornil, C. Van Dyck, and J. Cornil, "Energy Level Alignment at Interfaces Between Au (111) and Thiolated Oligophenylenes of Increasing Chain Size: Theoretical Evidence of Pinning Effects," *Adv. Theory Simulations*, vol. 1, no. 3, p. 1700020, 2018.
- [289] D. K. Owens and R. C. Wendt, "Estimation of the Surface Free Energy of Polymers," *J. Appl. Polym. Sci.*, vol. 13, pp. 1741–1747, 1969.
- [290] A. Ulman, "Formation and Structure of Self-Assembled Monolayers," *Chem. Rev.*, vol. 96, pp. 1533–1554, 1996.
- [291] C. Vericat, M. E. Vela, and R. C. Salvarezza, "Self-assembled monolayers of alkanethiols on Au(111): Surface structures, defects and dynamics," *Phys. Chem. Chem. Phys.*, vol. 7, no. 18, pp. 3258–3268, 2005.
- [292] N. Prathima *et al.*, "Thermal study of accumulation of conformational disorders in the self-assembled monolayers of C8 and C18 alkanethiols on the Au(111) surface," *Langmuir*, vol. 21, no. 6, pp. 2364–2374, 2005.
- [293] O. Zenasni, A. C. Jamison, and T. R. Lee, "The impact of fluorination on the structure and properties of self-assembled monolayer films," *Soft Matter*, vol. 9, no. 28, pp. 6356–6370, 2013.
- [294] F. Cecchet *et al.*, "Theoretical calculations and experimental measurements of the vibrational response of p-NTP SAMs: An orientational analysis," *J. Phys. Chem. C*, vol. 114, no. 9, pp. 4106–4113, 2010.
- [295] J. U. Nielsen, M. J. Esplandiu, and D. M. Kolb, "4-nitrothiophenol SAM on Au(111) investigated by in situ STM, electrochemistry, and XPS," *Langmuir*, vol. 17, no. 11, pp. 3454–3459, 2001.
- [296] M. Futamata, C. Nishihara, and N. Goutev, "Electrochemical reduction of p-nitrothiophenol-self-assembled monolayer films on Au(111) surface and coadsorption of anions and water molecules," *Surf. Sci.*, vol. 514, no. 1–3, pp. 241–248, 2002.
- [297] M. Wirde, U. Gelius, and L. Nyholm, "Self-assembled monolayers of cystamine and cysteamine on gold studied by XPS and voltammetry," *Langmuir*, vol. 15, no. 19, pp. 6370–6378, 1999.
- [298] M. H. Schoenfisch and J. E. Pemberton, "Air stability of alkanethiol self-assembled monolayers on silver and gold surfaces," *J. Am. Chem. Soc.*, vol. 120, no. 18, pp. 4502–4513, 1998.
- [299] H. Tsutsumi, S. Furumoto, M. Morita, and Y. Matsuda, "Electrochemical behavior of a 4-nitrothiophenol modified electrode prepared by the self-assembly method," *Journal of Colloid And Interface Science*, vol. 171, no. 2, pp. 505–511, 1995.
- [300] Q. Ding *et al.*, "Basal-Plane Ligand Functionalization on Semiconducting 2H-MoS₂ Monolayers," *ACS Appl. Mater. Interfaces*, vol. 9, no. 14, pp. 12734–12742, 2017.
- [301] W. S. Hu, Y. T. Tao, Y. J. Hsu, D. H. Wei, and Y. S. Wu, "Molecular orientation of evaporated pentacene films on gold: Alignment effect of self-assembled monolayer," *Langmuir*, vol. 21, no. 6, pp. 2260–2266, 2005.
- [302] W. Azzam, A. Bashir, P. Ulrich Biedermann, and M. Rohwerder, "Formation of highly ordered and orientated gold islands: Effect of immersion time on the molecular adlayer"
-

- structure of pentafluorobenzenethiols (PFBT) SAMs on Au(111),” *Langmuir*, vol. 28, no. 27, pp. 10192–10208, 2012.
- [303] K. Rajalingam, L. Hallmann, T. Strunskus, A. Bashir, C. Wöll, and F. Tuzcek, “Self-assembled monolayers of benzylmercaptan and para-cyanobenzylmercaptan on gold: Surface infrared spectroscopic characterization,” *Phys. Chem. Chem. Phys.*, vol. 12, no. 17, pp. 4390–4399, 2010.
- [304] F. Laffineur *et al.*, “Comparison between CH₃(CH₂)₁₅SH and CF₃(CF₂)₃(CH₂)₁₁SH Monolayers on Electrodeposited Silver,” *Langmuir*, vol. 20, no. 8, pp. 3240–3245, 2004.
- [305] R. G. Nuzzo, E. M. Korenic, and L. H. Dubois, “Studies of the temperature-dependent phase behavior of long chain n-alkyl thiol monolayers on gold,” *J. Chem. Phys.*, vol. 93, no. 1, pp. 767–773, 1990.
- [306] M. D. Porter, T. B. Bright, D. L. Allara, and C. E. Chidsey, “Spontaneously Organized Molecular Assemblies. 4. Structural Characterization of n-Alkyl Thiol Monolayers on Gold by Optical Ellipsometry, Infrared Spectroscopy, and Electrochemistry,” *J. Am. Chem. Soc.*, vol. 109, no. 12, pp. 3559–3568, 1987.
- [307] P. E. Laibinis, G. M. Whitesides, D. L. Aliara, Y. T. Tao, A. N. Parikh, and R. G. Nuzzo, “Comparison of the Structures and Wetting Properties of Self-Assembled Monolayers of n-Alkanethiols on the Coinage Metal Surfaces, Cu, Ag, Au,” *J. Am. Chem. Soc.*, vol. 113, no. 19, pp. 7152–7167, 1991.
- [308] T. Patois *et al.*, “Microtribological and corrosion behaviors of 1H,1H,2H,2H-perfluorodecanethiol self-assembled films on copper surfaces,” *Surf. Coatings Technol.*, vol. 205, no. 7, pp. 2511–2517, 2010.
- [309] W. E. Ford, F. Abraham, F. Scholz, G. Nelles, G. Sandford, and F. Von Wrochem, “Spectroscopic characterization of fluorinated benzylphosphonic acid monolayers on AlO_x/Al Surfaces,” *J. Phys. Chem. C*, vol. 121, no. 3, pp. 1690–1703, 2017.
- [310] E. J. Sturrock, Q. Chen, P. H. Borchardt, and N. V. Richardson, “Coverage dependent change in orientation for the adsorption of benzyl mercaptan on Au(1 1 1),” *J. Electron Spectros. Relat. Phenomena*, vol. 135, no. 2–3, pp. 127–134, 2004.
- [311] M. Osawa, N. Matsuda, K. Yoshii, and I. Uchida, “Charge transfer resonance Raman process in surface-enhanced Raman scattering from p-aminothiophenol adsorbed on silver: Herzberg-Teller contribution,” *J. Phys. Chem.*, vol. 98, no. 48, pp. 12702–12707, 1994.
- [312] C. P. McCoy, J. F. Cowley, S. P. Gorman, G. P. Andrews, and D. S. Jones, “Reduction of *Staphylococcus aureus* and *Pseudomonas aeruginosa* colonisation on PVC through covalent surface attachment of fluorinated thiols,” *J. Pharm. Pharmacol.*, vol. 61, no. 9, pp. 1163–1169, 2009.
- [313] M. Alt *et al.*, “Processing follows function: Pushing the formation of self-assembled monolayers to high-throughput compatible time scales,” *ACS Appl. Mater. Interfaces*, vol. 6, no. 22, pp. 20234–20241, 2014.
- [314] C. E. D. Chidsey and D. N. Loiacono, “Chemical Functionality in Self-Assembled Monolayers: Structural and Electrochemical Properties,” *Langmuir*, vol. 6, no. 3, pp. 682–691, 1990.
- [315] R. Colorado and T. R. Lee, “Wettabilities of self-assembled monolayers on gold generated from progressively fluorinated alkanethiols,” *Langmuir*, vol. 19, no. 8, pp. 3288–3296, 2003.
- [316] N. V. Venkataraman, Stefan Zürcher, A. Rossi, S. Lee, N. Naujoks, and N. D. Spencer, “Spatial tuning of the metal work function by means of alkanethiol and fluorinated

- alkanethiol gradients,” *J. Phys. Chem. C*, vol. 113, no. 14, pp. 5620–5628, 2009.
- [317] D. M. Alloway *et al.*, “Tuning the Effective Work Function of Gold and Silver Using ω -Functionalized Alkanethiols: Varying Surface Composition through Dilution and Choice of Terminal Groups,” *J. Phys. Chem. C*, vol. 113, no. 47, pp. 20328–20334, 2009.
- [318] K. Asadi, Y. Wu, F. Cholamrezaie, P. Rudolf, and P. W. M. Blom, “Single-layer pentacene field-effect transistors using electrodes modified with self-assembled monolayers,” *Adv. Mater.*, vol. 21, no. 41, pp. 4109–4114, 2009.
- [319] R. Li *et al.*, “Direct structural mapping of organic field-effect transistors reveals bottlenecks to carrier transport,” *Adv. Mater.*, vol. 24, no. 41, pp. 5553–5558, 2012.
- [320] A. Kanjilal, L. Ottaviano, V. Di Castro, M. Beccari, M. G. Betti, and C. Mariani, “Pentacene grown on self-assembled monolayer: Adsorption energy, interface dipole, and electronic properties,” *J. Phys. Chem. C*, vol. 111, no. 1, pp. 286–293, 2007.
- [321] S. Tatara, Y. Kuzumoto, and M. Kitamura, “Surface properties of substituted-benzenethiol monolayers on gold and silver: Work function, wettability, and surface tension,” *Jpn. J. Appl. Phys.*, vol. 55, p. 03DD02, 2016.
- [322] C. Stadler, S. Hansen, I. Kröger, C. Kumpf, and E. Umbach, “Tuning intermolecular interaction in long-range-ordered submonolayer organic films,” *Nat. Phys.*, vol. 5, no. 2, pp. 153–158, 2009.
- [323] H. H. Choi, K. Cho, C. D. Frisbie, H. Sirringhaus, and V. Podzorov, “Critical assessment of charge mobility extraction in FETs,” *Nat. Mater.*, vol. 17, no. 1, pp. 2–7, 2017.
- [324] I. Campbell *et al.*, “Controlling Schottky energy barriers in organic electronic devices using self-assembled monolayers,” *Phys. Rev. B*, vol. 54, no. 20, pp. R14321–R14324, 1996.
- [325] D. Boudinet, G. Le Blevenec, C. Serbutoviez, J. M. Verilhac, H. Yan, and G. Horowitz, “Contact resistance and threshold voltage extraction in n -channel organic thin film transistors on plastic substrates,” *J. Appl. Phys.*, vol. 105, no. 8, p. 084510, 2009.
- [326] P. Marmont *et al.*, “Improving charge injection in organic thin-film transistors with thiol-based self-assembled monolayers,” *Org. Electron.*, vol. 9, no. 4, pp. 419–424, 2008.
- [327] X. Cheng *et al.*, “Controlling electron and hole charge injection in ambipolar organic field-effect transistors by self-assembled monolayers,” *Adv. Funct. Mater.*, vol. 19, no. 15, pp. 2407–2415, 2009.
- [328] K. Y. Wu, S. Y. Yu, and Y. T. Tao, “Continuous modulation of electrode work function with mixed self-assembled monolayers and its effect in charge injection,” *Langmuir*, vol. 25, no. 11, pp. 6232–6238, 2009.
- [329] U. Zschieschang, J. W. Borchert, M. Geiger, F. Letzkus, J. N. Burghartz, and H. Klauk, “Stencil lithography for organic thin- film transistors with a channel length of 300 nm,” *Org. Electron.*, vol. 61, no. June, pp. 65–69, 2018.
- [330] J. Collet, O. Tharaus, and D. Vuillaume, “Low-voltage, 30 nm channel length, organic transistors with a self-assembled monolayer as gate insulating films,” *Appl. Phys. Lett.*, vol. 76, p. 1941, 2000.
- [331] U. Palfinger *et al.*, “Fabrication of n- and p-type organic thin film transistors with minimized gate overlaps by self-aligned nanoimprinting,” *Adv. Mater.*, vol. 22, no. 45, pp. 5115–5119, 2010.
- [332] S. G. Higgins *et al.*, “Self-Aligned Megahertz Organic Transistors Solution-Processed

- on Plastic,” *Adv. Electron. Mater.*, vol. 1, no. 5, p. 1500024, 2015.
- [333] A. Tkatchenko, L. Romaner, O. T. Hofmann, E. Zojer, C. Ambrosch-Draxl, and M. Scheffler, “Van der waals interactions between organic adsorbates and at organic/inorganic interfaces,” *MRS Bull.*, vol. 35, no. 6, pp. 435–442, 2010.
- [334] I. N. Hulea, S. Russo, A. Molinari, and A. F. Morpurgo, “Reproducible low contact resistance in rubrene single-crystal field-effect transistors with nickel electrodes,” *Appl. Phys. Lett.*, vol. 88, no. 11, p. 113512, 2006.
- [335] D. Ovchinnikov, A. Allain, Y. S. Huang, D. Dumcenco, and A. Kis, “Electrical transport properties of single-layer WS₂,” *ACS Nano*, vol. 8, no. 8, pp. 8174–8181, 2014.
- [336] M. J. Mleczko *et al.*, “Contact Engineering High Performance n-Type MoTe₂ Transistors,” *Nano Lett.*, vol. 19, p. 6352–6362, 2019.
- [337] G. Horowitz, R. Hajlaoui, D. Fichou, and A. El Kassmi, “Gate voltage dependent mobility of oligothiophene field-effect transistors,” *J. Appl. Phys.*, vol. 85, no. 6, pp. 3202–3206, 1999.
- [338] A. B. Chwang and C. Daniel Frisbie, “Field effect transport measurements on single grains of sexithiophene: Role of the contacts,” *J. Phys. Chem. B*, vol. 104, no. 51, pp. 12202–12209, 2000.
- [339] R. A. Street and A. Salleo, “Contact effects in polymer transistors,” *Appl. Phys. Lett.*, vol. 81, no. 15, pp. 2887–2889, 2002.
- [340] K. P. Puntambekar, P. V. Pesavento, and C. D. Frisbie, “Surface potential profiling and contact resistance measurements on operating pentacene thin-film transistors by Kelvin probe force microscopy,” *Appl. Phys. Lett.*, vol. 83, no. 26, pp. 5539–5541, 2003.
- [341] L. Bürgi, T. J. Richards, R. H. Friend, and H. Sirringhaus, “Close look at charge carrier injection in polymer field-effect transistors,” *J. Appl. Phys.*, vol. 94, no. 9, pp. 6129–6137, 2003.
- [342] H. Klauk *et al.*, “Contact resistance in organic thin film transistors,” *Solid.state Electron.*, vol. 47, pp. 297–301, 2003.
- [343] E. J. Meijer, G. H. Gelinck, E. van Veenendaal, B.-H. Huisman, D. M. de Leeuw, and T. M. Klapwijk, “Scaling behavior and parasitic series resistance in disordered organic field-effect transistors,” *Appl. Phys. Lett.*, vol. 82, no. 25, pp. 4576–4578, 2003.
- [344] J. Zaumseil, K. W. Baldwin, and J. A. Rogers, “Contact resistance in organic transistors that use source and drain electrodes formed by soft contact lamination,” *J. Appl. Phys.*, vol. 93, no. 10, pp. 6117–6124, 2003.
- [345] G. B. Blanchet, C. R. Fincher, M. Lefenfeld, and J. A. Rogers, “Contact resistance in organic thin film transistors,” *Appl. Phys. Lett.*, vol. 84, no. 2, pp. 296–298, 2004.
- [346] R. J. Chesterfield *et al.*, “Variable temperature film and contact resistance measurements on operating n-channel organic thin film transistors,” *J. Appl. Phys.*, vol. 95, no. 11 I, pp. 6396–6405, 2004.
- [347] N. Yoneya, M. Noda, N. Hirai, K. Nomoto, M. Wada, and J. Kasahara, “Reduction of contact resistance in pentacene thin-film transistors by direct carrier injection into a few-molecular-layer channel,” *Appl. Phys. Lett.*, vol. 85, no. 20, pp. 4663–4665, 2004.
- [348] S. H. Jin, C. A. Lee, K. D. Jung, H. Shin, B. G. Park, and J. D. Lee, “Performance improvement of scaled-down top-contact OTFTs by two-step-deposition of pentacene,” *IEEE Electron Device Lett.*, vol. 26, no. 12, pp. 903–905, 2005.
- [349] K. Myny *et al.*, “Self-aligned surface treatment for thin-film organic transistors,” *Appl. Phys. Lett.*, vol. 88, no. 22, p. 222103, 2006.

-
- [350] A. Molinari, I. Gutiérrez, I. N. Hulea, S. Russo, and A. F. Morpurgo, "Bias-dependent contact resistance in rubrene single-crystal field-effect transistors," *Appl. Phys. Lett.*, vol. 90, no. 21, p. 212103, 2007.
- [351] W. L. Kalb, F. Meier, K. Mattenberger, and B. Batlogg, "Defect healing at room temperature in pentacene thin films and improved transistor performance," *Phys. Rev. B*, vol. 76, no. 18, p. 184112, 2007.
- [352] T. Minari, T. Miyadera, K. Tsukagoshi, Y. Aoyagi, and H. Ito, "Charge injection process in organic field-effect transistors," *Appl. Phys. Lett.*, vol. 91, no. 5, pp. 2005–2008, 2007.
- [353] D. Kumaki, T. Umeda, and S. Tokito, "Reducing the contact resistance of bottom-contact pentacene thin-film transistors by employing a Mo Ox carrier injection layer," *Appl. Phys. Lett.*, vol. 92, no. 1, p. 013301, 2008.
- [354] A. Benor and D. Knipp, "Contact effects in organic thin film transistors with printed electrodes," *Org. Electron.*, vol. 9, no. 2, pp. 209–219, 2008.
- [355] C. Reese and Z. Bao, "Detailed characterization of contact resistance, gate-bias-dependent field-effect mobility, and short-channel effects with microscale elastomeric single-crystal field-effect transistors," *Adv. Funct. Mater.*, vol. 19, no. 5, pp. 763–771, 2009.
- [356] H. Kim, R. C. Y. Auyeung, S. H. Lee, A. L. Huston, and A. Piqué, "Laser forward transfer of silver electrodes for organic thin-film transistors," *Appl. Phys. A*, vol. 96, no. 2, pp. 441–445, 2009.
- [357] S. P. Tiwari, W. J. Potscavage, T. Sajoto, S. Barlow, S. R. Marder, and B. Kippelen, "Pentacene organic field-effect transistors with doped electrode-semiconductor contacts," *Org. Electron.*, vol. 11, no. 5, pp. 860–863, 2010.
- [358] J. Smith *et al.*, "The influence of film morphology in high-mobility small-molecule: Polymer blend organic transistors," *Adv. Funct. Mater.*, vol. 20, no. 14, pp. 2330–2337, 2010.
- [359] M. Kitamura, Y. Kuzumoto, W. Kang, S. Aomori, and Y. Arakawa, "High conductance bottom-contact pentacene thin-film transistors with gold-nickel adhesion layers," *Appl. Phys. Lett.*, vol. 97, no. 3, p. 033306, 2010.
- [360] A. Hoppe, D. Knipp, B. Gburek, A. Benor, M. Marinkovic, and V. Wagner, "Scaling limits of organic thin film transistors," *Org. Electron.*, vol. 11, no. 4, pp. 626–631, 2010.
- [361] Y. Xu, R. Gwoziecki, I. Chartier, R. Coppard, F. Balestra, and G. Ghibaudo, "Modified transmission-line method for contact resistance extraction in organic field-effect transistors," *Appl. Phys. Lett.*, vol. 97, p. 063302, 2010.
- [362] C. W. Sohn, T. U. Rim, G. B. Choi, and Y. H. Jeong, "Analysis of contact effects in inverted-staggered organic thin-film transistors based on anisotropic conduction," *IEEE Trans. Electron Devices*, vol. 57, no. 5, pp. 986–994, 2010.
- [363] Y. Y. Noh, X. Cheng, M. Tello, M. J. Lee, and H. Sirringhaus, "Controlling contact resistance in top-gate polythiophene-based field-effect transistors by molecular engineering," *Semicond. Sci. Technol.*, vol. 26, no. 3, p. 034003, 2011.
- [364] J. Youn, G. R. Dholakia, H. Huang, J. W. Hennek, A. Facchetti, and T. J. Marks, "Influence of thiol self-assembled monolayer processing on bottom-contact thin-film transistors based on n-type organic semiconductors," *Adv. Funct. Mater.*, vol. 22, no. 9, pp. 1856–1869, 2012.
- [365] M. Kitamura, Y. Kuzumoto, and Y. Arakawa, "Short-channel, high-mobility organic thin-film transistors with alkylated dinaphthothienothiophene," *Phys. Status Solidi C*,
-

-
- vol. 10, no. 11, pp. 1632–1635, 2013.
- [366] A. Kumatani, Y. Li, P. Darmawan, T. Minari, and K. Tsukagoshi, “On practical charge injection at the metal/organic semiconductor interface,” *Sci. Rep.*, vol. 3, p. 1026, 2013.
- [367] S. Singh *et al.*, “Reduction of contact resistance by selective contact doping in fullerene n-channel organic field-effect transistors,” *Appl. Phys. Lett.*, vol. 102, no. 15, p. 153303, 2013.
- [368] K. Nakayama *et al.*, “High-Mobility Organic Transistors with Wet-Etch-Patterned Top Electrodes: A Novel Patterning Method for Fine-Pitch Integration of Organic Devices,” *Adv. Mater. Interfaces*, vol. 1, no. 5, p. 1300124, 2014.
- [369] T. Uemura *et al.*, “Split-gate organic field-effect transistors for high-speed operation,” *Adv. Mater.*, vol. 26, no. 19, pp. 2983–2988, 2014.
- [370] K. Fukuda, Y. Takeda, M. Mizukami, D. Kumaki, and S. Tokito, “Fully solution-processed flexible organic thin film transistor arrays with high mobility and exceptional uniformity,” *Sci. Rep.*, vol. 4, p. 3947, 2014.
- [371] H. J. Yun *et al.*, “Dramatic inversion of charge polarity in diketopyrrolopyrrole-based organic field-effect transistors via a simple nitrile group substitution,” *Adv. Mater.*, vol. 26, no. 43, pp. 7300–7307, 2014.
- [372] T. Zimmerling and B. Batlogg, “Improving charge injection in high-mobility rubrene crystals: From contact-limited to channel-dominated transistors,” *J. Appl. Phys.*, vol. 115, no. 16, p. 164511, 2014.
- [373] M. Uno *et al.*, “Short-Channel Solution-Processed Organic Semiconductor Transistors and their Application in High-Speed Organic Complementary Circuits and Organic Rectifiers,” *Adv. Electron. Mater.*, vol. 1, no. 12, p. 1500178, 2015.
- [374] U. Kraft, J. E. Anthony, E. Ripaud, M. A. Loth, E. Weber, and H. Klauk, “Low-voltage organic transistors based on tetraceno[2,3-b]thiophene: Contact resistance and air stability,” *Chem. Mater.*, vol. 27, no. 3, pp. 998–1004, 2015.
- [375] G. De Tournadre, F. Reisdorffer, R. Rödel, O. Simonetti, H. Klauk, and L. Giraudet, “High voltage surface potential measurements in ambient conditions: Application to organic thin-film transistor injection and transport characterization,” *J. Appl. Phys.*, vol. 119, no. 12, p. 125501, 2016.
- [376] T. Uemura *et al.*, “On the Extraction of Charge Carrier Mobility in High-Mobility Organic Transistors,” *Adv. Mater.*, vol. 28, no. 1, pp. 151–155, 2016.
- [377] S. Lai, P. Cosseddu, and A. Bonfiglio, “A method for direct contact resistance evaluation in low voltage coplanar organic field-effect transistors,” *Appl. Phys. Lett.*, vol. 110, no. 15, p. 153304, 2017.
- [378] Y. Hu, D. X. Cao, A. T. Lill, L. Jiang, C. Di, and X. Gao, “Effect of Alkyl-Chain Length on Charge Transport Properties of Organic Semiconductors and Organic Field-Effect Transistors,” *Adv. Electron. Mater.*, vol. 4, p. 11800175, 2018.
- [379] L. L. Jiang *et al.*, “Realizing low-voltage operating crystalline monolayer organic field-effect transistors with a low contact resistance,” *J. Mater. Chem. C*, vol. 7, no. 12, pp. 3436–3442, 2019.
- [380] A. F. Paterson *et al.*, “On the Role of Contact Resistance and Electrode Modification in Organic Electrochemical Transistors,” *Adv. Mater.*, vol. 31, p. 1902291, 2019.
-

Publications

Scientific papers

J. W. Borchert, U. Zschieschang, F. von Wrochem, B. Peng, P. K. L. Chan, S. Ludwigs, H. Klauk, *in preparation*

J. W. Borchert, U. Zschieschang F. Letzkus, M. Giorgio, M. Caironi, J. N. Burghartz, S. Ludwigs, H. Klauk, *in preparation*

J. W. Borchert, U. Zschieschang, F. Letzkus, M. Giorgio, R. T. Weitz, M. Caironi, J. N. Burghartz, S. Ludwigs, H. Klauk, Flexible low-voltage high-frequency organic thin-film transistors, *Science Advances*, 6 (2020) eaaz5156

J. W. Borchert, B. Peng, F. Letzkus, J. N. Burghartz, P. K. L. Chan, K. Zojer, S. Ludwigs, H. Klauk, Small contact resistance and high-frequency operation of flexible low-voltage inverted coplanar organic transistors, *Nature Communications*, 10 (2019) 1119

J. W. Borchert, U. Zschieschang, F. Letzkus, M. Giorgio, M. Caironi, J. N. Burghartz, S. Ludwigs, H. Klauk, Record static and dynamic performance of flexible organic thin-film transistors, *2018 IEEE International Electron Devices Meeting (IEDM)*, DOI: 10.1109/IEDM.2018.8614641

U. Zschieschang, J. W. Borchert, M. Giorgio, M. Caironi, F. Letzkus, J. N. Burghartz, U. Waizmann, J. Weis, S. Ludwigs, H. Klauk, Roadmap to gigahertz organic transistors, *Advanced Functional Materials*, 30 (2020) 1903812

S. Elsaegh, U. Zschieschang, J. W. Borchert, H. Klauk, H. Zappe, Y. Manoli, Compact DC modeling of organic thin-film transistors including their parasitic non-linear contact effects based on a novel extraction method, *IEEE Transactions on Electron Devices*, 66 (2019) 4907

M. Krammer, J. W. Borchert, A. Petritz, E. Karner-Petritz, G. Schider, B. Stadlober, H. Klauk, K. Zojer, Critical evaluation of organic thin-film transistor models, *Crystals*, 9 (2019) 85

U. Zschieschang, J. W. Borchert, M. Geiger, F. Letzkus, J. N. Burghartz, H. Klauk, Stencil lithography for organic thin-film transistors with a channel length of 300 nm, *Organic Electronics*, 61 (2018) 65

Other publications not related to the subject of this thesis

J. W. Borchert, I. A. Stewart, S. Ye, A. R. Rathmell, B. J. Wiley, K. I. Winey, Effects of length dispersity and film fabrication on the sheet resistance of copper nanowire transparent conductors, *Nanoscale*, 7 (2015) 14496

C. A. Kendziora, R. Furstenberg, M. Papantonakis, V. Nguyen, J. Borchert, J. Byers, R. A. McGill, Infrared photothermal imaging of trace explosives on relevant substrates, *Proc. SPIE*, 8709 (2013) 87090O-1

J. Großer, R. Furstenberg, C. A. Kendziora, M. Papantonakis, J. Borchert, R. A. McGill, Modeling of the heat transfer in laser-heated particles on surfaces, *International Journal of Heat and Mass Transfer*, 55 (2012) 8038

S. M. O'Malley, S. Y. Yi, R. Jimenez, J. Corgan, J. Borchert, J. Kuchmek, M. R. Papantonakis, R. A. McGill, D. M. Bubb, Matrix-assisted pulsed laser deposition of croconic acid, a diprotic organic ferroelectric, *Applied Physics A: Materials Science & Processing*, 105 (2011) 635

S. M O'Malley, M. Amin, J. Borchert, R. Jimenez, M. Steiner, J. M. Fitz-Gerald, Formation of rubrene nanocrystals by laser ablation in liquids utilizing MAPLE deposited thin films, *Chemical Physics Letters*, 595 (2014) 171

Conferences

- International Workshop on Active- Matrix Flatpanel Displays and Devices
Kyoto, Japan
Invited Oral Presentation July 2019
- Materials Research Society (MRS) Spring Meeting
Phoenix, AZ, USA
Oral Presentation, Poster (accepted) April 2019, 2020
- IEEE International Electron Devices Meeting (IEDM)
San Francisco, CA, USA
Oral Presentation December 2018
- SPIE Optics & Photonics
San Diego, CA, USA
Oral Presentation August 2018, 2020
- European Conference on Molecular Electronics (ECME)
Linköping, Sweden
Poster August 2019
- International Conference on Organic Electronics (ICOE)
Bordeaux, France
Poster June 2018
- Materials for Organic Electronics
Heidelberg, Germany
Poster June 2018
- Materials Research Society (MRS) Fall Meeting
Boston, MA, USA
Oral Presentation November 2017